

THÈSE

Presented at

SHANGHAI JIAOTONG UNIVERSITY, SHANGHAI, CHINA

Prepared at

L'U.F.R DES SCIENCES ET TECHNIQUES
DE L'UNIVERSITÉ DE FRANCHE-COMTÉ

in collaboration with

DEPARTMENT OF APPLIED MECHANICS AND ENGINEERING
SOUTHWEST JIAOTONG UNIVERSITY, CHENGDU, CHINA

in order to obtain the

**GRADE DE DOCTEUR
DE L'UNIVERSITÉ DE FRANCHE-COMTÉ
Spécialité : Science pour l'ingénieur**

and the

DOCTOR DEGREE OF SOUTHWEST JIAOTONG UNIVERSITY

**EXPERIMENTS, MODELLING AND NUMERICAL
SIMULATION OF THE SINTERING PROCESS FOR
METALLIC OR CERAMIC POWDERS**

par

Jiupeng SONG

Defence on 2 April 2007, defence committee:

Reviewers	Randall GERMAN	Professor, Mississippi State University (USA)
	Yves BIENVENU	Professor, Ecole des Mines de Paris (France)
	Jean-François HÉTU	Group leader, IMI, NRC-CNRC (Canada)
Chairman	Xiangguo ZENG	Professor, Sichuan University (China)
Examinators	Hua ZHAO	Professor, Southwest Jiaotong University (China)
	Lixun CAI	Professor, Southwest Jiaotong University (China)
Advisor	Jean-Claude GELIN	Professor, ENSMM de Besancon (France)
Co-advisor	Thierry BARRIÈRE	Associate Professor, HDR, ENSMM de Besancon (France)

Abstract

Sintering process is the important stage in powder injection moulding (PIM). Predicting the shrinkages and mechanical properties of the final sintered components is important for the design of injection mould and process parameters. The thesis focuses on the modeling, identification and numerical simulations of the sintering process. The experiment investigations are conducted for the sintering of PIM component in 316L stainless steel and alumina.

The macroscopic sintering model based on the continuum mechanics is adopted in the study. In the employed thermal elasto-viscoplastic constitutive law, the expressions of shear and bulk viscosity modulus are derived from the viscous-elastic analogy and the creep models for diffusions. The empirical equations for evaluating the sintering stress and grain growth are introduced in the sintering model. In order to obtain the accurate simulation results, the identification for the model's parameters are conducted. For the sintering parts in 316L stainless steel powders, the densification is very fast and mainly accomplished in a narrow temperature range. The identifications are carried out for the three sintering stages respectively. The gravitational beam-bending tests are used to identify the parameters in the viscosity modulus. Afterwards, the sintering experiments in dilatometer are carried out to obtain the *in-situ* shrinkage curves. It results in the next identification for the parameters in the expression of sintering stress. For the sintering parts in alumina, the densification occurs in the wider temperature range with relatively low rates. The identification for the parameters in the sintering model is conducted for the entire sintering process with *in-situ* shrinkage rate and shrinkage curves obtained from dilatometer tests. The determined viscosity and sintering stress for both materials are reasonable by comparing with the data in literatures.

The numerical simulations based on the presented sintering model and identified parameters are realized by finite element method. Both the in-house software built on Matlab[®] and the commercial software Abaqus[®] are used for the simulations of

sintering. The inhomogeneous green density distributions are imported into the sintering simulations. It represents the effect of segregation between the powders and binders in injection moulding process. The initial density fields are obtained by the bi-phasic injection simulations. The simulations have been carried out for the sintering of several components. The obtained results show that gravity, friction and inhomogeneous green density have the apparent effects on the uneven shrinkages and distortions of the sintered parts. The strengths of the sintered components are predicted based on the evaluated density issued of the numerical simulations and a series of empirical expressions. The simulation results of shrinkages, distortions and strength are compared with the experimental ones.

Key words: Sintering, Powder injection moulding, Modelling, Identification, Numerical simulation

Table of Contents

List of Figures	VII
List of Tables	XIV
List of Symbols.....	XV
Acknowledgments.....	XX
Chapter 1 Introduction	1
<i>1.1 Research Motivations</i>	<i>1</i>
<i>1.2 Research Objectives</i>	<i>2</i>
<i>1.3 Thesis Outline.....</i>	<i>4</i>
Chapter 2 Literature Review	5
<i>2.1 Introduction of sintering.....</i>	<i>5</i>
2.1.1 Driving Forces of Sintering.....	5
2.1.2 Sintering Mechanisms	7
2.1.3 Stages of Sintering	8
<i>2.2 Physical Models and Numerical Simulation of Sintering.....</i>	<i>9</i>
2.2.1 Microscopic Models.....	10
2.2.1.1 Models of Initial Stage.....	10
2.2.1.2 Intermediate Stage Models.....	13
2.2.1.3 Models of Final Stage	14
2.2.1.4 Combined-stage Model	15
2.2.2 Mesoscopic Models.....	15
2.2.3 Macroscopic Models	18
2.2.3.1 Phenomenological Model for Constitutive Parameters.....	19
2.2.3.2 Micromechanical Model of Constitutive Parameters	19
2.2.3.3 Experimental Model for Constitutive Parameters	20
<i>2.3 Summary.....</i>	<i>21</i>
Chapter 3 Experimental Investigations of Sintering Processes	24
<i>3.1 Material Characterization.....</i>	<i>24</i>
3.1.1 316L Stainless Steel PIM Feedstock	24
3.1.2 Alumina PIM Feedstock.....	25
<i>3.2 Specimen Preparation</i>	<i>26</i>
3.2.1 Injection Molding.....	26
3.2.2 Debinding.....	27
3.2.3 Presintering	29
<i>3.3 Sintering Procedures</i>	<i>30</i>

3.3.1 Sintering in Furnace	31
3.3.3 Gravitational Beam-bending Tests in Sintering.....	32
3.3.4 The tests of <i>In-situ</i> Sintering Strength.....	33
3.3.5 Testing Procedures of Post-sintering Strength.....	35
<i>3.4 Experimental Results for 316L Stainless Steel Powders.....</i>	<i>36</i>
3.4.1 Effects of Debinding and Presintering	36
3.4.2 Effects of Temperature Cycle on Densification.....	39
3.4.3 Effects of Heating Rate on Densification	40
3.4.4 Microstructural Evolutions.....	41
3.4.5 Measured <i>In-situ</i> Strength	43
3.4.6 Deflections in Gravitational Beam-bending Tests	44
3.4.7 Measured Post-sintering Strength.....	46
<i>3.5 Experimental Results for Alumina Powders.....</i>	<i>49</i>
3.5.1 Effects of Debinding	49
3.5.2 Densification Behaviors in Non-isothermal Sintering.....	50
3.5.2.1 Effects of Temperature on Densification in Non-isothermal Sintering Conditions.....	51
3.5.2.2 Effects of Heating Rate on Densification in Non-isothermal Sintering	53
3.5.3 Densification Behaviors in Isothermal Sintering.....	55
3.5.4 Microstructural Evolutions.....	58
3.5.4.1 Effects of Temperature on Microstructures	58
3.5.4.2 Effects of Heating Rate on Microstructures	59
3.5.4.3 Effects of Holding Time on Microstructures.....	60
<i>3.6 Conclusions</i>	<i>60</i>
Chapter 4 Development of Phenomenological Sintering Model.....	62
<i>4.1 General Definitions</i>	<i>62</i>
<i>4.2 Governing Equations.....</i>	<i>63</i>
4.2.1 Mass Conservation	63
4.2.3 Energy Conservation	64
<i>4.3 Boundary Conditions.....</i>	<i>65</i>
4.3.1 Mechanical Boundary Conditions	65
<i>4.4 Constitutive Sintering Law</i>	<i>66</i>
4.4.1 Thermo-elasto-viscoplastic Model of Sintering Bodies	66
4.4.2 Elastic Strain of Sintering Body.....	68
4.4.3 Thermal Strain in Sintering Body.....	69
<i>4.5 Determination of Viscosity Modulus.....</i>	<i>73</i>
4.5.1 Elastic-Viscous Analogy	73
4.5.2 Uniaxial Viscosity	74
4.5.3 Viscous Poisson's Ratio.....	76
<i>4.6 Determination of Sintering Stress.....</i>	<i>77</i>
4.6.1 Sintering Stress for 316L Stainless Steel Powders	78

4.6.2 Sintering Stress for Alumina Powders.....	79
4.7 Grain Growth.....	79
4.7.1 Grain Growth Model for 316L Stainless Steel	80
4.7.2 Grain Growth Model for Alumina.....	80
4.8 Model for Strength Prediction.....	81
4.8.1 Microstructural factors	82
4.8.2 Strength Prediction Model.....	84
4.9 Summary.....	85
Chapter 5 Identification of the Parameters for Sintering Model	87
5.1 Principles of Identification through Experiments.....	87
5.1.1 Gravitational Beam-bending Tests	87
5.1.2 Free Sintering in Dilatometer	89
5.2 Parameter Identification for 316L Stainless Steel.....	90
5.2.1 Identification of the Parameters for Viscosity Modulus	90
5.2.2 Identification of the Sintering Stress Parameters.....	92
5.2.3 Discussions.....	94
5.3 Parameter Identification for Alumina	95
5.3.1 Identification Algorithm.....	95
5.3.2 Identification for Non-isothermal Sintering	97
5.3.3 Identification for Isothermal Sintering	101
5.3.5 Discussions.....	106
5.4 Summary.....	110
Chapter 6 Numerical Simulation of Sintering Processes.....	112
6.1 FE Simulation of Sintering Processes	112
6.1.1 FE Simulation by the Code on Matlab®	112
6.1.2 FE Simulation by Abaqus®	114
6.1.2.1 Realization by User Subroutine CREEP	114
6.1.2.2 Realization with User Subroutine UMAT	116
6.2 Sintering Simulations for Tensile Test Specimens.....	117
6.2.1 Simulations on Matlab®	118
6.2.1.1 Simulations with the Homogeneous Green Density.....	118
6.2.1.2 Simulations with the Inhomogeneous Green Density	121
6.2.2 Simulations on Abaqus®	124
6.2.2.1 Effects of Gravity on Shrinkage.....	125
6.2.2.2 Effects of Inhomogeneous Green Density on Shrinkage.....	126
6.2.2.3 Effects of Friction on Shrinkage	129
6.3 Sintering Simulations for the Wheel Part.....	132
6.3.1 Numerical Prediction of the Density and Shrinkages in the Sintered Part	132
6.3.2 Shrinkages Measured in Experiments	135

6.4 Sintering Simulations for Hip Implant Part	137
6.4.1 Heat Transfer Analysis for Hip Implant	138
6.4.2 Viscous Analysis for Sintering of Hip Implant.....	139
6.5 Simulations for Beam-bending Tests in Sintering.....	142
6.6 Evaluation of the Mechanical Strength.....	146
6.6.1 Evaluation of the Post-sintering Strength.....	146
6.6.2 Evaluation of the <i>In-situ</i> Sintering Strength.....	147
6.7 Summary.....	149
Chapter 7 Conclusions and Perspectives	152
7.1 Conclusions	152
7.1.1 Improvements from Sintering Experiments	152
7.1.2 Improvements from Modeling and Simulation for Sintering Process	153
7.1.3 Complete PIM Process Modeling and Simulation	156
7.2 Future Work.....	157
Appendix: Bi-phasic Injection Simulation for Predicting Segregation in PIM.....	159
A.1 Governing Equations Based on Mixture Theory.....	159
A.1.1 Determination of Filling Flow Front	159
A.1.2 Volume Saturation and Mass Conservation.....	160
A.1.3 Momentum Conservation and Exchange.....	160
A.2 Viscous Behaviors for Bi-phasic Modelling.....	161
Bibliography.....	163

List of Figures

Figure 2.1: Two-sphere sintering model showing that the reduction of the free energy during sintering by the formation of interparticle bond instead of the free surfaces of solid-vapor interfaces.6

Figure 2.2: Grain growth reduces the free energy of the sintering body by eliminating the grain boundary area.7

Figure 2.3: Neck growth between three particles to show various mass transport paths during sinter bonding (Adapted from [GER 97]).8

Figure 2.4: Microstructure evolutions in PIM sintering involving: (a) loose powder at the beginning of sintering, (b) neck formation and growth in the initial stage, (c) Interconnected pores in the intermediate stage, and (d) isolated pores and grain growth in the final stage (Adapted from [GER 97]).8

Figure 2.5: Geometrical description of the two-sphere particle model to describe the neck growth and densification in the initial sintering stage. 11

Figure 2.6: The interconnected pores in cylindrical shape located on the boundaries of tetrakaidecahedron grains in the intermediate stage of sintering [GER 96]. 13

Figure 2.7: The isolated spherical pores located at the boundary corners tetrakaidecahedron grains during the final sintering stage [GER 96]. 14

Figure 2.8: Two-dimensional kinetic Monte Carlo Potts model for the mesoscopic simulations of microstructural evolutions in porous materials during sintering process [MOR 04]. 16

Figure 2.9: Microstructural evolutions obtained by mesoscopic simulations based on two-dimensional kinetic Monte Carlo Potts model for sintering. (Adapted from [BRA 05]). 17

Figure 3.1: SEM photo of the PIM feedstock composed of gas-atomized 316L stainless steel powders and wax-based binders. 25

Figure 3.2: SEM photographs of the PIM feedstock composed of alumina powders and binders. 26

Figure 3.3: Injection molding machine and the designed molds in the experiments [BAR 00]. 27

Figure 3.4: Debinding oven and batch furnace used in the experiments. 28

Figure 3.5: Heating cycles associated to the debinding process for the injection molded parts in 316L stainless steel powders: (a) carried out in oven, (b) in batch furnace subsequently. 29

Figure 3.6: Thermal cycles of the debinding stage II at 500 °C for 1 hour and the subsequent presintering at 800 °C or 900 °C for 1 hour, corresponding to 316L stainless steel injection molded parts in the same batch furnace. 30

Figure 3.7: The horizontal dilatometer used in the experiments: (a) photograph of the

equipment, (b) sample holder and container in dilatometer [NET ETH].....	32
Figure 3.8: The sketch of gravitational beam-bending tests in sintering process, experiments carried in batch furnace to determine the viscosity of sintered body.....	33
Figure 3.9: A section view of the Flaming Tensile Tester (FTT), used to measure the transverse rupture strength (TRS) of <i>in-situ</i> sintering and post-sintering [OLE 01].....	34
Figure 3.10: The apparatus used for flaming tensile tests.....	34
Figure 3.11: The apparatus used for tensile tests: (a) before loading, (b) after rupture.....	35
Figure 3.12: Evolution of the mass and pycnometer volume in debinding and presintering process due to the removal of binder.....	36
Figure 3.13: The SEM photos on specimens: (a) powders and the remained binders after debinding stage I in the oven, (b) almost total removal of the binder and formation of the necks between the particles after the debinding stage II and presintering in furnace.	37
Figure 3.14: The relative density and theoretical density of the presintered 316L stainless steel specimens, obtained by experiments.	38
Figure 3.15: Appearance of the 316L stainless steel tensile test specimens at different stages during debinding and presintering processes: (a) From molded part to the debinded one after stage I, it becomes fragile but no shrinkages after stage I debinding in the oven, (b) From the part after stage I debinding to the one after stage II debinding and presintering in the furnace, the part reaches the strength of 100 MPa from the fragile state while it undergoes a small shrinkage of 0.5%.	39
Figure 3.16: Piloting of the temperature cycle and the induced evolution in shrinkage. Sintering of the cylindrical specimen in 316L stainless steel powders, heating to 1360 °C at rate 8 °C/min then holding it for 1 h.	40
Figure 3.17: Shrinkage rates vs. heating rates, obtained by sintering experiments of 316L stainless steel powder in dilatometer.	41
Figure 3.18: Microstructures on surfaces of the specimens in 316L stainless steel powder sintered under vacuum conditions. Except for Figure (h), the observed specimens were heated to different temperature with heating rate 5 °C/min then cooled directly with a rate 20 °C/min. Figure (h) shows the result of sintering that includes an additional holding period for 1 hour before the cooling.....	43
Figure 3.19: <i>In-situ</i> strength measured by flaming tensile tests on presintered specimens in 316L stainless steel powders.	44
Figure 3.20: Deflections of the bending specimens in 316L stainless steel powders after heating to different temperatures then cooling rapidly to room temperature in the batch furnace, no holding period is applied.....	45
Figure 3.21: Sintering deflections and deflection rates of the bending specimens in 316L	

stainless steel powders.....	46
Figure 3.22: The stress vs. stain curves obtained by tensile tests for 316L stainless steel specimens, sintered at different temperatures.....	47
Figure 3.23: Some of the tensile test specimens in 316L stainless steel sintered at different temperatures.	47
Figure 3.24: Influence of sintering temperature on the ultimate strain and stress, obtained by tensile tests on 316L stainless steel specimens.	48
Figure 3.25: Transverse rupture strength (TRS) of 316L stainless steel specimens sintered at different temperatures, obtained by three-point bending tests.....	49
Figure 3.26: Evolution of the mass and pycnometer volume of molded alumina specimens obtained by solvent and thermal debinding processes.....	50
Figure 3.27: Shrinkage and shrinkage rate vs. sintering time measured by the sintering experiment on alumina specimen in dilatometer corresponding to the thermal cycle of heating to 1550 °C at 10 °C/min, then holding for 2h, and cooling at 20 °C/min: (a) shrinkage, (b) shrinkage rate.....	51
Figure 3.28: Shrinkage and shrinkage rate versus sintering temperature, measured by the sintering experiment on alumina specimen in dilatometer. Heating to 1600 °C at rate 10 °C/min without holding.	52
Figure 3.29: Shrinkage and shrinkage rate versus temperature measured through the sintering experiments on alumina specimens in dilatometer: (a) shrinkage, (b) shrinkage rate. The thermal cycles are heating to 1600 °C at rate 2.5 °C/min, 5 °C/min, 10 °C/min, 15 °C/min and 20 °C/min respectively.....	54
Figure 3.30: The measured peak shrinkage rates and the corresponded temperatures vs. the constant values of heating rate of alumina specimens sintered in dilatometer: (a) peak shrinkage rate, (b) temperature at peak shrinkage rate. The thermal cycles consist in heating up to 1600 °C by different heating rates from 2.5 °C/min to 20 °C/min.....	55
Figure 3.31: The measured shrinkage curves in the sintering with the thermal cycles heating to various peak temperatures from 1300 °C to 1600 °C at 20 °C/min, and then holding for 2 h.....	56
Figure 3.32: Evolution of shrinkage and relative density in the isothermal sintering at various temperatures from 1300 °C to 1600 °C for 2 h. The previous thermal cycle is heating to temperatures of isothermal sintering at 20 °C/min.....	57
Figure 3.33: The microstructures of the sintered alumina specimens after the thermal cycles of heating at 10 °C/min to various peak temperatures without holding and then cooling to room temperature at 20 °C/min.	58
Figure 3.34: The microstructures of the sintered alumina specimens after the thermal cycles of heating to 1600 °C at various heating rates without holding and then cooling to	

room temperature at 20 °C/min.....	59
Figure 3.35: The microstructures of the sintered alumina specimens after the thermal cycles of heating to 1550 °C at 10 °C/min without or with holding time , and then cooling to room temperature at 20 °C/min.....	60
Figure 4.1: Thermo-elasto-viscoplastic model of sintering bodies for the entire sintering process including elastic strain, thermal strain and viscoplastic strain in series.....	67
Figure 4.2: Shrinkage curves measured by dilatometer showing the viscoplastic and thermal strains of the sintering bodies.	68
Figure 4.3: The sketches of Newtonian and Bingham models for viscoplastic models.	70
Figure 4.4: A diagram to show the local stress state of the sintering body that undergoes shape and volume changes.....	71
Figure 4.5: The relationship between the viscous Poisson’s ratio and relative density of the porous materials.....	77
Figure 4.6: Comparison of the proposed models to determine the neck size ratio.	82
Figure 4.7: The relationship between stress concentration factor and neck size Ratio.	84
Figure 5.1: A sketch of the simply supported beam model for beam-bending tests.....	88
Figure 5.2: Variation of grain size in sintering to 10 °C/min to different temperatures without holding.	91
Figure 5.3: Fitting of equation (4.33) with identified parameter <i>A</i> according to the uniaxial viscosity values obtained by gravitational bending tests.	92
Figure 5.4: The shrinkage curve obtained by numerical simulation with identified parameters and the experimental one obtained by dilatometer test, corresponding to heating up to 1360 °C at rate 8 °C/min and then holding 1 h.	93
Figure 5.5: The shrinkage rate and shrinkage of alumina powders in the non-isothermal sintering at various heating rates, obtained from the numerical model with the parameters in literatures. The corresponded experimental curves from dilatometer test are shown for comparison.	98
Figure 5.6: The shrinkage rate and shrinkage of alumina powders in the non-isothermal sintering at different heating rates, obtained from the numerical model with the identified model parameters. The corresponded experimental curves from dilatometer are shown for comparison.	100
Figure 5.7: The shrinkage rate and shrinkage of alumina powders in the non-isothermal sintering with various heating rates, issued of the calculations based on the numerical model. The parameters in sintering model are obtained by interpolation from the identified ones. The corresponded experimental curves from dilatometer are shown for comparison.....	101

Figure 5.8: The shrinkage and relative density of alumina specimens just after heating to various temperatures at 20 °C/min, without holding.....102

Figure 5.9: The uniaxial viscosity and sintering stress versus the temperature in the heating stage at 20 °C/min, obtained by the model with the identified parameters presented in Table 5.5.....103

Figure 5.10: Evolution of the grain size versus temperature in the heating stage at 20 °C/min, obtained by the model with identified parameters presented in Table 5.5.....103

Figure 5.11: The evolution of shrinkage rate in the thermal cycles in which it heats to 1300 °C and 1600 °C respectively and then holds for 2 h, obtained by the model with the identified parameters presented in Table 5.5 and Table 5.7. The experimental curves in dilatometer are shown for comparisons.....105

Figure 5.12: The evolution of shrinkage in the thermal cycles in which it heats to different temperatures and then holds for 2 h, obtained by the model with the identified parameters presented in Table 5.5 and Table 5.7. The experimental curves in dilatometer are shown for comparison.105

Figure 5.13: The calculated uniaxial viscosity of alumina specimens with the identified parameters as shown in Table 5.5 and Table 5.7: (a) in non-isothermal sintering at different heating rates, (b) in isothermal sintering after heating at 20 °C/min to different holding temperatures.....107

Figure 5.14: The calculated sintering stress of alumina specimens with the identified parameters as shown in Table 5.5 and Table 5.7: (a) in non-isothermal sintering at different heating rates, (b) in isothermal sintering after heating to different temperatures by 20 °C/min.109

Figure 6.1: Dimension of the tensile test specimens in 316L stainless steel feedstock after injection moulding.118

Figure 6.2: The FEM model for the tensile test specimen with the homogeneous initial relative density fixed at 0.6.119

Figure 6.3: Final contours of the relative density after sintering in the sintered tensile tests specimens, obtained by numerical simulation.....119

Figure 6.4: Dimensions of the tensile test specimens before and after sintering to show the shrinkage.120

Figure 6.5: Shrinkage of the sintered tensile test specimen in three orthogonal directions, obtained from a homogeneous green part.121

Figure 6.6: Initial contours of the relative density in the tensile test specimen made from 316L stainless steel powders, obtained by bi-phasic injection simulations.....122

Figure 6.7: Final contours of the relative density in the tensile test specimen after sintering, obtained numerical simulation.122

Figure 6.8: Shrinkage of the sintered tensile test specimen in three orthogonal directions, with inhomogeneous green density contours..... 123

Figure 6.9: Change in dimension of the tensile test specimens, obtained by experiments: (a) sintered part, (b) injection moulded part..... 124

Figure 6.10: FEM mesh for the sintering simulation of tensile test specimen. 124

Figure 6.11: Final shrinkages of sintered tensile test specimen in three orthogonal directions to show the effect of gravity..... 126

Figure 6.12: The initial relative density of tensile test specimen in 316L stainless steel powders, obtained from the bi-phasic injection simulation in 3D. 127

Figure 6.13: The evolution of relative density in sintering process at three selected nodes in the FEM model of tensile test specimen. 128

Figure 6.14: Final shrinkages of sintered tensile test specimen in three orthogonal directions indicating the effect of inhomogeneous green density and gravity on the shrinkage.129

Figure 6.15: Final shrinkages of sintered tensile test specimen in three orthogonal directions with the effects of friction, homogeneous green density and gravity..... 130

Figure 6.16: Final shrinkages of sintered tensile test specimen in three orthogonal directions with the effects of friction, inhomogeneous green density and gravity..... 131

Figure 6.17: Configurations for a wheel part in 316L stainless steel powder:..... 132

Figure 6.18: The FE model for sintering processes of the 316L stainless steel part in wheel shape. 133

Figure 6.19: Contours of the initial relative density, obtained from bi-phasic injection simulation. 133

Figure 6.20: Contours of the final relative density in the part sintered to 1360 °C at heating rate 8 °C/min, with 1 h of the last holding stage. 134

Figure 6.21: Final shrinkages of the sintered part in radial, tangential and thickness directions, resulting from simulation. 135

Figure 6.22: Positions of 20 points chosen to measure the shrinkages of the sintered part..... 135

Figure 6.23: Shrinkages of the sintered part in three different directions: (a) measured by vernier caliper at 20 chosen points, (b) obtained from FE simulation.136

Figure 6.24: Shapes of the hip implants: (a) medical product, (b) prototype in research after injection moulding. 137

Figure 6.25: FE model of the hip implant component. 137

Figure 6.26: Temperature field for the hip implant in alumina..... 138

Figure 6.27: Contours of the final relative density in the sintered hip implant..... 139

Figure 6.28: Shrinkage contours of the sintered hip implant in three orthogonal directions.140

Figure 6.29: Comparison of shrinkage variations between the simulation results from Abaqus® and the sintering experimental ones in dilatometer.140

Figure 6.30: Dimensional change of the hip implants in alumina: (a) injection moulded, (b) sintered.141

Figure 6.31: FE model for beam-bending tests under gravity in sintering furnace.....142

Figure 6.32: Density evolution and shape distortions of the bending test specimens in the sintering processes.144

Figure 6.33: Variation of the final shrinkages in sintered bending test specimens.145

Figure 6.34: Comparison of the deflections in simulations and experiments at middle position of the bending test specimens when it is heated to different temperatures in sintering.145

Figure 6.35: Numerical prediction for the yield strength and ultimate tensile strength of the sintered parts in 316L stainless steel and the experimental data for comparisons....147

Figure 6.36: Numerical prediction for the *in-situ* sintering strength of 316L stainless steel parts.148

List of Tables

Table 2.1: Values of the constants n , m and B in the neck growth Equation (2.3), [GER 96], [RAH 03].....	12
Table 3.1: Parameters of 316L stainless steel PIM feedstock.....	24
Table 3.2: Chemical compositions of 316L stainless steel powders.....	25
Table 3.3: Parameters of the alumina PIM feedstock.....	25
Table 3.4: Parameters of injection process for 316L stainless steel and alumina.....	27
Table 4.1: Analogy of linear elastic and viscous models.	74
Table 4.2: Empirical expressions proposed to calculate neck size ratio.....	82
Table 4.3: Material constants of thermal softening factor	85
Table 5.1: Identified material parameters of viscosity.....	92
Table 5.2: Identified values for sintering stress material parameter C for the thermal cycle heating up to 1360 °C at 8 °C/min then holding 1 h.	93
Table 5.3: Material parameters of alumina in [Kan 04].....	97
Table 5.4: Initial values for optimization of the parameters in the sintering model of alumina....	97
Table 5.5: Identified parameters in the sintering model of alumina in non-isothermal sintering at different hearing rates.....	99
Table 5.6: Parameters for various hearing rates in the sintering model of alumina in non-isothermal sintering, obtained by linear interpolation from Table 5.5.....	100
Table 5.7: Identified parameters in the sintering model of alumina for the isothermal sintering stage at various holding temperatures, after the heating stages at 20 °C/min.....	104
Table 6.1: Changes of the relative density due to sintering at three nodes in FEM model of the tensile test specimen.....	128
Table 6.2: Comparison in final dimensions of the sintered tensile test specimens between the experimental results and numerical simulations.....	131
Table 6.3: The maximum and minimum shrinkages under the effects of different factors.....	132
Table 6.4: Identified parameters in sintering model of alumina for the thermal cycle of hip implant in sintering.....	139
Table 6.5: Shrinkage values of alumina hip implant after sintering obtained from experiment [LIK 06].	141

List of Symbols

A_{ss} :	solid-solid interface (grain boundary) area
A_{sv} :	solid-vapor interface (surface) area
b :	width of the bending test specimen
\mathbf{B} :	strain rate interpolation matrix
c_0 :	heat capacity of porous material
\mathbf{C}_e :	elastic compliance matrix
D :	diameter of the powder particles
D_b :	grain boundary diffusion coefficient
D_{b0} :	grain boundary diffusion frequency
\mathbf{D}_e :	elastic stiffness matrix
D_s :	surface diffusion coefficient
D_{s0} :	surface diffusion frequency
D_v :	volume (lattice) diffusion coefficient
D_{v0} :	volume diffusion frequency
E :	elastic modulus for porous material
E_0 :	elastic modulus for wrought material
E_f :	free energy of the sintering body
$\dot{\epsilon}_{vp}$:	voluminal viscoplastic strain rate
\mathbf{f} :	body force applied in the sintering part
\mathbf{g} :	gravitational acceleration
G :	diameter of grain
G_0 :	shear viscosity modulus of wrought material

G_p :	shear viscosity modulus of porous material
$g(T)$:	thermal softening factor
h :	thickness of the bending test specimen
I :	second order identity tensor
I_z :	moment of inertia about z axis
k :	Boltzmann's constant
k_0 :	thermal conductivity of wrought material
K_c :	stress concentration factor
k_{eff} :	effective thermal conductivity of porous material
k_h :	heating rate
K_p :	bulk viscosity modulus of porous material
L :	instantaneous length of the specimen
L_0 :	initial length of the specimen
L_s :	span distance of the beam
m :	mass of the specimen
mf :	microstructural factors of the sintered components
M_z :	bending moment about z axis
n :	normal vector of the surface
N :	interpolation function in finite element formula
p_s :	pressure of sintering atmosphere
q :	unit loading due to the gravity of the beam
Q_b :	activation energy of grain boundary diffusion
Q_G :	activation energy for grain growth
Q_s :	activation energy of surface diffusion

Q_v :	activation energy of volume diffusion
Q_{vf} :	activation energy of viscous flow
R :	gas constant
r_0 :	radius of the powder particles
r_n :	neck surface radius
t :	time
T :	absoulute temperature
\mathbf{u} :	displacement field
\mathbf{u}_n	nodal values of displacement
$\dot{\mathbf{u}}_n$	nodal values of displacement rate
V_{ap} :	appaarent volume
V_{pores} :	volume of pores in porous material
V_{py} :	volume measure by pycnometer
V_{total} :	apparent volume of porous material
X :	diameter of the neck (sintering bonding) between the particles
\bar{X} :	spatial position in the model
α :	thermal expansion coefficient
δ :	deflection at middle position of the bending test specimen
$\dot{\delta}$:	deflection rate at the middle position of the bending test specimen
δ_b :	grain boundary thickness
δ_s :	thickness of surface diffusion
$\delta(i, j)$:	Kronecker's delta function
$\dot{\boldsymbol{\varepsilon}}$:	total strain rate
$\dot{\boldsymbol{\varepsilon}}_c$:	creep strain rate

$\dot{\epsilon}_e$	elastic strain rate
ϵ_{eng}	engineering strain of the specimen in tensile test
$\dot{\epsilon}_{th}$	thermal strain rate
ϵ_{true}	true strain of the specimen in tensile test
$\dot{\epsilon}_{vp}$	viscoplastic strain rate
$\dot{\epsilon}'_{vp}$	deviatoric viscoplastic strain rate
ϕ	dihedral angle
γ_{ss}	solid- solid interface energy or grain boundary energy
γ_{sv}	solid-vapor interface energy or surface energy
η_0	effective viscosity of wrought material
η_z	uniaxial viscosity of porous material
λ	uniaxial shrinkage of the specimen in dilatometer
$\dot{\lambda}$	uniaxial shrinkage rate of the specimen in dilatometer
μ_f	coefficient of friction
ν_e	elastic Poisson's ratio for porous material
ν_e^0	elastic Poisson's ratio for wrought material
ν_{vp}	viscous Poisson's ratio of porous material
θ	porosity factor of the materials
ρ	relative density of porous materials
ρ_0	initial relative density
ρ_{ap}	apparent density of porous materials
ρ_n	nodal values of relative density

ρ_{th}	theoretical density (the density of wrought material)
σ	Cauchy stress
σ'	deviatoric stress
σ_0	strength of wrought material
$\bar{\sigma}_0$	strength of the wrought materials at room temperature
σ_c	applied stress inducing creep
σ_f	distributed load of friction
σ_L	capillary stress or local sintering stress
σ_m	mean stress
σ_p	predicted strength by the model
σ_y^0	yield strength of wrought material
σ_y	yield strength of sintered component
σ_{UTS}^0	ultimate tensile strength of wrought material
σ_{UTS}	ultimate tensile strength of sintered component
τ	shear stress
Ω	atomic or molecular volume

Acknowledgments

I would like to express my sincere gratitude to my thesis advisors, Professor Jean-Claude Gelin (ENSMM, France) and Professor Baosheng Liu (Southwest Jiaotong University, China), for their guidance, encouragement and support in the entire duration of this research. Their vast knowledge on material processing technology and work enthusiasm for research are proved to be valuable in assisting me in performing this dissertation and building my career in research. I am also grateful to Dr. Thierry Barriere (ENSMM, France), the co-advisor of my thesis, for his continuous and constructive discussions, as well as his works on powder injection moulding.

I would like to thank Dr. Ghassaue Ayad (Femto-ST/LMARC, France) for his work on bi-phasic injection simulations as presented in the thesis. I am obligated to David Renault (Odesim Inc., France) for his program on sintering simulation on Matlab[®]. I am grateful to the mechanical engineers in LMARC Pascal Robinet, Camille Garcin and Betty Baudinot for their assistance on my experimental works. I would like thank Dr. Dimitriy Liksonov (LMARC) for his experimental work on hip implants.

I would like to thank Professor Randall M German (CAVS, Mississippi State University) for reviewing the thesis and participating in the defense. I also would like to thank Professor Yevs Bienvenu (Center of Material, Ecole de Mine de Paris) and Dr. Jean-François Héту (Industrial Material Institute, NRC-CNRC, Canada) for reviewing the thesis.

I would like to thank the French government for the scholarship for the co-tutorial Ph.D. student that makes me possible to carry out this research in France.

Finally but importantly, I extend my deepest gratitude to my wife Hanyu Li for her continuous supports throughout the course for preparing this thesis. I am also grateful for the encouragements and supports from my parents and parents-in-law.

Chapter 1 Introduction

1.1 Research Motivations

Powder injection molding (PIM) of ceramics was first demonstrated in USA in 1930s and was in commercial production by the 1940s. Afterwards it was employed to produce metallic products in 1970s. PIM includes four basic steps. The metallic or ceramic powders are mixed with the binder such as wax or polyethylene to produce the feedstock. The feedstock is subsequently injected into the mould cavities to get the green parts in desired shape. The injection machines and moulds used are the same as those used to inject plastics except that the parts have to be treated against wear by the hard inorganic powders injected. The following step is the removal of the binder, called debinding. The thermal, solvent or catalyst debinding are the common used methods. The sintering process is then employed to densify the porous parts after debinding. The final dimensions and properties are obtained after sintering.

PIM has the notable advantages as plastic injection moulding process. The parts can be made with high productivity, low cost, good accuracy, and the process is applicable to intricate shapes. Simultaneously, PIM has the remarkable attributes of powder metallurgy (PM). It can produce a wide range of components in refractory metals, composite materials, porous materials, high performance alloys, ceramics, and so on. PIM has been regarded as one of the most promising technologies to produce metallic or ceramic components. It has been used to manufacture various products for automotive, aerospace and aircraft, medical equipments, industrial tools, electronic equipments and so on [GER 03 a]. The market of the products manufactured by PIM is expanding constantly. It is predicted that the sale of PIM products will reach two billion US dollars towards the year 2010 [COR 04].

The sintering process for powder injection moulded parts does not differ significantly from that normally used for die-pressed compacts, but the large fraction of porosity (generally in the range of 30-50%) in the brown parts after debinding and

the small particle size makes sintering of PIM parts special, with large shrinkage (10-15%) and fast sintering kinetics. Under this condition, the questions associated to how to achieve the good dimensional accuracy and the desired mechanical properties is one of the key issues to extend the PIM process application fields.

For PIM technology, it is necessary to design the injection moulds and the related process according to the final properties of the components. In order to solve this inverse problem, the trial and error method is often used. Alternatively, numerical simulations are the cost-effective way to optimize the PIM process design. During the main steps of PIM, sintering is the final and major one. It determines the final dimensional accuracy and mechanical properties of the components. All the defects induced in the previous steps, including the mixing, injection and debinding ones are exposed and enlarged during the sintering.

Although sintering theory has been developed for about 50 years, the models and numerical simulations are far behind the practices. This is due to the underdeveloped knowledge of material science associated to sintering [GER 02]. Instead of investigating the sintering mechanisms, this research work concentrates on the development of a continuum sintering model from the mechanical aspects. The entering parameters in the model are identified by experiments. The numerical simulations are performed to predict the dimensional changes of the sintering bodies and the final mechanical properties. The work provides the reference for designing the powder volume fraction in the feedstock, the geometries of the injection mold cavities and the PIM process parameters involved in injection, debinding and sintering.

1.2 Research Objectives

In this study, the two kinds of commercial-available feedstock composed both from 316L stainless steel and alumina are used. These materials are typical of metallic and ceramic PIM components. The research objectives involving the two materials are as following:

- 1. Experimental investigations of the densification behaviors of 316L stainless steel and alumina.** Dilatometer tests are employed to measure the shrinkage during sintering. The influences of heating rate, sintering temperature and holding time on the densification behaviors are investigated. The microstructure evolutions in the sintered components under different sintering conditions are observed through the scanning electronic microscopy (SEM).
- 2. Modeling the sintering process based on the continuum mechanics.** A thermal elasto-viscoplastic constitutive law is used to describe the deformations of the sintering parts. The determination of the constitutive parameters such as viscosity modulus and sintering stress are necessary.
- 3. Identifying the parameters in the sintering model.** The parameters in the model are very important for numerical simulations. In the present study, the gravitational beam-bending tests are employed to determine the viscosity of the sintering parts in 316L stainless steel. The shrinkage and shrinkage rate curves are obtained from the sintering experiments in dilatometer. The combinations of these experimental data are then used to identify the sintering model parameters.
- 4. Numerical simulation of the sintering process based on the finite element method (FEM).** Based on the employed sintering model and identified parameters, numerical simulations are carried out by FEM. The calculated shrinkages and distortions issued from numerical simulations are verified by the experimental results.
- 5. Building the model of strength evaluation to predict the strength of final sintered components.** The final strength is dependent on the porosity and microstructures in the resulting sintered components. Some empirical models have been proposed for that purpose. With the results obtained from sintering simulation, the influence of the sintering process parameters on the final strength can be evaluated. The model is justified by the strength test experiments.

6. Combination of the simulations of injection and sintering. An in-house software based on a bi-phasic injection model has been developed at LMARC. This model is used to predict the segregation effects arising in the powder injection process [BAR 00]. The density contours obtained from injection simulations can be introduced into the sintering simulation as an initial condition. The influences of segregation effects on the final sintered components can be analyzed by the above simulations.

1.3 Thesis Outline

The thesis is organized according to the following scheme. A brief introduction of the research motivations and objectives is presented in Chapter 1. In Chapter 2, a literature review is introduced. It concerns the sintering mechanisms, previous works on modeling and numerical simulations for sintering. The experimental investigations on 316L stainless steel and alumina powders sintering are presented in Chapter 3. The adopted phenomenological model for sintering based on continuum mechanics and strength evaluation model is introduced in Chapter 4. In Chapter 5, the identification of the parameters in the model is presented. The numerical simulations with FEM are described in Chapter 6. The conclusions of this research and the suggested future work are summarized in Chapter 7. A brief introduction of the bi-phasic injection model for PIM is presented in Appendix.

Chapter 2 Literature Review

Sintering is a widely used processing technology in powder metallurgy and ceramic industries. According to the ISO definition of sintering, it is the thermal treatment of a powder or compact at a temperature below the melting point of the main constituent, for the purpose of increasing its strength by bonding together the particles. During sintering the green bodies shaped by die pressing, injection molding, slip casting, extrusion or spraying undergo the shrinkages in dimensions and then final high dense or full dense products are obtained. Sintering mechanisms can be divided into several types by means of mass transport mechanisms largely occurring at the atomic level [GER 97]. The sintering mechanisms associated with solid-state diffusion falls into solid-state sintering. Most polycrystalline materials are sintered through this process. Most sintering cycles generate a transient liquid phase that can improve the mass transport rate. It is called liquid-state sintering. For amorphous materials, viscous flow is the main mass transport mechanism during the process considered as viscous sintering. When the external pressure is used during sintering process, this process is classified as pressure-assisted sintering.

In this research work, pressureless solid-state sintering is used to densify the 316L stainless steel and alumina ceramic PIM components. This chapter reviews the literature on the theory of solid-state sintering.

2.1 Introduction of sintering

2.1.1 Driving Forces of Sintering

The sintering process is accompanied by reducing the free energy of the system. The impetus to reduce the free energy is considered as the sintering driving force, that includes the force associated to the curvature of the particle surfaces, the externally applied pressure and the chemical reactions [RAH 03]. In the present research, sintering is performed without the external pressure or chemical reaction.

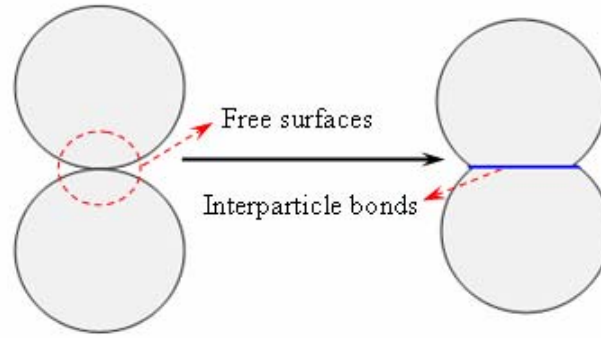


Figure 2.1: Two-sphere sintering model showing that the reduction of the free energy during sintering by the formation of interparticle bond instead of the free surfaces of solid-vapor interfaces.

The solid bonds formed between the particles during sintering can reduce the surface energy by removing the free surfaces. Figure 2.1 consists in the two-sphere sintering model that shows the formation of interparticle bond ($dA_{ss} > 0$), and the reduction of the free solid-vapor interfaces ($dA_{sv} < 0$) at the contact area between both particles. The change of the free energy of the sintering body due to interparticle bonding can be expressed as:

$$dE_f = \gamma_{sv} dA_{sv} + \gamma_{ss} dA_{ss} < 0 \quad (2.1)$$

where dE_f is the change of free energy, γ is the surface energy, A is the interface area, dA is the change of the interface area. The subscripts sv and ss denote the solid-vapor (surface) and solid-solid interface (grain boundary) respectively.

On the other hand, the elimination of the grain boundary area via grain growth or coarsening can also decrease the free energy of the sintering body, as shown in Figure 2.2. Grain growth reduces the solid-solid interface ($dA_{ss} < 0$), but the solid-vapor interface remains unchanged ($dA_{sv} = 0$). It does not contribute to densification, but reduces the free energy as follows:

$$dE_f = \gamma_{ss} dA_{ss} < 0 \quad (2.2)$$

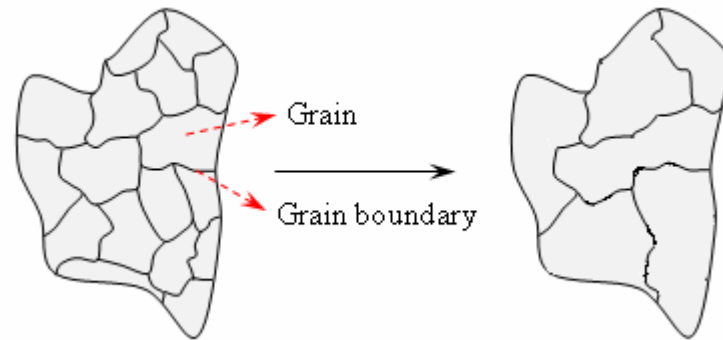


Figure 2.2: Grain growth reduces the free energy of the sintering body by eliminating the grain boundary area.

2.1.2 Sintering Mechanisms

There are various types of mass transport mechanisms occurring during the sintering process. Figure 2.3 shows the main sintering mechanisms of the solid-state sintering. The vacancies and atoms move along the particle surfaces (surface diffusion), along the grain boundaries (grain boundary diffusion), across pore spaces (evaporation-condensation), through the lattice interior (volume diffusion or lattice diffusion or viscous flow), and the dislocation motion under applied stress (plastic flow) [GER 97], [GER 98].

From Figure 2.3, it can be observed that the densification occurs only when the atoms move along the grain boundaries and create the continual mass flow into the pores. The centers of the particles move closer through diffusion. That leads to the macroscopic shrinkage of the sintering bodies. So grain boundary diffusion and volume diffusion contribute to densification. On the other hand, surface diffusion, evaporation-condensation are the coarsening mechanisms that occur without producing densification. All these diffusion mechanisms are favorable to the neck growth. Plastic flow is one of the most controversial aspects of the sintering theory. Recently experiments and calculations show that the plastic flow occurs when the sintering stress exceeds than the *in-situ* strength of the sintering body. Plastic flow is transient during the heating stage of sintering. That can lead to the rapid densification [GER 03].

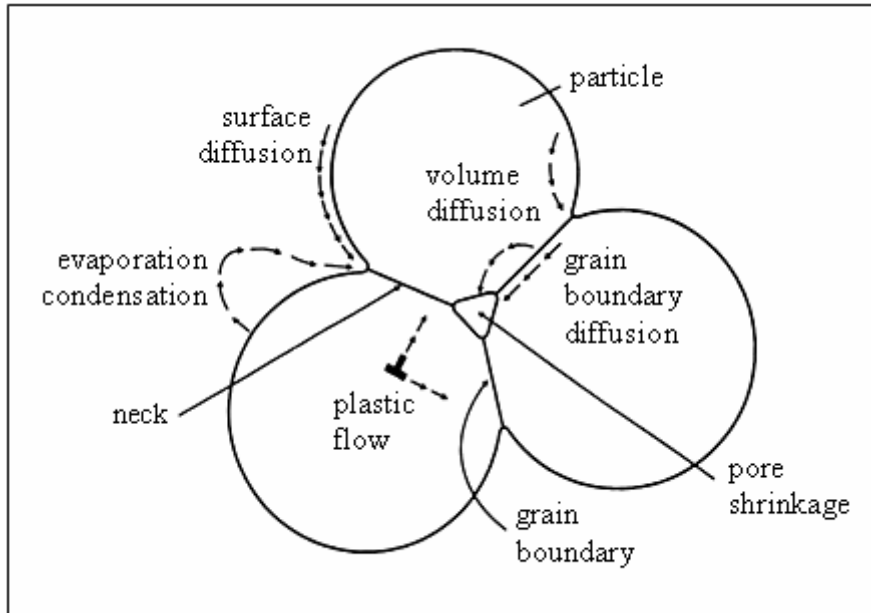


Figure 2.3: Neck growth between three particles to show various mass transport paths during sinter bonding (Adapted from [GER 97]).

2.1.3 Stages of Sintering

The entire sintering process is generally divided into three stages, based on the geometry of microstructures: (i) initial stage, (ii) intermediate stage, and then (iii) final stage [COB 61], [GER 98]. There is no clear-cut distinction between the stages, but each stage can be described by its general characters, as shown in Figure 2.4.

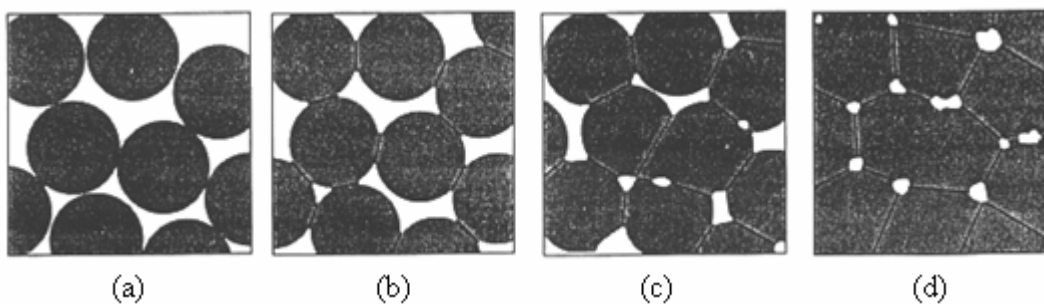


Figure 2.4: Microstructure evolutions in PIM sintering involving: (a) loose powder at the beginning of sintering, (b) neck formation and growth in the initial stage, (c) Interconnected pores in the intermediate stage, and (d) isolated pores and grain growth in the final stage (Adapted from [GER 97]).

In the initial stage, the loose particles rearrange their positions to form the new contacts with each other. Afterwards, the sintering necks are formed at the contact

area and begin to growth by the diffusion process. The initial stage ends when the neck radius is around 0.3 of the radius of the particle. The shrinkage occurs when the initial stage is about 4%.

The intermediate stage is most important for densification, since it determines the properties of the sintered components. The pores are rounding and interconnected like the cylindrical channel located at the grain boundaries. It undergoes rapidly the densification by reducing the cross section of the cylindrical pores. Finally, the pores become unstable and are pinched off from each other.

The final stage is characterized by the isolated pores located at the grain corners. It is also known as the coarsening involving growth of the larger grains and the consumption of the smaller grains. For the ideal cylindrical pores occupying at the grain boundaries, instability occurs at approximately 8% of the porosity. Considering the porosity distributions of the real materials, the pores begin to close at about 15% of the porosity and are all closed when the porosity is less than 5%.

2.2 Physical Models and Numerical Simulation of Sintering

In powder metallurgy and ceramic industries, the major goal of net-shaping is to produce the components with the required dimensions and properties. However, sintering is an intricate process that has not been understood totally. The dimensions and properties of the sintered components are influenced by many factors such as particle size, green density, heating rate, peak temperature, holding time, pressure and atmosphere. In industry, trial and error is widely used to obtain the appropriate geometries and process parameters. As expected from the development of sintering theory, numerical simulation is pushed to be more effective for the optimization of manufacturing by PIM.

Research on modeling and numerical simulations associated to the sintering process has been carried out for more than 40 years. The histories, development, achieved performance and the remaining barriers of sintering simulations were reviewed by German [GER 02]. In the early period from 1960 to 1970, efforts were

concentrated on building the well-known two-particle sintering models to describe the neck growth. From 1970 to 1980, the models for calculating the shrinkage in one dimension considering multiple mechanisms were presented. In the later 10 years, the models for pressure-assisted sintering were established. From 1990s, efforts were focused on building the continuum sintering models associated to FEM for the simulation of dimensional changes and density distributions of the sintering bodies, even for the components in complex shapes. Based on these works, the simulations perform an important step towards industrial applications [OLE 98]. From 2000 to date, new methods such as multi-scale modeling and artificial intelligence (AI) are now increasingly be used in sintering simulations.

There is no unique classification of the various established sintering models. According to the major approach of the modeling process, there are three kinds of distinct sintering models: (i) microscopic model (physically-based), (ii) mesoscopic model (stereological) and (iii) macroscopic model (phenomenological) [ZHA 05].

2.2.1 Microscopic Models

2.2.1.1 Models of Initial Stage

The microscopic models are established from the particles level. The two-particle model is the typical one to simulate the neck growth and the densification during the initial sintering stage. The typical geometries of the two-particle model are shown in Figure 2.5. The model consists of two particles in spherical shape with diameter D , associated to the diameter description on of the neck X , neck surface radius r_n , and overlap distance y .

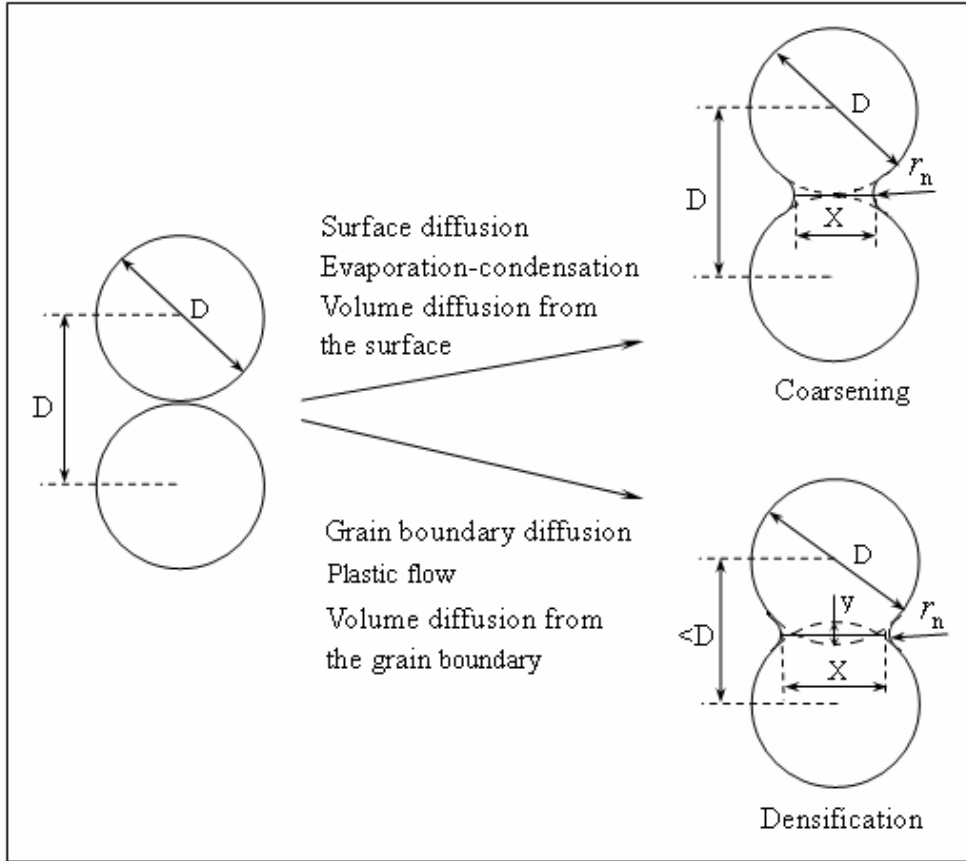


Figure 2.5: Geometrical description of the two-sphere particle model to describe the neck growth and densification in the initial sintering stage.

Various earlier models were established to estimate the neck growth during the initial stage of sintering [FRE 45], [KUC 49], [KIN 55], [COL 58], [JOH 63]. The neck size ratio X/D can be expressed as follows:

$$\left(\frac{X}{D}\right)^n = \frac{Bt}{D^m} \quad (2.3)$$

where t is the isothermal sintering time, B is a term that results from several material and geometric constants. Table 2.1 lists the values for n , m and B for different mass transport mechanisms.

Table 2.1: Values of the constants n , m and B in the neck growth Equation (2.3), [GER 96], [RAH 03].

Mechanisms	n	m	B^a
Surface diffusion	7	4	$56D_s\gamma_{sv}\Omega^{4/3}/kT$
Evaporation-condensation	3	2	$(3P\gamma_{sv}/\rho_{th}^2)(\pi/2)^{1/2}(M/kt)^{3/2}$
Volume diffusion on the surface	4	3	$160D_v\gamma_{sv}\Omega/kT$
Volume diffusion on the grain boundary	5	3	$80D_v\gamma_{sv}\Omega/kT$
Grain boundary diffusion	6	4	$20\delta_b D_b\gamma_{sv}\Omega/kT$
Viscous flow	2	1	$3\gamma_{sv}/\eta$
Plastic flow	2	1	$9\pi\gamma_{sv}bD_v/kT$

^aSymbols: γ_{sv} is the surface energy. D_s , D_v and D_b are the diffusion coefficients for surface, volume and grain boundary diffusion. δ_b is grain boundary thickness. ρ_{th} is theoretical density. Ω is atomic volume. M is molecular weight. P is vapor pressure. η is viscosity. b is Burgers vector. k is the Boltzmann's constant. T is the absolute temperature.

From the two-sphere model as shown in Figure 2.5, the shrinkage of sintered body is approximately determined by the ratio of the overlap distance y to the initial distance between both sphere centers D as follows:

$$\frac{\Delta L}{L_0} = \frac{y}{D} \quad (2.4)$$

where the shrinkage $\Delta L/L_0$ is the length change of the sintering part divided by the initial length. Shrinkage is actually a negative value as here the sign is ignored. There is an approximate geometrical relationship expressed as follows:

$$h = \frac{y}{2} = \frac{X^2}{8D} \quad (2.5)$$

By combining Equation (2.4) and Equation (2.5), the macroscopic shrinkage is then

related to the neck size as follows:

$$\frac{\Delta L}{L_0} = \left(\frac{X}{2D} \right)^2 \quad (2.6)$$

The combination of both Equation (2.3) and Equation (2.6) leads to the expression of the shrinkage during the initial sintering stage as follows:

$$\left(\frac{\Delta L}{L_0} \right)^{n/2} = \frac{Bt}{2^n D^m} \quad (2.7)$$

2.2.1.2 Intermediate Stage Models

In the intermediate stage, the geometry of the grain is regarded as tetrakaidecahedron and the highly interconnected pores are assumed to be cylindrical ones located at the grain boundaries, see Figure 2.6 [COB 61].

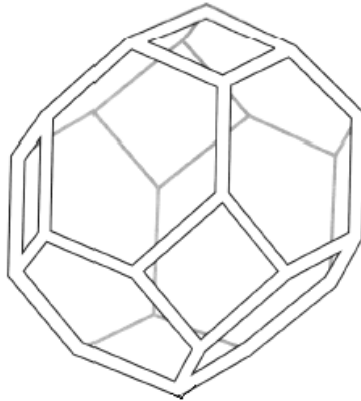


Figure 2.6: The interconnected pores in cylindrical shape located on the boundaries of tetrakaidecahedron grains in the intermediate stage of sintering [GER 96].

The Nabarro-Herring creep equation and Coble's creep equation were established to describe the volume diffusion and grain boundary diffusion process of the polycrystalline materials at the high temperature [NAB 48], [HER 50], [COB 63]. Coble has adapted these equations to calculate the shrinkage of the sintering body, as following [COB 70]:

$$\frac{dL}{Ldt} = -\frac{40D_v \gamma_{sv} \Omega}{3G^2 r kT} \quad (2.8)$$

$$\frac{dL}{Ldt} = -\frac{47.5\delta_b D_b \gamma_{sv} \Omega}{G^3 r k T} \quad (2.9)$$

where dL/dt is the derivative of the length of sintering body with respect to time, so the left side of the equations are the strain rate. G denotes grain size and r is the radius of the cylindrical pores. Equation (2.8) is for volume diffusion from grain boundary, and Equation (2.9) is for grain boundary diffusion.

2.2.1.3 Models of Final Stage

The final stage is characterized by the isolated pores at grain boundary corners. The widely accepted geometry model in the final stage has spherical pores at the 24 corners of the tetrakaidecahedron grain, as shown in Figure 2.7 [COB 61]. As the sintering proceeds, the density of the sintering body increases due to the fact that the shrinkage acts to close the pores.

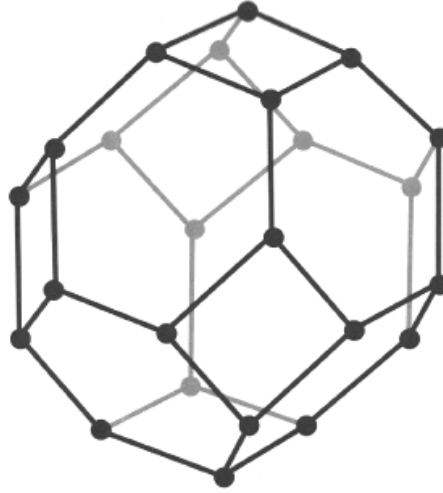


Figure 2.7: The isolated spherical pores located at the boundary corners tetrakaidecahedron grains during the final sintering stage [GER 96].

Based on Coble's work, Kang suggested the equations for calculating the density change of the sintered body in the final stage as follows [KAN 04]:

$$\frac{d\rho}{dt} = \frac{441D_v \gamma_{sv} \Omega}{kTG^3} (1-\rho)^{1/3} \quad (2.10)$$

$$\frac{d\rho}{dt} = \frac{733D_b\gamma_{sv}\Omega}{kTG^4} \quad (2.11)$$

where ρ is the relative density of the sintered body, defined as:

$$\rho = \frac{\rho_{ap}}{\rho_{th}} \quad (2.12)$$

where ρ_{ap} is the apparent density. Equation (2.10) is valid for volume diffusion from grain boundary, while Equation (2.11) stands for grain boundary diffusion.

2.2.1.4 Combined-stage Model

The above discussed models based on the simplified geometries are aimed to the sintering process in an unique stage. Based on these works, Johnson and co-workers derived a combined-stage model for the entire sintering process including initial, intermediate and final stages [HAN 92], [JOH 03]. By employing the geometric factors and other assumptions of the simplified models, a general model for grain boundary and volume diffusion has been derived as follows:

$$\frac{d\rho}{\rho dt} = \frac{3\gamma_{sv}\Omega}{kT} \left(\frac{\delta_b D_b \Gamma_b}{G^4} + \frac{D_v \Gamma_v}{G^3} \right) \quad (2.13)$$

where Γ_b and Γ_v are the geometric factors for grain boundary diffusion and volume diffusion respectively. The geometric factors changes continually in order to characterize the microstructural evolutions as the sintering proceeds. So Γ_b and Γ_v are defined as:

$$\Gamma_b = \frac{\alpha C_k C_b}{C_\lambda C_a C_h}, \quad \Gamma_v = \frac{\alpha C_k C_v}{C_\lambda C_a C_h} \quad (2.14)$$

The parameters entering in Equation (2.14) can be understood from sintering microstructural model of sintering developed in [DEH 84].

2.2.2 Mesoscopic Models

The microscopic models are based on the simplified geometries such as two or several spherical particles. These microstructural models consider various mass

transport mechanisms in sintering, but they cannot predict the microstructural modifications of the materials, which governs the mechanical, thermal and electrical properties of the resulting sintered components. Due to its importance, many researchers focus on the development of mesoscopic models to predict the real microstructures of the sintering body. It involves the methods associated to Potts models, front tracking models, vertex models, phase field models, and cellular automata [HOL 01]. The most commonly used one is the kinetic Monte Carlo Potts model, as introduced in the following reference [TIK 03], [MOR 04], [BRA 05].

In the kinetic associated to Monte Carlo Potts model for sintering, the particles composed of grains and pores are divided into many hexagonal cells, as shown in Figure 2.8. The white cells represent the pores. The cells in colors or grey levels indicate the difference in their crystal orientation. Each of the cells is assigned to a random orientation number $q = [1, 2, \dots, q_t]$, where q_t is the total number of grain orientations. For crystals, the value of q_t is 64 [MOR 04]. The cells associated to pores are assumed to take the state $q = 0$. A grain boundary segment is defined to lie between two sites of unlike orientations. In other words, two adjacent cells having the same orientation number are considered to be a part of the same grain, otherwise they belong to different grains.

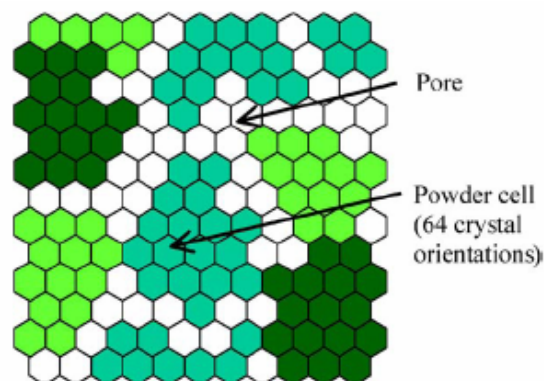


Figure 2.8: Two-dimensional kinetic Monte Carlo Potts model for the mesoscopic simulations of microstructural evolutions in porous materials during sintering process [MOR 04].

The grain boundary energy is specified by defining an interaction between nearest-neighbor cells. The total system energy is defined as:

$$E_f = \frac{1}{2} J \sum_{i=1}^N \sum_{j=1}^n (1 - \delta(S_i, S_j)) \quad (2.15)$$

where J is a positive constant that sets the scale of the grain boundary energy, $\delta(S_i, S_j)$ is the Kronecker's delta function, S_i is the orientation at a randomly selected cell i , S_j is the orientation of its nearest-neighbors and n is the total number of the nearest neighbor cells. N is the total number of randomly selected cells. The sum is taken over all nearest-neighbors. Each pair of nearest-neighbor contributes J to the system energy in case of of unlike orientation. Otherwise, it takes value zero.

Grain boundary migrations are simulated by selecting a cell randomly and changing its orientation to one of the nearest-neighbors' orientations. The probability of orientation change is defined as:

$$p = \begin{cases} p = 1, \Delta E_f \leq 0 \\ p = \exp\left(\frac{-\Delta E_f}{kT}\right), \Delta E_f > 0 \end{cases} \quad (2.16)$$

where ΔE_f is the change of energy due to the change of orientation.

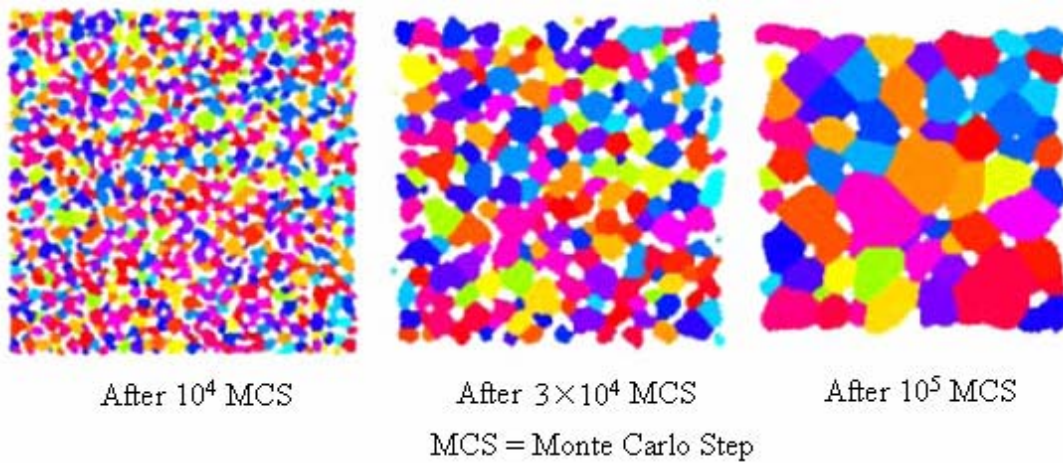


Figure 2.9: Microstructural evolutions obtained by mesoscopic simulations based on two-dimensional kinetic Monte Carlo Potts model for sintering. (Adapted from [BRA 05]).

Figure 2.9 is an example of the results obtained from two-dimensional Monte Carlo Potts simulations. It can be observed that the simulations can predict the microstructural evolution during sintering that includes the grain growth and the pore migrations.

2.2.3 Macroscopic Models

Since 1990s, research in the sintering field has been shifted to the emphasis on various mass transport mechanisms for prediction of the component distortions, densification mechanisms and microstructures [GER 02]. The macroscopic models have been developed to predict the shrinkages and distortions of the parts arising in sintering. It is important for the design of dies or moulds in PIM, as well as the sintering process parameters. In these works, the sintering body is regarded globally as a compressible continuum even though it is composed of solid and pores. The goal of macroscopic modeling is to develop a proper constitutive law of the porous continuum that can be used to describe the densification and distortion behaviors during sintering. The linear viscoplastic constitutive law is the most widely used one in the macroscopic sintering models [BOR 88 a], [LIP 97], [OLE 98], [BOU 99], [KRA 04]. It can be expressed as follows:

$$\dot{\boldsymbol{\epsilon}}_{vp} = \frac{\boldsymbol{\sigma}'}{2G_p} + \frac{\sigma_m - \sigma_s}{3K_p} \mathbf{I} \quad (2.17)$$

where $\dot{\boldsymbol{\epsilon}}_{vp}$ is the viscoplastic strain rate, $\boldsymbol{\sigma}'$ is the deviatoric stress tensor, $\sigma_m = \text{tr}(\boldsymbol{\sigma})/3$ is the mean stress and $\text{tr}(\boldsymbol{\sigma})$ is the stress tensor trace, \mathbf{I} is second order identity tensor, G_p and K_p are respectively the shear and bulk viscosity moduli of the porous material, σ_s is the sintering stress. G_p , K_p and σ_s are the material and process parameters. Their values depend on the relative density, temperature, and the microstructural factors such as grain and pore size.

Various models have been developed to determine G_p , K_p and σ_s in the constitutive law. Generally they can be classified into three types that include the

phenomenological, microstructural and experimental ones. Some representative models are introduced briefly in the following.

2.2.3.1 Phenomenological Model for Constitutive Parameters

Skorohod and Olevsky have proposed a purely phenomenological model to determine the parameters in the viscoplastic constitutive law by employing the rheology of the porous continuum [SKO 72], [OLE 98]. The bulk and shear viscosity moduli and sintering stress can be expressed as follows:

$$G_p = (1 - \theta)^2 \eta \quad (2.18)$$

$$K_p = \frac{4}{3} \frac{(1 - \theta)^3}{\theta} \eta \quad (2.19)$$

$$\sigma_s = \frac{3\gamma_{sv}}{r_0} (1 - \theta)^2 \quad (2.20)$$

where $\theta = 1 - \rho$ is the porosity factor, η is viscosity of the wrought materials, r_0 is the radius of the spherical particle. The viscosity η is dependent on the temperature:

$$\eta = \eta_0 \exp\left(\frac{Q_{VF}}{RT}\right) \quad (2.21)$$

where Q_{VF} is the activation energy of the viscous flow, R is the gas constant, η_0 is the viscosity of the wrought materials at room temperature.

The above phenomenological model has only a limited number of the parameters to be determined. So it is easy to be implemented in numerical simulations, but this model is restricted in terms of predictability.

2.2.3.2 Micromechanical Model of Constitutive Parameters

Riedel and co-workers used micromechanical sintering models to determine the constitutive parameters in the macroscopic models in considering different mass transport mechanisms [RIE 94], [SVO 94], expressed as follows:

$$G_p = \left(\frac{\rho_0}{\rho}\right)^{\frac{2}{3}} \left(\frac{\rho - \rho_0}{1 - \rho_0}\right)^2 \frac{\rho r_0^3}{90D_{\text{iff}}(T)} \quad (2.22)$$

$$K_p = \left(\frac{\rho_0}{\rho}\right)^{\frac{2}{3}} \left(\frac{\rho - \rho_0}{1 - \rho_0}\right)^2 \frac{\rho r_0^3}{54D_{\text{iff}}(T)} \quad (2.23)$$

$$\sigma_s = \frac{8\gamma_{\text{sv}}}{r_0} \left(\frac{\rho_0}{\rho}\right)^{\frac{1}{3}} \rho \quad (2.24)$$

where ρ_0 is the initial relative density of the sintering body, D_{iff} is a diffusion term. The grain boundary diffusion can be written in the following form [MCM 92]:

$$D_{\text{iff}}(T) = \frac{\Omega \delta_b D_{b0} \exp(-Q_b / RT)}{kT} \quad (2.25)$$

where Q_b is the activation energy of grain boundary diffusion, D_{b0} is the grain boundary diffusion frequency.

Based on the previous works, Kraft built a comprehensive model for solid state sintering considering all the mechanisms and factors in the entire sintering process, but it remains difficulties to determine properly so many parameters in the model [KRA 04].

2.2.3.3 Experimental Model for Constitutive Parameters

Bouvard and co-workers designed proper experiments to determine the viscosity modulus and sintering stress of WC-Co and alumina powders [BOU 99], [GIL 01], [KIM 03]. The model assumed that the stress level of the sintering body is so low that the relationship between stress and strain rate tensor can be regarded as the linear one. The constitutive equation Equation (2.17) can be expressed by three equations as follows:

$$\dot{\boldsymbol{\epsilon}}_{\text{vp}} = \dot{\boldsymbol{\epsilon}}_s + \dot{\boldsymbol{\epsilon}}_{\text{vp}} \quad (2.26)$$

$$\dot{\boldsymbol{\epsilon}}_s = \frac{-\sigma_s}{3K_p} \mathbf{I} \quad (2.27)$$

$$\dot{\boldsymbol{\epsilon}}_{\text{vp}} = \frac{\boldsymbol{\sigma}'}{2G_p} + \frac{\sigma_m}{3K_p} \mathbf{I} \quad (2.28)$$

where $\dot{\boldsymbol{\epsilon}}_s$ is the strain rate tensor due to the free sintering, $\dot{\boldsymbol{\epsilon}}_{\text{vp}}$ is the viscoplastic strain rate tensor due to the external loading. The experiments of free sintering and uniaxial loading sintering of cylindrical specimens in dilatometer are employed to

measure the uniaxial strain rate $\dot{\varepsilon}_z^{\text{vp}}$ and the radial strain rate $\dot{\varepsilon}_r^{\text{vp}}$. The uniaxial viscosity η_z and the viscous Poisson's ratio ν_{vp} are determined by the following expressions:

$$\eta_z = \frac{\dot{\varepsilon}_z^{\text{vp}}}{\sigma_z} \quad (2.29)$$

$$\nu_{\text{vp}} = -\frac{\dot{\varepsilon}_z^{\text{vp}}}{\dot{\varepsilon}_r^{\text{vp}}} \quad (2.30)$$

where σ_z is the applied external stress on the specimen. By the analogy with linear elastic theory, the shear and bulk viscosity modulus can be calculated in using the following expressions:

$$G_p = \frac{\eta_z}{2(1 + \nu_{\text{vp}})} \quad (2.31)$$

$$K_p = \frac{\eta_z}{3(1 - 2\nu_{\text{vp}})} \quad (2.32)$$

Afterwards, the sintering stress can be obtained with Equation (2.27).

Instead of using many physical or material parameters, the above experimental model is relatively simple. However, the proper experiments should be designed for different materials.

2.3 Summary

Sintering is an important process to produce the metallic and ceramic powder products. It determinates the final dimensions and mechanical properties. On the other hand, sintering is a complicate process that involves many physical and chemical phenomena. The mechanisms of sintering have not yet been totally understood. The sintering process is influenced by many factors such as heating rate, peak temperature, holding time, sintering atmosphere and initial density. Investigation on the sintering behaviors of various materials is important for optimization of the process.

Researches on modeling and numerical simulations of sintering have been carried out for more than 40 years including modeling at different scales:

The microscopic models aim to simulate the mass transport mechanisms between several particles. It is useful for better understanding of the physical process of sintering.

The mesoscopic models choose the representative cell or element in the sintering body, and simulate the microstructural evolutions including densification and grain growth. The mechanical properties of sintered components are determined by the material characteristics at the mesoscopic level such as grain size, pore shape and distributions.

The continuum models at the macroscopic level are close to the industrial sintering practices due to their merits in prediction of the dimensional shrinkages and distortions of the sintered bodies.

There are many achievements for each sintering model types, but neither of them is perfect. Research continues on the subject and recent works may be noted [PAN 05], [KRA 05], [OLE 05], [KIA 05], [VAG 05].

The main barriers and challenges of modeling and numerical simulations of sintering can be underlined as follows [GER 02], [OLE 05]:

- The models should include not only the isothermal stage during sintering, but also the heating and cooling stages. Experiments illustrate that the densification is mainly accomplished in the heating stage, and the cooling stage is important for the final mechanical properties of the components.
- The models should be independent of the particle and pore shapes. Most of the existing models are based on spherical particle shape, cylindrical or spherical pore shape. It could be strongly different from the real situation in the sintering process.
- Some phenomena occurring at the microstructural level should be considered. The simulations should be able to describe non-uniform packing of the particles in the initial stage of sintering, including the agglomeration.
- The non-thermal mechanical factors such as phase transition, chemical reaction,

influence of sintering atmosphere, oxidization phenomena *etc.*, have to be included in the models.

- The effective links are required between the microscopic, mesoscopic and macroscopic models.
- The existing models should include the *in-situ* damage criteria of the sintering body. It is necessary for prediction of the distortion, defects or mechanical properties of the final sintered components.
- The effective optimization methods should be developed in complement to the simulation models. It is well expected that numerical software package can help to determine the optimal design of the tools and process parameters.

Chapter 3 Experimental Investigations of Sintering Processes

The experimental investigations focused on the sintering mechanisms associate to green bodies after injection molding and debinding. It involves densification, shape distortion, microstructural evolutions phenomena, as well as the post- and *in-situ* sintering strength of the resulting components. The results obtained by experiments were employed to develop the sintering models, to identify the parameters in the models and validate the simulation results. PIM process includes mixing, injection molding, debinding and sintering as main process steps. In the present work, the commercially available feedstock after mixing and pelletization composed of metallic or ceramic powders and the binder were used in experiments.

3.1 Material Characterization

3.1.1 316L Stainless Steel PIM Feedstock

316L stainless steel feedstock was provided by Advanced Metal Working Particles Inc, USA. The wax-based binders were used for the feedstock. Some of the parameters of the feedstock provided by the supplier are listed in Table 3.1.

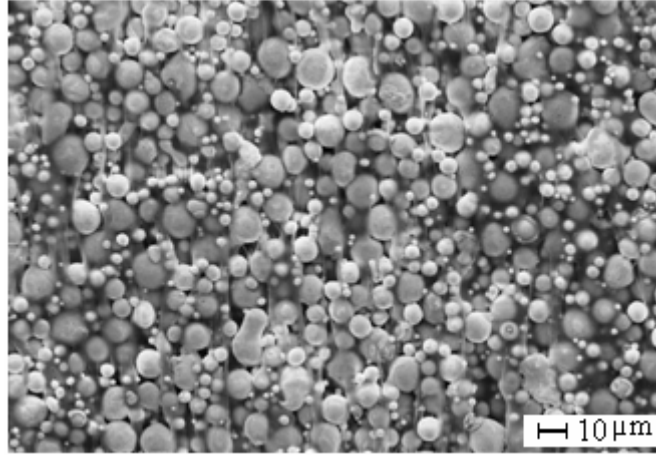
Table 3.1: Parameters of 316L stainless steel PIM feedstock.

Parameters	Values
Pycnometer density	5.164 g/cm ³
Solid loading	approx. 62 vol.%
Viscosity (175 °C)	approx. 827 Pa·s

The chemical composition of the gas-atomized powders is shown in Table 3.2. The microstructural photographs of the feedstock observed by scanning electronic microscope (SEM) is shown in Figure 3.1. The powders are of spherical shape with a particle size smaller than 45 μm and $D_{80} = 16 \mu\text{m}$.

Table 3.2: Chemical compositions of 316L stainless steel powders.

	C	Ni	Cr	Mo	Mn	Si	P	S	Fe
Wt.%	0.024	10.8	16.9	2.1	1.14	0.52	0.027	0.011	Balance


Figure 3.1: SEM photo of the PIM feedstock composed of gas-atomized 316L stainless steel powders and wax-based binders.

3.1.2 Alumina PIM Feedstock

The ELUTEC[®] A-99-S model alumina PIM feedstock provided by Zschimmer & Schwarz was also used in the experiments. The approximate parameters of the feedstock provided by the producer are listed in Table 3.3.

Table 3.3: Parameters of the alumina PIM feedstock.

	Parameters	Values
Alumina powders	Purity	99.8%
	Solid loading	81.5 wt.%
	D ₅₀	0.7 μm
	Density (25°C)	approx. 1.2 g/cm ³
	Melting point	approx. 112 °C
Binder	Water solubility (20 °C)	approx. wt. 65%
	Viscosity (140 °C)	approx. 2.3 Pa·s
	Viscosity (160 °C)	approx. 2.2 Pa·s

The SEM photo of the feedstock is shown in Figure 3.2, in which the white particles are alumina, and the black color corresponds to binder.

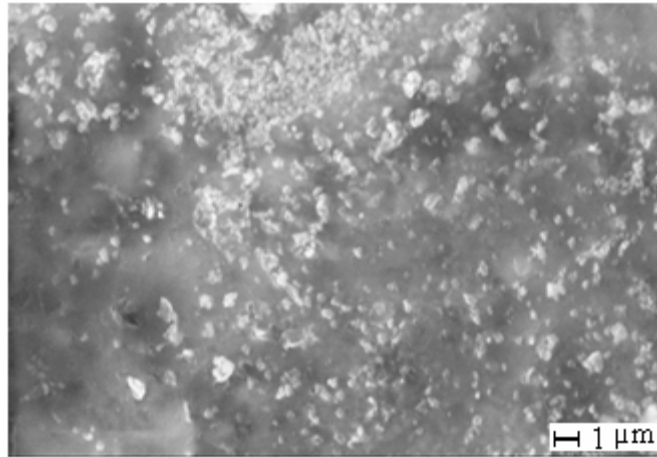


Figure 3.2: SEM photographs of the PIM feedstock composed of alumina powders and binders.

3.2 Specimen Preparation

3.2.1 Injection Molding

Injection molding is the step that consists to shape the feedstock into the desired geometries in PIM processing. The step includes heating the feedstock to sufficient temperature to make it melt, forcing the molten flow into the mould cavities, packing at high pressure, then cooling and ejecting the molded parts out of the molds. In the experimental work, an injection machine (Boy 22M) was used, as shown in Figure 3.3(a). The maximum clamping force of the machine is 22 ton, the maximum shot volume is 30.4 cm^3 , the diameter of screw is 22 mm, the maximum injection speed is 160 mm/s, the specific injection pressure corresponding to the maximum hydraulic pressure is 1672 bars. A mold has been designed and manufactured for the tests and is shown in Figure 3.4 (b) [BAR 00]. It contains five cavities. Two of them are in the shape of tensile test specimens with one or two injection gates respectively. Another two are in the shape of specimen for bending test specimens with one or two injection gates. The last one is a cavity that corresponding to a wheel shape.



Figure 3.3: Injection molding machine and the designed molds in the experiments [BAR 00].

The experimental and numerical studies focusing on optimizing the injection process of the above 316L stainless steel and alumina feedstock were carried out in LMA [BAR 00], [LIN 06]. The process parameters of injection are listed in Table 3.4.

Table 3.4: Parameters of injection process for 316L stainless steel and alumina PIM feedstock.

Parameters	316L stainless steel	Alumina
Injection temperature (°C)	165	190
Mold temperature (°C)	60	50
Injection time (s)	0.5	0.5
Injection pressure (bar)	100	100
Holding pressure (bar)	60	60
Rotation speed of screw (rpm)	100	100

3.2.2 Debinding

Debinding process is employed to remove the binder in the molded components. It depends on the ingredients of the binders in the feedstock.

Thermal debinding was used to remove the wax-based binders in the moulded parts of the 316L stainless steel powders. The heating process was implemented by two sequent stages, firstly in a debinding oven at a maximum temperature up to 300 °C with argon as protective air, and secondly in a batch furnace capable of a

maximum temperature equal 1600 °C in vacuum. Both equipments are shown in Figure 3.4.

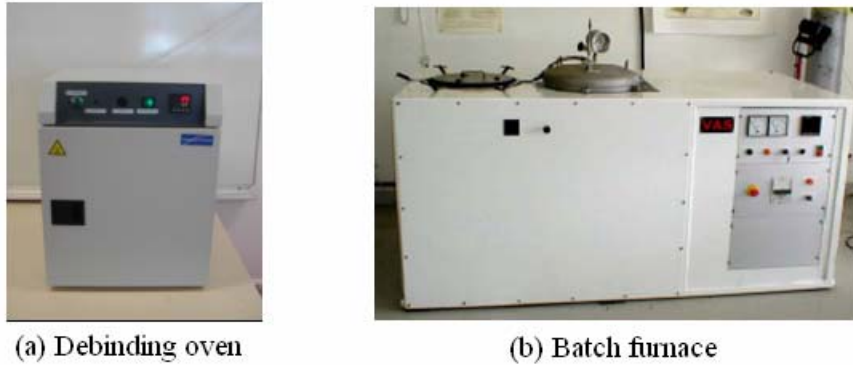
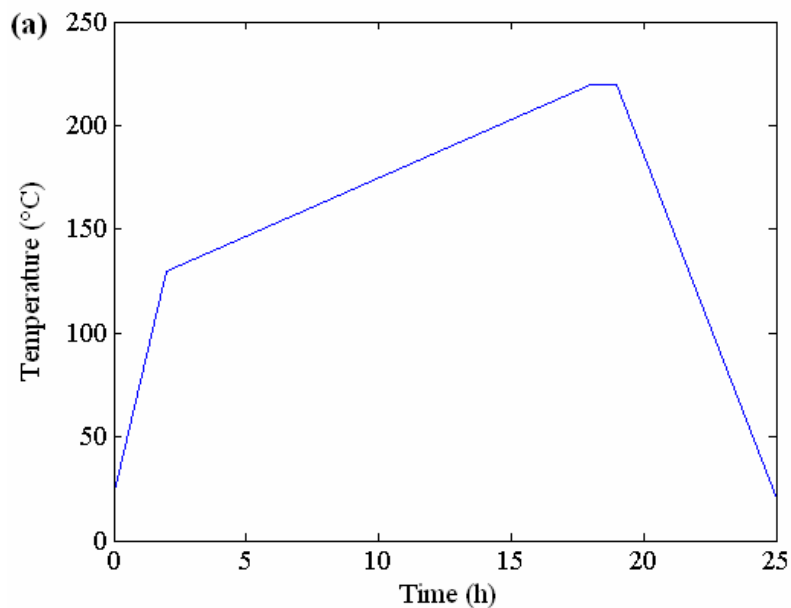


Figure 3.4: Debinding oven and batch furnace used in the experiments.

The debinding process was firstly carried out in the Servathin oven with the heating cycle as shown in Figure 3.5 (a). It consists of three steps:

- (1) heating up to 130 °C at the rate 0.625 °C/min,
- (2) continuing to heat up to 220 °C at lower rate 0.1 °C/min,
- (3) holding at 220 °C for 1 hour.

The above procedure was mainly aimed to remove the wax, which is the main ingredient of the binders. The slow heating rate used later was aimed to avoid the appearance of eventual distortions and defects occurring during debinding process.



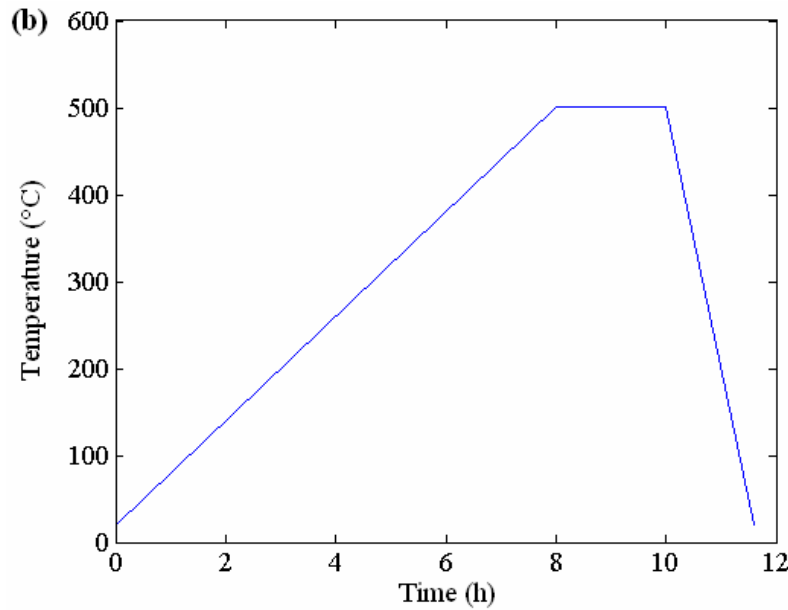


Figure 3.5: Heating cycles associated to the debinding process for the injection molded parts in 316L stainless steel powders: (a) carried out in oven, (b) in batch furnace subsequently.

Afterwards, the components were moved into the Eurotherm Automation batch furnace for the higher debinding cycle. The temperature was heated up to 500 °C at 2 °C/min and then held for 2 h, for the purpose to remove the polymers of the binder, as shown in Figure 3.5 (b).

For the injection moulded parts of alumina feedstock, the moulded parts were debinded at 70 °C in water as solvent for 24 h, and followed by thermal debinding in the batch furnace. The temperature was heated up to 500 °C at the rate equal to 2 °C/min and then held for 1 hour. The solvent debinding was environmentally compatible and cost-saving, but the process is slow, especially in the late stage of debinding. So the solvent and thermal debinding techniques were combined in this work to remove the binders effectively.

3.2.3 Presintering

The debinded parts are frangible and prone to distort during the sintering process. Presintering can improve the strength of the parts that can reduce the distortion of sintering bodies [GER 03 c]. Experiments showed that the presintering was necessary for the specimens in 316L stainless steel powder to be proceeded in

the subsequent sintering tests. The alumina specimens after debinding were also frangible, but there were little distortions during sintering.

The peak temperature chosen for the presintering of 316L stainless steel PIM components after debinding is usually 800 °C or 900 °C [LIU 01], [KOS 05]. In the experiments, the presintering at 800 °C and 900 °C were carried out respectively. The heating rate was 2 °C/min and the holding time at the peak temperature was 1 hour. The cooling rate was 10 °C/min. As the debinding stage II and presintering were realized in the same furnace, the heating cycles consisting of two sequent processes can be expressed by a single graph, as shown in Figure 3.6.

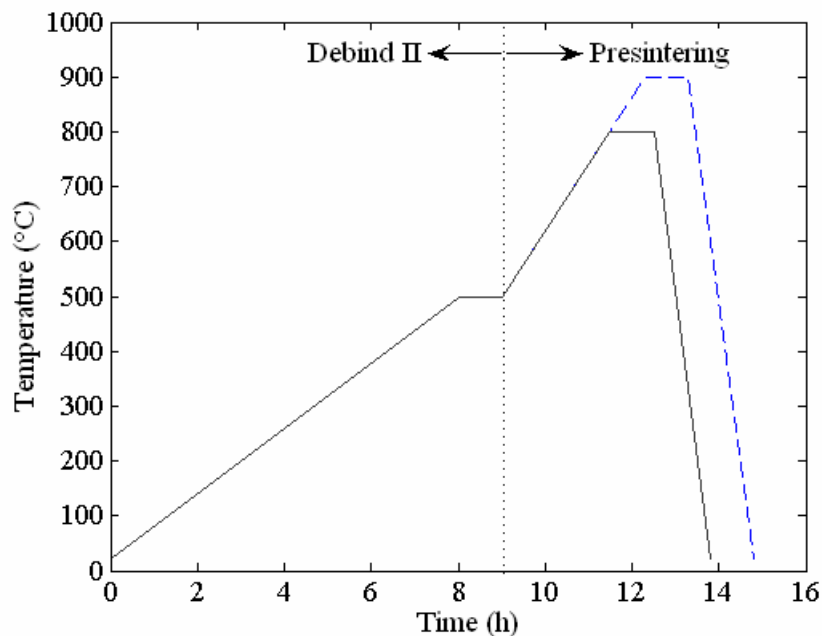


Figure 3.6: Thermal cycles of the debinding stage II at 500 °C for 1 hour and the subsequent presintering at 800 °C or 900 °C for 1 hour, corresponding to 316L stainless steel injection molded parts in the same batch furnace.

3.3 Sintering Procedures

The presintered specimens were sintered afterwards in the batch furnace to investigate the dimensional changes and microstructural evolutions. Besides, the sintering experiments in dilatometer and the gravitational beam-bending tests in sintering were carried out to identify the parameters in the constitutive models.

3.3.1 Sintering in Furnace

The batch furnace shown in Figure 3.4(b) was used to sinter the specimens for tensile test and bending test, as well as the wheel part as shown in Figure 3.3(b). The sintering was carried out in vacuum conditions. Various thermal cycles with different parameters of peak temperature, heating rate and holding time were employed to investigate the densification behaviors of the components. The sintered parts issued from experiments were used to measure their dimensional changes and to test their mechanical properties. The obtained experimental results were employed to validate the results of FEM simulations. The microstructures of the sintered parts were observed using a Scanning Electric Microscope (LEO 435VP®).

3.3.2 Sintering in Dilatometer

Sintering experiments were realized in an horizontal dilatometer to investigate the *in-situ* shrinkages and shrinkage rates in length associated to the small cylindrical specimens, as shown in Figure 3.7. The sample holder or container and the pushrod are made in alumina. The pushrod can detect the dimensional changes of the cylindrical specimen in length by a connected displacement sensor. The force loaded by the pushrod is 15 centinewton. The diameter of the pushrod is about 3 mm. So the pressure acting on the end of the cylindrical specimen is less than 425 Pa. It has the influences on the densification behaviours of the specimen. The vertical dilatometer that can control the pressure could be used to get the more accurate results. A thermal couple is installed in the sample container to measure the sintering temperature. The maximum working temperature in the furnace associated to dilatometer is 1650 °C.

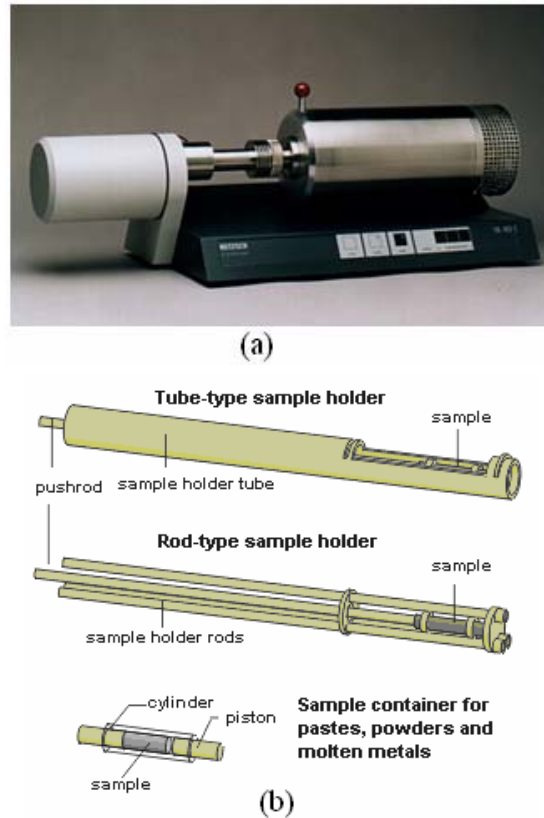


Figure 3.7: The horizontal dilatometer used in the experiments: (a) photograph of the equipment, (b) sample holder and container in dilatometer [NET ETH].

In the present experiment, the tube-type sample holder was used in the dilatometer for solid-state sintering of 316L stainless steel powder and alumina specimens. Argon was used as a protective atmosphere for 316L stainless steel specimens. The alumina specimens were sintered simply in air. The dimensions of specimens are 12 mm length and 6 mm diameter approximately. The thermal cycles were piloted by a computer system.

3.3.3 Gravitational Beam-bending Tests in Sintering

Gravitational beam-bending tests are often used to determine the viscosity of the sintering body [LEE 03], [BLA 05]. The sizes of presintered bending specimens composed 316L stainless steel powder were 78.70 ± 0.19 mm in length, 14.95 ± 0.12 mm in width and 3.33 ± 0.05 mm in thickness. The bending span was chosen equal 40 mm with supports in alumina, as shown in Figure 3.8. The experiments were also

carried out in batch furnace under vacuum condition. For measurement, the specimen was heated to different peak temperatures at the same heating rate equal 10 °C/min, and then cooled rapidly. At high temperature, the *in-situ* sintering specimens reduced significantly their strength, and the gravitational load induced bending deflection of the specimens. The deflections in sintering were measured at room temperature after cooling. An assumption was made to support these measurements, that claimed that the deformation of the specimen was produced only in the sintering period.

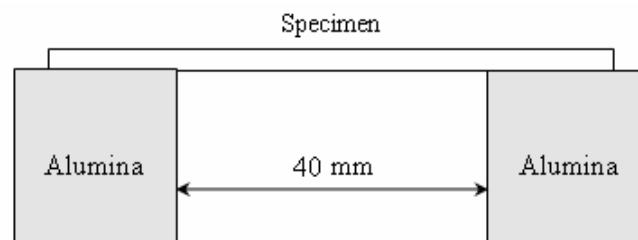


Figure 3.8: The sketch of gravitational beam-bending tests in sintering process, experiments carried in batch furnace to determine the viscosity of sintered body.

3.3.4 The tests of *In-situ* Sintering Strength

During the sintering process, bonding between the particles increases the strength of the sintered body, while thermal softening effects reduce simultaneously the strength [GER 03 c]. *In-situ* strength is an important parameter for the numerical analysis of densification and resulting distortion of the sintering body. Flaming tensile tester (FTT) is a widely used equipment to measure the *in-situ* strength of the sintering body [SHO 99], [OLE 01], [XU 02 a]. An outline of FTT is shown in Figure 3.9.

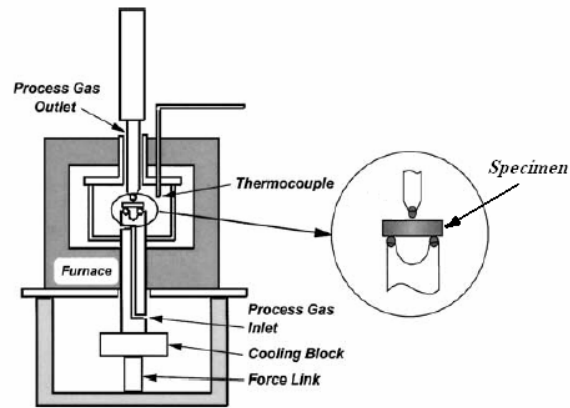


Figure 3.9: A section view of the Flaming Tensile Tester (FTT), used to measure the transverse rupture strength (TRS) of *in-situ* sintering and post-sintering [OLE 01].

The equipment used for FTT experiments is shown in Figure 3.10. The FTT apparatus was mounted on the Instron-6025 tensile test machine by virtue of a furnace and temperature controlling system. The proper apparatus were manufactured for the three-point bending test according to the MPIF standard 41 [MPI 73]. The distance between the supporting rods was 25.4 mm. The radii of the supporting rods and the indenter were 3.1 mm. The bending test specimen was in rectangular shape of length 31.7 mm, width 12.7 mm and thickness 6.35 mm. The loading speed was assigned to 192 N s^{-1} . The tests were carried out for 316L stainless steel presintered specimens.

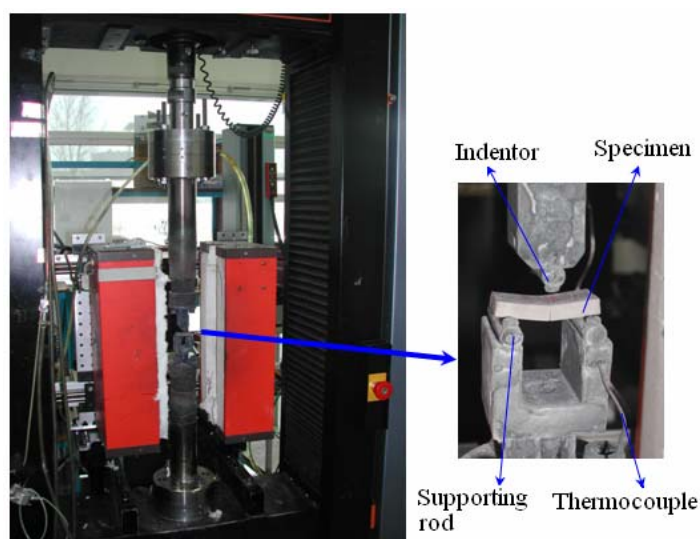


Figure 3.10: The apparatus used for flaming tensile tests.

3.3.5 Testing Procedures of Post-sintering Strength

Post-sintering strength is in fact the final strength of the sintered components at room temperature. It is one of the most important parameters to indicate the final mechanical properties of the final products. In the experiments, the three-point bending tests were carried out to measure the transverse rupture strength (TRS) of the sintered specimens. The apparatus and loading procedure are the same as the test of *in-situ* strength, but conducted in the room temperature without using the furnace.

The tensile tests were also mounted on an Instron-6025 tensile test machine to determine the ultimate tensile strength (UTS) and elongation of the sintered parts. The tensile test specimens were made firstly by injection molding as shown in Figure 3.3 (b), and then undergone debinding, presintering, as well as sintering. For the tensile tests, both ends of the specimen were clamped directly by fixtures of the tensile test equipment. The loading increases continuously at a rate equal 192 N s^{-1} in the experiments, by applying it to one end of the specimen. A displacement sensor was fixed on the middle of the specimen to measure elongation or engineering strain of the specimen. The tensile test apparatus is shown in Figure 3.11.

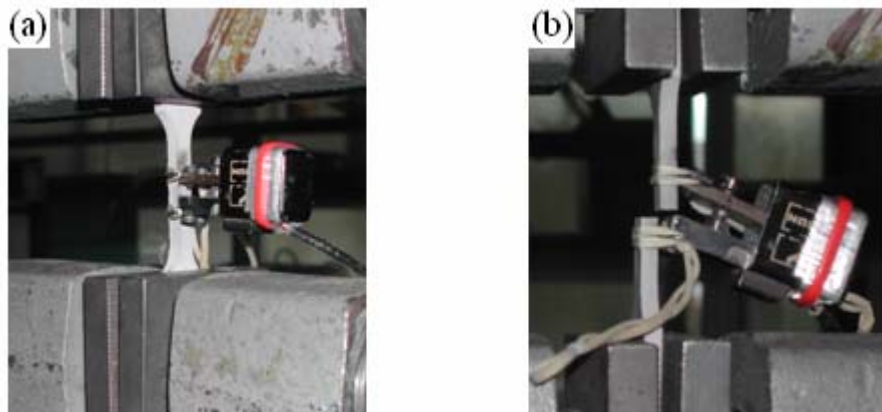


Figure 3.11: The apparatus used for tensile tests: (a) before loading, (b) after rupture.

3.4 Experimental Results for 316L Stainless Steel Powders

3.4.1 Effects of Debinding and Presintering

During the debinding and presintering processes, the binders were removed from the molded bodies. A precise balance from Mettler Toledo® (AB 204 model) with resolution 0.4 g, and a helium pycnometer (AccuPyc 1330 model) were used to measure the mass and pycnometer volumes of the specimens.

The evolution of the mass and volume measured by pycnometer during debinding and presintering are shown in Figure 3.12. It can be observed that most of the binders are removed in the debinding stage. In the debinding stage I corresponding to a peak temperature equal 220 °C, carried out in the oven, about 77.4 wt.% or 85.4 vol.% of the binders are removed. In the debinding stage II corresponding to a peak temperature equal 500 °C in furnace, removal of the binder is made up to 95.9 wt.% or 99.7 vol.%.

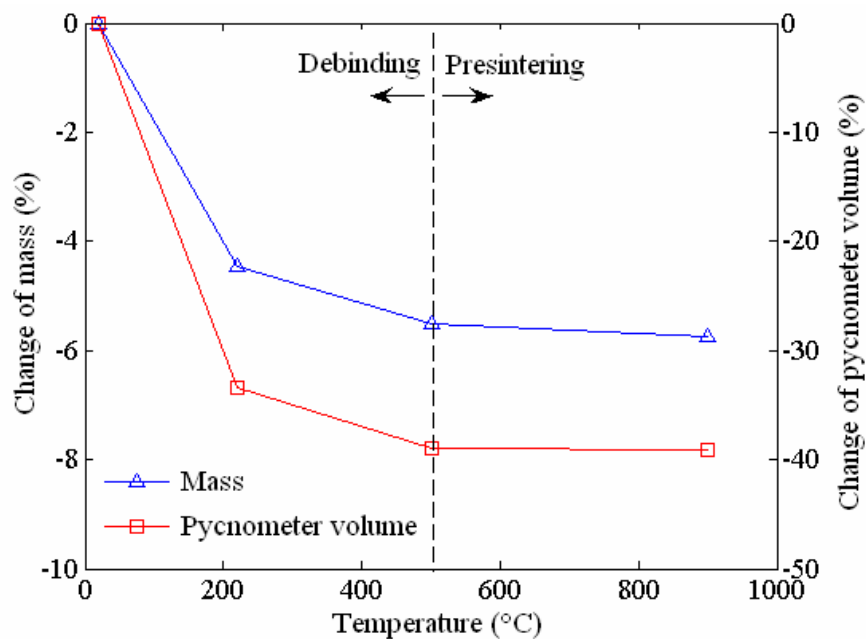


Figure 3.12: Evolution of the mass and pycnometer volume in debinding and presintering process due to the removal of binder.

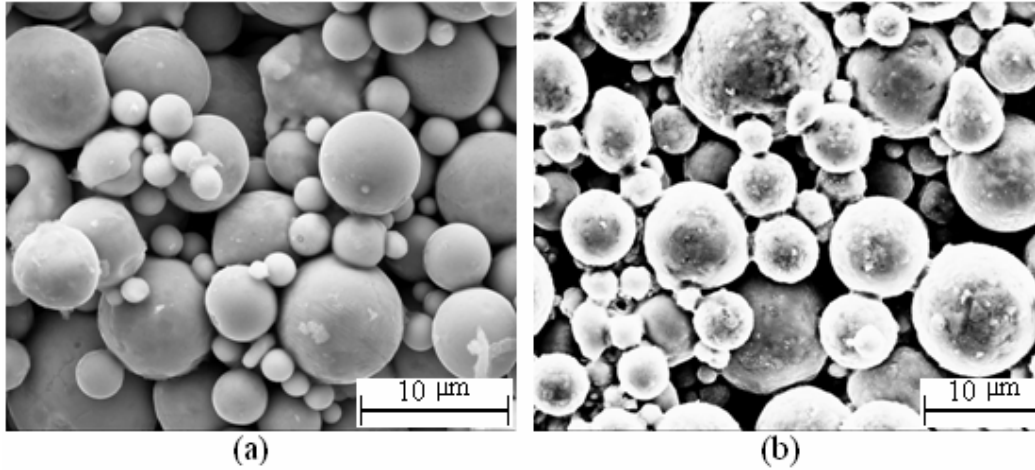


Figure 3.13: The SEM photos on specimens: (a) powders and the remained binders after debinding stage I in the oven, (b) almost total removal of the binder and formation of the necks between the particles after the debinding stage II and presintering in furnace.

After the debinding firstly carried out in oven, it remains still some binders between the particles, see Figure 3.13(a). By the following debinding stage II and presintering at 900 °C during 1 hour, almost all the binders are eliminated and the sintering bonding occurs between the particles. In the presented parts, there are only the powders. So the pycnometer density of the presintered specimens is equal to the theoretical density of the used 316L stainless steel.

By measuring the mass, apparent volume and pycnometer volume of the presintered cylindrical specimens, the theoretical density ρ_{th} of the material, the apparent density ρ_{ap} and relative density ρ of the specimen can be expressed as below:

$$\rho_{th} = \frac{m}{V_{py}}, \quad \rho_{ap} = \frac{m}{V_{ap}}, \quad \rho = \frac{\rho_{ap}}{\rho_{th}} \quad (3.1)$$

where m is the mass of the specimen, V_{py} is the pycnometer volume and V_{ap} is the apparent volume. Figure 3.14 shows the testing results for 10 specimens.

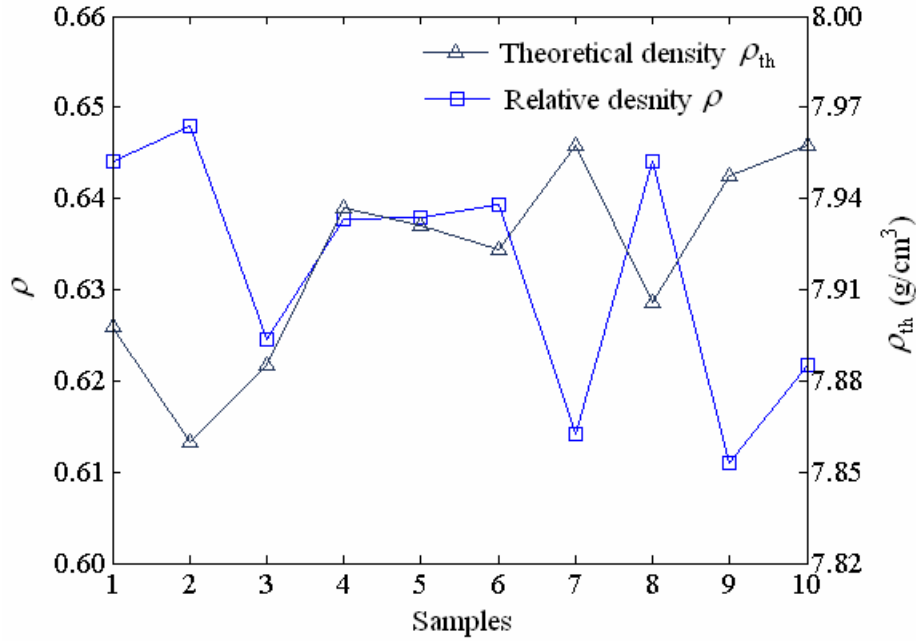


Figure 3.14: The relative density and theoretical density of the presintered 316L stainless steel specimens, obtained by experiments.

Discrepancy of the measured densities may be induced by inhomogeneity of the feedstock, the powder segregation effects in injection process, as well as the influence of some debinding and presintering factors. Figure 3.14 shows that the mean value of the relative density is 0.632, the theoretical density is 7.922 g/cm³, the apparent density is 5.007 g/cm³. The measured value of the relative density is higher than the one provided by the feedstock manufacturer, given to be 0.62, due to the small shrinkage of 0.5% in size of the specimens after presintering.

In Figure 3.15, the tensile test specimens before and after debinding and presintering are compared to show the slight change in their dimension. In fact, the injection moulded specimens become brittle after debinding in the oven due to removal of the binders that may provide the adhesion between the particles. However, the neck formation between the particles during presintering will increase the strength of the parts. The UTS obtained from the tensile tests of presintered specimens are about 100 MPa.

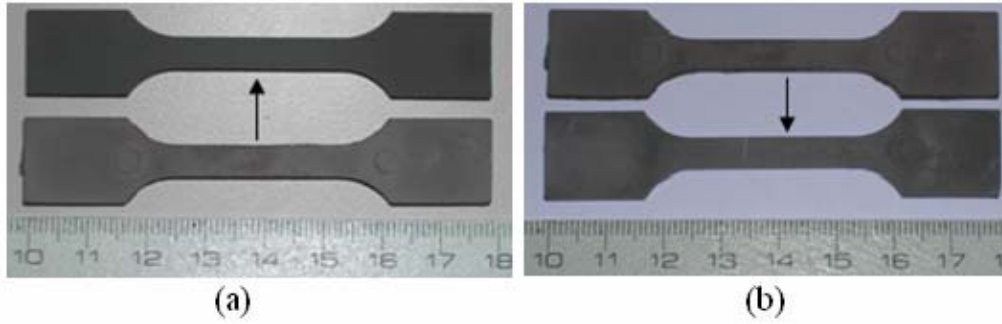


Figure 3.15: Appearance of the 316L stainless steel tensile test specimens at different stages during debinding and presintering processes: (a) From molded part to the debinded one after stage I, it becomes fragile but no shrinkages after stage I debinding in the oven, (b) From the part after stage I debinding to the one after stage II debinding and presintering in the furnace, the part reaches the strength of 100 MPa from the fragile state while it undergoes a small shrinkage of 0.5%.

3.4.2 Effects of Temperature Cycle on Densification

The typical thermal cycle of sintering includes heating to peak temperature, holding and afterwards cooling periods, as presented in Figure 3.16 from the results of experiments in the dilatometer. It manifests the relationship between the densification behaviors and the sintering temperature. The shrinkage and shrinkage rate are defined as follows:

$$\lambda = \frac{L - L_0}{L_0}, \quad \dot{\lambda} = \frac{d\lambda}{dt}, \quad (3.2)$$

where λ and $\dot{\lambda}$ are respectively the uniaxial shrinkage and shrinkage rate, measured by the tests in dilatometer, L_0 and L are initial and instantaneous lengths of the specimen.

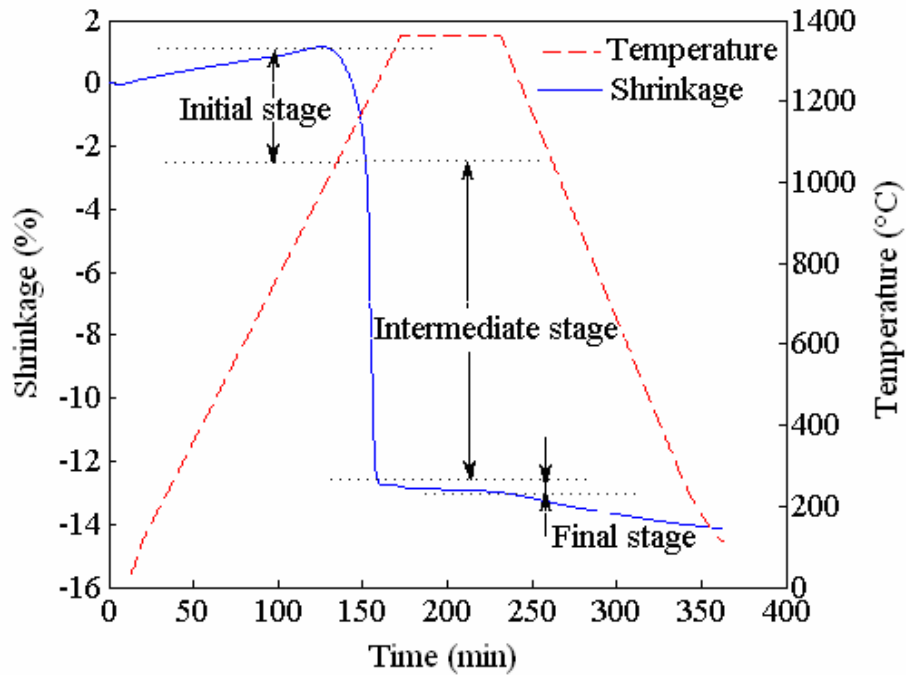


Figure 3.16: Piloting of the temperature cycle and the induced evolution in shrinkage. Sintering of the cylindrical specimen in 316L stainless steel powders, heating to 1360 °C at rate 8 °C/min then holding it for 1 h.

It can be observed that the densification of 316L stainless steel powder begins in the range of temperature between 1050 °C and 1080 °C. Before the starting of sintering at this temperature, there exists only the effect of linear thermal dilatation. The last cooling period represents the linear thermal shrinkage, too. Besides these two periods, which represents the preheating and cooling with only thermal dilatation, the real process of sintering can be divided into three stages, see Figure 3.16. The sintering begins in the initial stage, and then it subjects to the rapid shrinkage in the intermediate stage, afterwards the shrinkage becomes much slower in the final stage to finish the sintering process. This sintering model is in accordance with the classical sintering theory, as discussed in Chapter 2.1.3.

3.4.3 Effects of Heating Rate on Densification

In Figure 3.16 it is shown that the densification happens mainly in the period of increasing temperature (said heating period). Heating rate is in fact one of the most important process parameters of sintering processes. Different heating rates were

tested in the sintering experiments in dilatometer. The results are shown in Figure 3.17.

It can be observed that the maximum shrinkage rate depend on the heating rates but their peaks locate both in a narrow range of temperature. In fact, this narrow range spans merely from 1250 °C to 1270 °C. It is obvious that rapid sintering is favorable to densification, but fast sintering can induce cracks in sintered body due to the high thermal or stress gradients [GER 97].

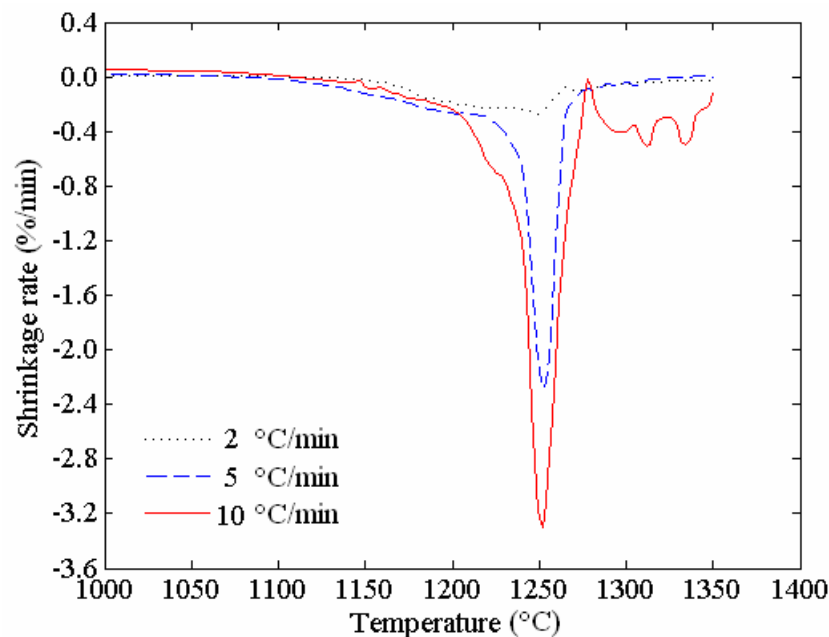
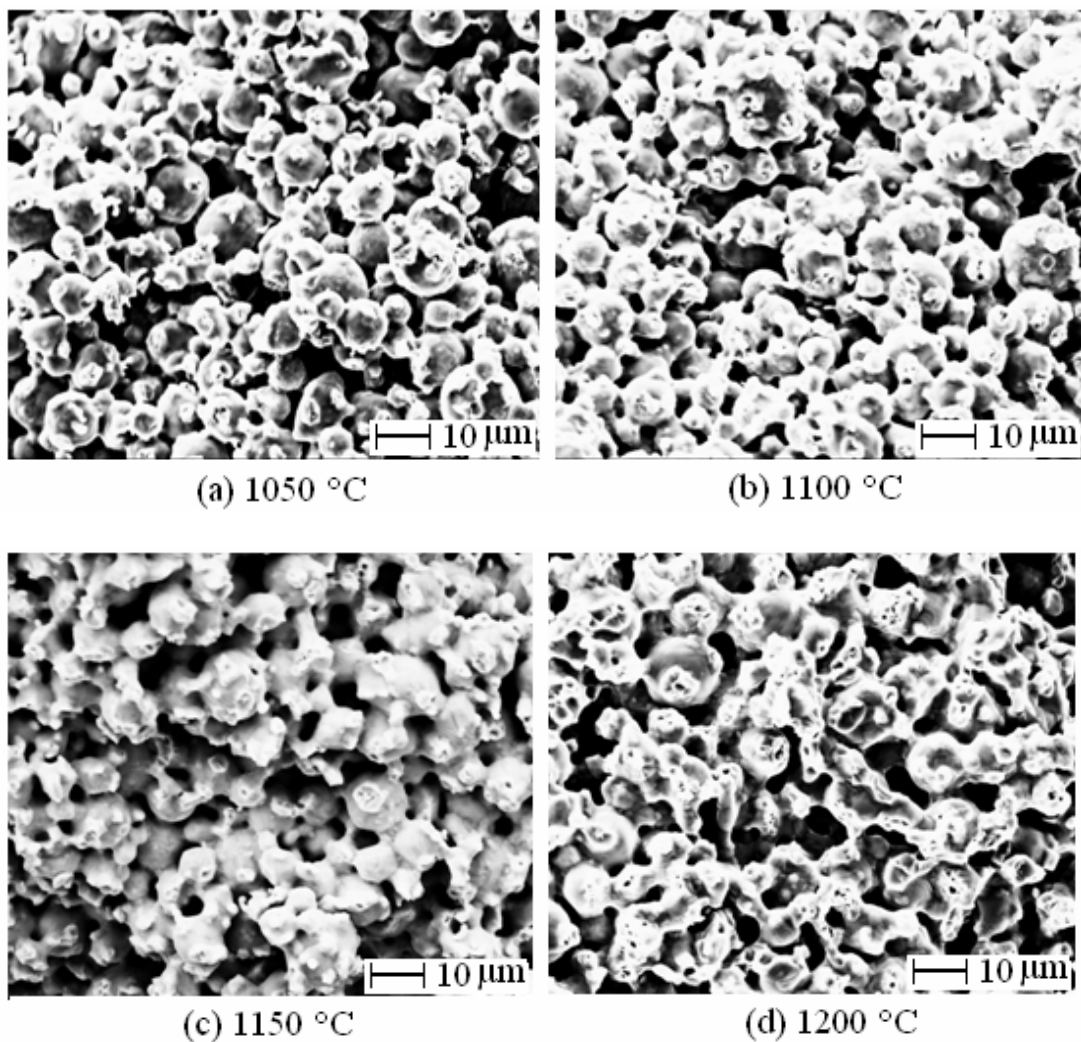


Figure 3.17: Shrinkage rates vs. heating rates, obtained by sintering experiments of 316L stainless steel powder in dilatometer.

3.4.4 Microstructural Evolutions

During the sintering process, the evolution in microstructure happens simultaneously with the densification. Microstructures on surfaces of the sintered parts at different temperatures are shown in Figure 3.18. From 1050 °C to 1200 °C, the sintering is at its initial stage. This stage is characterized by the neck formations and neck growth between the particles. The spherical shape of the particles can still be recognized. In the temperature range from 1250 °C to 1300 °C, the pores among the particles become interconnected, which appears the intermediate stage of sintering. The densification is developing rapidly in this stage. When the

temperature arrives to 1350 °C, the densification is mainly finished and the sintering comes into its final stage. The pores become isolated at the corners of the grain boundaries. The grain growth or coarsening is also the main characteristic in this last stage. It involves the growth of larger grains and the consumption of smaller grains, called Ostwald ripening. During the holding period at 1350 °C, the closed pores continue to reduce or vanish, and the grain sizes increase. The short holding time is appropriate for obtaining the final components with appropriate densifications and microstructures.



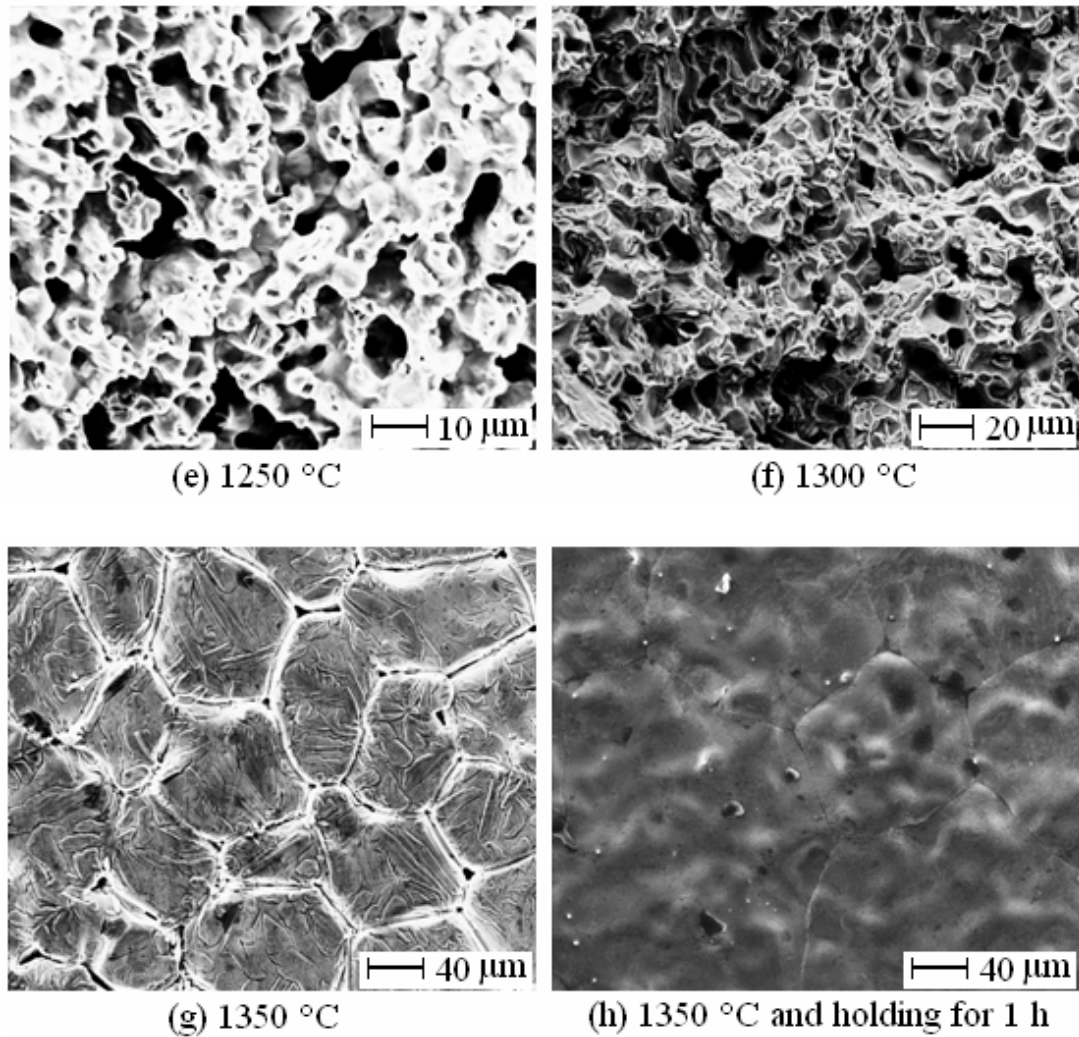


Figure 3.18: Microstructures on surfaces of the specimens in 316L stainless steel powder sintered under vacuum conditions. Except for Figure (h), the observed specimens were heated to different temperature with heating rate 5 °C/min then cooled directly with a rate 20 °C/min. Figure (h) shows the result of sintering that includes an additional holding period for 1 hour before the cooling.

3.4.5 Measured *In-situ* Strength

The results of flaming tensile tests are shown in Figure 3.18, with the heating rate equal 10 °C/min during the tests. The UTS is measured when the specimens are heated to the instant temperature without holding. In the temperature ranges 800 °C - 850 °C, *in-situ* strength decreases due to thermal softening effects. Afterwards, the effects of sintering bonding between the particles become greater than thermal softening. The *in-situ* strength increases in the heating period from 850 °C to 950 °C. After 950 °C, the influence of thermal softening becomes again the dominant effect.

The specimens lose significantly their strength.

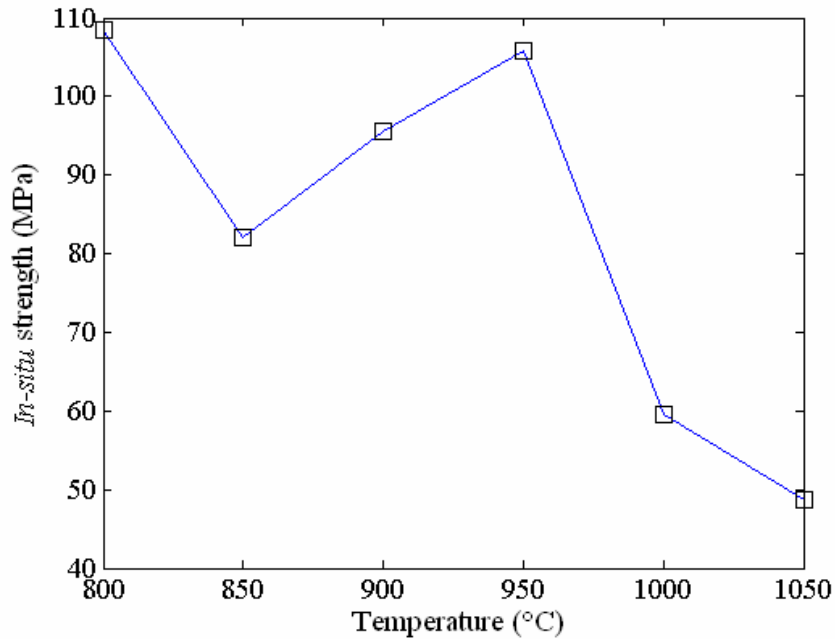


Figure 3.19: *In-situ* strength measured by flaming tensile tests on presintered specimens in 316L stainless steel powders.

3.4.6 Deflections in Gravitational Beam-bending Tests

At high temperature, the sintered bodies represent their low strength states. The sintered beams, issued from a pre-sintering treatment, are prone to show deflection under the gravitational load. The measurement on deflections of the gravitational beams can be used to identify the viscosity of the sintered powders. It provides also the validation for results of the numerical simulation that can be obtained based on the proposed model and identified parameters. The specimens after sintering to various temperatures are shown in Figure 3.20. The heating rate employed is 10 °C/min. It can be observed that the obvious deflection begins in the temperature range from 1050 °C to 1100 °C. Afterward the deflection increases, especially after 1200 °C. At 1350 °C, the deflection of the specimen is difficult to measure due to the great distortions.

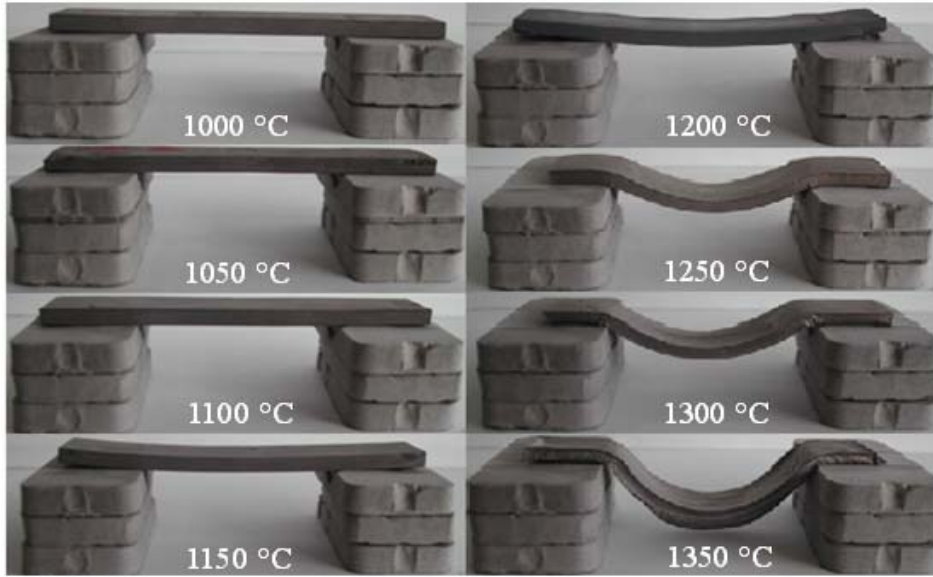


Figure 3.20: Deflections of the bending specimens in 316L stainless steel powders after heating to different temperatures then cooling rapidly to room temperature in the batch furnace, no holding period is applied.

The deflection at the middle position of the bending test specimen is measured. Based on the assumption mentioned in Chapter 3.3.3, the deflection rate can be determined by the following expression:

$$\dot{\delta} = \frac{\Delta\delta}{\Delta t} = \Delta\delta \frac{\Delta T}{k_h} \quad (3.3)$$

where $\Delta\delta$ is the change in deflection, ΔT is the change in temperature, k_h is heating rate, $\dot{\delta}$ is deflection rate. The measured deflections and deflection rates determined by Equation (3.3) are shown in Figure 3.21. It can be observed that the deflection rate increases with the rising of temperature before until 1250 °C. In the temperature range from 1250 °C to 1300 °C, the rapid densification induces strengthening of the specimen. This effect makes slower significantly the deflection. The deflection rate reduces in spite of the increase of temperature. However, the calculated deflection rate reaches at 1350 °C is not exact because the deflection can no more be measured precisely.

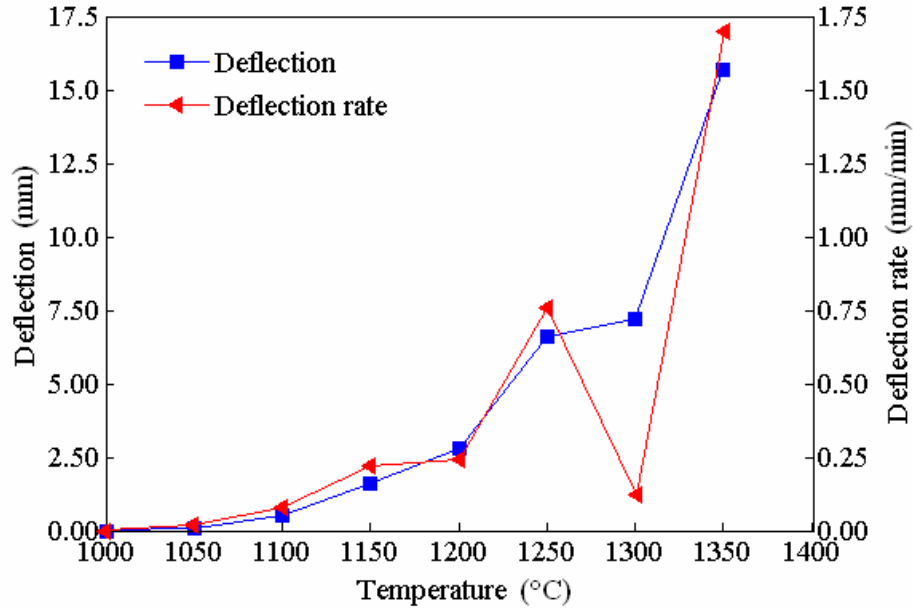


Figure 3.21: Sintering deflections and deflection rates of the bending specimens in 316L stainless steel powders.

3.4.7 Measured Post-sintering Strength

Particle bonding in sintering increases significantly the mechanical properties of sintered components, by example their strength, hardness, ductility and wear resistance. In order to investigate precisely the influences of sintering temperature on the strength of sintered components, the relationship between true strain and true stress in the tensile tests is analysed. True strain and true stress can be evaluated by the following expressions:

$$\varepsilon_{\text{true}} = \ln(1 + \varepsilon_{\text{eng}}), \quad \sigma_{\text{true}} = \frac{F(1 + \varepsilon_{\text{eng}})}{A_0} \quad (3.4)$$

where $\varepsilon_{\text{true}}$ is true strain, ε_{eng} is the engineering strain or elongation, σ_{true} is true stress, F is the loading force, A_0 is the initial area in section of the sintered specimen.

The true stress vs. true strains curves, obtained by experiments, are shown in Figure 3.22. Some of the specimens used in the tensile tests are shown in Figure 3.23. The experiments to obtain sintered specimens with peak temperature from 1320°C to 1380 °C were carried out by Barriere [BAR 00]. Barriere used the Swift

model to identify the hardening behavior by the tensile test curve 6 in Figure 3.22. The hardening curve can be fitted in the form $\sigma_o = \sigma_y + k \varepsilon^n$ with the parameters $\sigma_y = 200 \text{ MPa}$, $k = 1013 \text{ MPa}$, $n = 0.38$ [BAR 02].

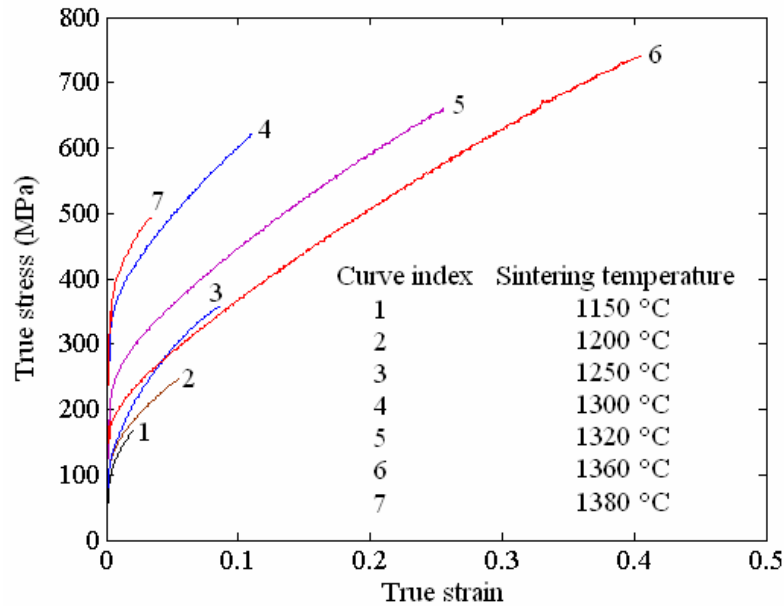


Figure 3.22: The stress vs. strain curves obtained by tensile tests for 316L stainless steel specimens, sintered at different temperatures.



Figure 3.23: Some of the tensile test specimens in 316L stainless steel sintered at different temperatures.

The sintering temperature has important influence on UTS and elongation of the specimens. As a general rule, UTS and elongation of the specimen increase

according to the rising of sintering temperature below a limited value. This limited value is 1380 °C in experiments that results in fast decreasing of the strength in the sintered specimen. The liquid phase induced by over sintering reduces remarkably the mechanical properties of the sintered components.

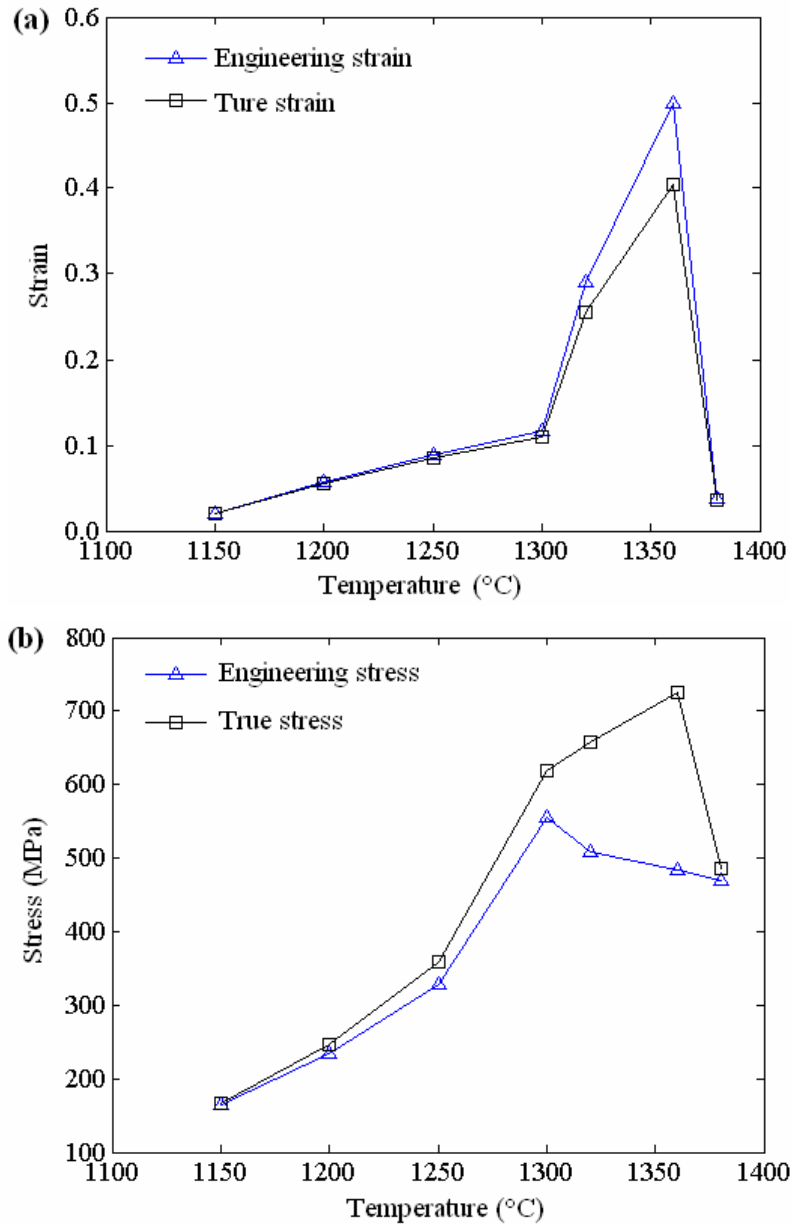


Figure 3.24: Influence of sintering temperature on the ultimate strain and stress, obtained by tensile tests on 316L stainless steel specimens.

The TRS (transverse rupture strength) obtained from three point bending tests can be determined through following way:

$$\sigma_{\text{TRS}} = \frac{3FL_s}{2bh^2} \quad (3.5)$$

where σ_{TRS} is the transverse rupture strength, L_s is the distance between both supporting rods, b is the width of the specimen, and h is the thickness of the specimen. The obtained σ_{TRS} of the specimens sintered to different temperature is shown in Figure 3.25. As the rising of sintering temperature, it improves the densification, that contributes to the increase of TRS.

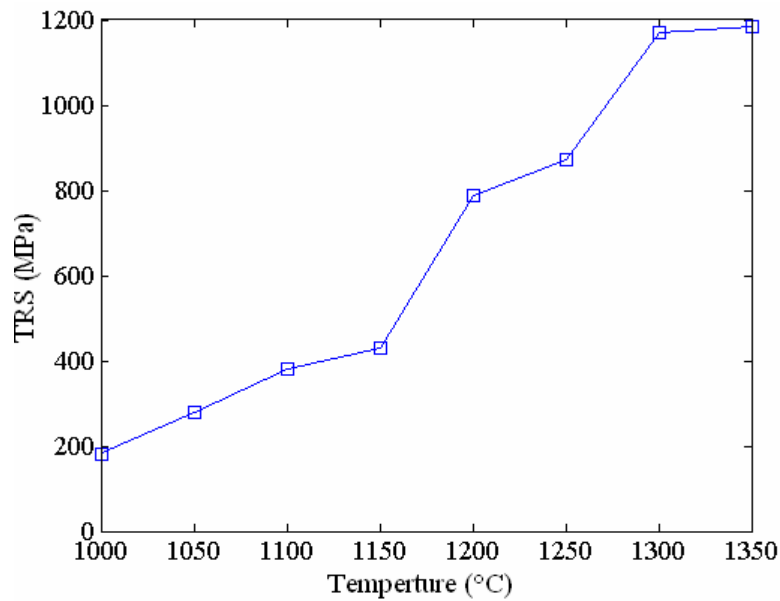


Figure 3.25: Transverse rupture strength (TRS) of 316L stainless steel specimens sintered at different temperatures, obtained by three-point bending tests.

3.5 Experimental Results for Alumina Powders

3.5.1 Effects of Debinding

The solid loading of alumina feedstock provided by the manufacturer is 81.5 wt.%, as presented in Table 3.3. The theoretical density of 99.8% type alumina is 3.91 g/cm^3 [NET TEC], resulting in calculated solid loading equal to 57.5 vol.%. By measuring the volume of the specimens with pycnometer, it can be observed that the

solvent debinding removes 88% of the binder in volume, and the next thermal debinding removes nearly all the remaining binder, as shown in Figure 3.26.

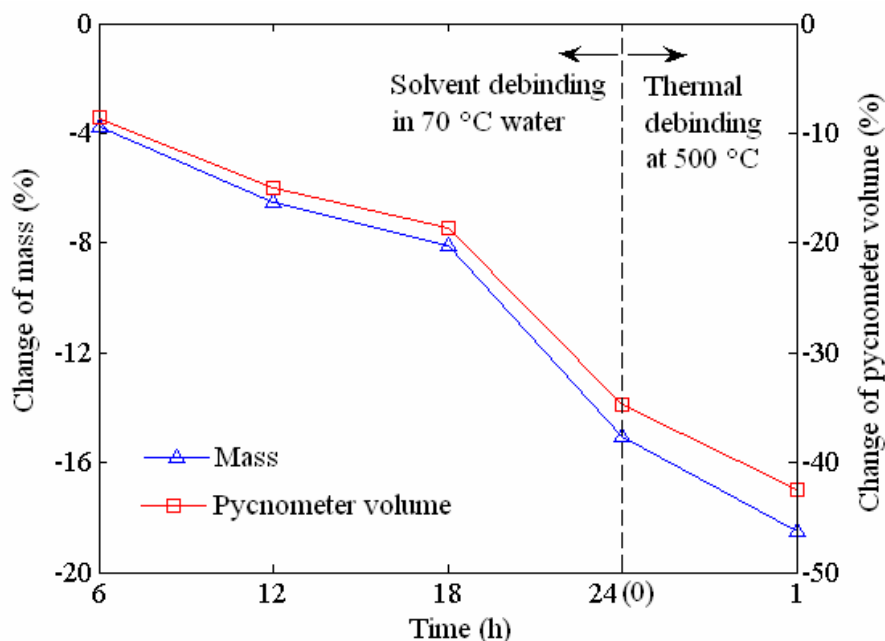


Figure 3.26: Evolution of the mass and pycnometer volume of molded alumina specimens obtained by solvent and thermal debinding processes.

3.5.2 Densification Behaviors in Non-isothermal Sintering

The typical thermal cycle for sintering includes heating, holding and cooling periods. The densification behaviours are different during various periods. The shrinkage and shrinkage rate curves of alumina specimen, measured by dilatometer, are shown in Figure 3.27. The temperature cycle is first heating up to 1550 °C at a rate equal to 10 °C/min, holding 2 h, and then cooling to room temperature at 20 °C/min. It can be observed that the densification is mainly accomplished in heating period. The densification continues in the holding period at much lower rate. The shrinkage rate decreases abruptly when the temperature stops to increase at the peak temperature. The different densification behaviors of the specimens in alumina powders for non-isothermal and isothermal sintering are investigated below.

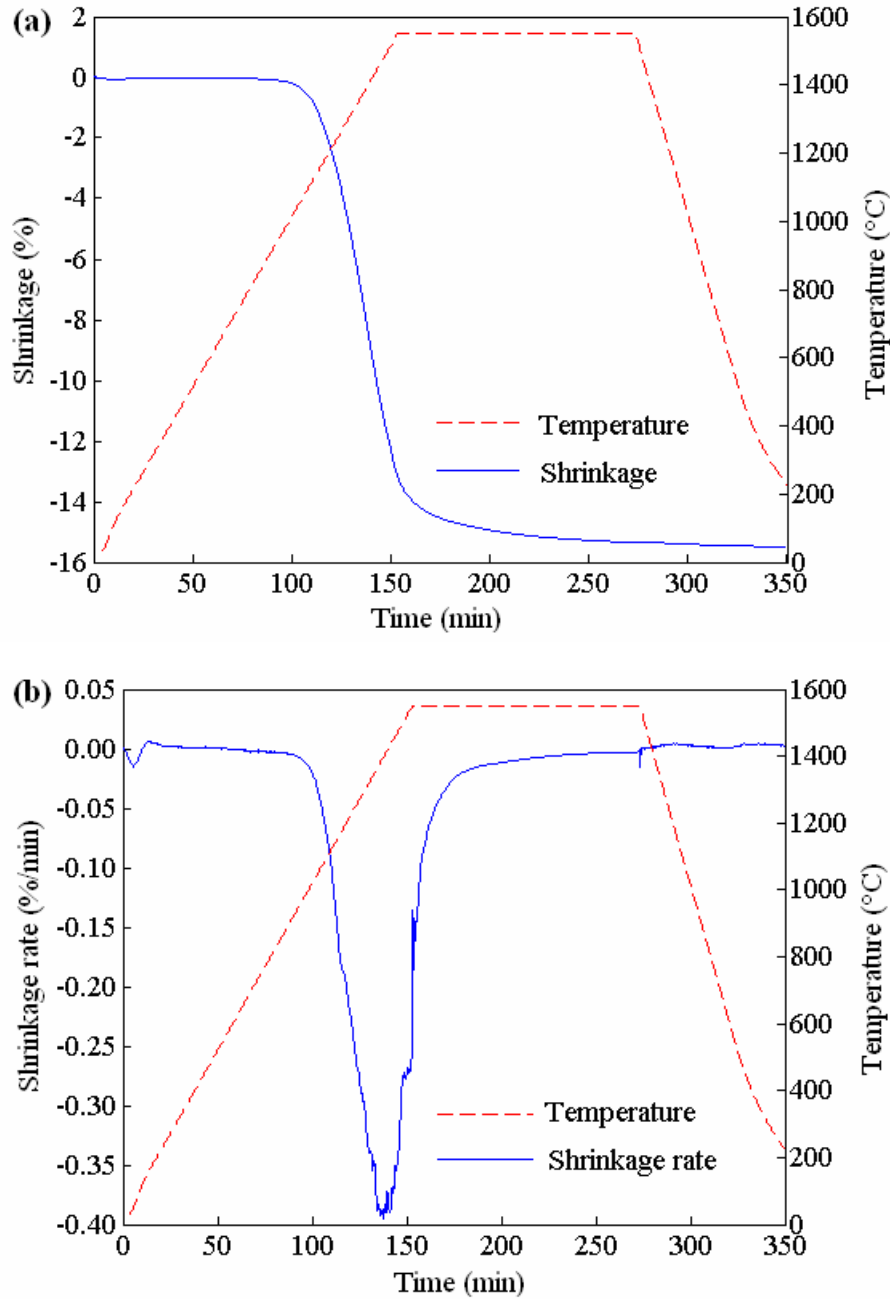


Figure 3.27: Shrinkage and shrinkage rate vs. sintering time measured by the sintering experiment on alumina specimen in dilatometer corresponding to the thermal cycle of heating to 1550 °C at 10 °C/min, then holding for 2h, and cooling at 20 °C/min: (a) shrinkage, (b) shrinkage rate.

3.5.2.1 Effects of Temperature on Densification in Non-isothermal Sintering Conditions

The densification of alumina specimen appears to be diffusion controlled sintering. It depends on the atomic mobility and the microstructural sintering stress. The increasing of the sintering temperature can accelerate the sintering process

because the atoms become more active. Figure 3.28 shows the experimental curves of shrinkage and shrinkage rate vs. sintering temperatures with a thermal cycle up to 1600 °C with constant heating rate 10 °C/min. It can be observed that the densification begins at about 850 °C and increases very slowly until 1050 °C. Afterwards, the shrinkage rate increases rapidly. The maximum shrinkage rate occurs at about 1380 °C.

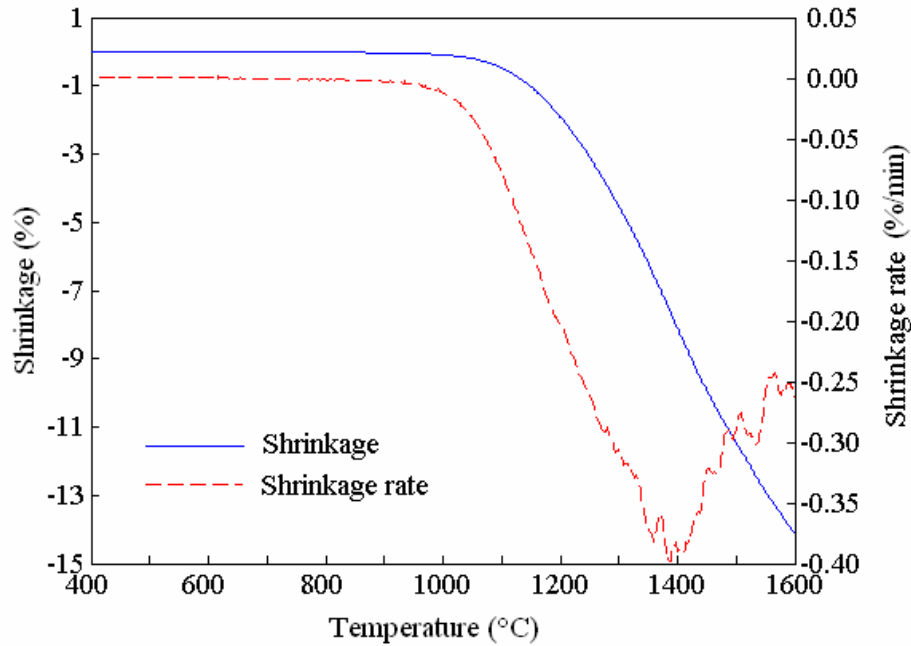


Figure 3.28: Shrinkage and shrinkage rate versus sintering temperature, measured by the sintering experiment on alumina specimen in dilatometer. Heating to 1600 °C at rate 10 °C/min without holding.

For alumina powder, the thermal expansion is so small that it can be neglected. With the assumption of isotropic shrinkage during the sintering, the instantaneous relative density ρ can be determined as follows:

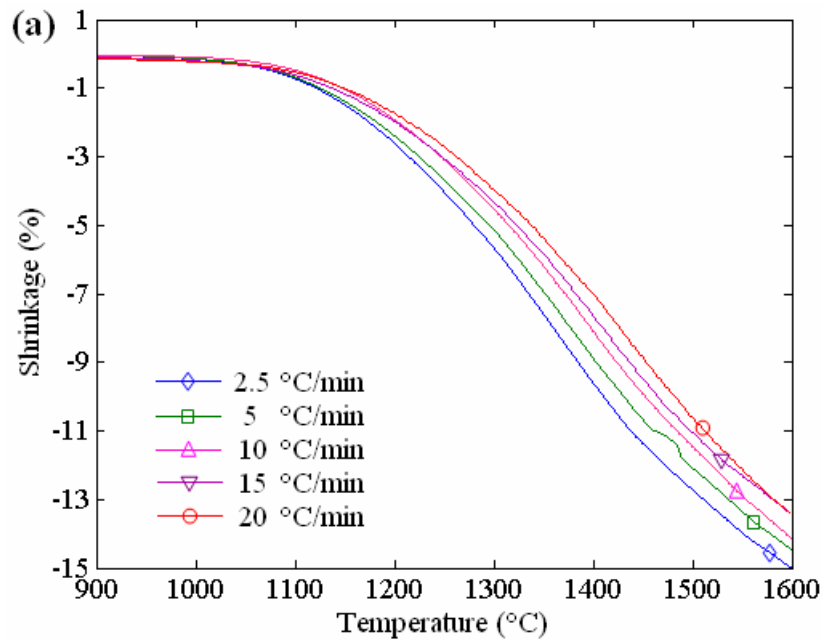
$$\rho = \frac{\rho_0}{(1 + \lambda)^3} \quad (3.6)$$

where ρ_0 is the initial relative density of the debinded specimens before sintering, λ is the shrinkage defined in Equation (3.2). For the alumina feedstock used in experiment, ρ_0 is the solid loading equal 0.58. In Figure 3.28, the shrinkage at

1600 °C is -14.13%, the relative density is 0.92. So the densification is realized mainly in the heating period of sintering.

3.5.2.2 Effects of Heating Rate on Densification in Non-isothermal Sintering

Heating rate is an important parameter of the sintering process. Fast heating induces thermal gradients in the sintering body that accelerate sintering. The driving force for densification in sintering is sensitive to the thermal gradients [GER 96]. As shown in Figure 3.29(a), the shrinkage is somewhat greater for the thermal cycles with lower heating rates to reach the same peak temperature. In Figure 3.29(b) it shows that the faster heating results in the greater peak values of shrinkage rate.



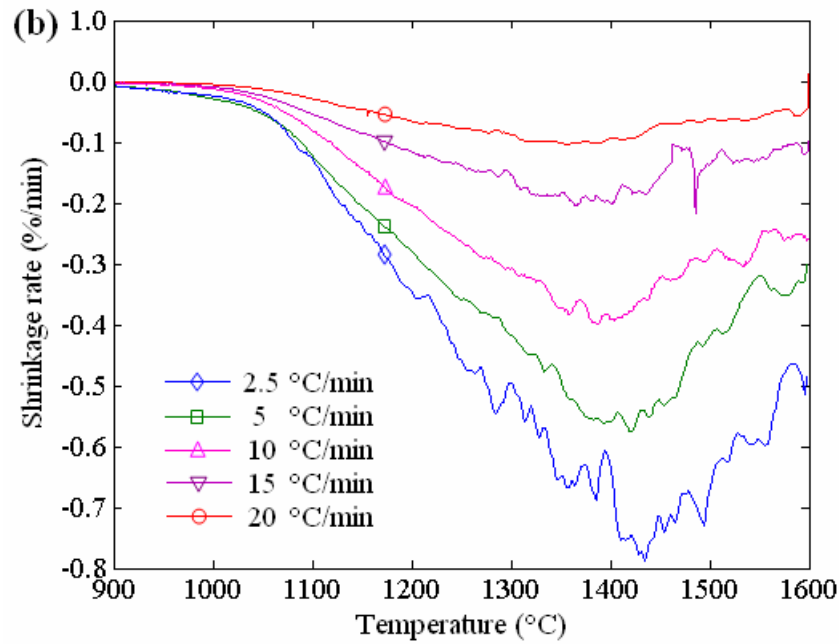
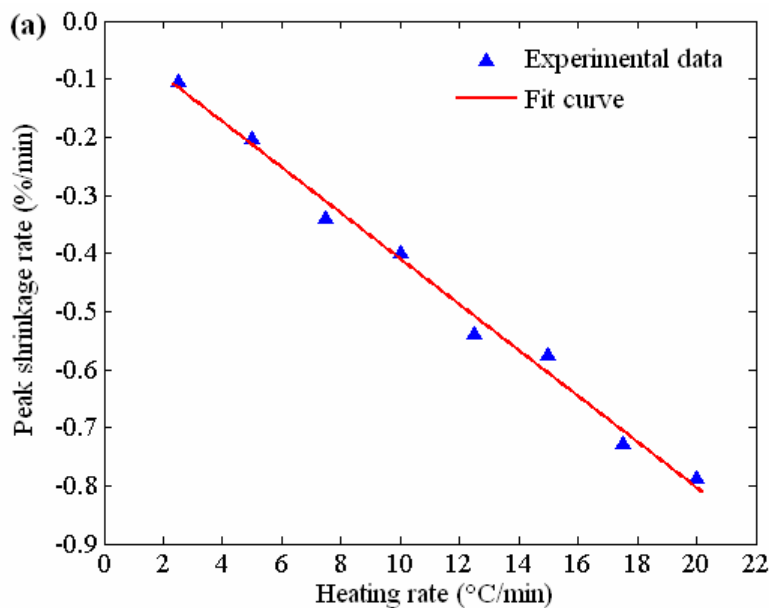


Figure 3.29: Shrinkage and shrinkage rate versus temperature measured through the sintering experiments on alumina specimens in dilatometer: (a) shrinkage, (b) shrinkage rate. The thermal cycles are heating to 1600 °C at rate 2.5 °C/min, 5 °C/min, 10 °C/min, 15 °C/min and 20 °C/min respectively.

Rapid heating can also postpone the appearance of peak shrinkage rate to higher temperature. The effects of heating rate on peak shrinkage rate and the corresponding temperature are investigated by the sintering experiments. Different heating rates are tested, which ranges from 2.5 °C/min to 20 °C/min, as shown in Figure 3.30.



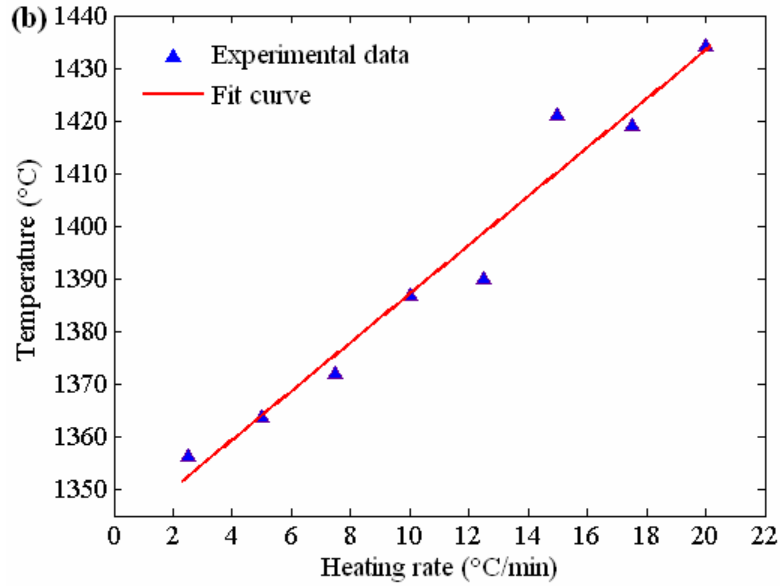


Figure 3.30: The measured peak shrinkage rates and the corresponded temperatures vs. the constant values of heating rate of alumina specimens sintered in dilatometer: (a) peak shrinkage rate, (b) temperature at peak shrinkage rate. The thermal cycles consist in heating up to 1600 °C by different heating rates from 2.5 °C/min to 20 °C/min.

The linear polynomials are used to fit the experimental data shown in Figure 3.2 9 and Figure 3.30, as in the following expressions:

$$\dot{\lambda}_{\text{peak}} = -0.0170 - 0.0394k_h, \quad T_{\text{peak}} = 1341 + 4.621k_h \quad (3.7)$$

where $\dot{\lambda}_{\text{peak}}$ is the peak shrinkage rate in unit (%/min), k_h is the heating rate in unit (°C/min), T_{peak} is the temperature at the peak shrinkage rate in unit °C.

3.5.3 Densification Behaviors in Isothermal Sintering

The most common used temperatures used for the sintering of alumina are from 1100 °C to 1650 °C [GER 96], [OPF 98], [ZUO 04]. It mainly depends on the particle size of the powders. In order to compare the densification behaviors of alumina specimens at various holding temperatures, the thermal cycles employed consist to heat from 1300 °C to 1600 °C at 20 °C/min, and then holding for 2h. The measured shrinkages are shown in Fig. 3.31.

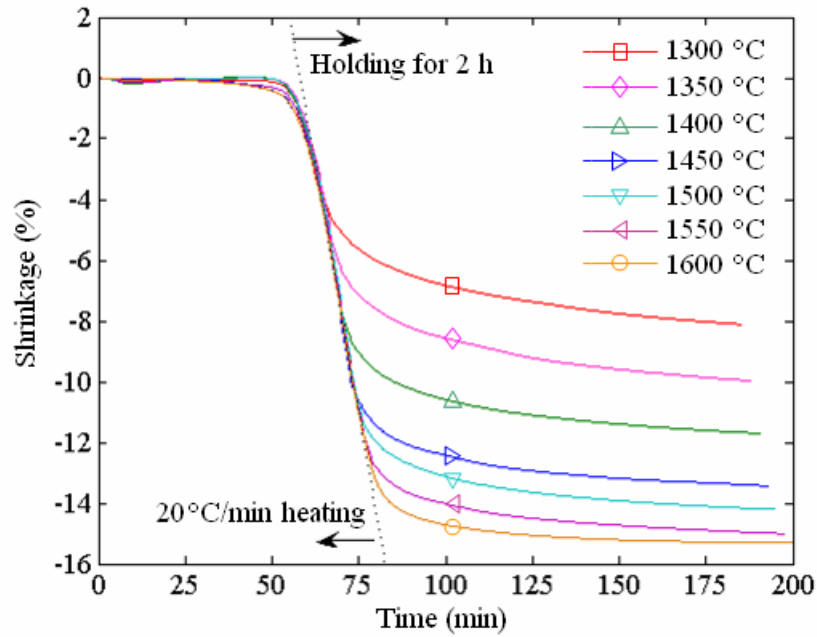
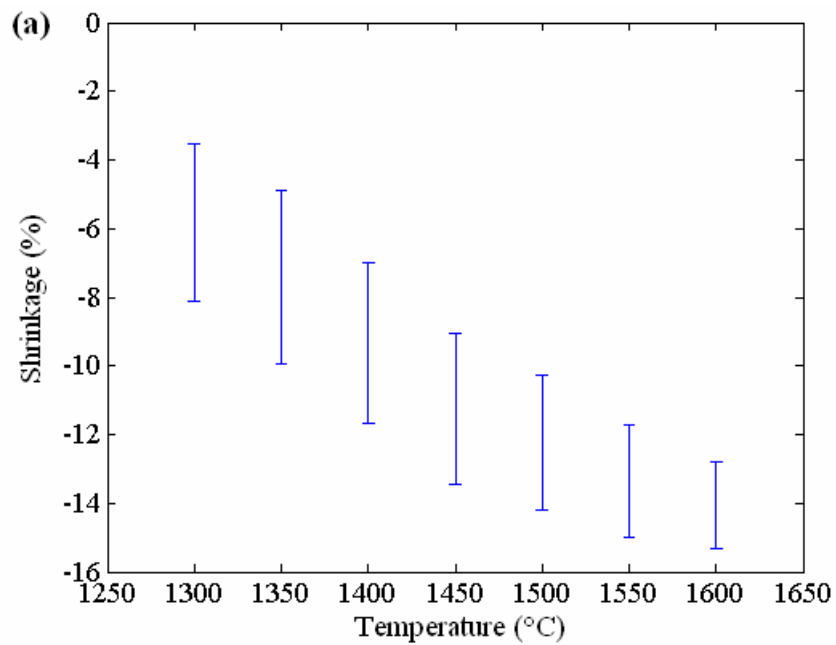


Figure 3.31: The measured shrinkage curves in the sintering with the thermal cycles heating to various peak temperatures from 1300 °C to 1600 °C at 20 °C/min, and then holding for 2 h.

The evolution of shrinkage and relative density in the holding duration for 2h at various temperatures are shown in Figure 3.32.



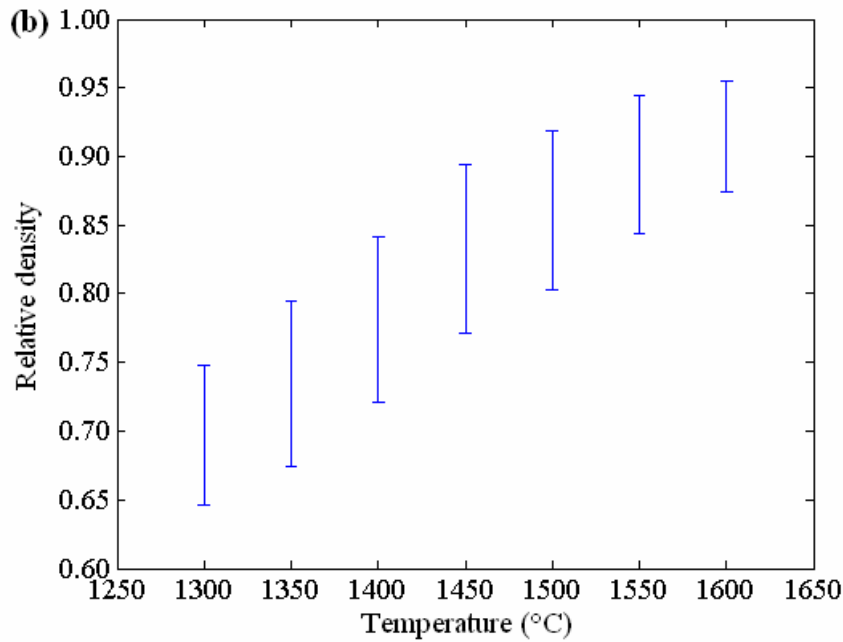


Figure 3.32: Evolution of shrinkage and relative density in the isothermal sintering at various temperatures from 1300 °C to 1600 °C for 2 h. The previous thermal cycle is heating to temperatures of isothermal sintering at 20 °C/min.

It can be observed that when the temperature of isothermal sintering is below 1500°C, the changes of shrinkage and relative density in the 2 h holding period are nearly the same. The shrinkages during the holding periods are from -2.2% to -2.5%. It seems independent on the holding temperature. However, when the isothermal sintering temperature is higher than 1500 °C, the shrinkages during the 2 h holding periods are smaller as the elevation of temperature, from -1.97% to -1.25%. It is due to after 2 h duration at the temperature over than 1500 °C, the relative density has exceeded than 0.92. According to the theory of sintering, it has come into the final stage of sintering [COB 61], [GER 96], [KAN 04]. In the final stage of sintering, the pores among the grain boundaries become to close or vanish. The densification at this stage is slow and small.

3.5.4 Microstructural Evolutions

In the sintering of alumina powders, the microstructural evolutions include the decrease of the porosity and the grain growth. The fracture surfaces without polish of the sintered parts after various thermal cycles in dilatometer are observed by SEM.

3.5.4.1 Effects of Temperature on Microstructures

The debinded alumina specimens are sintered with the thermal cycles of heating to 1300 °C, 1400 °C, 1500 °C and 1600 °C at 10 °C/min without holding, and then cooling to the room temperatures at 20 °C/min. The SEM photos of the fracture surfaces are shown in Figure 3.33.

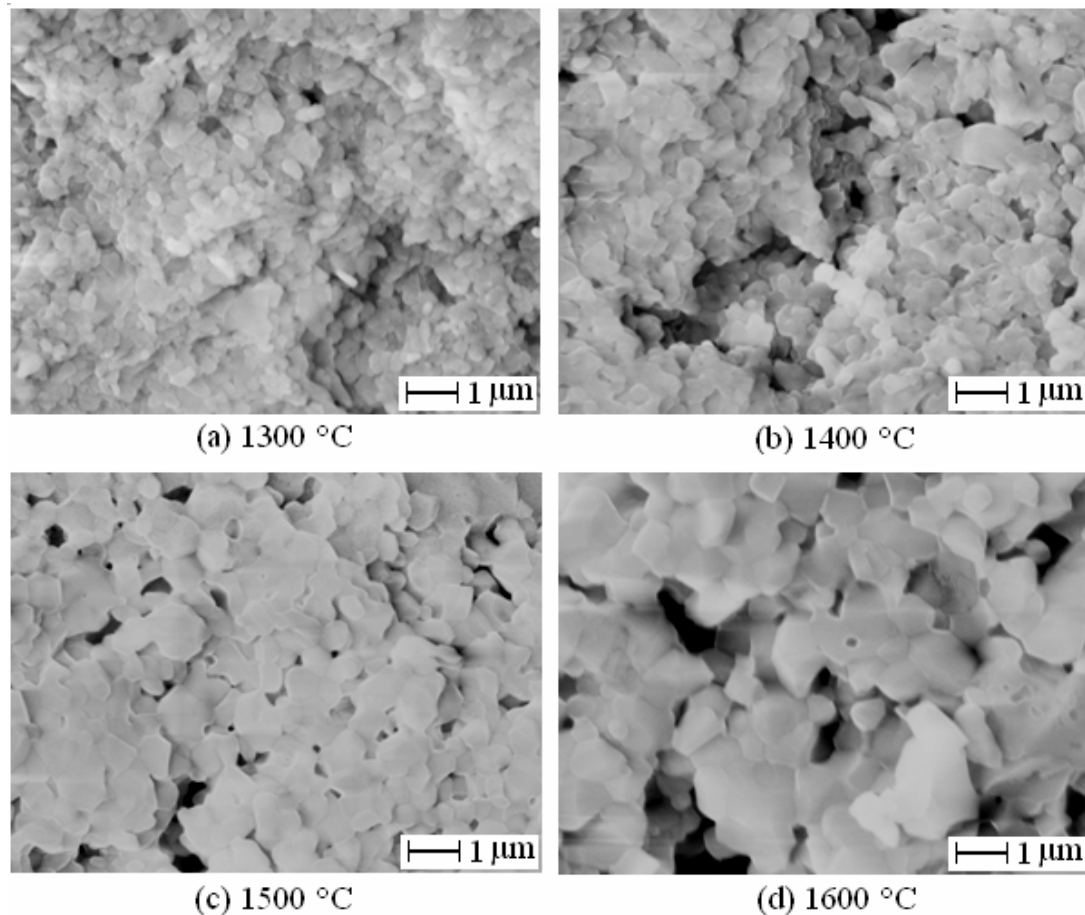


Figure 3.33: The microstructures of the sintered alumina specimens after the thermal cycles of heating at 10 °C/min to various peak temperatures without holding and then cooling to room temperature at 20 °C/min.

The measured shrinkages of the sintered specimens as shown in Figure 3.33 (a),

(b), (c) and (d) by dilatometer are -5.265%, -9.636%, -12.172% and -14.836% respectively. According to the Equation (3.6), the final relative densities of the specimens are 0.682, 0.786, 0.856 and 0.939 respectively. It can be observed that as the improving of the sintering temperature, the relative density increases, but the grain size also increases rapidly. In Figure 3.33, the grain size of specimen sintered at 1600 °C is nearly 2-4 times of the one sintered at 1300 °C. It occurs at only in 30 min.

3.5.4.2 Effects of Heating Rate on Microstructures

The heating rate has important effects not only on the relative density of the sintered parts, but also on the final grain size. The microstructures of the sintered specimens are observed after the heating to 1600 °C at various heating rates without holding, and then cooling to room temperature at 20 °C, as shown in Figure 3.34.

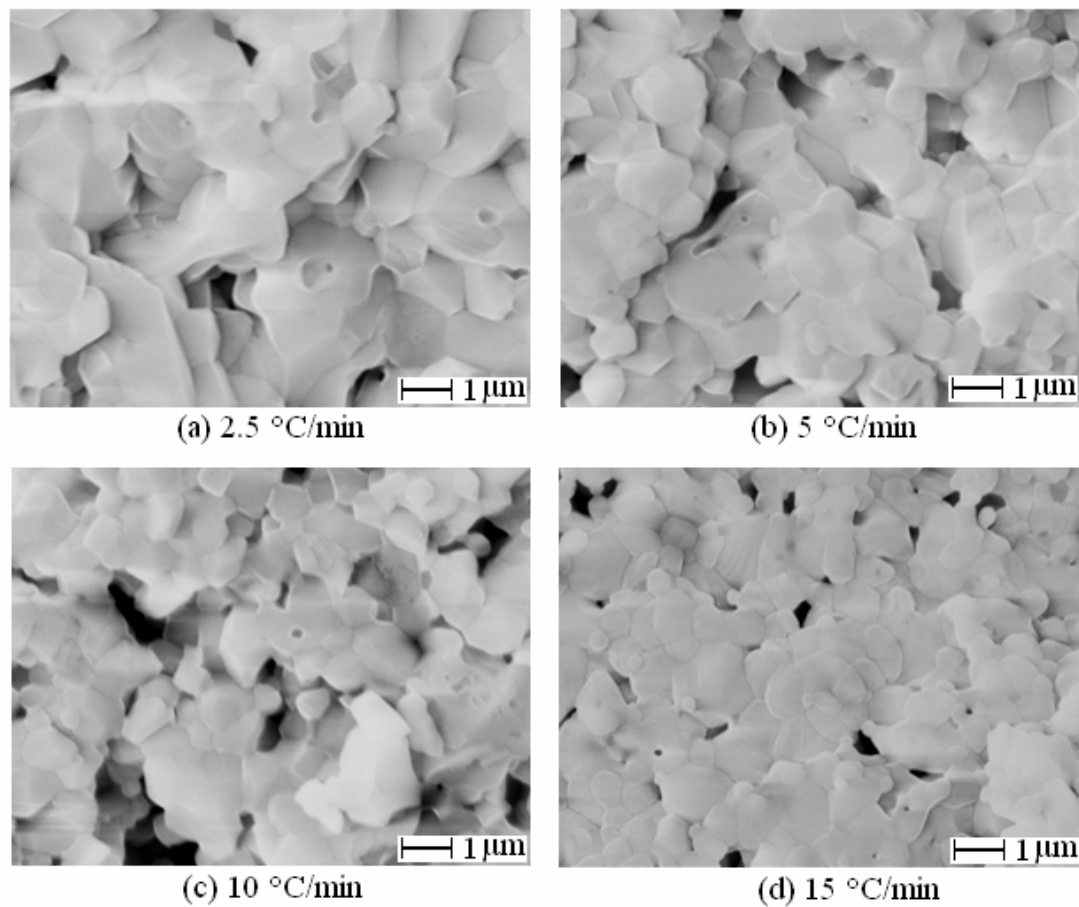


Figure 3.34: The microstructures of the sintered alumina specimens after the thermal cycles of heating to 1600 °C at various heating rates without holding and then cooling to room temperature at 20 °C/min.

With the measured shrinkages by dilatometer, the calculated final relative densities of the sintered specimens shown in Figure 3.34 (a), (b), (c) and (d) are 0.954, 0.939, 0.939 and 0.916 respectively. It can be seen that with the same peak temperature in sintering, the heating rate has small effects on the final relative density. However, it has the apparent effects on the grain size of the sintered parts, as shown in Figure 3.34. Rapid heating is favorable to obtain the sintered parts with fine grain size.

3.5.4.3 Effects of Holding Time on Microstructures

Holding at the high temperature in sintering can improve the final relative density of the sintered parts, but it induces the increase of the grain size. The microstructures of the two specimens after the thermal cycles of heating at 10 °C/min to 1550 °C without holding and holding for 3h are shown in Figure 3.35. The relative density of the sintered parts as presented in Figure 3.35 (a) and (b) are 0.915 and 0.943 respectively.

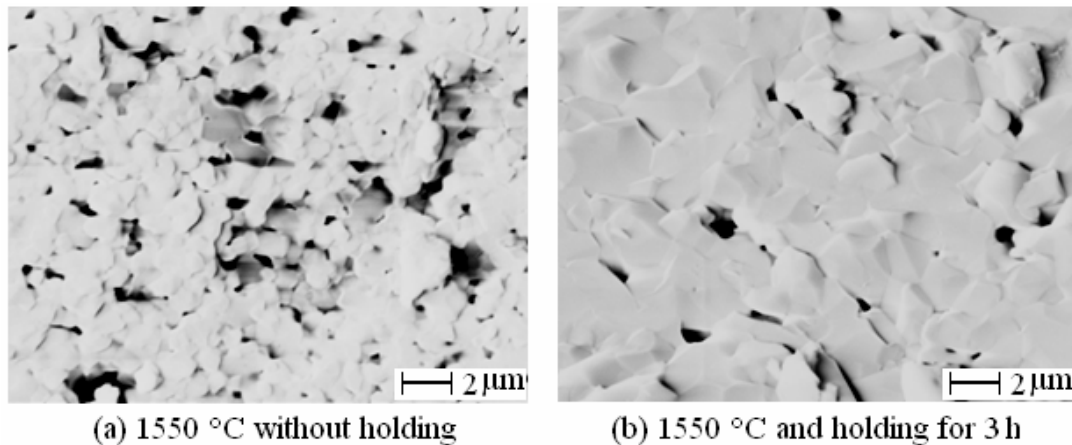


Figure 3.35: The microstructures of the sintered alumina specimens after the thermal cycles of heating to 1550 °C at 10 °C/min without or with holding time , and then cooling to room temperature at 20 °C/min.

3.6 Conclusions

Different experimental procedures associated to the sintering processes are introduced in the chapter. The results represent the original contribution of the present work of the present work and lead to the detailed discussion on the sintering

of metallic and ceramic PIM components. The investigations on experimental results permit to draw out the following conclusions:

- The studies made by dilatometer show that the debinded specimens in 316L stainless steel powder are prone to distort at high temperature due to the low *in-situ* strength, even though the action of pushrods is very slight. However, the debinded alumina specimens exhibit the good abilities to resist to the distortions in sintering. Presintering is a good way for the 316L stainless steel specimens to reach the total debinding, and to improve the *in-situ* strength. It can be applied to reduce the distortions in sintering.
- The densification is mainly realized during the period of increasing temperature in sintering process. Many data of the material parameters in the literatures are valid only for isothermal sintering. For the non-isothermal sintering, it is necessary to identify the material parameters by experiments.
- There is a threshold of temperature at which the obvious densification occurs. It depends on the ingredients of the powder material and particle size. In the present experiments, the densifications of 316L stainless steel and alumina powders start at about 1050 °C and 850 °C respectively.
- Densification proceeds rapidly in the intermediate stage of sintering. For 316L stainless steel powder, it represents a very narrow range of temperature from 1250 °C to 1300 °C. For alumina powder, the range is relatively wide, from 1050 °C to 1550 °C.
- The mechanical properties of the final components are strongly dependent on the results of densification. The main influent factors include initial density, material characteristics, thermal cycle, and other factors of sintering.
- The densification behaviors are sensitive to the heating rate parameter, for both the PIM components in metallic or ceramic powder. Rapid sintering is generally favorable for densification.

Chapter 4 Development of Phenomenological Sintering Model

For the purpose of sintering simulation, which is aimed to optimize the sintering process and the injection mold design, the macroscopic model of sintering based on continuum mechanics is employed. A phenomenological model is used to describe the densification behaviors issued of the observation and measurement in experiments. The determination of the parameters in the adopted constitutive law is introduced. This model is used to predict the shrinkages and density evolutions of the sintered components. Simultaneously, the model used to predict the *in-situ* and post-sintering strength is also presented.

4.1 General Definitions

The green body after injection molding and debinding is a porous medium. It includes solid skeleton and voids (pores). Equivalent behaviors of the porous medium in sintering can be described by the continuum mechanics, for the interest of realistic simulation of the sintering processes. The solid skeleton, made up of powder particles, is assumed to behave as nonlinear viscous isotropic solid. The voids are isotropically distributed. So the overall response of the porous material is therefore isotropic [OLE 98].

During the sintering process, the pores shrink or vanish under the effect of sintering stress or external force. So the porous material of green body represents its shrinkage property. Relative density and porosity are both apparent parameters used to describe the densification level of the porous material. The porosity θ is defined by the following expressions:

$$\theta = \frac{V_{\text{pores}}}{V_{\text{total}}} \quad (4.1)$$

where V_{pores} is the volume of the pores in the porous material, and V_{total} is the total

apparent volume of porous material including the solid skeleton and the pores. From the definition of relative density ρ as Equation (2.12), it yields the following relationship:

$$\rho = 1 - \theta \quad (4.2)$$

As the densification proceeds in sintering, it reduces the porosity and intensifies the relative density. For the wrought material or fully densified material, it should be $\theta = 0$ or $\rho = 1$.

4.2 Governing Equations

4.2.1 Mass Conservation

During densification, the apparent volume of sintering body reduces, but there is no change in mass of the powder skeleton. Neglecting mass of the air in the porous, the evolution of the relative density is governed by the mass conservation. The equation can be expressed as following:

$$\dot{\rho} + \rho \cdot \dot{\epsilon} = 0 \quad (4.3)$$

where the voluminal strain rate $\dot{\epsilon}$ is the trace of strain rate tensor, expressed as:

$$\dot{\epsilon} = \text{tr}(\dot{\boldsymbol{\epsilon}}) = \dot{\epsilon}_{kk} \quad (4.4)$$

4.2.2 Momentum Conservation

The momentum conservation equation describes the mechanical equilibrium of the sintering body and can be written as:

$$\nabla \cdot \boldsymbol{\sigma} + \mathbf{f} = \rho_{\text{ap}} \frac{\partial^2 \mathbf{u}}{\partial t^2} \quad (4.5)$$

where $\boldsymbol{\sigma}$ is the Cauchy stress tensor, \mathbf{f} is external body force applied on the sintering part, \mathbf{u} is the displacement field and t is the current processing sintering time. The sintering can be considered as quasi-static process. The inertia forces in the right side of Equation (4.5) are often neglected. ρ_{ap} is the apparent density of

the porous materials, as defined in Equation (3.1).

For PIM components, the sintering is generally a pressureless one. The external applied force \mathbf{f} mainly refers to the gravity of the sintering body, expressed as following:

$$\mathbf{f} = \rho_{\text{ap}} \mathbf{g} \quad (4.6)$$

where \mathbf{g} is gravitational acceleration vector.

4.2.3 Energy Conservation

The sintering process represents a coupled thermo-mechanical phenomenon. The deformations of the sintered bodies are strongly dependent of the temperature evolution. The conservation energy equation is expressed as:

$$\rho_{\text{ap}} c_{\text{eff}} \dot{T} - \nabla \cdot (k_{\text{eff}} \nabla T) = \beta (\boldsymbol{\sigma} : \dot{\boldsymbol{\epsilon}}_{\text{vp}} - \sigma_s \dot{\epsilon}) \quad (4.7)$$

where c_{eff} and k_{eff} are the effective heat capacity and thermal conductivity of the porous material, $\beta (0 \leq \beta \leq 1)$ represents the share of viscoplastic work dissipated into heat, $\dot{\boldsymbol{\epsilon}}_{\text{vp}}$ is the viscoplastic strain, $\dot{\epsilon}$ is voluminal strain rate.

For free sintering, the stress and viscoplastic strain rate are at the low-level importance. So the dissipative energy can be neglected. So Equation (4.7) can be simplified as following:

$$\rho_{\text{ap}} c_{\text{eff}} \dot{T} - \nabla \cdot (k_{\text{eff}} \nabla T) = 0 \quad (4.8)$$

Equation (4.8) is the heat transfer equation that controls the temperature distributions in the sintering body. The apparent density ρ_{ap} in Equation (4.8) is coupled with Equations (4.3) and (4.5).

The heat capacity and thermal conductivity of porous materials are dependent of the relative density, or the porosity. c_{eff} is the function of temperature and porosity, as following [OLE 00 c]:

$$c_{\text{eff}} = c_0(T) \bar{c}(\theta) \quad (4.9)$$

where $c_0(T)$ is the heat capacity function of the fully densified materials, $\bar{c}(\theta)$ is function of θ .

Thermal conductivity decreases when the porosity increases, unless the gas in the pores has higher thermal conductivity than in the solid material. An empirical expression for the dependence of the thermal conductivity on porosity could be expressed as following [GER 96]:

$$\frac{k_{\text{eff}}}{k_0} = \frac{1 - \theta}{1 + \chi\theta^2} \quad (4.10)$$

where k_0 is the thermal conductivity of the fully densified material, the coefficient χ expresses the sensitivity of thermal conductivity to the presence of pores. Analysis on several materials, which can represent a variety of pore sizes and shapes, gives 11 for the best value of χ . When the porosity θ is less than 30%, the following linear expression could be considered as appropriate:

$$\frac{k_{\text{eff}}}{k_0} = 1 - \omega\theta \quad (4.11)$$

where the coefficient ω is between 1 and 2.

4.3 Boundary Conditions

4.3.1 Mechanical Boundary Conditions

The whole boundary of the sintering body is divided into two parts, expressed as following:

$$\Gamma = \Gamma_c + \Gamma_f \quad (4.12)$$

where Γ is the total surfaces of the sintering body, Γ_c is the surfaces contacted with the substrate, Γ_f is the free surfaces exposed in the sintering atmosphere.

Then the boundary conditions in loads and displacements can be expressed as:

$$\begin{aligned}
 \forall \bar{X} \in \Gamma_f, \quad \boldsymbol{\sigma} \cdot \mathbf{n} &= \mathbf{p}_s \\
 \forall \bar{X} \in \Gamma_c, \quad \mathbf{u} \cdot \mathbf{n} &= 0 \\
 \forall \bar{X} \in \Gamma_c, \quad \boldsymbol{\tau} &= \boldsymbol{\sigma}_f
 \end{aligned} \tag{4.13}$$

where \bar{X} is the spatial position in the model, \mathbf{n} is the normal vector related to the surface, $\boldsymbol{\tau}$ is the shear stress, $\boldsymbol{\sigma}_f$ is the distributed load associated to friction, \mathbf{p}_s is the pressure of sintering atmosphere. The Coulomb friction law can be used to determine the distributed friction between the sintering body and the substrate [OLE 00 b], defined as following:

$$\forall \bar{X} \in \Gamma_c, \quad \boldsymbol{\sigma}_f = \mu_f \boldsymbol{\sigma}_n \tag{4.14}$$

where μ_f is the friction coefficient, $\boldsymbol{\sigma}_n$ is the normal stress of the contacted surfaces.

4.3.2 Thermal Boundary Conditions

The temperature of sintering body changes with the thermal cycle in the furnace. The parts absorb the heat via thermal conduction, convection and radiation. The thermal boundary conditions can be expressed as:

$$\forall \bar{X} \in \Gamma, \quad T = f(\bar{X}, t) \tag{4.15}$$

where $f(\bar{X}, t)$ is the temperature distribution function. For the sintering of small components, the temperature gradients in the sintering body are small, unless the heating process is very rapid. However, there are usually temperature gradients in the furnace [GER 96].

4.4 Constitutive Sintering Law

4.4.1 Thermo-elasto-viscoplastic Model of Sintering Bodies

At the high temperature encountered in sintering, the densification of the polycrystalline materials are controlled by diffusion processes, which can be

regarded as creep deformation [COB 63], [FOL 61], [HER 50], [NAB 48], [NAB 00], [NAB 02]. So the deformation of the sintered body including shrinkage and distortion is rate dependence. The viscoplastic constitutive law in continuum mechanics can be used to describe this process. On the other hand, the thermal expansions are observed in the experimental results coming from dilatometer experiments. However, there are some evidences showing that the green parts are elastic at room temperature. There exists an elastic to viscous transition region during sintering [CAI 97 a], [CAI 97 b], [CAI 97 c]. The elastic strain and thermal strain due to the change in temperature should also be considered [GAS 00], [ZHA 02 a]. The thermal elasto-viscoplastic model of the sintered bodies is shown in Figure 4.1.

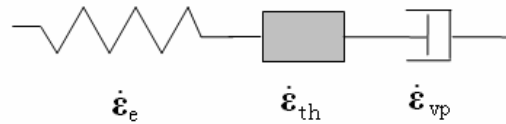


Figure 4.1: Thermo-elasto-viscoplastic model of sintering bodies for the entire sintering process including elastic strain, thermal strain and viscoplastic strain in series.

The strain rate $\dot{\boldsymbol{\epsilon}}$ consists of three parts: elastic strain rate $\dot{\boldsymbol{\epsilon}}_e$, thermal strain rate $\dot{\boldsymbol{\epsilon}}_{th}$ and viscoplastic (creep) strain rate $\dot{\boldsymbol{\epsilon}}_{vp}$, as pointed out in the following equation:

$$\dot{\boldsymbol{\epsilon}} = \dot{\boldsymbol{\epsilon}}_e + \dot{\boldsymbol{\epsilon}}_{th} + \dot{\boldsymbol{\epsilon}}_{vp} \quad (4.16)$$

The above thermo-elasto-viscoplastic model is in good agreement with the experimental results. The obtained shrinkage curves versus sintering temperature are shown in Figure 4.2. For sintering of 316L stainless steel, thermal expansion is obvious. It is the dominant one before the temperature rising to about 1050 °C. After this temperature, the viscoplastic strain increases greatly until the end of the holding stage. However, for alumina powders, the observed thermal strain is so small in the heating stage. This is due to the small coefficient of thermal expansion of alumina and the large porosity of the green specimens with open pores. In the cooling stage,

the observed linear thermal expansion of alumina specimen is about $1.34 \times 10^{-6} \text{ }^\circ\text{C}^{-1}$. The elastic strain is relatively small in the pressureless sintering case.

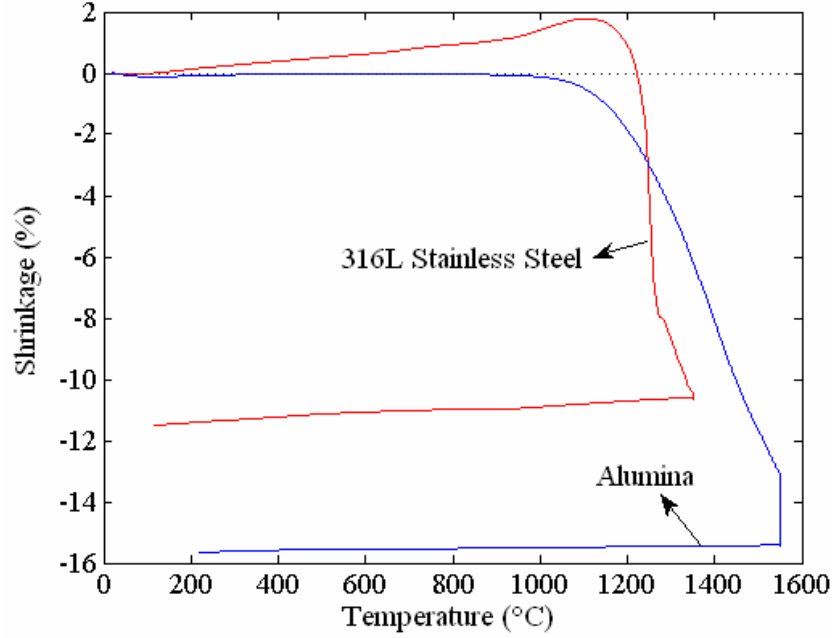


Figure 4.2: Shrinkage curves measured by dilatometer showing the viscoplastic and thermal strains of the sintering bodies.

4.4.2 Elastic Strain of Sintering Body

The part of elastic strain rate is assumed to be linear and isotropic. It can be expressed from the following expression:

$$\dot{\boldsymbol{\varepsilon}}_e = \mathbf{C}_e \dot{\boldsymbol{\sigma}} \quad (4.17)$$

where \mathbf{C}_e is the elastic compliance matrix. Equation (4.17) can also be expressed in the rate form of Hooke's law, as following:

$$\dot{\boldsymbol{\sigma}} = \mathbf{D}_e \dot{\boldsymbol{\varepsilon}}_e = \mathbf{D}_e (\dot{\boldsymbol{\varepsilon}} - \dot{\boldsymbol{\varepsilon}}_{th} - \dot{\boldsymbol{\varepsilon}}_{vp}) \quad (4.18)$$

where \mathbf{D}_e is elastic stiffness matrix. For the isotropic materials, \mathbf{D}_e is defined as:

$$\mathbf{D}_e = \frac{E}{(1+\nu_e)(1-2\nu_e)} \begin{bmatrix} 1-\nu_e & \nu_e & \nu_e & 0 & 0 & 0 \\ \nu_e & 1-\nu_e & \nu_e & 0 & 0 & 0 \\ \nu_e & \nu_e & 1-\nu_e & 0 & 0 & 0 \\ 0 & 0 & 0 & 1-2\nu_e & 0 & 0 \\ 0 & 0 & 0 & 0 & 1-2\nu_e & 0 \\ 0 & 0 & 0 & 0 & 0 & 1-2\nu_e \end{bmatrix} \quad (4.19)$$

where E is the elastic Young's modulus, ν_e is elastic Poisson's ratio. For porous materials, E and ν_e are the functions of relative density:

$$E = E_0 \exp(-b_0(1-\rho)) \quad (4.20)$$

$$\nu_e = \nu_e^0 \sqrt{\frac{\rho}{3-2\rho}} \quad (4.21)$$

where E_0 and ν_e^0 are the elastic Young's modulus and Poisson's ratio of the wrought material, b_0 is a constant [MOO 89].

4.4.3 Thermal Strain in Sintering Body

The thermal strains are mainly due to thermal expansion that can be expressed as:

$$\dot{\boldsymbol{\varepsilon}}_{th} = \alpha \dot{T} \mathbf{I} \quad (4.22)$$

where α is the thermal expansion coefficient, \dot{T} is the incremental temperature rate, \mathbf{I} is second order identity tensor. α can be determined by the experiments carried out in the dilatometer.

4.4.4 Viscoplastic Strain of Sintering Body

The linear-viscous (Newtonian) and Bingham models have been used to describe the material response during the sintering stage, as shown in Figure 4.3.

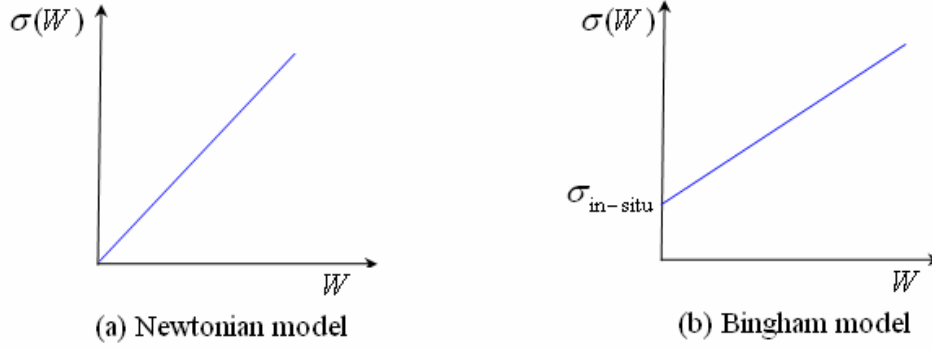


Figure 4.3: The sketches of Newtonian and Bingham models for viscoplastic models.

In Figure 4.3, W is the equivalent strain, $\sigma(W)$ is the equivalent stress [OLE 98].

$\sigma_{\text{in-situ}}$ is the *in-situ* strength of the sintering body.

For Newtonian model, it is analogous to the Hooke's law for the isotropic linear elastic materials, as expressed in the following equation:

$$\boldsymbol{\sigma} = (2G_p \dot{\boldsymbol{\epsilon}}'_{vp} + K_p \dot{\epsilon}_{vp} \mathbf{I}) + \sigma_s \mathbf{I} \quad (4.23)$$

where $\boldsymbol{\sigma}$ is the Cauchy stress tensor, $\dot{\boldsymbol{\epsilon}}'_{vp}$ is deviatoric viscoplastic strain rate, $\dot{\epsilon}_{vp} = \text{tr}(\dot{\boldsymbol{\epsilon}}_{vp})$ is volumetric strain rate due to viscoplastic strains, \mathbf{I} is second order identity tensor, G_p and K_p are the shear and bulk viscosity modulus of the porous material, σ_s is the sintering stress that drives the densification process. Equation (4.23) is the basic constitutive expression associated to continuum theory of sintering. The left hand side of equation ($\boldsymbol{\sigma}$) is the externally applied stress. The first part of the right side of the equation ($2G_p \dot{\boldsymbol{\epsilon}}'_{vp} + K_p \dot{\epsilon}_{vp} \mathbf{I}$) is the material resistance. The second part of the side of the equation ($\sigma_s \mathbf{I}$) is the sintering factor. In case of free sintering, the externally applied stress $\boldsymbol{\sigma}$ is equal to zero. When the sintering stress σ_s is equal to zero, the porous material is under the external pressure without sintering.

In order to analysis the dimensional change of the sintering body, Equation (4.23) can be written in the inverse expression as following:

$$\dot{\boldsymbol{\varepsilon}}_{vp} = \frac{\boldsymbol{\sigma}'}{2G_p} + \frac{\sigma_m - \sigma_s}{3K_p} \mathbf{I} \quad (4.24)$$

where $\boldsymbol{\sigma}'$ is the deviatoric stress tensor, $\sigma_m = \text{tr}(\boldsymbol{\sigma})/3$ is the mean stress, In right side of Equation (4.24), the first term determines the shape distortion of the sintering body, and the second one determines the volume change or density evolution. The local stress state can be shown as in Figure 4.4. It has to be observed that the densification occurs only when the sintering stress σ_s is greater than the hydrostatic stress σ_m .

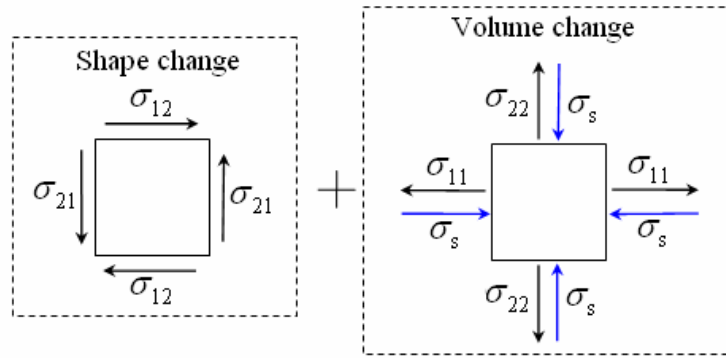


Figure 4.4: A diagram to show the local stress state of the sintering body that undergoes shape and volume changes.

G_p , K_p and σ_s are the material parameters to be determined. Generally, they are influenced by the factors such as relative density, temperature, grain size, pore size, as well as the physical parameters of the material such as diffusion coefficient, activation energy. There are phenomenological, micromechanical and experimental methods that can be used to determine the above parameters, as discussed in Chapter 2. In this study, the continuum mechanics and diffusion equations were used to determine G_p , K_p and σ_s expressions. The parameters in these expressions were identified from experimental results issued from the sintering tests described in Chapter 4.

In the classical solid-state sintering theory, the densification is controlled by the

diffusion. However, it cannot well explain the rapid densification phenomenon arising from many industrial sintering cycles, using as example 316L stainless steel. German presented a mechanical view of sintering process [GER 03 b]. The densification is controlled by the comparison between the *in-situ* strength and sintering stress of the sintering body. In sintering, thermal softening effect reduces the strength of the green part, while the sintering bonding increases its strength. When the *in-situ* strength is less than the sintering stress, the produced plastic flows induces the rapid densification. In the initial sintering stage, the strength of the part is greater than the sintering stress. The densification is governed by diffusion. The shrinkage is small and slowly. As the temperature increases, the strength is less than the sintering stress. So the rapid densification happens. The main densification results from this period. In the later stage, sintering bonding increases the strength and the grain growth reduces the sintering stress. The plastic flow disappears and the diffusion-controlled densification dictates again.

A Bingham model is proposed to describe the rapid densification behaviours of the materials due to the plastic flow. Olevsky derived the expressions of the viscoplastic constitutive law based on Bingham model [OLE 98], [OLE 00]. However, it is too complicated to be implemented in numerical simulation. The simplified method consists in the same constitutive law as Equation (4.23) or Equation (4.24) and to change only the sintering stress based the concept of Bingham model. Lu introduced the following expression into Equation (4.24) [LU 01]:

$$\sigma_s = \sigma_L - \sigma_{in-situ} \quad (4.25)$$

where $\sigma_{in-situ}$ is *in-situ* sintering strength of the material. σ_L is capillary stress or local sintering stress. Blaine changed the Equation (4.23) into the following [BLA 02]:

$$\boldsymbol{\sigma} = (2G_p \dot{\boldsymbol{\epsilon}}_{vp}' + K_p \dot{\boldsymbol{\epsilon}}_{vp} \mathbf{I}) + (\sigma_s - \sigma_{in-situ}) \mathbf{I} \quad (4.26)$$

$\sigma_{in-situ}$ is approximate and not well founded. It is chosen as a constant value equal to 1MPa in [BLA 02]. In Equation (4.25) and Equation (4.26), there is a problem in

confusing the concept of bulk sintering stress and local sintering stress. In Bingham model, the plastic flow occurs when the local sintering strength is over than the *in-situ* sintering strength. However, the sintering stress used in the constitutive equation of the continuum sintering model is the bulk one. There is a big difference between these two kinds of sintering stress. For example, the local sintering stress of stainless steel powders by injection moulding is about 6 MPa when the shrinkage is about 2%, while the corresponding bulk sintering stress is near 0.7 MPa [GER 03 b].

In the numerical sense, the simplification of Bingham model as Equation (4.25) and Equation (4.26) is to find a proper sintering stress. In order to avoid determining the value of local sintering stress and *in-situ* sintering stress, the constitutive law as Equation (4.23) or Equation (4.24) is used for the entire sintering process. For the rapid densification in the small temperature range like the case of 316L stainless steel, the process is divided into three stages based on the experimental results shown in Figure 3.16. The sintering stress and viscosity modulus are identified for three stages respectively. For the material like alumina, the densification is relatively slow. The viscosity modulus and sintering stress can be identified without dividing into several stages. So in this study, the comparison between local sintering stress and *in-situ* strength to determine whether there exists plastic flows is not carried out. The unique constitutive equation is employed for both diffusion and plastic flow controlled densification. The parameters of the model are identified by the experimental results. It is easier to be realized and also easy to guarantee the accuracy of numerical simulation results.

4.5 Determination of Viscosity Modulus

4.5.1 Elastic-Viscous Analogy

The elastic-viscous analogy is proposed to define the shear and bulk viscosity modulus for sintering materials [BOR 88 a]. The analogy of the parameters in linear elastic and viscous models is shown in Table 4.1.

Table 4.1: Analogy of linear elastic and viscous models.

Linear elastic model	Linear viscous model
Stress	Stress
Strain	Strain rate
Elastic modulus	Viscous modulus
Elastic Poisson's ratio	Viscous Poisson's ratio

So according to the generalized Hooke's elasticity law, the shear and bulk viscosity modulus can be expressed from the following equations:

$$G_p = \frac{\eta_z}{2(1 + \nu_{vp})}, \quad K_p = \frac{\eta_z}{3(1 - 2\nu_{vp})} \quad (4.27)$$

where η_z and ν_{vp} are the uniaxial viscosity and viscous Poisson's ratio of the porous material.

4.5.2 Uniaxial Viscosity

For most common linear viscous materials, the shear viscosity modulus can be determined by the following expressions [OLE 98]:

$$G_p = G_0 \rho^2 \quad (4.28)$$

where G_0 is the shear viscosity modulus of the wrought material. Due to the fact that Equation (4.28) is an approximate one, Pertersson postulated the following expression for uniaxial viscosity [PER 04]:

$$\eta_z = \eta_0 \rho^2 \quad (4.29)$$

where η_z is the uniaxial viscosity of porous material, η_0 is the effective viscosity of wrought material.

As discussed in Chapter 2, only the grain boundary diffusion and volume diffusion from the grain boundaries contribute to the densification of sintering bodies. Cobel and Nabarro-Herring creep models are proposed respectively to describe these two kinds of diffusion mechanisms of the polycrystalline materials at high temperature. Coble creep model can be expressed as [COB 63]:

$$\dot{\epsilon}_c = \frac{47.5 \sigma_c \delta_b D_b \Omega}{kTG^3}, \quad D_b = D_{b0} \exp(-Q_b / RT) \quad (4.30)$$

where $\dot{\epsilon}_c$ is creep strain rate, σ_c is applied stress that induces the creep. For free sintering, σ_c is equal to sintering stress. In pressure-assisted sintering condition, σ_c includes external pressure and sintering stress. δ_b is grain boundary thickness, D_b is gain boundary diffusion coefficient, D_{b0} is grain boundary diffusion frequency. Q_b is the activation energy of grain boundary diffusion. G is grain size, k is Boltzmann's constant, R is gas constant, T is absolute temperature, Ω is atomic or molecular volume.

For volume diffusion, Nabarro-Herring creep model is expressed as the following [NAB 48], [COB 63]:

$$\dot{\epsilon}_c = \frac{10\sigma_c D_v \Omega}{kTG^2}, \quad D_v = D_{v0} \exp(-Q_v / RT) \quad (4.31)$$

where D_v is volume diffusion coefficient, D_{v0} is volume diffusion frequency. Q_v is the activation energy of volume diffusion.

The effective viscosity of the wrought materials due to the creep at high temperature can be defined by the following equation:

$$\eta_0 = \frac{\sigma_c}{\dot{\epsilon}_c} \quad (4.32)$$

Combining Equation (4.29) to (4.32), the uniaxial viscosity of the porous materials can be expressed as the following:

$$\eta_z = \frac{ATG^m \rho^2}{\exp(-B/T)} \quad (4.33)$$

The involved parameters m , A and B are of the following forms:

$$\text{For grain boundary diffusion, } m = 3, \quad A = \frac{k}{47.5\delta_b D_{b0}\Omega}, \quad B = Q_b / R \quad (4.34)$$

$$\text{For volume diffusion, } m = 2, \quad A = \frac{k}{10D_{v0}\Omega}, \quad B = Q_v / R \quad (4.35)$$

Generally, grain boundary diffusion and volume diffusion occur when the homologous temperature reaches 0.7 or above. Homologous temperature refers to

the ratio of a materials temperature to its melting temperature. At lower temperature of the region with the homologous temperature above 0.7, the grain boundary diffusion is the dominant one. This is due to the fact that activation energy of grain boundary diffusion is less than that of the volume diffusion. In this case the temperature is enough to activate the grain boundary diffusion, but not the volume diffusion. For example, Q_b for 316L stainless steel is 167 kJ/mol, while Q_v is 280 kJ/mol [GER 96]. At the relatively higher temperature, volume diffusion dictates the creep process. It is due to the larger number of diffusion paths in the bulk, as compared with the relatively few paths for diffusion along the grain boundaries. The most useful process for densification of PIM materials is usually the grain boundary diffusion [GER 97].

Based on the above discussion, the uniaxial viscosity of the porous material at the high temperature can be determined by the Equation (4.33). In that equation, A and B are the most important parameters to be determined. Unfortunately, it is difficult to find the accurate values of parameters A and B from the literature. The calculated values for the viscosity of the materials vary with orders of magnitude based on the data from different sources. In the present study, experimental methods are used to identify the proper values of A and B , that can guarantee the accuracy of the numerical simulation results.

4.5.3 Viscous Poisson's Ratio

In order to obtain the shear viscosity modulus and bulk viscosity modulus in the Equation (4.25), another parameter viscous Poisson's ratio should be determined. The direct method to measure the Poisson's ratio consists in loading sintering experiments in the dilatometer. This type of dilatometer experiment can be used to measure the *in-situ* shrinkage of the cylindrical specimens both in the axial and radial directions. However, the experiments need the loading dilatometer that can measure the axial and radial shrinkages simultaneously. On the other hand, the

measured results are influenced by the factors as loading force, temperature cycles, *etc*, [GIL 01], [PER 04].

Bordia proposed the following approximate relationship between the viscous Poisson's ratio and the relative density [BOR 88 a]:

$$\nu_{vp} \approx \frac{1}{2} \sqrt{\frac{\rho}{3-2\rho}} \quad (4.36)$$

The viscous Poisson's ratio calculated based on Equation (4.36) are shown in Figure 4.4. In both equations, the boundary conditions are well satisfied. It means that ν_{vp} is near to 0 for $\rho = 0$. When the material is in fully dense state ($\rho = 1$), ν_{vp} is equal to 0.5, which indicates that the incompressible condition of the wrought material is satisfied. Petersson carried out the sintering experiments under loading in dilatometer for WC-Co powders. The viscous Poisson's ratio calculated from Equation (4.36) is close to the experimental one [PER 04], that is used in this study.

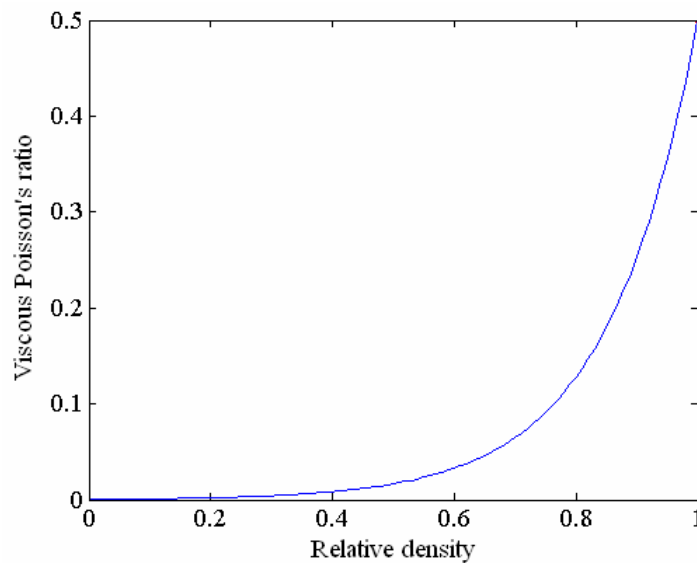


Figure 4.5: The relationship between the viscous Poisson's ratio and relative density of the porous materials.

4.6 Determination of Sintering Stress

Sintering stresses have the important impact on the sintering kinetics. The local sintering stress is used to measure the stress acting on the microstructures due to the

reduction of the surface energy. It can be calculated based on the Laplace equation by considering the different microstructures at various sintering stages [GER 97], [GER 03 b]. On the other hand, the driving force for sintering at the macroscopic level is called bulk sintering stress, as employed in the viscoplastic constitutive law. It depends on not only the microstructures, but also the porosity of the materials. Many equations were proposed to calculate the bulk sintering stress [ASH 90], [SVO 94], [RIE 94], [OLE 98], [SHI 99], [GER 03 b], [KRA 04], [HE 05]. In all these equations, the bulk sintering stress is the function of the porosity, surface energy and particle size. For numerical simulation purpose, the most critical aspect is no longer to choose the expression, but to determining the parameters in the equation accurately. In the present study, the constitutive parameter σ_s refers to the bulk sintering stress. The two proposed equations issued from references are used to calculate the sintering stress of 316L stainless steel and alumina respectively. The experimental method is used to identify the coefficients in related physical expressions.

4.6.1 Sintering Stress for 316L Stainless Steel Powders

The expression of sintering stress proposed by Olevsky has been widely used for the numerical simulation of stainless steel sintering [GER 98], [ZHA 02], [BLA 02], assuming that it is proportional to the square of relative density and the reciprocal of particle radius, as in the following equation:

$$\sigma_s = \frac{C\rho^2}{r_0} \quad (4.37)$$

where r_0 is the average radius of the powder particles, C is the material constant dependent of the surface energy of the material. Although Equation (4.37) is proposed for the initial sintering stage, it has been used for the intermediate and final stages by other researchers. In this study, the parameter C is identified by experiments for different sintering stages.

4.6.2 Sintering Stress for Alumina Powders

The following expression is proposed to calculate the sintering stress of ceramics when the microstructural pores are the open ones [DU 92]:

$$\sigma_s = \frac{6(2\gamma_{sv} - \gamma_{ss})}{G} \rho^2 \left(\frac{2\rho - \rho_0}{1 - \rho_0} \right) \quad (4.38)$$

where γ_{sv} is the surface energy, γ_{ss} is grain boundary energy. He and Ma [HE 05] used this equation to calculate the sintering stress of alumina powders during the initial stage when the relative density is less than 0.9. Although there are some equations proposed to determine the sintering stress under the closed pore condition at the final sintering stage, the typical sintering stress calculated by different models is in the order of 1 MPa [GER 03 b]. Hsueh evaluated the sintering stress as a constant 1 MPa for alumina throughout the sintering [HSU 86]. On the other hand, it is not easy to divide the sintering process into several stages definitely by the state of the pores. Due to this fact, Equation (4.38) is used for the entire process of sintering. It has the advantage to keep the continuity of sintering stress. In Equation (4.38), the values of interfacial energies γ_{sv} and γ_{ss} are usually in the small range of 0.3~1.5 J/mol. The grain size G is the most sensitive parameter for sintering stress. For alumina powders, the experimental data are used to identify the parameters in the grain growth law.

4.7 Grain Growth

Grain growth plays an important role in sintering because the excessive grain size will not only obstruct the densification, but influences the final mechanical properties of the sintered component. Zhang reviewed various empirical models of grain growth for various materials [ZHA 02 b], [ZHA 05]. In the study, the proper grain growth models are chosen for 316L stainless steel and alumina powders respectively.

4.7.1 Grain Growth Model for 316L Stainless Steel

The following equation is chosen for simulation of the grain growth behaviour of the 316L stainless steel powders in sintering [KAS 92], [CHI 92], [KWO 01]:

$$\frac{dG}{dt} = \frac{D \exp(-Q_G / RT)}{G} \quad (4.40)$$

where Q_G is the activation energy for grain growth. For 316L stainless steel, when the temperature is less than 1200 °C, $Q_G = 315.8$ kJ/mol, otherwise $Q_G = 50$ kJ/mol [KAS 92]. D is a material constant that will be determined by the measured grain sizes with SEM photos.

4.7.2 Grain Growth Model for Alumina

During the sintering of the alumina powders, grain growth is controlled by surface diffusion. The rate of grain growth can be expressed as [BRO 82]:

$$\frac{dG}{dt} = \frac{110D_s \delta_s \gamma_{ss} \Omega}{kTG^3} (1 - \rho)^{-\frac{4}{3}} \quad (4.40)$$

where k is Boltzmann's constant, γ_{ss} is grain boundary energy, Ω is molecular volume, T is absolute temperature, δ_s is the thickness for surface diffusion, and D_s is the surface diffusion coefficient dependent of the temperature as:

$$D_s = D_{s0} \exp(-Q_s / RT) \quad (4.41)$$

where D_{s0} is the surface diffusion frequency factor, Q_s is the activation energy of surface diffusion and R is the gas constant. Combining Equation (4.40) and (4.41) yields to:

$$\frac{dG}{dt} = \frac{M \exp(-N/T)}{TG^3} (1 - \rho)^{-\frac{4}{3}} \quad (4.42)$$

where

$$M = \frac{110D_{s0} \delta_s \gamma_{ss} \Omega}{k}, \quad N = \frac{Q_s}{R} \quad (4.43)$$

M and N parameters will be identified based on the data obtained by

experiments conducted in dilatometer.

4.8 Model for Strength Prediction

Prediction of the strength is one of the important issues for optimizing the sintering process. Many empirical models are proposed to predict the post-sintering strength of the components made by powder metallurgy. For one kind of these models, the strength is only a function of the relative density. It improves when the relative density increases. Olevsky presented a brief review of these models [OLE 01]. However, these models are unable to explain some physical phenomena. In the initial sintering stage, the strength of the sintering body increases due to the neck growth, but the density changes little. On the other hand, in the final sintering stage, the vanishing of the closed pores among the intersection of the grain boundaries also increases the strength with little increasing of the density. So the microstructural factors are necessary to be considered in the strength evaluation model. Although the Bingham model has been simplified in the constitutive law, evaluating the *in-situ* strength is useful for controlling the distortion during sintering. The strength of the porous materials can be expressed through the following expressions:

$$\sigma_p = \sigma_0 f(\rho, mf) \quad (4.44)$$

where σ_p is the predicted strength associated to the model. It can be the yield strength or ultimate tensile strength. σ_0 is the strength of the wrought material. mf is the microstructural factor of the sintered components. ρ and mf are dependent of the sintering process. The evolution of the density contours can be obtained from the numerical simulation based on the above sintering models. The important aspect is to determine the microstructural factor mf . It depends on the factors such as neck size, coordination number of the grain and stress concentration factor [GER 03 b].

4.8.1 Microstructural factors

Neck size ratio X/D is the often used parameter to evaluate the sintering bonding effects. There are several empirical equations proposed to calculate the neck size, as listed in Table 4.2. The comparison of these models is shown in Figure 4.6.

Table 4.2: Empirical expressions proposed to calculate neck size ratio

Skorohod [SKO 72]	German [GER 03 b]	Helle <i>et al.</i> [Hel 85]
$\left(\frac{X}{D}\right)^2 = 1 - \left(\frac{\theta}{\theta_0}\right)^{\frac{4}{3}}$	$\left(\frac{X}{D}\right)^2 = 4 \left[1 - \left(\frac{\rho_0}{\rho}\right)^{1/3} \right]$	$\left(\frac{X}{D}\right)^2 = \frac{1}{3} \left[1 - \left(\frac{\theta}{\theta_0}\right) \right]$

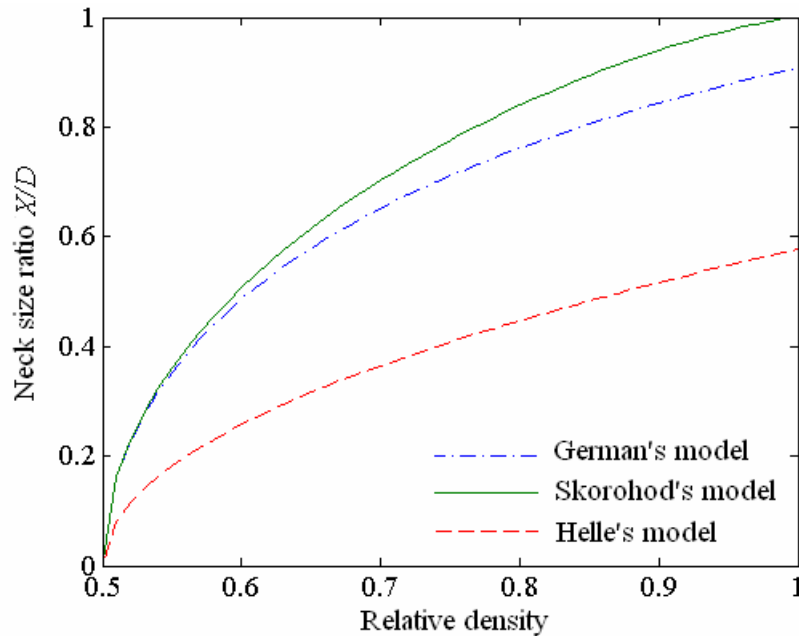


Figure 4.6: Comparison of the proposed models to determine the neck size ratio.

It can be observed that the expression proposed by German is close to Skorohod's one. Although Skorohod proposed the expression for all sintering stages, German gave a limitation of the expression that he proposed to restrict its validation when X/D is not great than 0.5. In his opinion, when the ratio of neck size reaches 0.5, it doesn't continue to increase and nearly keep the constant of 0.5. The densification goes on by increasing the coordination number continually. Compared with the both expressions, the one proposed by Helle seems underestimating the neck size ratio.

In the presintering and initial sintering stage, the densification is not significant. However, the experimental results show that the strength of the sintered parts increases greatly. The empirical expressions of neck size ratio in Table 4.1 are functions of relative density or porosity. So it is not valid to describe the neck growth behaviors in the presintering or initial sintering stage. In this stage, the temperature is relatively low. For most of the materials, neck growth is controlled by surface diffusion. Sovoboda proposed the following equations to determine the neck size ratio controlled by surface diffusion [SVO 95]:

$$\left(\frac{X}{D}\right)^{\frac{9}{2}} = \frac{d\left(\frac{X}{D}\right)}{dt} (2\sqrt{2}\phi)^3 \frac{\gamma_s \Omega}{k(r_p)^4} \frac{\delta_s D_s(T)}{T(t)} \quad (4.45)$$

where ϕ is dihedral angle. The neck size is dependent of the temperature cycle, particle size and material parameters.

Stress concentration factor is used to describe the influences of the neck curvature on the strength of the sintered components. It is the function of the neck size ratio. The following expression is proposed to determine the strength concentration factor [XU 02 b], [SUR 03]:

$$K_c = \exp(0.0946(\ln(\frac{X}{8D}))^2 + 0.1746 \ln(\frac{X}{8D}) + 0.4576) \quad (4.46)$$

where K_c is the stress concentration factor. The dependence of K_c on the neck size ratio is shown in Figure 4.7.

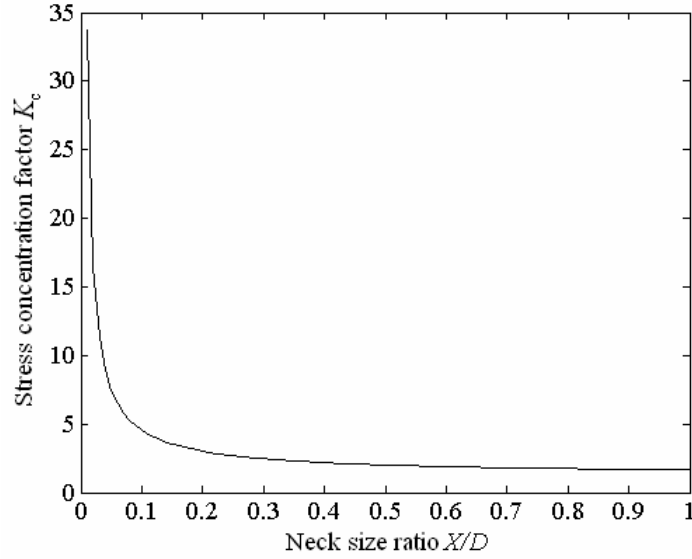


Figure 4.7: The relationship between stress concentration factor and neck size Ratio.

4.8.2 Strength Prediction Model

For the porous materials, the following expressions are proposed to determine the yield strength and ultimate tensile strength [SUR 03]:

$$\sigma_y = \sigma_y^0 \frac{1-\theta}{K_c} \quad (4.47)$$

$$\sigma_{UTS} = \sigma_{UTS}^0 \frac{1-\theta}{1 + \alpha_s (K_c - 1)\theta} \quad (4.48)$$

where α_s is a constant, the superscript 0 indicates the strength the wrought material, and the subscript y and UTS indicate the yield strength and ultimate tensile strength.

For evaluating the *in-situ* sintering strength, the thermal softening effect should be considered, expressed as:

$$\sigma_0 = \bar{\sigma}_0 g(T) \quad (4.49)$$

where $\bar{\sigma}_0$ is the strength of the wrought materials at room temperature, and $g(T)$ is the thermal softening factor. The following empirical expression is often used to determine the thermal softening factor:

$$g(T) = \frac{a}{1 + \exp\left(\frac{T-b}{c}\right)} \quad (4.50)$$

where a , b and c are the material constants. Suri reviewed these material constants for some steel, as shown in Table 4.3 [SUR 03].

Table 4.3: Material constants of thermal softening factor

Materials	a	$b(K)$	$c(K)$
Tool steel	1.02	1101.78	69.14
316L stainless steel	0.9532	1003	138.3
Fe-2Ni-1B(Fe-2Ni-0.7Cr)	1.019	764.6	112.5
Fe-10Cr-0.5B(Fe-9Cr-1.5Mo)	1.064	787.7	172.5

4.9 Summary

Predicting shrinkages and distortions of the sintering bodies is one of the important issues in the PIM process. In order to reach this goal, the using of continuum mechanics to model the sintering process is necessary. The sintering body is regarded as the compressible continuum medium. The porosity or relative density parameter is used to indicate the densification level in sintering. Like wrought material, the sintering body is also governed by the equations of mass, momentum and energy conservation. However, the material properties such as density, elastic modulus, thermal conductivity and heat capacity are dependent of the porosity that is evolving during the sintering process.

For the continuum sintering model, the most important aspect is to determine the constitutive law of the porous materials in high temperature. Experimental results show that the sintering body undergoes elastic, thermal and viscoplastic deformations. The elastic strain is small for pressureless sintering. The magnitudes of thermal expansions are dependent on the sintered materials. In our experiments, the thermal expansion of 316L stainless steel is obvious, but that of the alumina is very small. The viscoplastic strain is the main deformations of the sintering body. In

the adopted linear viscous law, viscosity modulus and sintering stress are the main parameters to be determined. The shrinkage behavior is governed by the ratio of sintering stress to bulk viscosity modulus. Simultaneously, the distortion of the sintering body is dependent on the shear viscosity modulus. Instead of using the totally microstructural models or experimental methods to determine these parameters, the combination of experimental and diffusion theory are employed. It can avoid the determination of so many microstructural physical parameters in the microstructural models, or the use of the equipments such as loading dilatometers. In the present study, the elastic-viscous analogy is used to obtain the expressions of shear and bulk viscosity modulus. The uniaxial viscosity is derived from the diffusion theory. The expressions often used for the sintering stress and grain growth law of 316L stainless steel and alumina powder are employed.

From the dilatometric studies, it can be observed that the main densification of 316L is conducted rapidly in a small range of temperature. However, the densification of alumina powder is relatively slow and in the wide range of temperature. Some researchers thought that it may exit the plastic flow during the rapid densification like 316L stainless steel powder. When the local sintering stress is greater than the *in-situ* sintering strength, the densification is controlled by the plastic flow. So the Bingham model is proposed to describe this process. In the study, the expression of Bingham model is simplified for its implementation into the numerical simulation. It takes the same form as the linear viscous law, the only differences are in the values of the sintering stress and viscosity modulus. For rapid densification as 316L stainless steel, the entire sintering process is divided into three stages. The viscosity modulus and sintering stress are identified respectively for each distinct stage.

The strength of the sintered components is dependent on the porosities and the microstructural factors. The empirical expressions are used to calculate the yield strength and ultimate tensile strength. The neck size ratio and strength concentration factor are considered in both models. For evaluation of the *in-situ* sintering strength, the thermal softening effects should be considered.

Chapter 5 Identification of the Parameters for Sintering Model

The determination of the parameters in the sintering model is important for obtaining the accurate results through numerical simulations. In fact, it is difficult to find the set of the appropriate parameters from the literature that can lead the simulation results close to the experimental ones. In the employed sintering models, the parameters in the viscosity modulus and sintering stress should be determined properly. The bulk viscosity modulus and sintering stress characterize the shrinkage behaviors of the sintering body, while the shear viscosity modulus relates to the distortion. From the experimental results, it can be observed that the 316L stainless steel green parts after injection molding and debinding is prone to be deformed in the sintering process. However, the debinded alumina specimens have the good ability to resist to the distortion in sintering. For 316L stainless steel, the gravitational beam-bending tests in the sintering process are used to identify the viscosity modulus parameters. Based on the identified viscosity modulus, the sintering experiments in dilatometer are used to identify the sintering stress parameters. For alumina, the beam-bending tests have not been made. The experiments in dilatometer are employed to identify the parameters of viscosity modulus and sintering stress simultaneously.

5.1 Principles of Identification through Experiments

5.1.1 Gravitational Beam-bending Tests

The beam-bending tests introduced in Chapter 3 are regarded as the simply supported beam test, as shown in Figure 5.1.

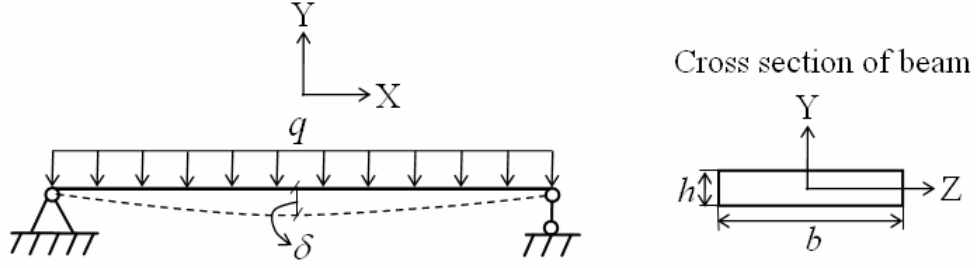


Figure 5.1: A sketch of the simply supported beam model for beam-bending tests.

The deflection of the elastic beam can be determined by the following equation [LEE 03]:

$$\frac{d^2y/dx^2}{[1 + (dy/dx)^2]^{3/2}} = \frac{M_z}{EI_z} \quad (5.1)$$

where M_z is bending moment about z axis, E is elastic modulus, and I_z is Z axis inertia moment. For the beam with rectangular cross section, M_z and I_z are calculated by the following expressions:

$$M_z = \frac{1}{8}q(L_s^2 - 4x^2), \quad I_z = \frac{1}{12}bh^3 \quad (5.2)$$

where L_s is span distance of the beam. In the experiments, it is equal to 40 mm. b and h are the width and thickness of the bending test specimens. $q = \rho_{ap}gbh$ is the unit loading due to the gravity of the beam. Here ρ_{ap} is the apparent density, g is gravitational acceleration. For the small amount of deflection, the $(dy/dx)^2$ can be ignored. So the deflection can be expressed as:

$$\frac{d^2y}{dx^2} = \frac{3\rho_{ap}g(L_s^2 - 4x^2)}{2Eh^2} \quad (5.3)$$

Considering the boundary conditions $y = 0$ at $x = \pm L_s/2$, the solution of Equation (5.3) is as the following:

$$y = -\frac{\rho_{ap}g}{2Eh^2}x^4 + \frac{3\rho_{ap}gL_s^2}{4Eh^2}x^2 - \frac{5\rho_{ap}gL_s^4}{32Eh^2} \quad (5.4)$$

At the position $x = 0$, the deflection takes the maximum value, expressed as:

$$\delta = -y_{\max} = \frac{5\rho_{\text{ap}}gL_s^4}{32Eh^2} \quad (5.5)$$

where δ is the deflection at middle position of the beam.

Based on the viscous-elastic analogy as shown in Table 4.1, the deflection δ in Equation (5.5) is replaced by the deflection rate $\dot{\delta}$, and the elastic modulus E is replaced by the uniaxial viscosity η_z . It yields below:

$$\dot{\delta} = \frac{5\rho_{\text{ap}}gL_s^4}{32\eta_z h^2} \quad (5.6)$$

The deflection δ and deflection rate $\dot{\delta}$ can be measured by beam-bending tests during sintering. So the uniaxial viscosity of the sintering body can be determined as:

$$\eta_z = \frac{5\rho_{\text{a}}gL_s^4}{32\dot{\delta}h^2} \quad (5.7)$$

Based on the determined densification rate $\dot{\delta}$, as shown in Figure 3.21, the uniaxial viscosity can be calculated by Equation (5.7).

5.1.2 Free Sintering in Dilatometer

In the sintering experiments in dilatometer, the external force induced by the pushrod is less than 30 cN. Meanwhile, the specimen is so small that the gravity and friction can be ignored. So the sintering process is regarded as the free sintering one. The elastic strain can be neglected. In the constitutive law as Equation (4.24), the stress tensor is equal to zero, so Equation (4.16) is simplified as:

$$\dot{\boldsymbol{\epsilon}} = \left(\alpha\dot{T} - \frac{\sigma_s}{3K_p}\right)\mathbf{I} \quad (5.8)$$

The shrinkage rate in the axial direction is expressed as:

$$\frac{dL}{Ldt} = \alpha\dot{T} - \frac{\sigma_s}{3K_p} \quad (5.9)$$

The left side of Equation (5.9) can be measured by the dilatometer. The thermal expansion coefficient can also be determined by the experiments directly. So the ratio of sintering stress to bulk viscosity modulus can be calculated as:

$$\frac{\sigma_s}{K_p} = 3\left(\alpha\dot{T} - \frac{dL}{Ldt}\right) \quad (5.10)$$

5.2 Parameter Identification for 316L Stainless Steel

5.2.1 Identification of the Parameters for Viscosity Modulus

As presented in Equation (4.27), the shear and bulk viscosity moduli are the functions of uniaxial viscosity and viscous Poisson's ratio. In the study, the empirical equation (4.36) is used to determine the viscous Poisson's ratio. So parameters A and B in Equation (4.33) related to uniaxial viscosity should be identified. Based on data obtained through the beam-bending tests, the uniaxial viscosity at different sintering temperature can be calculated by Equation (5.7). The identification of A and B parameters in the model is based on an optimization procedure consisting to fit the model and experiment as close as possible, expressed as:

$$\begin{cases} \min F(x) \\ F(x) = \sum_{i=1}^n |\eta_z^e(T_i, x) - \eta_z^m(T_i, x)|^2 \\ x = [A, B] \end{cases} \quad (5.11)$$

where $\eta_z^e(T_i, x)$ is the uniaxial viscosity obtained from beam-bending tests, $\eta_z^m(T_i, x)$ is the uniaxial viscosity used in the proposed model. $F(x)$ is the mean residual squares of the error, where as $i = 1, \dots, n$ indicates different values of the sintering temperature, x is the set of material parameters to be identified.

Grain boundary diffusion is the main mechanism for the densification process related to 316L stainless steel powders. In uniaxial viscosity model associated to Equation (4.33), grain size is the important parameter for the uniaxial viscosity. So the parameter D in the grain growth law (4.40) should be determined firstly. In our experiments, the microstructural evolutions of 316L stainless steel powders in sintering have been observed by SEM. However, the average grain size has not been measured. Koseski *et al* investigated the changes of grain size in sintering for 316L

stainless steels powders [KOS 05]. In their experiments, the material characteristics of gas-atomized powders are close to the feedstock used in our experiments. The particle size is $18.9 \mu\text{m}$ for D_{90} in their powders and the particle size is $16 \mu\text{m}$ for D_{80} in the powders used in our experiments. They measured the average grain size for a thermal cycle corresponding to a heating up to $1360 \text{ }^\circ\text{C}$ at $10 \text{ }^\circ\text{C}/\text{min}$ and then holding for 1 h. The heating rate is the same as the one employed in our beam-bending tests. These data are used to determine the proper value of the material constant D in Equation (4.40). As D is chosen equal to $0.98 (\mu\text{m})^2/\text{s}$, the grain size variations for the heating stage, obtained from model and literature, are shown in Figure 5.2.

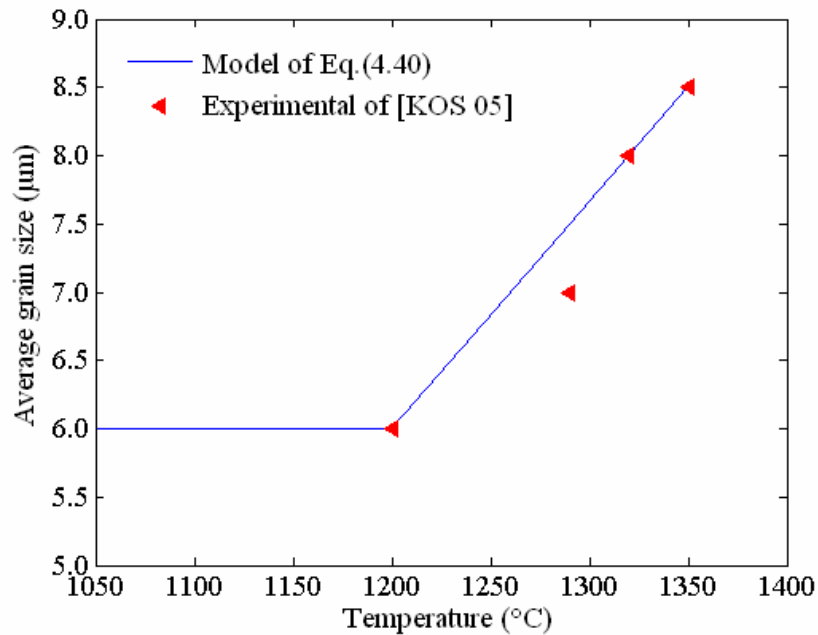


Figure 5.2: Variation of grain size in sintering to $10 \text{ }^\circ\text{C}/\text{min}$ to different temperatures without holding.

The optimization functions provided by Matlab[®] are employed to solve Equations (5.11). The parameter A and B are the variables to be optimized simultaneously. Meanwhile, one can optimize only parameter A or B as the other one can be derived from the literature. In the present study, the material parameter B is determined to be $2.01 \times 10^4 \text{ K}$, as Q_b is chosen to be 167 kJ/mol in

Equation (4.34) [GER 96]. Due to the fact that the viscosity of the 316L stainless steel green parts changes importantly in the entire sintering process, the optimization is carried out for the three stages distinctly. The identified parameters for uniaxial viscosity are indicated in Table 5.1.

Table 5.1: Identified material parameters of viscosity.

Sintering stages	A (Pa·s/(m ³ ·K))	B (K)
$0.000 < \rho \leq 0.645$	5.19×10^{15}	2.01×10^4
$0.645 < \rho \leq 0.930$	1.97×10^{15}	2.01×10^4
$0.925 < \rho \leq 1.000$	16.1×10^{15}	2.01×10^4

The uniaxial viscosity obtained from experiments and the proposed model with two optimized parameters is shown in Figure 5.3.

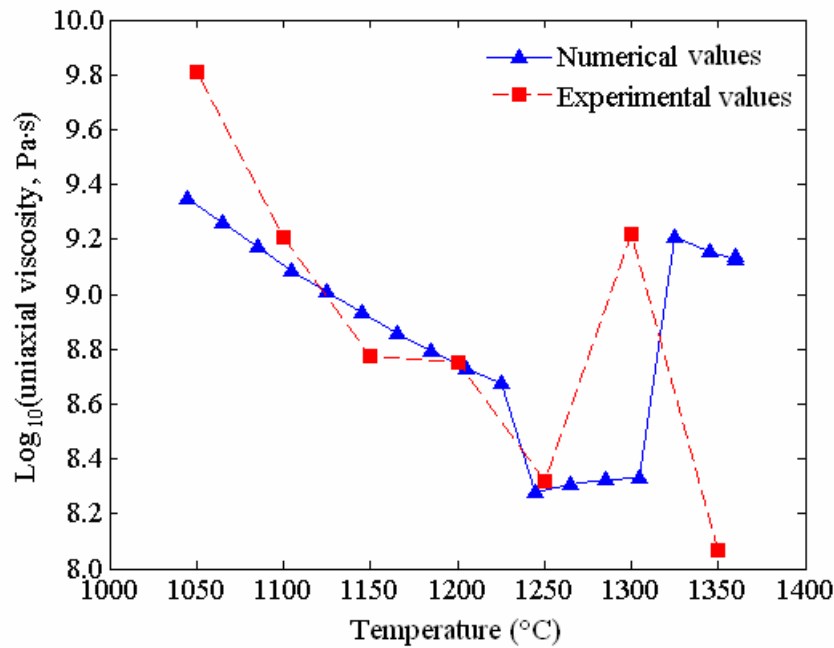


Figure 5.3: Fitting of equation (4.33) with identified parameter A according to the uniaxial viscosity values obtained by gravitational bending tests.

5.2.2 Identification of the Sintering Stress Parameters

Based on the identified parameters for viscosity modulus, the sintering stress can be determined from Equations (4.37) and (5.9). The dilatometer experimental data are used to identify C parameter in Equation (4.37). The optimization method is employed to make the shrinkage rate curve obtained from numerical simulation

close to the experimental one, expressed as:

$$\begin{cases} \min F(x) \\ F(x) = \sum_{i=1}^n |\lambda^m(T_i, x) - \lambda^e(T_i, x)|^2 \\ x = [C] \end{cases} \quad (5.12)$$

where λ^m and λ^e are the uniaxial shrinkage curves, calculated from Equation (5.9) and also measured by dilatometer experiments. An optimization procedure is conducted for the thermal heating cycle up to 1360 °C at 8 °C/min and then holding for 1 h, as shown in Figure 3.16. The identified values of C corresponding to different sintering stages are presented in Table 5.2.

Table 5.2: Identified values for sintering stress material parameter C for the thermal cycle heating up to 1360 °C at 8 °C/min then holding 1 h.

Sintering stages	C /(N/m)
$0.000 < \rho \leq 0.645$	0.696
$0.645 < \rho \leq 0.930$	6.454
$0.930 < \rho \leq 1.000$	1.640

The shrinkage curves obtained from dilatometer and the numerical simulation with the identified parameters are shown in Figure 5.4.

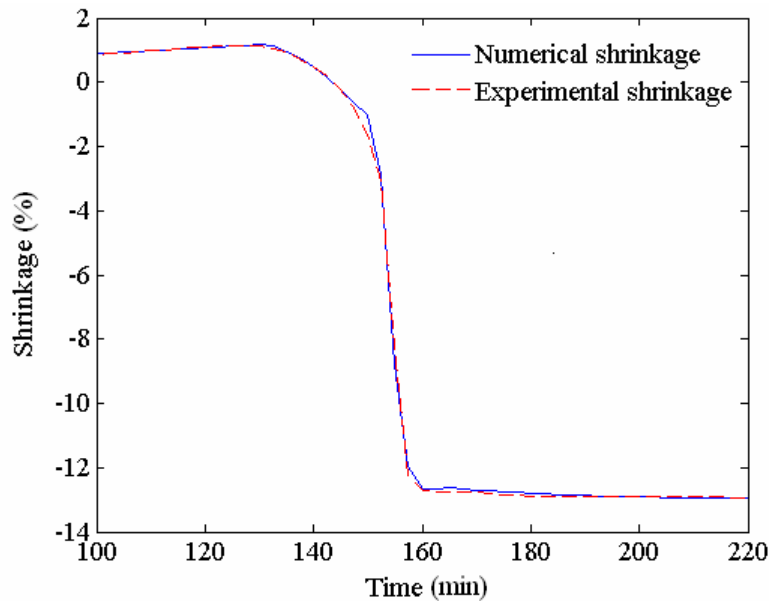


Figure 5.4: The shrinkage curve obtained by numerical simulation with identified parameters and the experimental one obtained by dilatometer test, corresponding to heating up to 1360 °C at rate 8 °C/min and then holding 1 h.

5.2.3 Discussions

The viscosity moduli and sintering stress are the critical parameters that control the sintering behaviour of the powder particles. However, it is difficult to determine the viscosity of the sintering body at high temperature. The available data that can be obtained from the literature vary in orders of magnitude. Blaine got the values of uniaxial viscosity in the range 0.2-0.6 GPa·s for 316L stainless steel powders compacted with boron [BLA 05]. Lame reported the values of uniaxial viscosity in the range 60-80 GPa·s for iron powder compacts [LAM 02]. Vagnon determined the uniaxial viscosity of 316L stainless steel powder compacts in the range 4-50 GPa·s [VAG 05]. Many factors can affect the measured viscosity values, such as the difference in material composition, particle size, green density, temperature cycle, measurement method, *etc.* In the related study, the identified uniaxial viscosity is in the range 0.194-2.55 GPa·s. In the beam-bending tests, the materials begin to flow when the temperature is greater than 1250 °C. There is large distortion of the bending specimen, as shown in Figure 3.20. So the measured deflection is not accurate. In future developments, the more precise beam-bending tests should be conducted with the proper dimensions and span distance. It should guarantee that the bending specimens can undergo the measurable deflections under earth's gravity without the distortions due to material flow.

Olevsky made a review of several empirical models for the sintering stress. All the mentioned works show that the sintering stress is generally in the order of 1 MPa. It ranges from 1/3 to 3 MPa, depending on the different assumptions in different models [OLE 98], [GER 03 b]. The identified sintering stress in the present work is in the range 0.01-0.69 MPa. According to the viscoplastic constitutive law expressed in Equation (4.24), the densification rate depends on the ratio of sintering stress to bulk viscosity modulus, but the distortion is dependent only on the shear viscosity modulus if the external force is small. In the above identification method, the ratio of sintering stress to bulk viscosity modulus is determined by dilatometer experiments. So the numerical simulation results obtained with identified parameters can predict the shrinkage behaviours of the sintering body accurately. However, the shear

viscosity modulus is a function of uniaxial viscosity and viscous Poisson's ratio. In the study, the beam-bending tests can provide the magnitude of the uniaxial viscosity, but not the accurate value. On the other hand, the empirical equation (4.36) is employed directly to determine the viscous Poisson's ratio. It should be verified whether it matches well with 316L stainless steel powder injection molded parts. So it is expected to realize the more precise tests and measurements for determination of the *in-situ* viscosity during the sintering, as example the sintering forging or the bending test in a dilatometer. It is necessary for predicting the distortions of sintered bodies accurately.

5.3 Parameter Identification for Alumina

5.3.1 Identification Algorithm

The dilatometer experiments have been used to identify the parameters in the sintering model for alumina powders. As indicated in Chapter 4, it involves the parameters A and B for uniaxial viscosity, as expressed in Equation (4.33) and Equation (4.34), and the parameter M and N for grain growth law, as expressed in Equation (4.42) and Equation (4.43). The experimental results show that the alumina powders have slower rate and wider temperature range for densification compared with 316L stainless steel.

A more accurate optimization algorithm can be used for parameter identification. The objective optimization function is built for both shrinkage rate and shrinkage subsequently. The shrinkage curve obtained from dilatometer tests of alumina powders in sintering shows that the thermal expansion is so small for alumina in the heating stage that it can be neglected.

In the viscoplastic constitutive law, the shrinkage rate or strain rate is related to the stress state in the sintering body. So the model should be determined accurately in the numerical simulation. Based on Equation (5.9), the first function for evaluating the error of the constitutive model can be defined as following:

$$\Delta_1 = \left| -\frac{1}{3K_p} \sigma_s - \frac{1}{L} \frac{dL}{dt} \right| \quad (5.13)$$

In the right side of Equation (5.13), the first term is the uniaxial shrinkage rate of the cylindrical specimen obtained from numerical simulation, and the second one is the corresponding values measured from experiments in dilatometer. So the function Δ_1 stands for the error of shrinkage rate.

Besides the shrinkage rate, the shrinkage is also important for optimizing the sintering model. It is a key parameter for the design of injection moulds in PIM process. So the second function is built to evaluate the error of shrinkage as following:

$$\Delta_2 = \left| -\int_0^t \frac{1}{3K_p} \sigma_s dt - \ln\left(\frac{L}{L_0}\right) \right| \quad (5.14)$$

where t is the sintering time. It is obvious that the error function Δ_2 of shrinkage is the integration of the error function Δ_1 of shrinkage rate. However, the curves of shrinkage rate measured by dilatometer are not smooth, as shown in Figure 3.29. The optimization results for shrinkage rate can not assure the good accuracy for the shrinkage after the integration over the time.

The time increments are prescribed to minimize the above equations. The optimization problem is formulated as a minimization one expressed as:

$$\begin{cases} \min F_i(x) \\ F_i(x) = \sum_{j=1}^n (\Delta_i(t_j, x))^2 \\ x = [A, B, M, N] \end{cases} \quad (5.15)$$

where $i = 1, 2$ is the number of error functions, $j = 1, \dots, n$ is the time step number, $F_i(x)$ is the mean residual squares distance of the error, x is the set of parameters to be identified. The optimization is implemented for the two error functions (5.13) and (5.14) sequentially. The results obtained after the optimization of $F_1(x)$ are regarded as the initial values for the optimization of $F_2(x)$.

In Chapter 3, it is shown that the densification behaviours of alumina powders are sensitive to heating rate. Generally, the entire sintering process includes heating, holding and cooling stages. The followed identifications are realized for non-isothermal and isothermal sintering respectively.

5.3.2 Identification for Non-isothermal Sintering

The densification of PIM components is mainly accomplished in the heating stage of sintering. However, the material parameters are often proposed for isothermal sintering. The parameters in the model for the sintering process of alumina in the literature, as presented in Chapter 4, are related in table 5.3 [Kan 04].

Table 5.3: Material parameters of alumina in [Kan 04].

Parameters	Values	Parameters	Values
$\delta_b D_b$	$8.6 \times 10^{-10} \text{ m}^3/\text{s}$	Q_s	493 kJ/mol
$\delta_s D_s$	$1.27 \times 10^{-7} \text{ m}^3/\text{s}$	γ_{sv}	0.71 J/ m ²
Q_b	418 kJ/mol	γ_{ss}	0.34 J/ m ²

Based on the data in [GER 06], the calculated molecular volume of alumina $4.256 \times 10^{-29} \text{ m}^3$ is used in the simulation. With the material parameters in Table 5.3, the calculated parameters in the sintering model for alumina are listed in Table 5.4. These parameters are used as the initial values for optimization.

Table 5.4: Initial values for optimization of the parameters in the sintering model of alumina.

Parameters	Values
A	$7.938 \times 10^{12} \text{ Pa}\cdot\text{s}/(\text{m}^3\cdot\text{K})$
B	$5.030 \times 10^4 \text{ K}$
M	$1.465 \times 10^{-11} \text{ K}\cdot\text{m}^4$
N	$5.933 \times 10^4 \text{ K}$

The calculated curves of shrinkage rate and shrinkage based on the sintering model with the parameters in Table 5.4 for the non-isothermal sintering process are shown in Figure 5.5. It includes the curves matched to different hearing rates. These

curves are compared with the experimental curves obtained from the dilatometer tests. It can be observed that the densification behaviors are significantly overestimated with the data presented in Table 5.4.

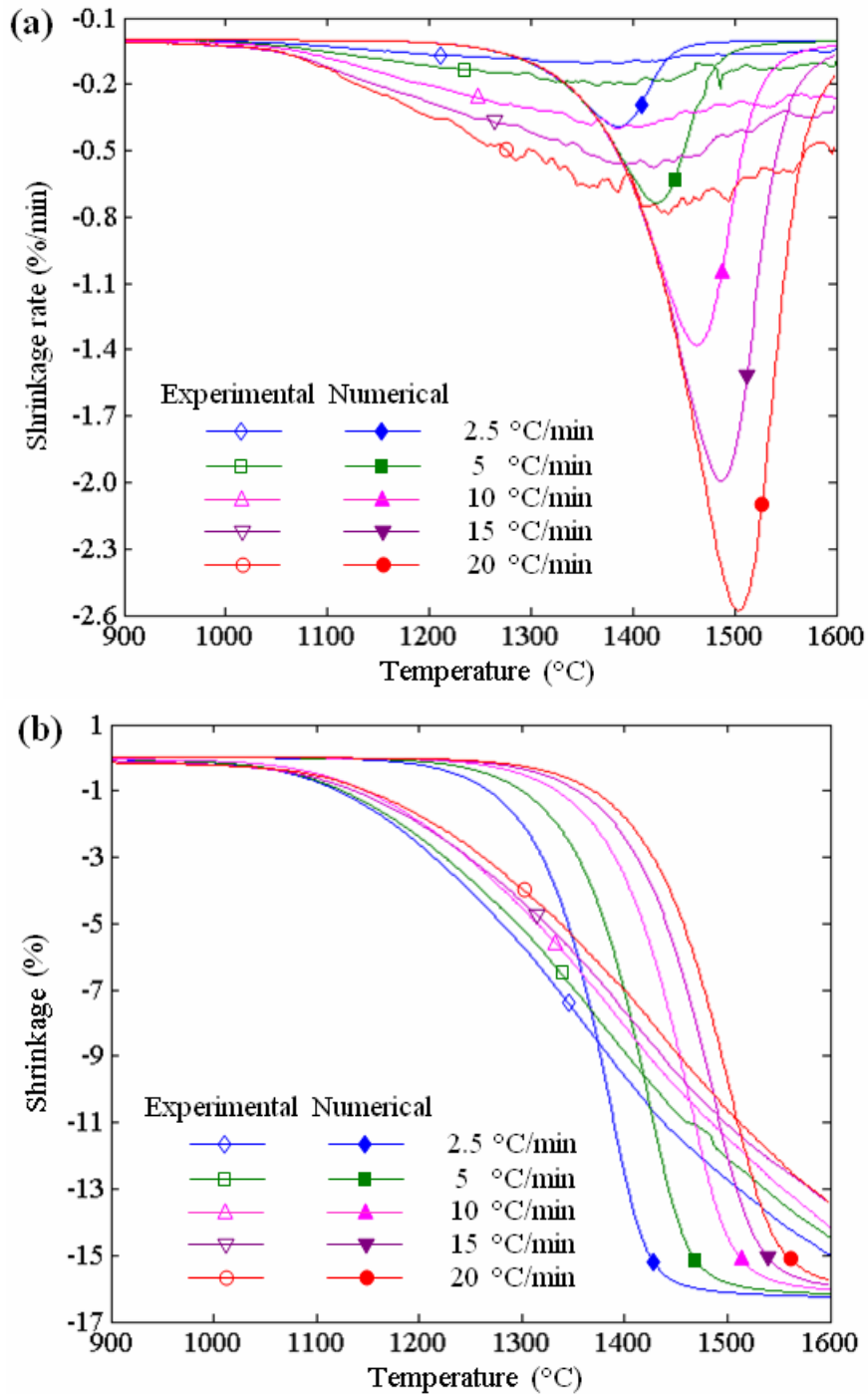


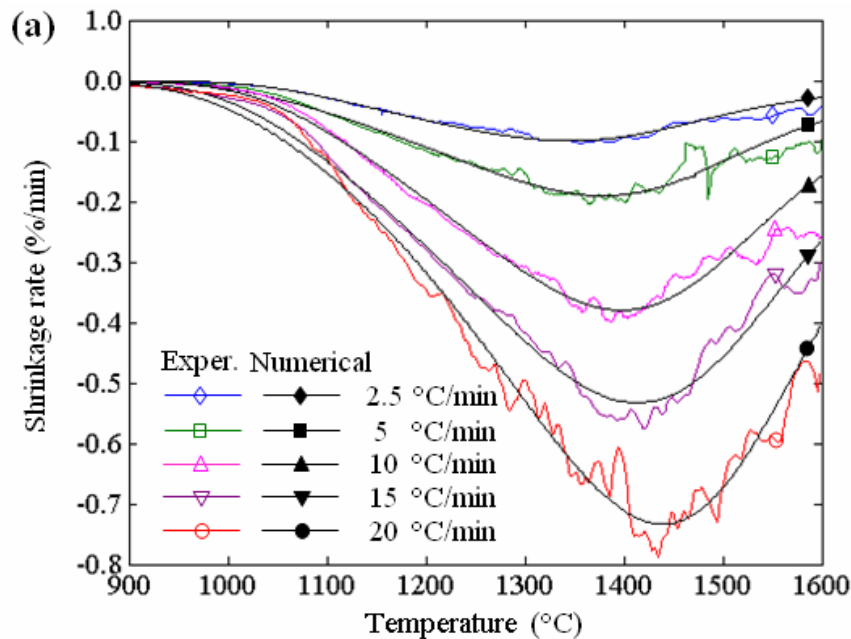
Figure 5.5: The shrinkage rate and shrinkage of alumina powders in the non-isothermal sintering at various heating rates, obtained from the numerical model with the parameters in literatures. The corresponded experimental curves from dilatometer test are shown for comparison.

So the optimization should be made to find the exact material parameters in the sintering model for the alumina specimens in our experiments. The identified parameters after optimization for the non-isothermal sintering with different heating rates are presented in Table 5.5.

Table 5.5: Identified parameters in the sintering model of alumina in non-isothermal sintering at different hearing rates.

	A (Pa·s/(m ³ ·K))	B (K)	M (K·m ⁴)	N (K)
2.5 °C/min	1.802×10^{11}	4.958×10^4	9.711×10^{-15}	3.595×10^4
5 °C/min	3.526×10^{12}	4.399×10^4	3.055×10^{-16}	2.963×10^4
10 °C/min	6.849×10^{11}	4.608×10^4	1.621×10^{-15}	3.154×10^4
15 °C/min	1.651×10^{12}	4.370×10^4	8.440×10^{-16}	2.946×10^4
20 °C/min	3.116×10^{12}	4.225×10^4	5.223×10^{-16}	2.824×10^4

The curves of shrinkage rate and shrinkage obtained from the numerical model with the identified parameters are shown in Figure 5.6. It can be observed that the results from the numerical model are in good agreement with the experimental ones. Parameter identification is an inverse problem and the solution is not unique. The above identified parameters do not represent the exact meaning in physical sense. They are only the numerical ones that can be employed in sintering model to make the simulation results match well the experimental ones.



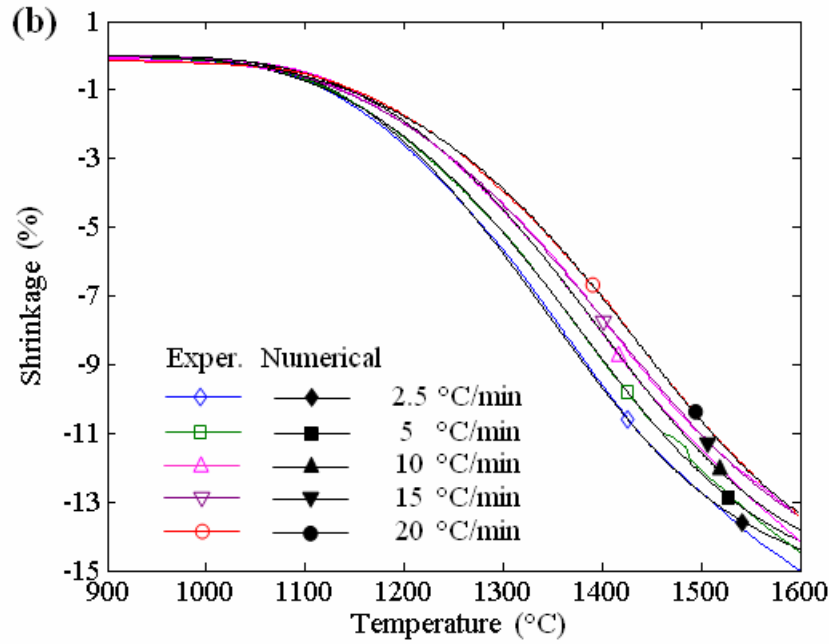


Figure 5.6: The shrinkage rate and shrinkage of alumina powders in the non-isothermal sintering at different heating rates, obtained from the numerical model with the identified model parameters. The corresponded experimental curves from dilatometer are shown for comparison.

For the non-isothermal sintering as presented above, the densification begins from the state of green specimens after debinding. The only difference for various thermal cycles is in their heating rates. By using linear interpolation with the identified parameters in Table 5.5, the parameters for the non-isothermal sintering with other heating rates such as 7.5 °C/min, 12.5 °C/min and 17.5 °C/min can be obtained, as shown in Table 5.6. The calculated curves of shrinkage rates and shrinkage are shown in Figure 5.7. It matches well the experimental results in dilatometer.

Table 5.6: Parameters for various hearing rates in the sintering model of alumina in non-isothermal sintering, obtained by linear interpolation from Table 5.5.

	A (Pa·s/(m ³ ·K))	B (K)	M (K·m ⁴)	N (K)
7.5 °C/min	1.147×10^{12}	4.503×10^4	9.631×10^{-16}	3.058×10^4
12.5 °C/min	9.682×10^{11}	4.489×10^4	1.232×10^{-15}	3.050×10^4
17.5 °C/min	2.158×10^{12}	4.297×10^4	6.831×10^{-16}	2.885×10^4

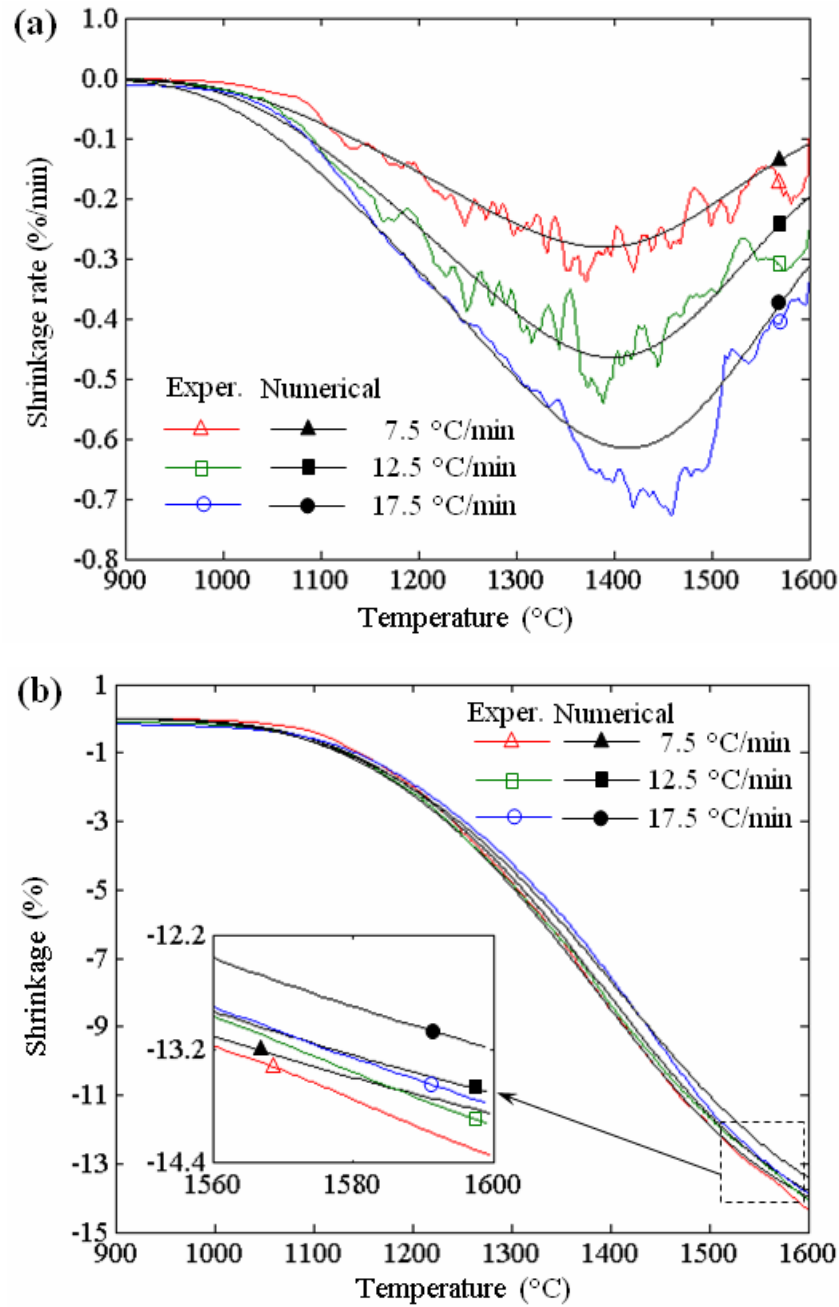


Figure 5.7: The shrinkage rate and shrinkage of alumina powders in the non-isothermal sintering with various heating rates, issued of the calculations based on the numerical model. The parameters in sintering model are obtained by interpolation from the identified ones. The corresponded experimental curves from dilatometer are shown for comparison.

5.3.3 Identification for Isothermal Sintering

In the thermal cycles of sintering, the isothermal stage generally follows the heating one. The densification behaviors in isothermal sintering are dependent on the previous non-isothermal sintering. In order to identify the material parameters in

the stage of isothermal sintering at various temperatures, the experiments in dilatometer are conducted by heating to different peak temperature at 20 °C/min and then holding for 2 h.

In order to take into account the effect of previously conducted heating period, the investigation must be made to justify the state just after the heating stage. Just after the stages heating to peak temperature at 20 °C/min, the measured shrinkage and calculated relative density are shown in Figure 5.8.

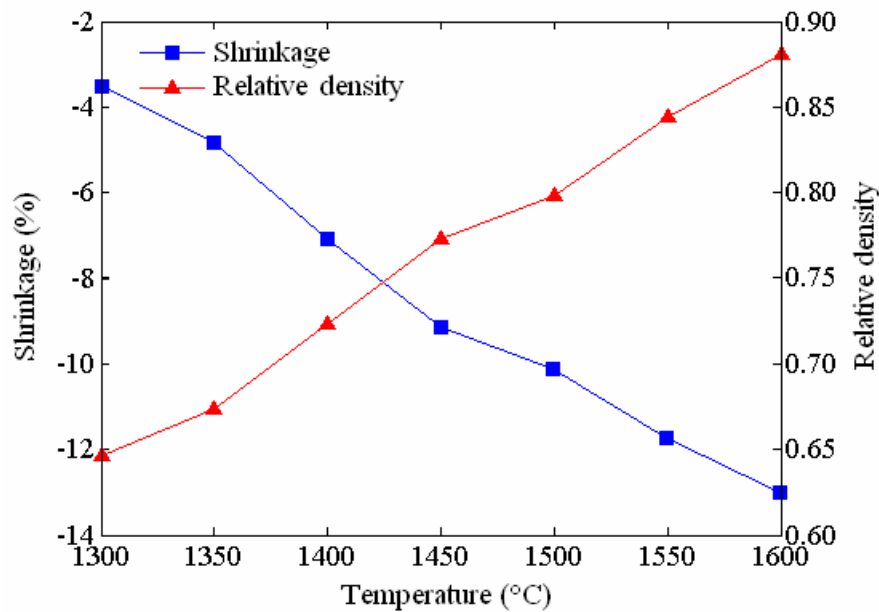


Figure 5.8: The shrinkage and relative density of alumina specimens just after heating to various temperatures at 20 °C/min, without holding.

It can be observed that the isothermal sintering at different temperatures are conducted based on the specimens at different densification levels. The specimens at the beginning of isothermal sintering have different properties, such as viscosity, sintering stress and grain size.

For the simulation of heating stage, the identified parameters with heating rate 20 °C/min, shown in Table 5.5, are used to simulate the densification behaviors. The uniaxial viscosity and sintering stress change with increasing of the temperature, as shown in Figure 5.9.

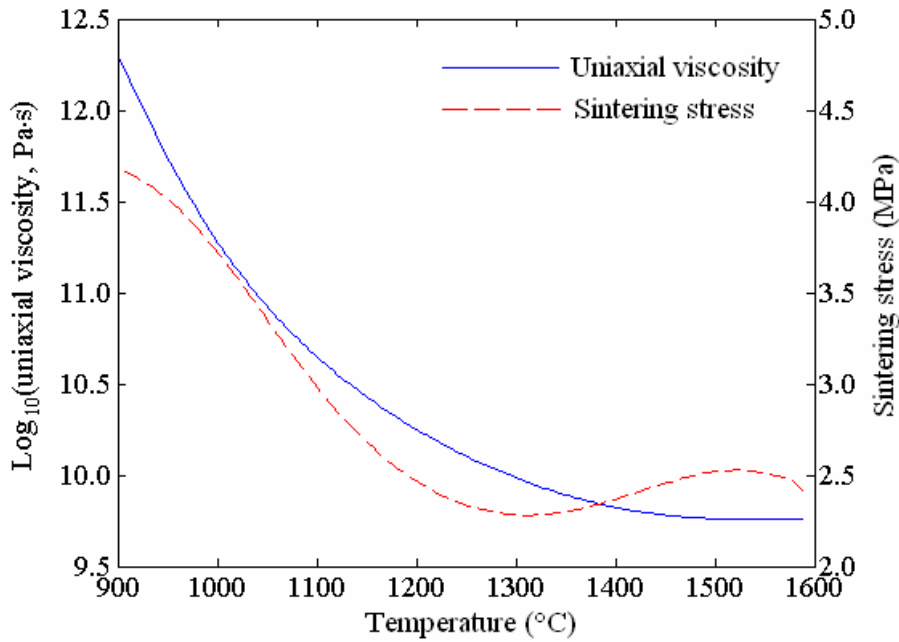


Figure 5.9: The uniaxial viscosity and sintering stress versus the temperature in the heating stage at 20 °C/min, obtained by the model with the identified parameters presented in Table 5.5.

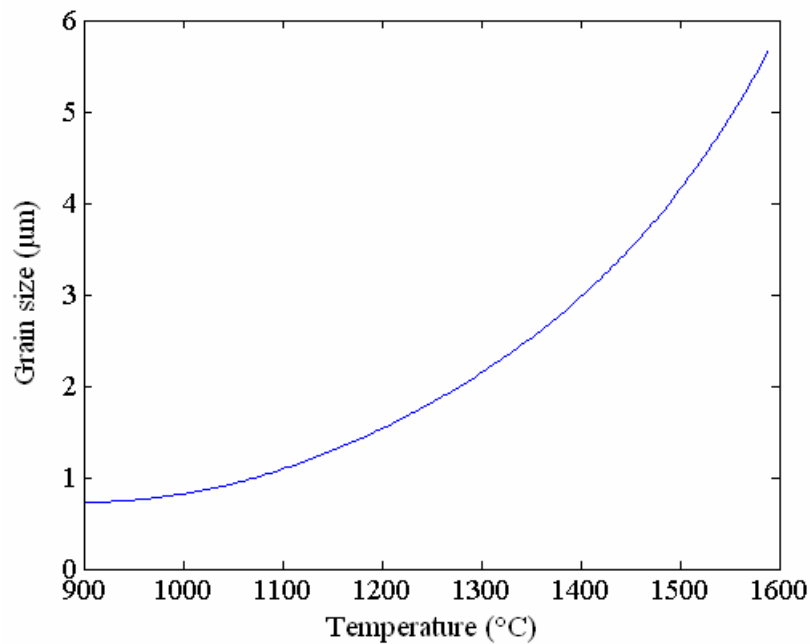


Figure 5.10: Evolution of the grain size versus temperature in the heating stage at 20 °C/min, obtained by the model with identified parameters presented in Table 5.5.

The uniaxial viscosity determined by Equation (4.33) decreases rapidly as the temperature increases. The sintering stress is determined by Equation (4.38). It shows firstly the significant decrease due to the rapid grain growth, then followed

with moderate increasing. The later phenomenon is induced by increasing of the density. As the densification goes on, it becomes the dominant factor that improves the sintering stress. The small decrease of the sintering stress at final stage is due to the continuation of grain growth, even though there exists still little increase of the density. The grain size is determined by Equation (4.40). Evolution of the grain size obtained by calculation for the heating period at 20 °C/min is shown in Figure 5.10.

The parameters identifications for different isothermal sintering stage are conducted by two steps. Firstly, the end state of heating stage should be determined. The identified parameters in Table 5.5 are used to calculate the shrinkage rates and shrinkages in heating stages at 20 °C/min. Secondly, the optimizations procedure as shown in Equation (5.13) to (5.15) are employed to find the proper parameters for the isothermal sintering at different temperatures. The determined parameters are presented in Table 5.7.

Table 5.7: Identified parameters in the sintering model of alumina for the isothermal sintering stage at various holding temperatures, after the heating stages at 20 °C/min.

	A (Pa·s/(m ³ ·K))	B (K)	M (K·m ⁴)	N (K)
1300 °C	6.421×10^{12}	4.234×10^4	2.714×10^{-11}	4.601×10^4
1350 °C	4.801×10^{12}	4.260×10^4	2.058×10^{-11}	4.587×10^4
1400 °C	6.285×10^{12}	4.097×10^4	2.062×10^{-11}	4.494×10^4
1450 °C	5.061×10^{12}	4.057×10^4	1.682×10^{-11}	4.463×10^4
1500 °C	6.517×10^{12}	4.172×10^4	2.642×10^{-11}	4.795×10^4
1550 °C	4.001×10^{12}	4.274×10^4	2.225×10^{-11}	4.878×10^4
1600 °C	5.820×10^{12}	4.180×10^4	1.864×10^{-11}	4.877×10^4

With the identified parameters, the results obtained from the model are in good agreement with the experimental ones. The shrinkage rate curves in the isothermal sintering at 1300 °C and 1600 °C are shown in Figure 5.11. The curves of shrinkage in the isothermal sintering at different temperatures are presented in Figure 5.12.

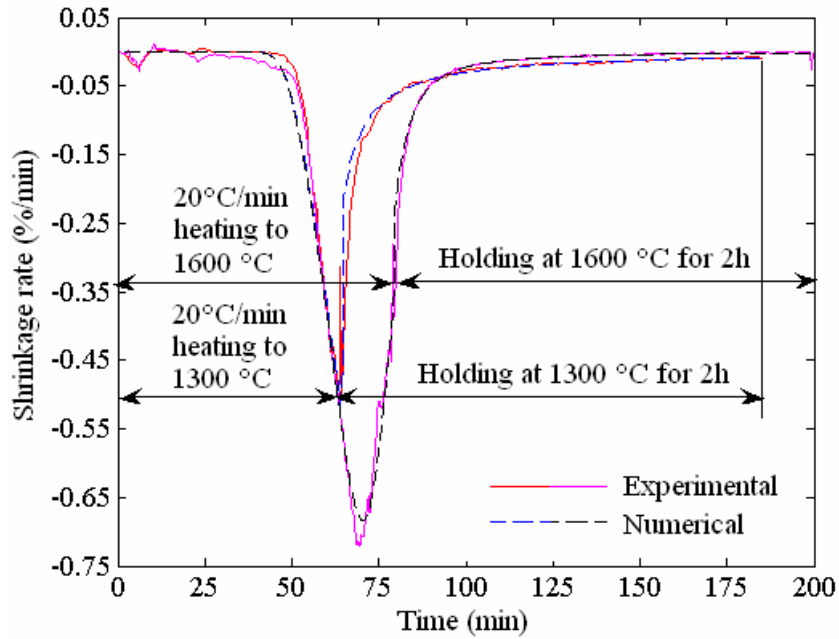


Figure 5.11: The evolution of shrinkage rate in the thermal cycles in which it heats to 1300 °C and 1600 °C respectively and then holds for 2 h, obtained by the model with the identified parameters presented in Table 5.5 and Table 5.7. The experimental curves in dilatometer are shown for comparisons.

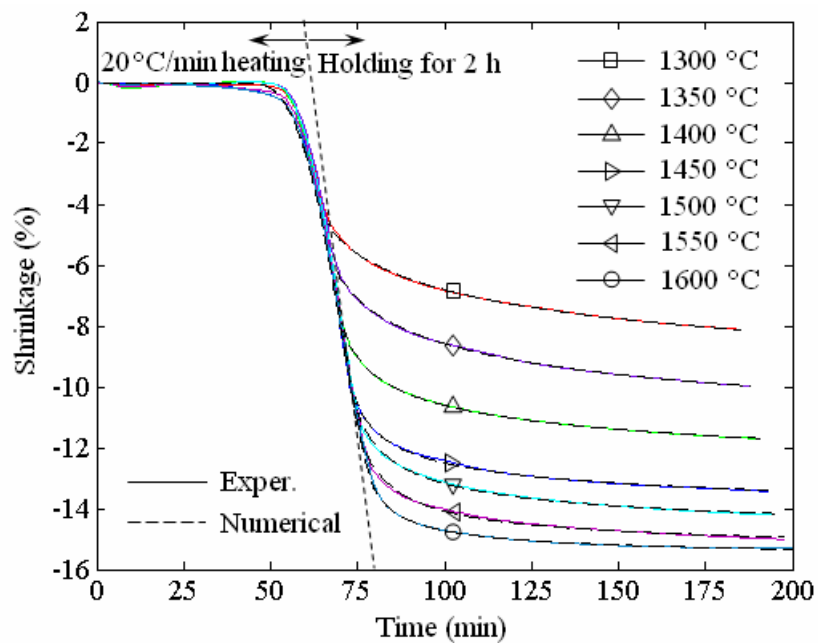


Figure 5.12: The evolution of shrinkage in the thermal cycles in which it heats to different temperatures and then holds for 2 h, obtained by the model with the identified parameters presented in Table 5.5 and Table 5.7. The experimental curves in dilatometer are shown for comparison.

5.3.5 Discussions

In the sintering model of alumina, the parameters to be identified are related to grain boundary diffusion and surface diffusion at the microstructural level during the sintering. It is in fact difficult to determine them accurately. In the present work, one focuses on the macroscopic phenomena observed from the sintering experiments in dilatometer. The macroscopic observation does not permit the determination of all parameters previously introduced by microscopic description, but it is more realistic for the application of numerical simulation in real cases. For the macroscopic model of sintering, the identification of the parameters is just to find the proper combinations of different effects that can make the exact prediction of final shrinkage and distortion in the components by numerical simulations. It can be observed, from the sintering experiments in dilatometer and batch furnace, that the alumina specimens undergo little distortion in sintering. This may be due to the *in-situ* sintering strength of alumina does not decrease abruptly at the high temperature as it is the case of stainless steel.

The experiments aimed to determine the viscosity, such as beam-bending tests or loading sintering in dilatometer, have not been carried out for alumina specimens. However, the results of shrinkage rate and shrinkage based on the model with the identified parameters present good agreements with the experimental ones. According to the viscoplastic constitutive law, it means that the ratio of sintering stress to bulk viscosity modulus is reasonably predicted. The results based on the model with the parameters provided in the references represent the significant difference from the experimental ones, as shown in Figure 5.5. However, these parameters are employed as the initial values in the optimization. The uniaxial viscosities calculated with the identified parameters in the non-isothermal and isothermal sintering stages are shown in Figure 5.13.

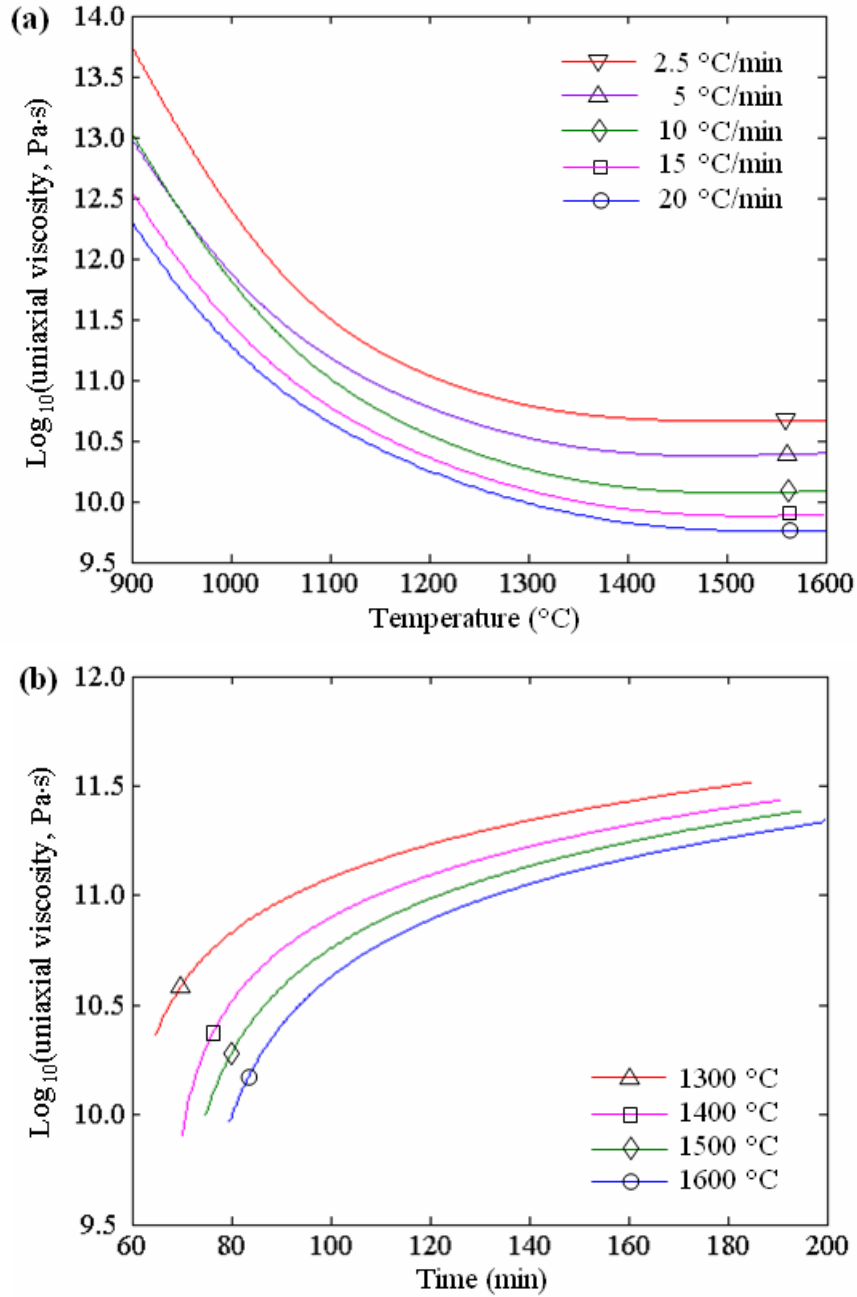


Figure 5.13: The calculated uniaxial viscosity of alumina specimens with the identified parameters as shown in Table 5.5 and Table 5.7: (a) in non-isothermal sintering at different heating rates, (b) in isothermal sintering after heating at 20 $^{\circ}\text{C}/\text{min}$ to different holding temperatures.

It can be observed that the uniaxial viscosity changes significantly in the sintering processes. There is no obvious shrinkage before the temperature reaches 900 $^{\circ}\text{C}$. It is due to the high viscosity of the specimens at low temperature. The maximum densification rate occurs at about 1400 $^{\circ}\text{C}$. The corresponding uniaxial viscosity at this temperature is in the order from 10^9 - 10^{11} Pa \cdot s. At the same

temperature, the uniaxial viscosity takes the lower value when the heating rate is higher before the temperature reaches 1400 °C. This phenomenon leads to the rapid densification rate for the fast heating cycles. After this temperature, combination of the grain growth and the increase of densification make the viscosity keeping nearly constant in spite of the elevation of temperature. In the following the isothermal sintering, the viscosity increases along the holding time due to the grain growth and densification. Kim measured uniaxial viscosity of the alumina powders during sintering. It is in the range of 2-40 GPa·s by the bending tests under several isothermal conditions from 1300°C to 1525 °C [KIM 03].

The uniaxial viscosity is sensitive to the activation energy of grain boundary diffusion Q_b . Many works are conducted to identify this parameter for alumina powders. He and Ma determined that Q_b is 342 kJ/mol for alumina with the coarse initial grain size of 7.0 μm , and 384 kJ/mol for that with the fine initial grain size of 0.9 μm at the temperature of 1600-1700 °C [HE 05]. Zuo calculated that Q_b is 469±20 kJ/mol for alumina under isothermal sintering conditions in the range of 1150-1350 °C [ZUO 04]. Fang evaluated that the value of Q_b for alumina under non-isothermal sintering conditions falls into the range of 478-1080 kJ/mol [FAN 04]. The identified value of Q_b depends on the different data measured from the experiments and the identification method. Many factors can affect the identified value of Q_b , such as the difference in material composition, particle size, green density, temperature cycle, method of measurement, *etc.*

The calculated sintering stress of alumina specimens with the identified parameters are shown in Figure 5.14. For the non-isothermal sintering, the sintering stress varies in the range of 2.1-4.3 MPa. In the relatively low temperature, the sintering stress decreases due to the grain growth. From about 1300 °C, the relative density increases rapidly, which results in the slight increase of sintering stress. At the final stage of sintering, the densification is at very low rate and the grain growth dominates again the change of the sintering stress. The sintering stress decreases

accordingly. In the isothermal holding sintering, the sintering stress falls into the range of 1.1-2.5 MPa. In the holding stage, the densification is very slow. The decrease of sintering stress is due to the increase of grain size. The calculated sintering stress varies in a small range corresponding to 1.1-4.3 MPa. It represents a good agreement with the results reported in [GER 03 b], [HSU 86].

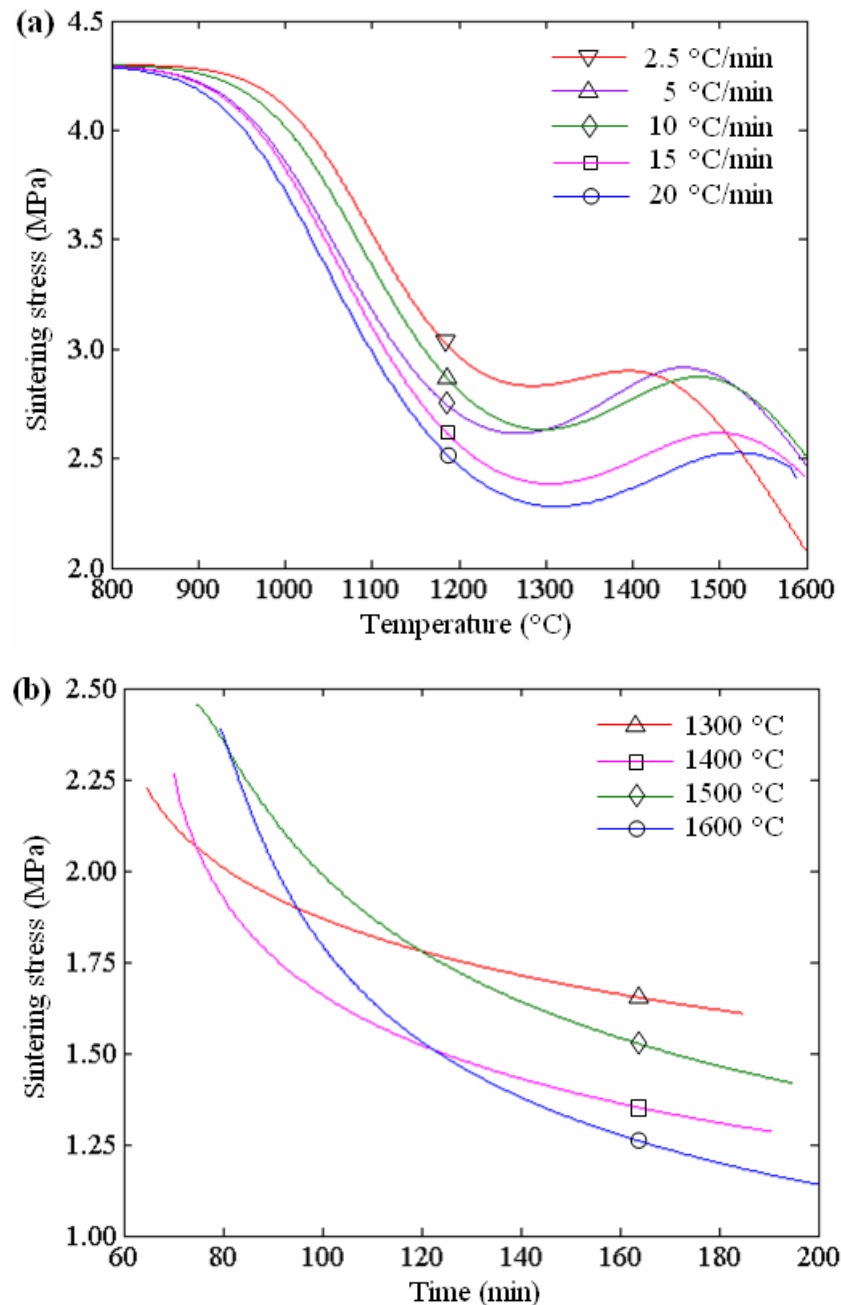


Figure 5.14: The calculated sintering stress of alumina specimens with the identified parameters as shown in Table 5.5 and Table 5.7: (a) in non-isothermal sintering at different heating rates, (b) in isothermal sintering after heating to different temperatures by 20 °C/min.

Although there are no special experiments for determining the viscosity of alumina specimens in sintering, the calculated uniaxial viscosity and sintering stress are considered reasonable by comparison with the data from various references. So the identified parameters can be acceptable for numerical simulation.

5.4 Summary

The parameters in the sintering model are dependent of the material characters, thermal cycles and the determination methods. There are important differences in the values of these parameters provided by various references. Identifying these parameters for the materials of interest by experiments is necessary for the behavior model in numerical simulations. The optimizations methods are employed in the parameter identification to the make the results based on the model match well the experimental ones.

For 316L stainless steel powders, the specimens are prone to distortion. The gravitational beam-bending in sintering are conducted to determine the parameters A and B of the uniaxial viscosity. After determination of viscosity modulus, the experimental results obtained from dilatometer tests are used to identify C parameter. Parameter D in the grain growth model is determined by the measured grain sizes from the reference. The densification of 316L stainless steel powder is conducted rapidly in a narrow temperature range in the intermediate stage of sintering. The identifications are carried out for three distinct stages of the sintering process respectively. Although the beam-bending tests in the study are not very precise, it can be used in the identification to make the uniaxial viscosity in the proper order. It is better than using directly the parameters from the literature or determining it only by the experimental data from dilatometer.

The beam-bending tests have not been conducted for the alumina specimens. The experimental data from dilatometer are used for identification of the parameters in the model. In alumina specimens, temperature range for densification is larger than that for 316L stainless steel. There is little distortion of the alumina specimens

in the sintering experiments. The optimization methods are applied on both shrinkage rate and shrinkage. The initial values for optimization are set to be the parameter values proposed in the literature. Hence the optimal sets of the parameters can be achieved. The calculated uniaxial viscosity and sintering stress with identified parameters are reasonable by comparison with the ones in references. So they can be used in the numerical simulations to predict the shrinkage rate and shrinkage in the sintering bodies.

The presented identifications are conducted for the prescribed thermal cycles. In order to predict the sintering process with numerical simulation, it is necessary to obtain the parameters for arbitrary thermal cycles. For the non-isothermal stage at constant heating rates in sintering of the alumina powders, the interpolation can be used to determine the parameters based on the identified values for the typical thermal cycles. However, it is still not applicable for the sintering process with the variation of heating rate. In the future, the more universal procedure for parameter determination is expected to be developed.

Chapter 6 Numerical Simulation of Sintering Processes

The numerical simulations of sintering processes based on the continuum model and the identified parameters have been realized by finite element method (FEM). The implementation of sintering model can be realized in the software properly developed by the research team. Another effective way is to implement the model into a commercial finite element packages using user-defined subroutine. For the former method, the obvious advantage is its flexibility. The researchers know well details of the software and can change anything in the source code. For the later one, one can take advantages of the commercial FE software, such as its powerful user-friendliness interfaces, suitability for complex configurations, stability and efficiency of the optimized algorithm, and the ease to be accepted by the industries. In the present study, the presented sintering model and identified parameters are introduced into the in-house software SinterForm on the platform Matlab[®] [GEL 99], [GEL 00], [REN 01]. On the other hand, the commercial FEM software Abaqus[®] is employed for sintering simulations, too. The sintering models are developed through the user subroutines. In Chapter 6, both ways of the FEM realization are introduced. The examples of sintering simulations are presented. The results are compared with the experimental ones to validate the models, the identified parameters and the numerical simulation methods.

6.1 FE Simulation of Sintering Processes

6.1.1 FE Simulation by the Code on Matlab[®]

In the FE simulation based on Matlab[®], the temperature gradients in the sintering bodies can be ignored. Such an assumption is reasonable as the PIM components are often in small dimensions, and the heating rate is the relatively slow one. The elastic strain can be neglected, too. Sometimes one can neglect the friction between the components and the supports, when its effects are not attentively

investigated. The coupled governing equations for mass and momentum conservation equations, as shown in Equation (4.3) and Equation (4.5), are solved by FEM. The velocity and relative density are chosen to be the main variables in the following interpolation forms [SON 05]:

$$\begin{aligned}\mathbf{u} &= \mathbf{N}\mathbf{u}_n \\ \dot{\boldsymbol{\varepsilon}} &= \mathbf{B}\dot{\mathbf{u}}_n \\ \rho &= \mathbf{N}\rho_n\end{aligned}\quad (6.1)$$

where \mathbf{N} is the interpolation function for displacement and relative density, \mathbf{B} is strain rate interpolation matrix. \mathbf{u}_n , $\dot{\mathbf{u}}_n$ and ρ_n stand for the nodal values of displacements, displacement rates and relative density. Galerkin method is applied to build the following FE modeling equations, expressed as:

$$\begin{aligned}\mathbf{M}_d(\mathbf{u}_n)\dot{\rho}_n + \mathbf{C}_d(\mathbf{u}_n, \dot{\mathbf{u}}_n)\rho_n &= 0 \\ \mathbf{K}_u(\mathbf{u}_n, \rho_n)\dot{\mathbf{u}}_n + \mathbf{F}_u(\rho_n) &= 0\end{aligned}\quad (6.2)$$

The matrices \mathbf{M}_d , \mathbf{C}_d , \mathbf{K}_u and \mathbf{F}_u are expressed by the following expressions:

$$\begin{aligned}\mathbf{M}_d(\mathbf{u}) &= \sum_e \int_{\Omega_e(\mathbf{u})} \mathbf{N}^T \mathbf{N} dV \\ \mathbf{C}_d(\mathbf{u}, \dot{\mathbf{u}}) &= \sum_e \int_{\Omega_e(\mathbf{u})} \mathbf{N}^T \text{tr}(\mathbf{B}\dot{\mathbf{u}}_n) \mathbf{N} dV \\ \mathbf{K}_u(\mathbf{u}, \rho, T) &= \sum_e \int_{\Omega_e(\mathbf{u})} \mathbf{B}^T \mathbf{A}(\rho, T) \mathbf{B} dV \\ \mathbf{F}_u(\rho) &= \sum_e \int_{\Omega_e(\mathbf{u})} (-\mathbf{N}^T f(\rho) + \mathbf{B}^T \sigma_s(\rho) \mathbf{I}) dV\end{aligned}\quad (6.3)$$

where \sum_e stands for the finite element assemblage operator, $\mathbf{A}(\rho, T)$ is a tensor that describes the viscoplastic constitutive behavior:

$$\begin{aligned}\boldsymbol{\sigma} &= \mathbf{A}(\rho, T) : \dot{\boldsymbol{\varepsilon}}_{vp} + \sigma_s \mathbf{I} \\ \mathbf{A}(\rho, T) &= 2G_p(\rho, T) \mathbf{I}_4 + \left(K_p(\rho, T) - \frac{2}{3} G_p(\rho, T) \right) \mathbf{I} \otimes \mathbf{I}\end{aligned}\quad (6.4)$$

where \otimes is the tensorial product operator, G_p and K_p are the shear and bulk viscosity moduli.

In free sintering process conditions, the external force f represents only the gravity effect, expressed as:

$$f(\rho) = -\rho_{th}(\mathbf{N}\rho)g[0 \ 0 \ 1]^T \quad (6.5)$$

where ρ_{th} is theoretical density (the density of wrought material), and g is gravitational acceleration.

The above discretized equations are solved by the FE software developed on Matlab[®]. The functions in Matlab[®] to solve ordinary differential equations are used in the developed program.

6.1.2 FE Simulation by Abaqus[®]

The commercial FEM software Abaqus[®] is often used for sintering simulation because of its powerful ability in solution of the nonlinear and coupled thermo-mechanical problems. Abaqus[®]/Standard is the implicit FEM procedure for the static or quasi-static analysis. The user subroutine CREEP is provided for the user to define his proper viscoplastic constitutive law. Simultaneously, the subroutine UMAT for user defined materials can also be used to define any constitutive law. The realization of sintering simulation by these two user subroutines are presented respectively as following.

6.1.2.1 Realization by User Subroutine CREEP

As introduced in Chapter 4, the sintering is a thermal-stress coupling process. As the mechanical dissipation in pressureless sintering is small, it can be neglected. Based on this assumption, the thermal-stress coupling can be regarded as the unilateral one in the sintering simulation. It means that the thermal and mechanical analysis can be separated into sequential steps, but the dependence of thermal analysis on mechanical dissipation is not taken into account. The analysis of stress or deformation field depends on the temperature field, while dependence of the temperature field on stress or deformation field is uncoupled. Under this assumption in analysis, the analysis of heat transfer can be carried out firstly. Then the obtained temperature field is inherited by the next stress and deformation analysis. The user subroutine CREEP is aimed to define the rate dependent viscoplastic behaviors (creep and swelling) of the materials. According the definition of CREEP, the

incremental viscoplastic strain includes two components:

$$\Delta \boldsymbol{\varepsilon}_{vp} = \frac{1}{3} \Delta \bar{\boldsymbol{\varepsilon}}_{sw} \mathbf{R} + \Delta \bar{\boldsymbol{\varepsilon}}_{cr} \mathbf{n} \quad (6.6)$$

where $\Delta \bar{\boldsymbol{\varepsilon}}_{sw}$ is the incremental volumetric swelling strain, $\Delta \bar{\boldsymbol{\varepsilon}}_{cr}$ is the uniaxial equivalent creep strain, \mathbf{R} is a matrix with the anisotropic swelling ratios in the diagonal if anisotropic swelling is defined. For isotropic swelling, \mathbf{R} is equal to the second order identity tensor \mathbf{I} , \mathbf{n} is the stress gradient of its deviatoric potential, defined as:

$$\mathbf{n} = \frac{\partial \tilde{q}}{\partial \boldsymbol{\sigma}} \quad (6.7)$$

The Von Mises stress potential is used in the present study, defined as:

$$\tilde{q} = \sqrt{\frac{3}{2} (\text{dev} \boldsymbol{\sigma} : \text{dev} \boldsymbol{\sigma})} \quad (6.8)$$

where $\text{dev} \boldsymbol{\sigma} = \boldsymbol{\sigma} + p \mathbf{I}$ is the deviatoric stress, and $p = -\text{tr}(\boldsymbol{\sigma})$ is the equivalent pressure stress. From Equation (6.7) and (6.8), it yields the following expression:

$$\mathbf{n} = \frac{3 \boldsymbol{\sigma}'}{2 \tilde{q}} \quad (6.9)$$

So the incremental viscoplastic strain in the user subroutine CREEP can be expressed as:

$$\Delta \boldsymbol{\varepsilon}_{vp} = \frac{1}{3} \Delta \bar{\boldsymbol{\varepsilon}}_{sw} \mathbf{I} + \Delta \bar{\boldsymbol{\varepsilon}}_{cr} \left(\frac{3 \boldsymbol{\sigma}'}{2 \tilde{q}} \right) \quad (6.10)$$

in which $\Delta \bar{\boldsymbol{\varepsilon}}_{sw}$ and $\Delta \bar{\boldsymbol{\varepsilon}}_{cr}$ should be defined according to the sintering model.

On the other hand, the viscoplastic constitutive law for the sintering bodies as Equation (4.24) can be written in the incremental form as:

$$\Delta \boldsymbol{\varepsilon}_{vp} = \frac{\boldsymbol{\sigma}'}{2G_p} \Delta t + \frac{\sigma_m - \sigma_s}{3K_p} \Delta t \mathbf{I} \quad (6.11)$$

Comparing Equations (6.10) and (6.11), $\Delta \bar{\boldsymbol{\varepsilon}}_{sw}$ and $\Delta \bar{\boldsymbol{\varepsilon}}_{cr}$ can be expressed as:

$$\Delta \bar{\boldsymbol{\varepsilon}}_{sw} = \frac{\sigma_m - \sigma_s}{K_p} \Delta t \quad (6.12)$$

$$\Delta \bar{\boldsymbol{\varepsilon}}_{cr} = \frac{\tilde{q}}{3G_p} \Delta t$$

The deformation tensor for geometrically nonlinear analysis is characterized by logarithmic strain in Abaqus[®]. The relative density should be updated in the subroutines for each incremental step by the expression:

$$\rho = \rho_0 \exp(-\varepsilon_{kk}) \quad (6.13)$$

In the above method, user subroutine CREEP is used to define the incremental viscoplastic strain. The thermal and elastic parameters are determined by the usual ways for the calculation of thermal and elastic strain.

6.1.2.2 Realization with User Subroutine UMAT

The user subroutine UMAT is aimed to define the mechanical constitutive behavior of the materials. It is necessary to define the material Jacobian matrix $\partial \Delta \boldsymbol{\sigma} / \partial \Delta \boldsymbol{\varepsilon}$. As the elastic strain is very small in pressureless sintering, it is ignored in the FEM simulation with UMAT. Based on the viscoplastic constitutive law in Equation (4.23), the stress can be expressed as:

$$\boldsymbol{\sigma} = 2G_p \dot{\boldsymbol{\varepsilon}}_{vp} + \left(K_p - \frac{2}{3} G_p \right) \dot{\boldsymbol{\varepsilon}}_{vp} \mathbf{I} + \sigma_s \mathbf{I} \quad (6.14)$$

The central difference method is used to obtain from Equation (6.14) in incremental form, as expressed in following ways:

$$\begin{aligned} \dot{f}_{t+\frac{1}{2}\Delta t} &= \frac{\Delta f}{\Delta t} \\ f_{t+\frac{1}{2}\Delta t} &= f_t + \frac{\Delta f}{2} \end{aligned} \quad (6.15)$$

where f is the function, f_t is its value at the beginning of the increment, Δf is the change in the function over the increment, and Δt is the time increment. Applying Equation (6.15) to Equation (6.14) gives:

$$\boldsymbol{\sigma}_t + \frac{\Delta \boldsymbol{\sigma}}{2} = 2G_p \frac{\Delta \boldsymbol{\varepsilon}}{\Delta t} + \left(K_p - \frac{2}{3} G_p \right) \frac{\Delta e_{vp}}{\Delta t} \mathbf{I} + \sigma_s \mathbf{I} \quad (6.16)$$

So the change in stress over the increment has the following form:

$$\Delta \boldsymbol{\sigma} = 4G_p \frac{\Delta \boldsymbol{\varepsilon}}{\Delta t} + 2 \left(K_p - \frac{2}{3} G_p \right) \frac{\Delta e_{vp}}{\Delta t} \mathbf{I} + 2\sigma_s \mathbf{I} - 2\boldsymbol{\sigma}_t \quad (6.17)$$

At the end of each increment, the stress is updated as:

$$\boldsymbol{\sigma}_{t+\Delta t} = \boldsymbol{\sigma}_t + \Delta \boldsymbol{\sigma} \quad (6.18)$$

The material Jacobian matrix takes the form:

$$\frac{\partial \Delta \boldsymbol{\sigma}}{\partial \Delta \boldsymbol{\varepsilon}} = \begin{bmatrix} a+b & a & a & 0 & 0 & 0 \\ a & a+b & a & 0 & 0 & 0 \\ a & a & a+b & 0 & 0 & 0 \\ 0 & 0 & 0 & b & 0 & 0 \\ 0 & 0 & 0 & 0 & b & 0 \\ 0 & 0 & 0 & 0 & 0 & b \end{bmatrix} \quad (6.19)$$

a and b in matrix (6.19) are expressed as :

$$a = 2(K_p - \frac{2}{3} G_p) / \Delta t, \quad b = 4G_p / \Delta t \quad (6.20)$$

In the incremental form of constitutive law, the shear and bulk viscosity modulus, as well as the sintering stress are regarded as the constants in each time increment. They are evaluated again at the end of increment. So the time step should be small to obtain accurate simulation results. As the elastic strain is ignored in the UMAT, its simulations are faster than the ones with user subroutine CREEP.

The grain growth laws for 316L stainless steel and alumina as in Equation (4.39) and (4.40) are changed into the incremental forms to evaluate the grain size in each time increment.

6.2 Sintering Simulations for Tensile Test Specimens

The injection moulded tensile test specimen in 316L stainless steel feedstock represents as dimensions as indicated in Figure 6.1. The presintered specimens are

sintered in the batch furnace, supported by the alumina substrates.

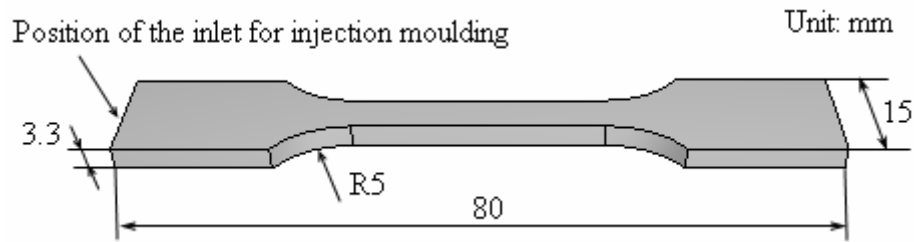


Figure 6.1: Dimension of the tensile test specimens in 316L stainless steel feedstock after injection moulding.

The numerical simulations are realized by implementation of the sintering model in FEM codes, which includes the self-developed one in research team based on the Matlab[®] platform and the commercial software Abaqus[®]. In the thermal cycle for simulation, the temperature is heated up to 1360 °C at 8 °C/min, and then held for 1h, as shown in Figure 3.16. The identified parameters presented in Table 5.1 and Table 5.2 are employed for the implemented model. The simulations are rcarried out for the tensile test specimens with one inlet for injection moulding. The corresponding cavity in the injection mould is shown in Figure 3.3. Due to symmetry of the specimen, half part is accounted in FE simulations.

6.2.1 Simulations on Matlab[®]

Tetrahedral elements are used to mesh the tensile specimen, and the resulting mesh composes 505 nodes and 1509 elements.

6.2.1.1 Simulations with the Homogeneous Green Density

The simulation is carried out firstly with a homogeneous green part. Its relative density is 0.6. The mesh and initial density contours, uniform everywhere, are shown in Figure 6.2. The final contours of relative density after sintering obtained by simulation are shown in Figure 6.3.

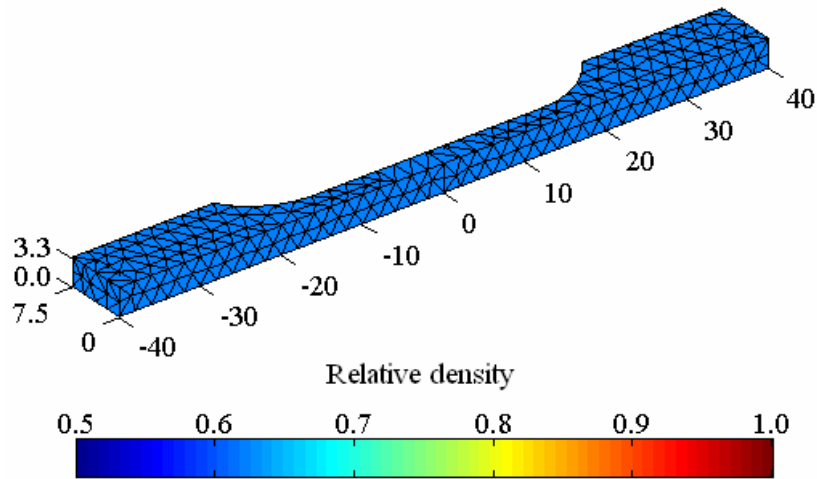


Figure 6.2: The FEM model for the tensile test specimen with the homogeneous initial relative density fixed at 0.6.

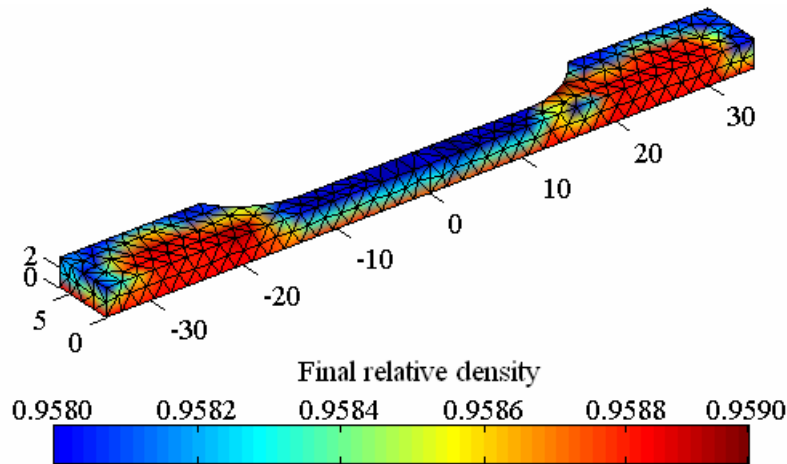


Figure 6.3: Final contours of the relative density after sintering in the sintered tensile tests specimens, obtained by numerical simulation.

It can be observed that the final density contours are still almost uniform, when the green part is a homogeneous one. The comparison between the dimensions of tensile test specimen before and after sintering is shown in Figure 6.4. For the small parts like tensile test specimens, the gravity has little effects on the densification if the support conditions are chosen suitably in sintering. The shrinkages in three orthogonal directions are presented in Figure 6.5.

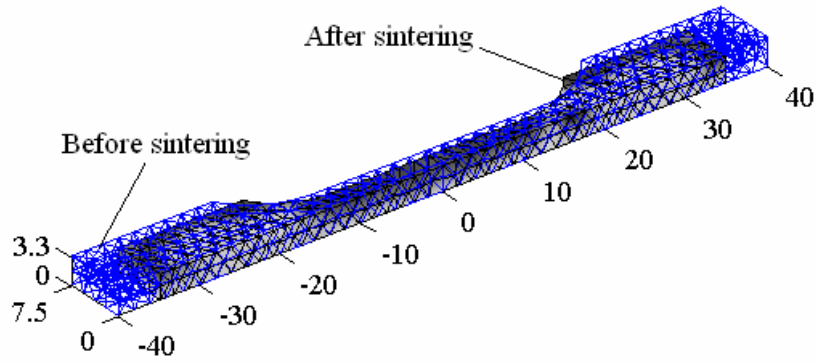
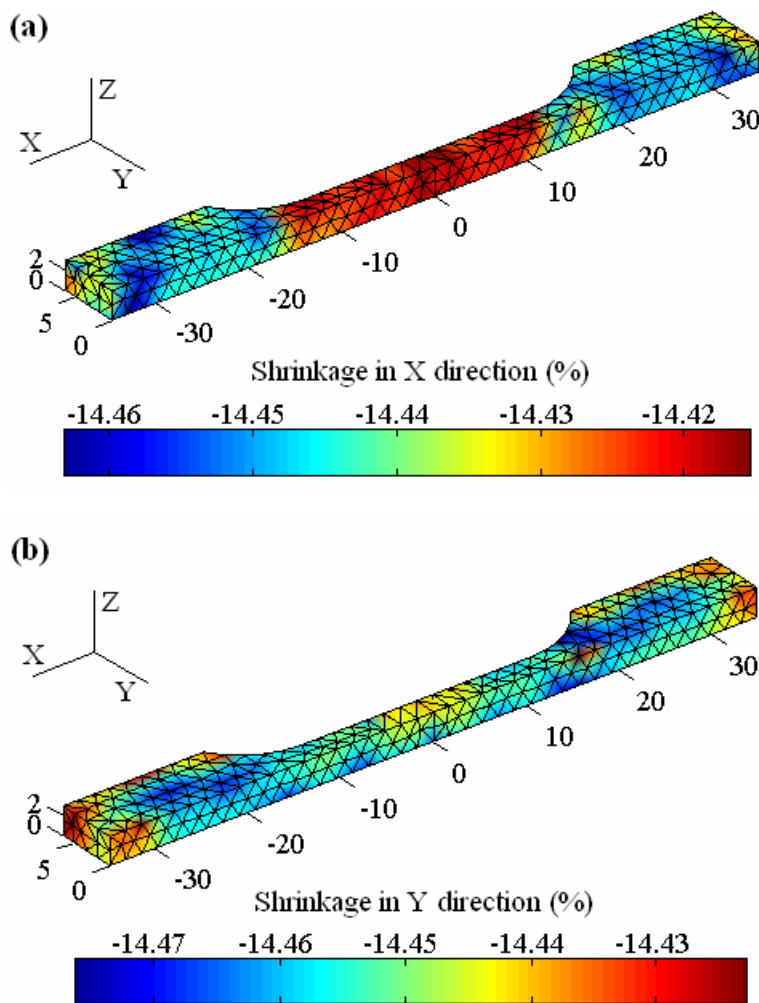


Figure 6.4: Dimensions of the tensile test specimens before and after sintering to show the shrinkage.



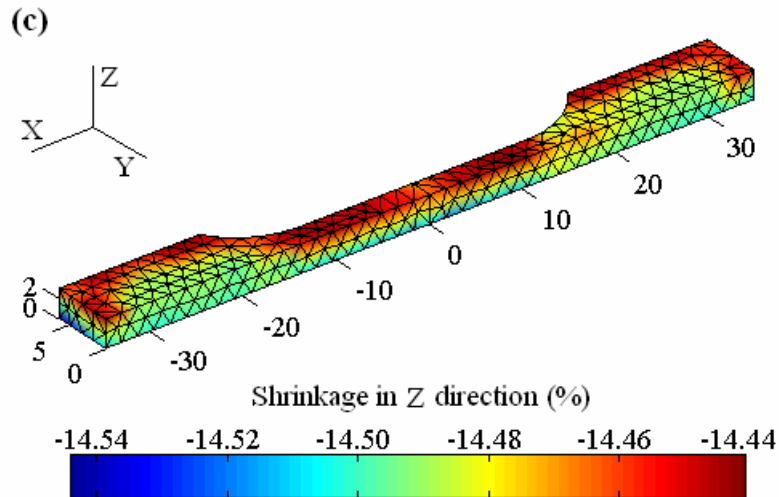


Figure 6.5: Shrinkage of the sintered tensile test specimen in three orthogonal directions, obtained from a homogeneous green part.

6.2.1.2 Simulations with the Inhomogeneous Green Density

In the powder injection process, the segregation occurs between the powders and the binders due to their different inertia. It induces inhomogeneous density contours in the green parts. This initial inhomogeneity affects the final dimensions and mechanical properties of the sintered components. A bi-phasic injection modelling can be used to predict the segregation effects of PIM injection, as presented in Appendix. An in-house software (FEAPIM[®]) for bi-phasic injection simulation has been developed. The predicted powder loading contours of the tensile test specimen are shown in Figure 6.6, for the injection moulding of a PIM mixture composed of 316L stainless steel powders. It is regarded as the initial contour of relative density in the sintered part.

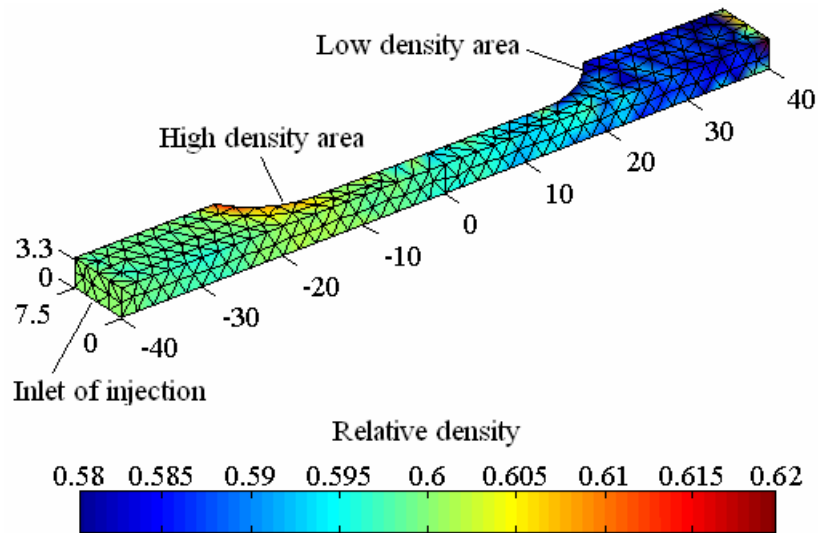


Figure 6.6: Initial contours of the relative density in the tensile test specimen made from 316L stainless steel powders, obtained by bi-phasic injection simulations.

The final density contours after sintering, obtained by numerical simulations, are shown in Figure 6.7.

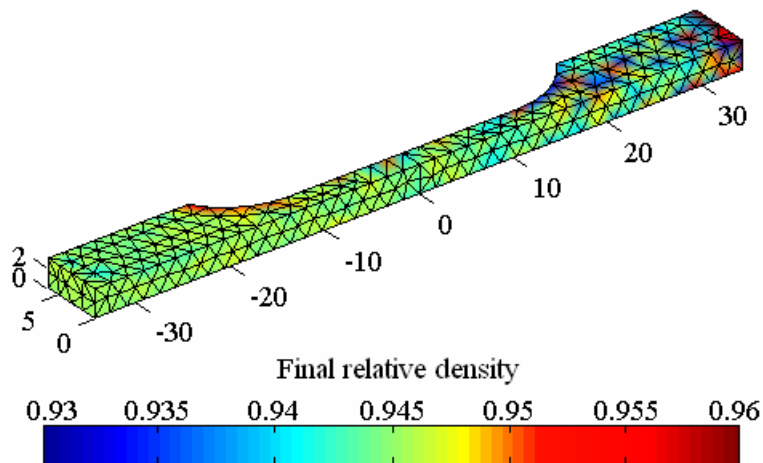


Figure 6.7: Final contours of the relative density in the tensile test specimen after sintering, obtained numerical simulation.

Even though the inhomogeneous distribution of green density due to the segregation and jetting effects arising in the injection step after the PIM process, the sintering process results in the sintered components with a nearly uniform density distribution. But it does not mean that we can neglect its effect, as the initial

inhomogeneity induces significant uneven shrinkage of the final components, as shown in Figure 6.8.

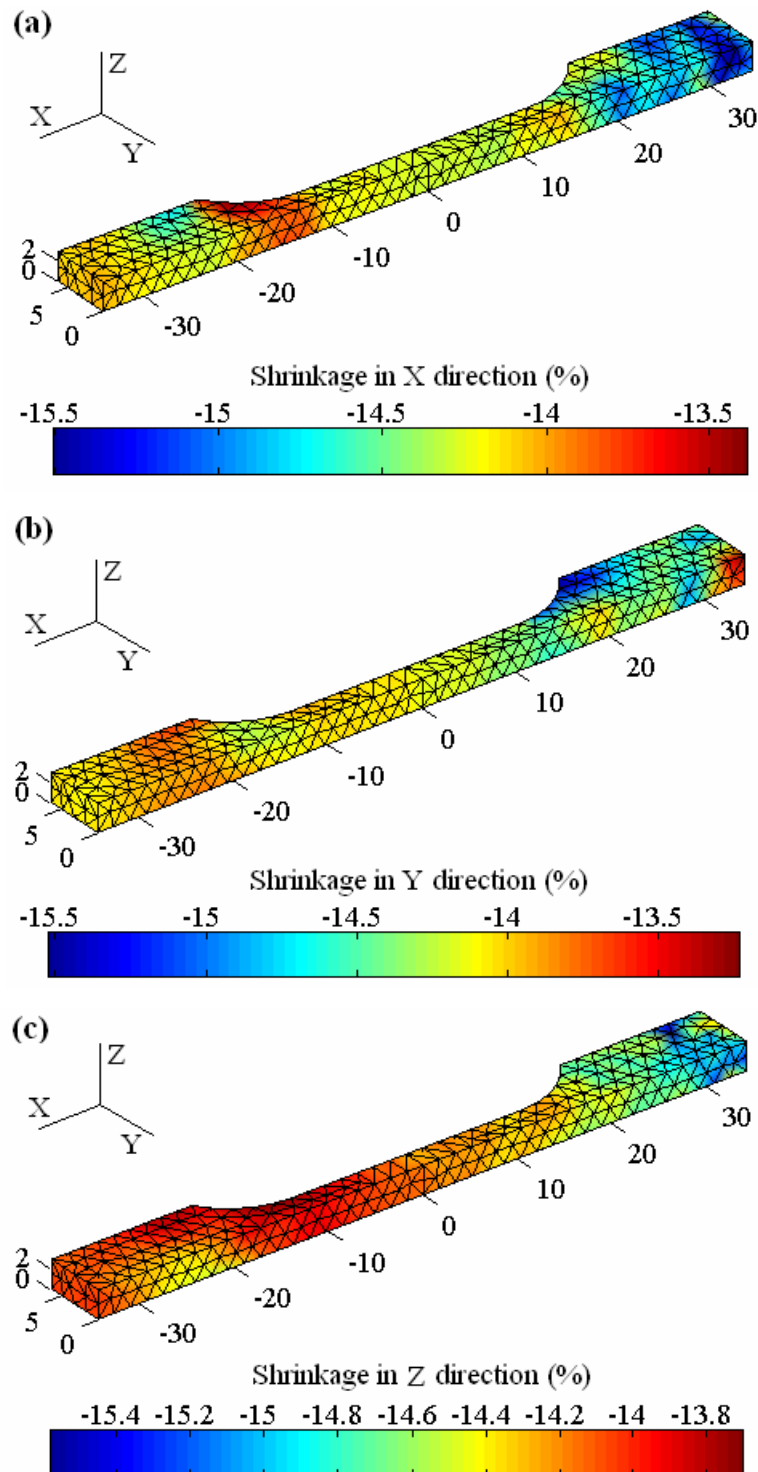


Figure 6.8: Shrinkage of the sintered tensile test specimen in three orthogonal directions, with inhomogeneous green density contours.

The mean shrinkages of the tensile test specimen measured by experiments are

-13.11%, -14.09% and -14.55% respectively in the length, width and thickness directions, as shown in Figure 6.9. The values in the length and width directions seem smaller than these obtained from simulation results, as the friction between the support substrate and the specimen is neglected in the simulation.

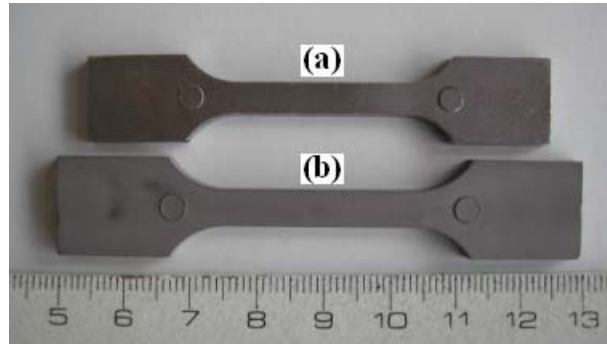


Figure 6.9: Change in dimension of the tensile test specimens, obtained by experiments: (a) sintered part, (b) injection moulded part.

6.2.2 Simulations on Abaqus®

The tensile test specimen is meshed with the C3D8RT element type, an 8-node thermally coupled Lagrangian brick, trilinear displacement and temperature, reduced integration, hourglass control. The alumina support is meshed with elements for rigid body, as shown in Figure 6.10. There are 1896 nodes and 1170 elements of the tensile test specimen in the FEM model.

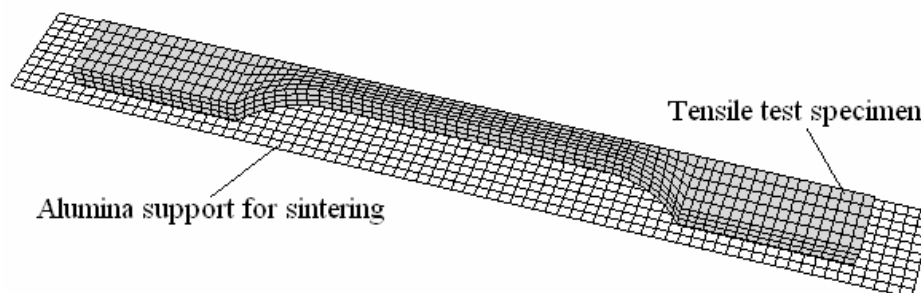


Figure 6.10: FEM mesh for the sintering simulation of tensile test specimen.

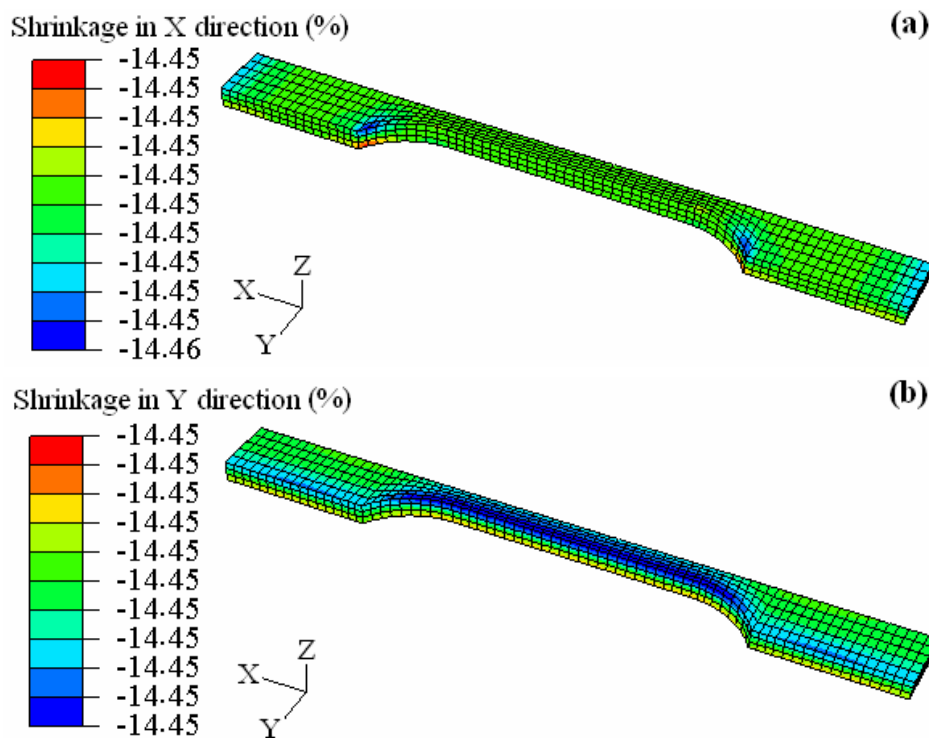
For 316L stainless steel powders, the material parameters are the following: Young modulus: 196 GPa, Poisson's ratio: 0.28, thermal conductivity: 14.6 W/(m°C)

[ZHA 02 a]. The thermal expansion coefficient is $1.12 \times 10^{-5} \text{ } ^\circ\text{C}^{-1}$, obtained from the dilatometer experimental data. The fully coupled thermal-stress analysis is chosen for simulation [GEL 06], [SON 06 a], [SON 06 b].

The prediction of uneven shrinkage in the sintering part is one of the important purposes of sintering simulation. Several factors such as gravity, inhomogeneous green density, and friction between the supports and the parts should be considered. The following simulations are realized to analyze the influence of these factors.

6.2.2.1 Effects of Gravity on Shrinkage

The elasto-viscoplastic constitutive law proposed in Chapter 4 is employed in the simulation by the CREEP user subroutine. An homogeneous green relative density equal to 0.6 is used in simulation. The final shrinkages of the sintered part are shown in Figure 6.11.



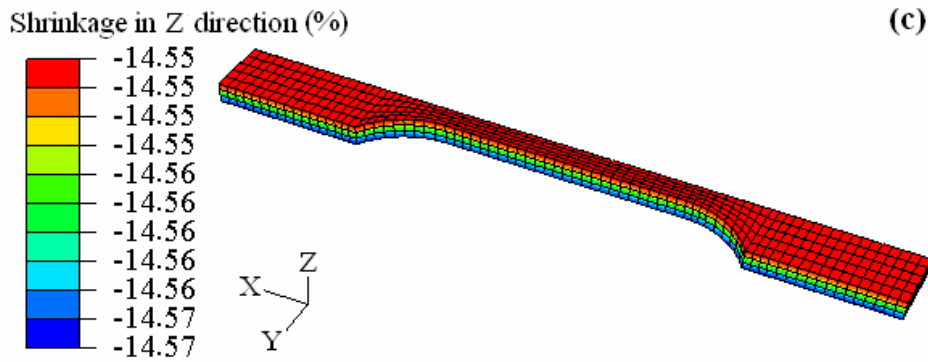


Figure 6.11: Final shrinkages of sintered tensile test specimen in three orthogonal directions to show the effect of gravity.

It can be observed that the shrinkages in the length and width directions are almost uniform, while the gravitational effect induces more uneven shrinkage in the thickness direction. However, the effect is very small if the tensile test specimen is supported by its whole bottom surface, as shown in Figure 6.10. In Figure 6.11, the uneven shrinkage in thickness direction corresponds to 0.8% of the difference, compared to the shrinkages in other directions. The influence of gravity on uneven shrinkage of the sintered body depends on its dimensions, support reaction, and initial density contours and values. As shown in the beam-bending tests, the gravity can make great distortion of the sintered parts by changing the support conditions. Olevsky analyzed the gravity effects on the anisotropic shrinkages and distortions of the sintering bodies [OLE 00 a], [OLE 00 b].

6.2.2.2 Effects of Inhomogeneous Green Density on Shrinkage

The inhomogeneous green density distributions have significant effects on final dimension of the sintered components. The homogeneity of the green parts is induced by the previous processes before the sintering, such as the mixture of powders and binders, pressing or injection moulding [BRA 98], [GER 04], [KRA 02], [REI 04], [ZAV 00]. In the present study, the important work has been realized to take into account the results of injection simulation into the simulation for sintering process. So the feedback information can be used to modify the injection moulding stage. The density contours obtained from injection moulding simulation are regarded as the initial conditions of sintering process.

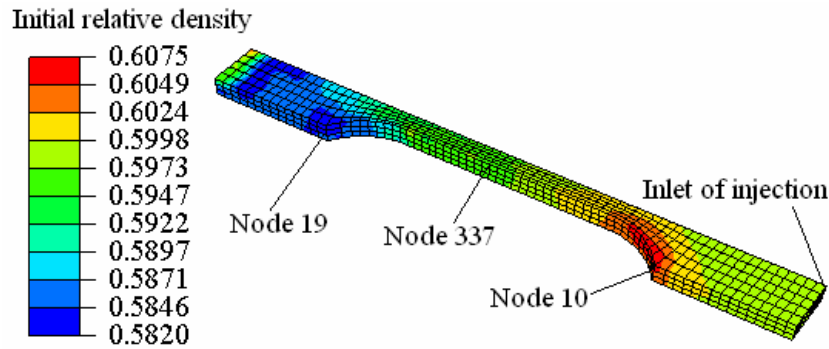


Figure 6.12: The initial relative density of tensile test specimen in 316L stainless steel powders, obtained from the bi-phasic injection simulation in 3D.

In this study, the initial density contours in the green parts after injection moulding are obtained by a bi-phasic approach and imported into the sintering models by interpolation, as shown in Figure 6.12.

Due to the segregations between the powder phase and binder one in the injection process, contours of the relative density are inhomogeneous. It will induce the uneven shrinkages in the sintering process. Three nodes in the FEM model with different initial relative density are chosen to trace the density variations during the sintering process, their positions are shown in Figure 6.12. The variation of relative densities at these three nodes, obtained by sintering simulation, is shown in Figure 6.13. The final shrinkages of the sintered body in three orthogonal directions are presented in Figure 6.14. It can be observed that the sintering process makes the final density of the sintered bodies almost uniform, while inhomogeneity of the initial density affects mainly uneven shrinkage of the sintered body.

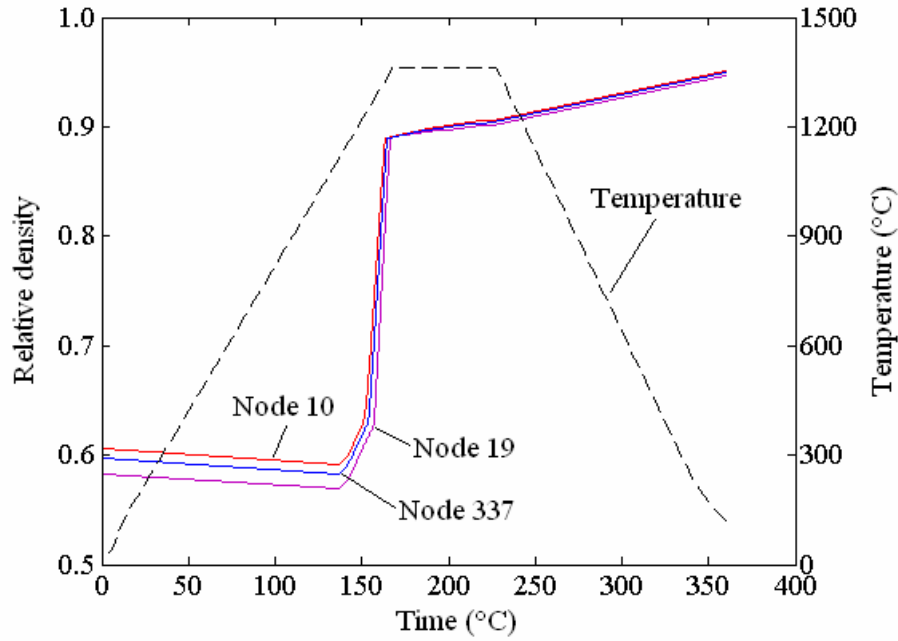
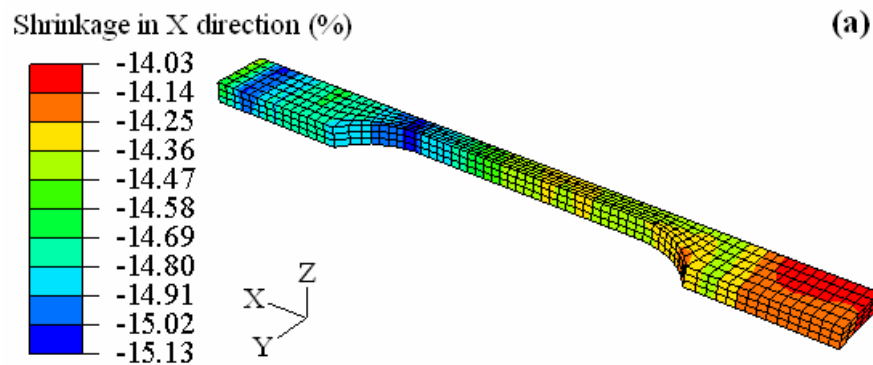


Figure 6.13: The evolution of relative density in sintering process at three selected nodes in the FEM model of tensile test specimen.

Table 6.1: Changes of the relative density due to sintering at three nodes in FEM model of the tensile test specimen.

Node number	Initial relative density	Final relative density
10	0.606	0.950
19	0.583	0.946
337	0.598	0.949

The uneven shrinkages in sintering due to inhomogeneity of the green parts are shown in Figure 6.14.



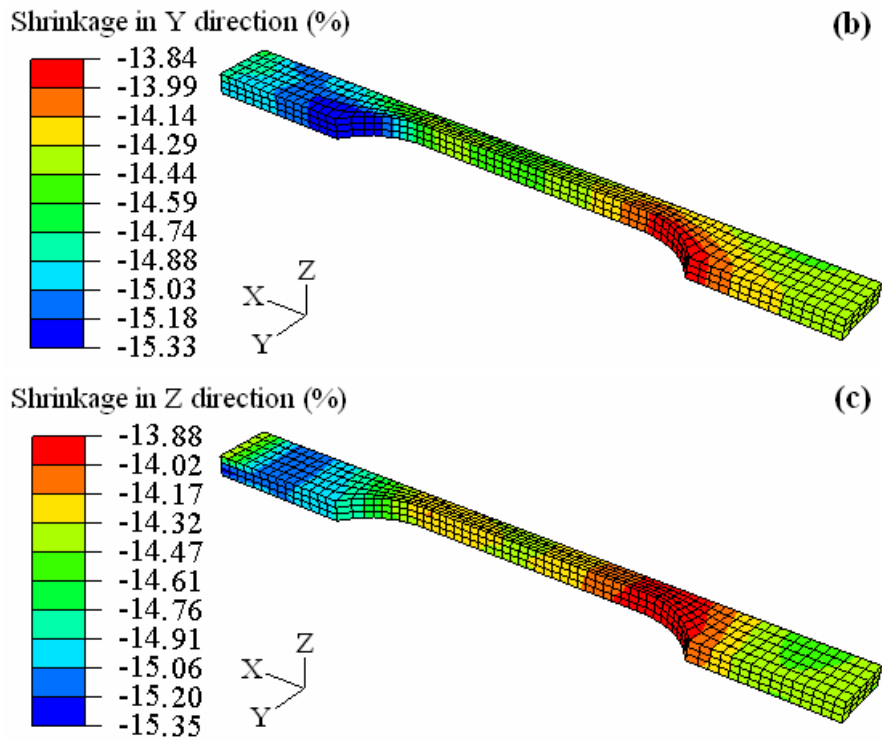


Figure 6.14: Final shrinkages of sintered tensile test specimen in three orthogonal directions indicating the effect of inhomogeneous green density and gravity on the shrinkage.

It can be observed that the minimum shrinkage in the width direction is -13.84%. At the same position the initial density takes the highest value 0.6075. Compared to the simulation with homogeneous green density conditions as shown in Figure 6.11, in which -14.45% of the mean shrinkage is obtained in width direction, 1.25% of the variation in green density distribution induces 4.22% variation in the final shrinkage.

6.2.2.3 Effects of Friction on Shrinkage

The experimental results show that the friction has the important effect on the final shrinkage of the sintered parts. The viscoplastic constitutive law for the sintering body is implemented in Abaqus[®] software through the user subroutine UMAT. For the free sintering, the Coulomb's frictional law is used in the simulation [OLE 02 b]. The experiments to determine the frictional coefficient have not been carried out yet. However, several values from 0.1 to 0.5 have been chosen as the frictional coefficient in the numerical simulations. The simulation with the frictional

coefficient equal to 0.5 is closer to experimental results. The simulations are conducted for homogeneous and inhomogeneous green density conditions respectively. The calculated shrinkages in three orthogonal directions are shown in Figure 6.15 and Figure 6.16.

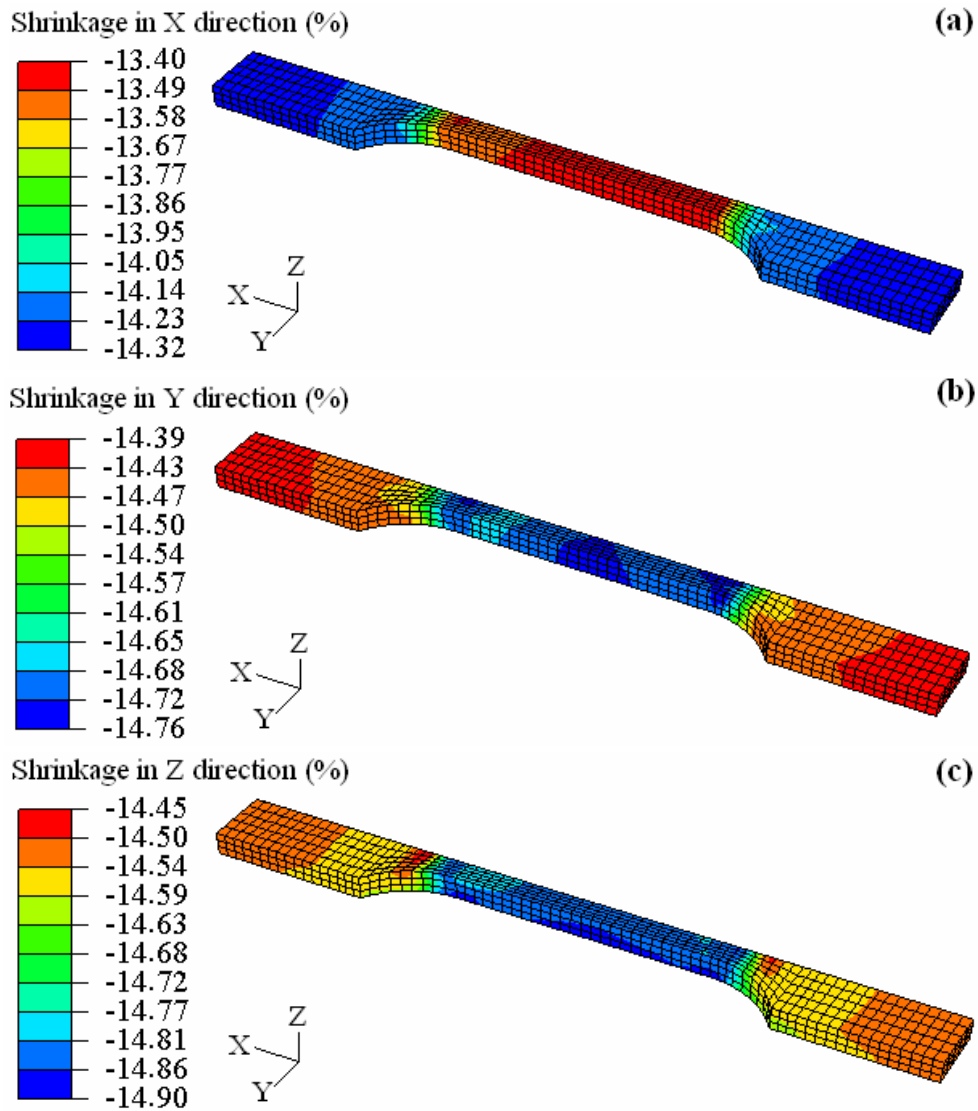


Figure 6.15: Final shrinkages of sintered tensile test specimen in three orthogonal directions with the effects of friction, homogeneous green density and gravity.

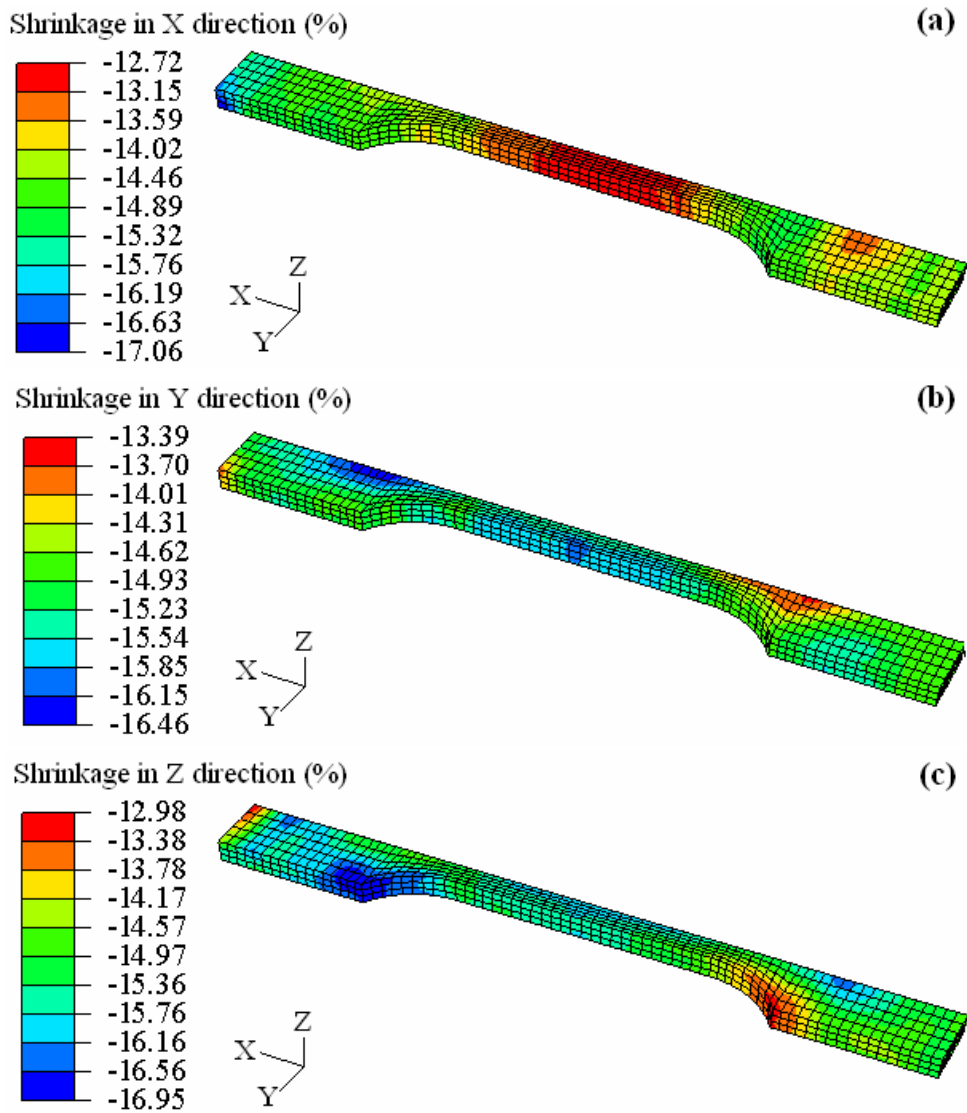


Figure 6.16: Final shrinkages of sintered tensile test specimen in three orthogonal directions with the effects of friction, inhomogeneous green density and gravity.

In Figure 6.16, the dimensions obtained from FE simulations of sintered parts are compared with the experimental ones, as shown in Table 6.2.

Table 6.2: Comparison in final dimensions of the sintered tensile test specimens between the experimental results and numerical simulations.

	Experimental (mm)	Numerical (mm)	Errors (%)
Length (Central)	69.05	68.77	0.41%
Width (Central)	4.80	4.56	5.00%
Width (End)	12.99	12.79	1.54%
Thickness (Central)	2.82	2.78	1.42%

Based on the above four simulations, a brief summary on the influences of

different factors on the shrinkage behaviors of sintered body is presented in Table 6.3. It can be observed that the inhomogeneity and friction have the obvious effects on uneven shrinkages of the sintered parts.

Table 6.3: The maximum and minimum shrinkages under the effects of different factors.

	Considered factors			Final shrinkages (%)		
	Gravity	Inhomogeneity	Friction	Max.	Min.	Δ
1	√			-14.57	-14.45	0.12
2	√	√		-15.35	-14.03	1.32
3	√		√	-14.90	-13.40	1.50
4	√	√	√	-16.95	-12.72	4.23

6.3 Sintering Simulations for the Wheel Part

The numerical simulation is also conducted for a more complex part in wheel shape, as shown in Figure 6.17.

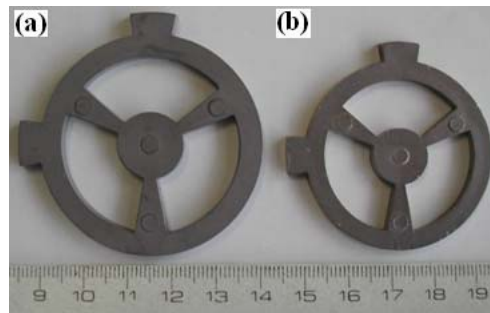


Figure 6.17: Configurations for a wheel part in 316L stainless steel powder: (a) injection moulded, (b) sintered.

6.3.1 Numerical Prediction of the Density and Shrinkages in the Sintered Part

The dimensions of the green part are shown in Figure 6.18: R1:7 mm, R2: 20 mm, R3: 25 mm, R4: 30 mm, and the thickness is 3.3 mm. The part is meshed with C3D8RT element type provided in Abaqus[®]. The fully coupled thermal-stress analysis solver is used with the user subroutine UMAT. The gravity, inhomogeneous green density and friction are considered in the simulation. The frictional coefficient between the part and the alumina support is set to be 0.5. The FE model for simulation is shown in Figure 6.18. The bi-phasic injection simulation has been

carried out previously to obtain the initial relative density distribution of the green part. In the bi-phasic injection simulation, the powder loading in feedstock of 316L stainless steel is set to be 0.62. In interpolated initial relative density contours for sintering simulation of the part are presented in Figure 6.19. The sintering simulation subjects to the temperature cycle as shown in Figure 3.16. The distribution of final relative density issued of sintering simulation is shown in Figure 6.20.

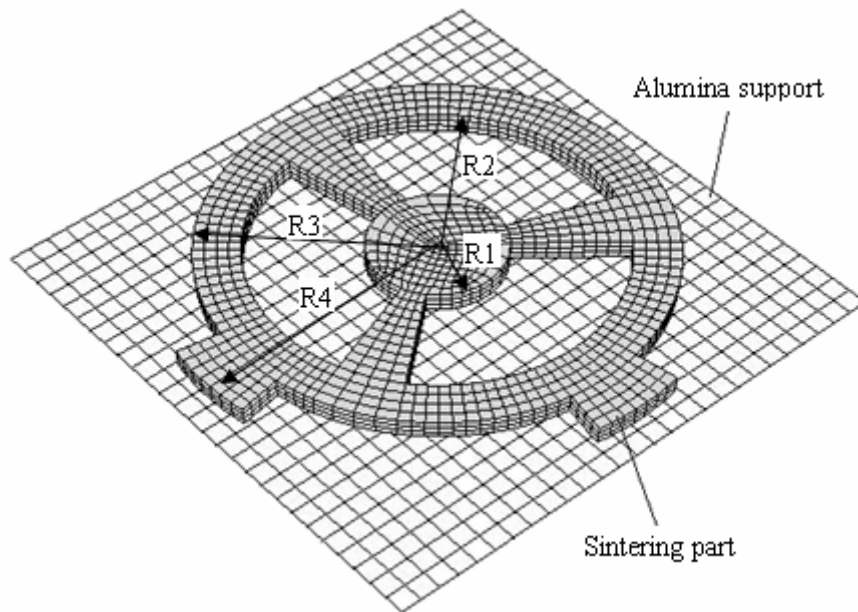


Figure 6.18: The FE model for sintering processes of the 316L stainless steel part in wheel shape.

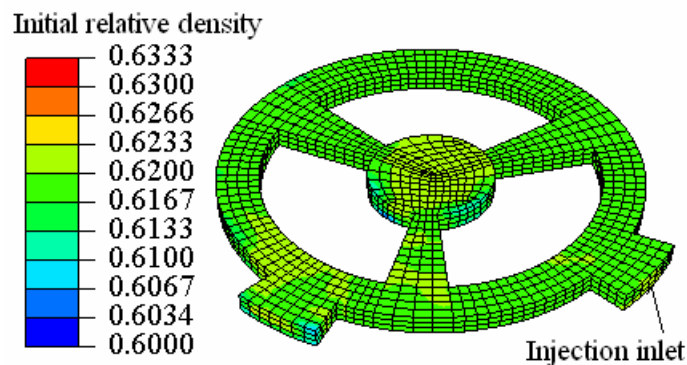


Figure 6.19: Contours of the initial relative density, obtained from bi-phasic injection simulation.

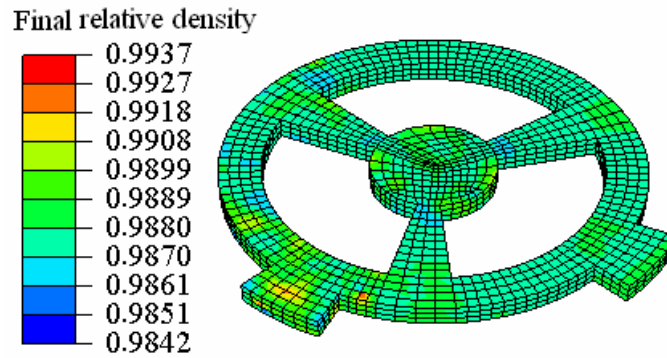
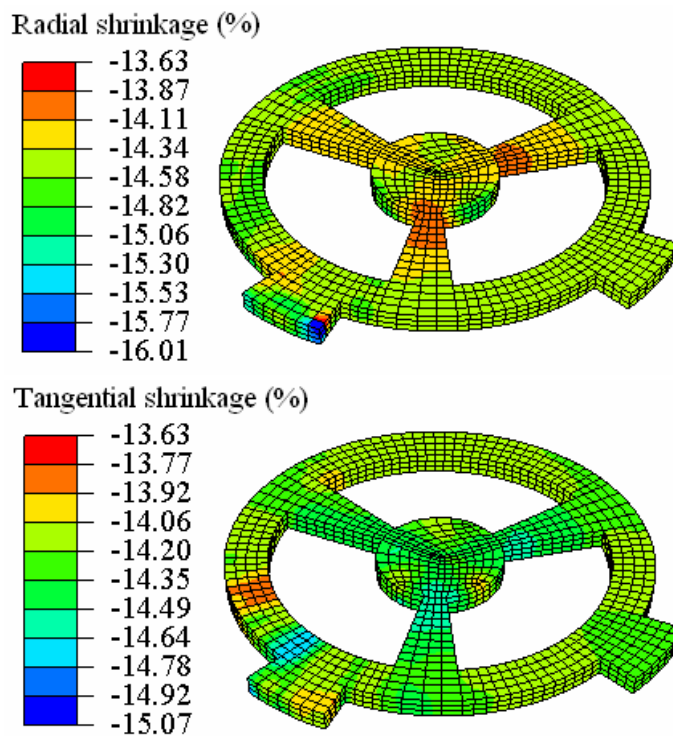


Figure 6.20: Contours of the final relative density in the part sintered to 1360 °C at heating rate 8 °C/min, with 1 h of the last holding stage.

The cylindrical coordinate system is used in the simulation for presentation of the results. Center of the part is set to be the origin of coordinate system. The final shrinkages in radial, tangential and thickness directions obtained by simulation are shown in Figure 6.21. It shows that the powder segregation predicted by bi-phasic injection simulation and friction has the apparent effects on final shrinkages of the sintered components. The uneven shrinkages of the sintered part are proved by the experimental results.



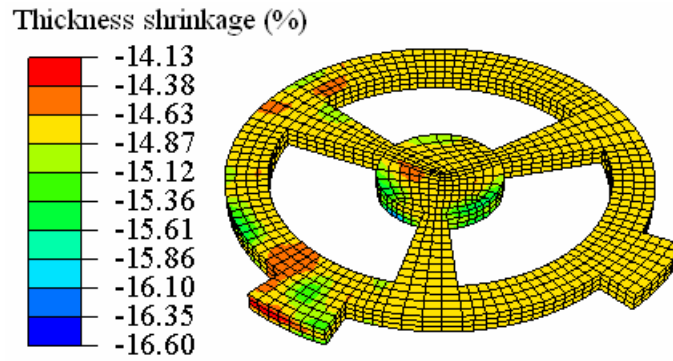


Figure 6.21: Final shrinkages of the sintered part in radial, tangential and thickness directions, resulting from simulation.

6.3.2 Shrinkages Measured in Experiments

In the experiments, the shrinkage values are measured by vernier caliper at 20 chosen points, as shown in Figure 6.22. The measured shrinkages in radial, tangential and thickness directions are presented in Figure 6.23(a). The shrinkage in thickness direction is greater than that in other directions. The uneven shrinkages are more apparent than the numerical simulation results. The corresponding values obtained from the FE simulation are shown in Figure 6.23(b).

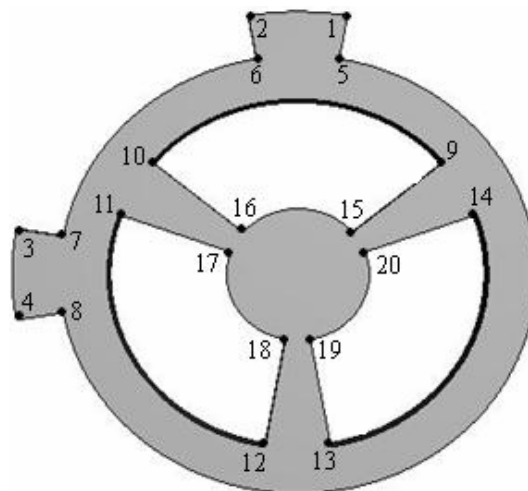


Figure 6.22: Positions of 20 points chosen to measure the shrinkages of the sintered part.

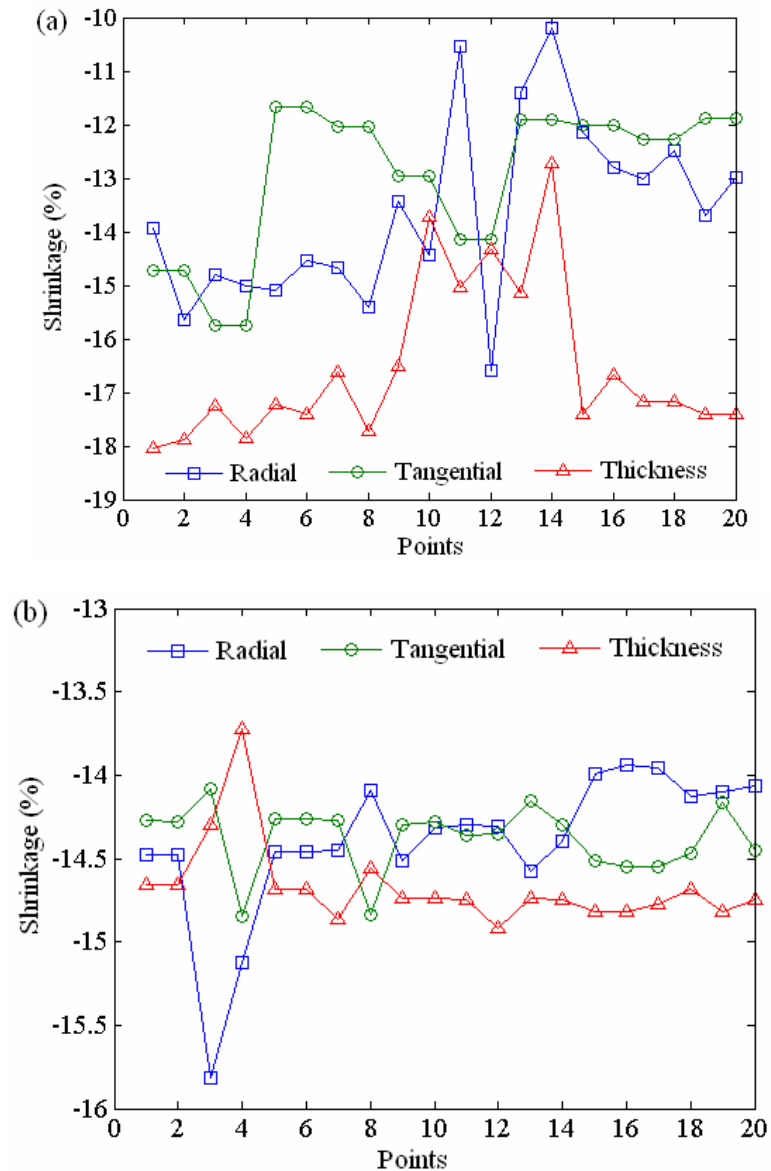


Figure 6.23: Shrinkages of the sintered part in three different directions: (a) measured by vernier caliper at 20 chosen points, (b) obtained from FE simulation.

It can be observed that the inhomogeneous shrinkages of the sintered parts issued from experiments are more evident than the numerical ones. This difference can be induced by many factors. For the more accurate results, the sintering experiments should be carried out for more parts and the more accurate measuring method should be employed. On the other hand, the more accurate bi-phasic injection simulation results should be obtained. The friction coefficient should also be determined more properly for the FE simulations.

6.4 Sintering Simulations for Hip Implant Part

The research on manufacturing the hip implants by PIM had been conducted in LMARC lab. It involves the use of the materials as 316L stainless steel, titanium and alumina [LIK 06]. The simplified prototype of hip implant used in the research is shown in Figure 6.24.

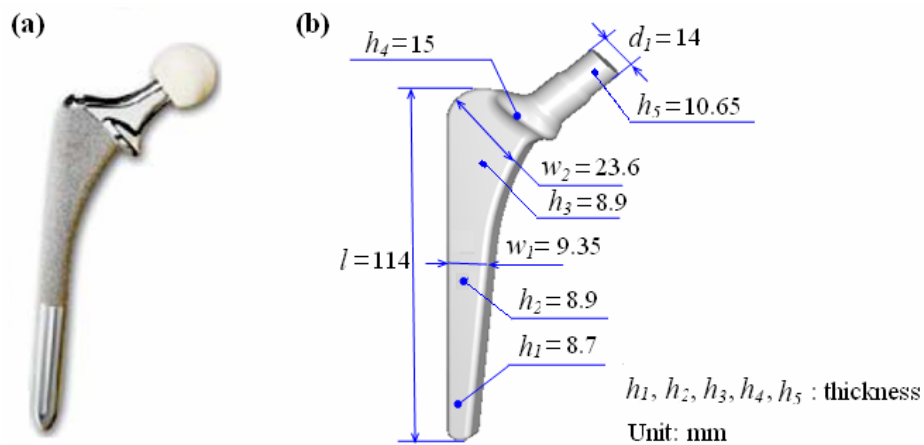


Figure 6.24: Shapes of the hip implants: (a) medical product, (b) prototype in research after injection moulding.

Due to the complex geometry of the model, the tetrahedral elements are used to mesh the part, as shown in Figure 6.25. The FEM model includes totally 2343 nodes and 10250 elements. The hip implant is supported by the alumina plate. In this simulation, gravity is considered, but the friction is ignored.

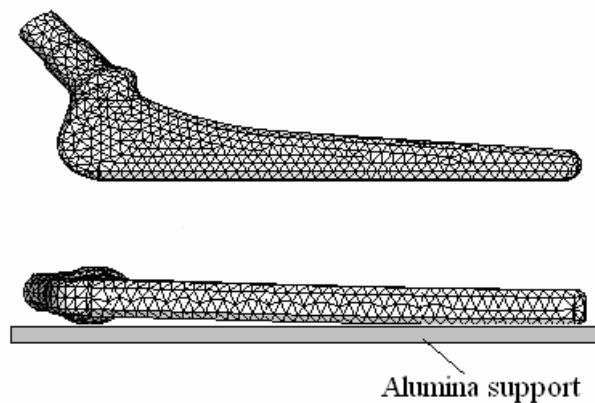


Figure 6.25: FE model of the hip implant component.

The numerical simulation for the sintering process of the hip implant in alumina powder is presented. The employed thermal cycle consists in heating to 1550 °C at 10 °C/min and then holding for 2h. As discussed in Chapter 4, temperature gradient in the sintered body can be ignored if the body is in small dimensions, and the heating rate is controlled to be a moderate value. For the hip implant, the dimensions are larger than the common PIM components. In addition, the thermal conductivity of alumina ceramics is less than the metals. The heat transfer analysis is realized to evaluate the temperature gradients in the sintering body, and then the viscous analysis is used to simulate the sintering process. This sequentially coupled thermal-stress analysis is cost-effective in computational time compared to the fully coupled thermal-stress analysis.

6.4.1 Heat Transfer Analysis for Hip Implant

In the heat transfer analysis, the thermal conductivity is chosen to be 39 W/(m·°C), and the specific heat capacity is equal to 775 J/(kg·°C) [GER 96]. The thermal boundary conditions on the surfaces of hip implant are set to be the temperature that changes with the thermal cycle employed in sintering. The temperature gradients at an instant in the heating stage are shown in Figure 6.26.

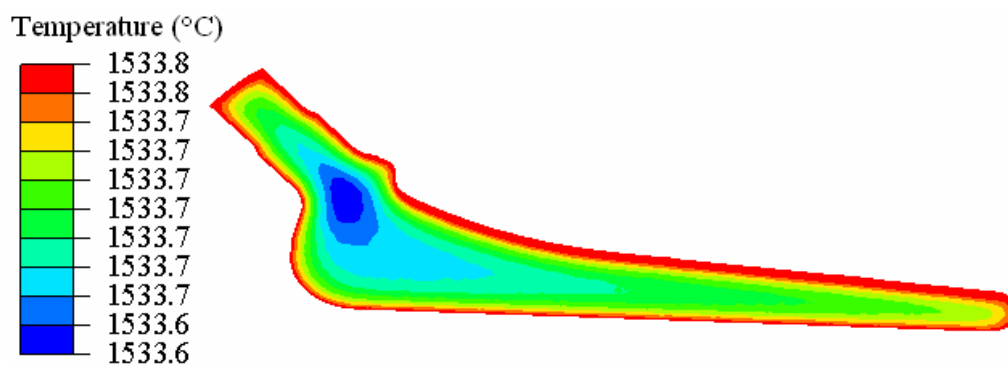


Figure 6.26: Temperature field for the hip implant in alumina.

It can be observed that the difference in temperature is less than 1 °C in the hip implant. In fact, the real temperature gradient in the part is greater than the one presented in Figure 6.26. In the present heat transfer simulation, the thermal

parameters of the dense alumina are used. It overestimates the heat transfer ability of porous alumina materials. On the other hand, the thermal condition represents also the simplification compared to the real conditions in the sintering furnace.

6.4.2 Viscous Analysis for Sintering of Hip Implant

The viscous analysis in Abaqus[®] is used for simulating the sintering process of the hip implant by user subroutine CREEP. The viscous analysis is made based on the temperature fields obtained by the preceding thermal analysis in same time step. The parameters identified by the methods provided in Chapter 5 are shown in Table 6.4.

Table 6.4: Identified parameters in sintering model of alumina for the thermal cycle of hip implant in sintering.

	A (Pa·s/(m ³ ·K))	B (K)	M (K·m ⁴)	N (K)
Heating at 10 °C/min	6.849×10^{11}	4.608×10^4	1.621×10^{-15}	3.154×10^4
Holding at 1550 °C	9.935×10^{12}	4.473×10^4	7.804×10^{-14}	3.809×10^4

The contours of final density issued of the numerical simulations are shown in Figure 6.27. Due to the gravity and the boundary conditions used in simulation, it results in an uneven shrinkage during sintering process, as presented in Figure 6.28. For the purpose to get more accurate results in simulation, the friction between the component and the support should be taken into account.

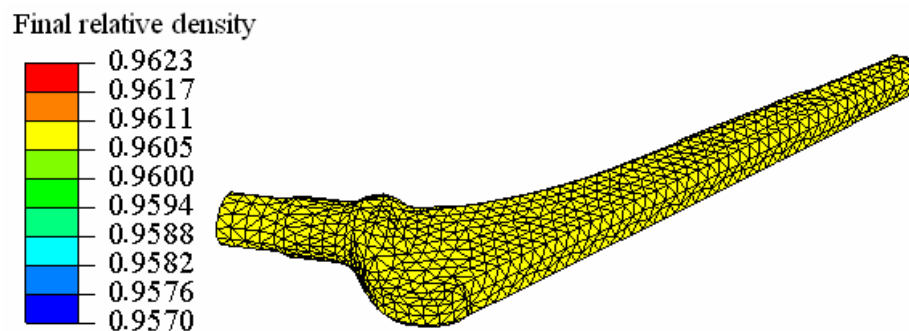


Figure 6.27: Contours of the final relative density in the sintered hip implant.

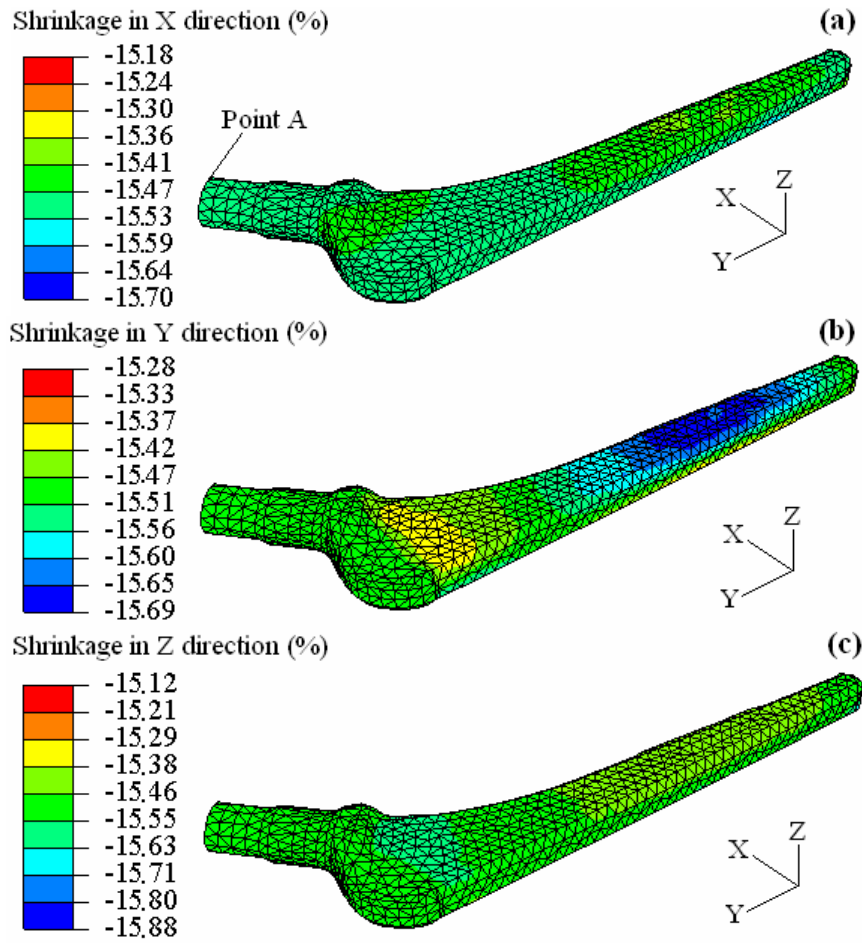


Figure 6.28: Shrinkage contours of the sintered hip implant in three orthogonal directions.

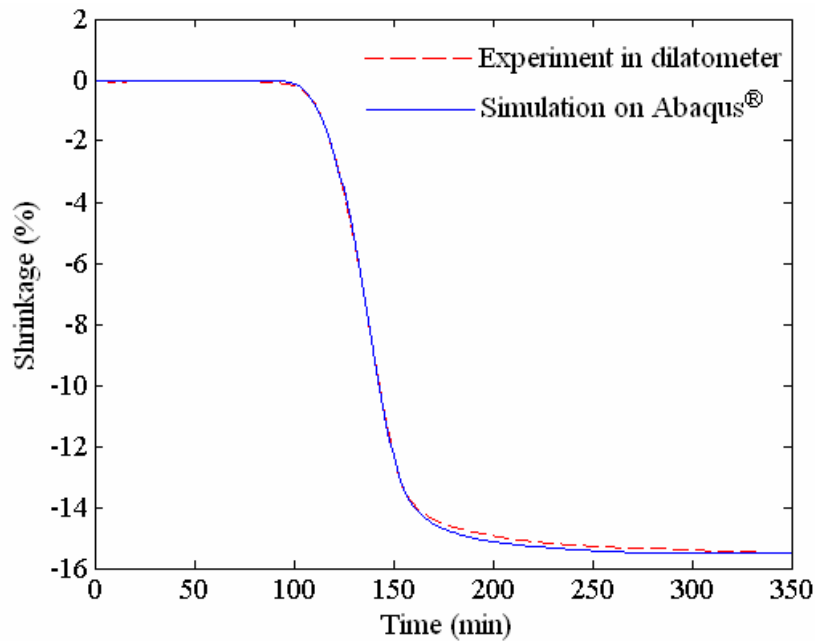


Figure 6.29: Comparison of shrinkage variations between the simulation results from Abaqus® and the sintering experimental ones in dilatometer.

To verify the simulation procedure, the evolution of the shrinkage during sintering is compared with the experimental data obtained by the dilatometer tests. The position at point A as shown in Figure 6.28(a) undergoes the nearly free sintering due to the little influence of gravity and friction. Evolution of the shrinkage at this point is shown in Figure 6.29. It is in good agreement with the experimental one during the whole sintering process. It proves the validity of the viscous analysis solver and user subroutine, as well as the identified parameters for the sintering simulation.

The dimensional change of the hip implant in alumina is shown in Figure 6.30.

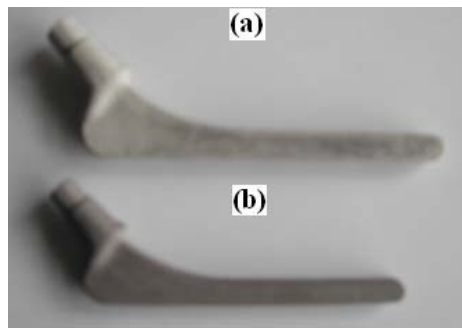


Figure 6.30: Dimensional change of the hip implants in alumina: (a) injection moulded, (b) sintered.

The shrinkage values measured by vernier caliper are presented in Table 6.5 [LIK 06]. The experimental results have more serious uneven shrinkage than the simulation results. In the future, it is expected to use the proper experimental methods, such as coordinate measuring machine (CMM), to measure the uneven shrinkages of the sintered parts in complex shape. These experimental results can be employed to verify the simulation results. Simultaneously, the more real contact conditions between the hip implant and the support should be considered in the simulation.

Table 6.5: Shrinkage values of alumina hip implant after sintering obtained from experiment [LIK 06].

Dimensions	l	d_1	h_1	h_2	h_3	h_4	h_5	w_1	w_2
Shrinkage (%)	13.2	15.9	16.1	16.9	18	14	15.5	15.9	12.3

6.5 Simulations for Beam-bending Tests in Sintering

The purpose of numerical simulation is to predict both the shrinkage of sintering bodies and its distortion. There are many factors that may contribute to the distortion, such as the low strength state of the sintering part in high temperature, external forces, stress gradients and the support conditions. The beam-bending tests show a good example of the distortion in sintering induced by gravity and support condition, as shown in Figure 3.20. The numerical simulations for the beam-bending tests are conducted to justify the ability of the sintering model and identified parameters in prediction of the distortions. The work has been realized on Abaqus[®] with the user subroutine UMAT. The FEM model is presented in Figure 6.31 [SON 06 c].

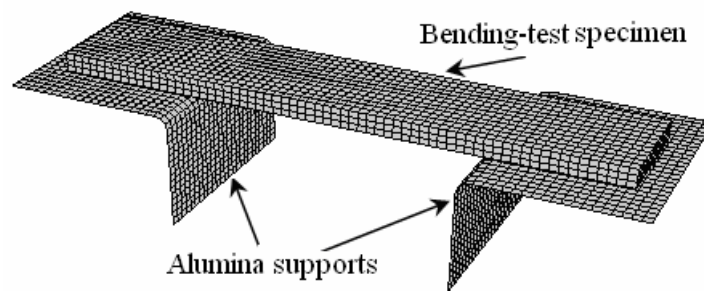
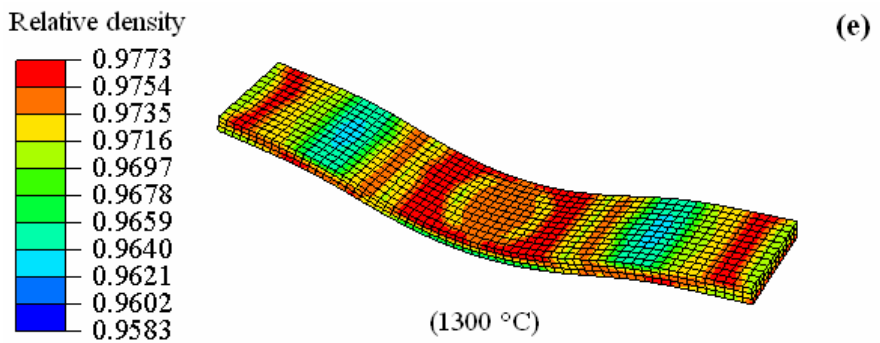
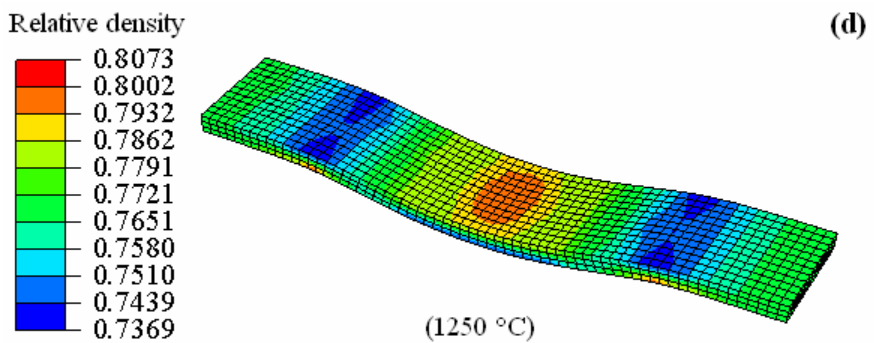
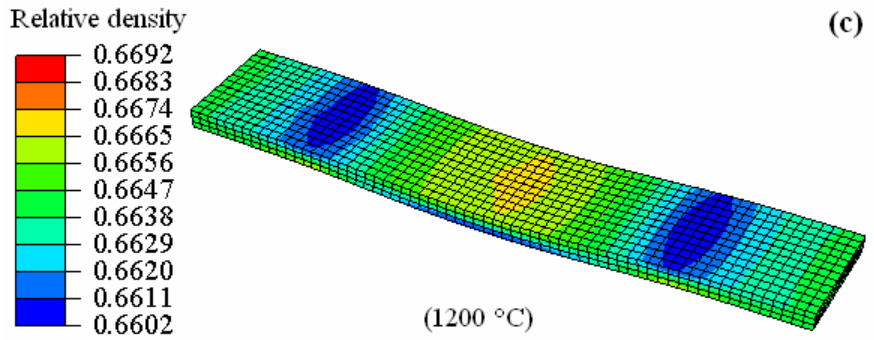
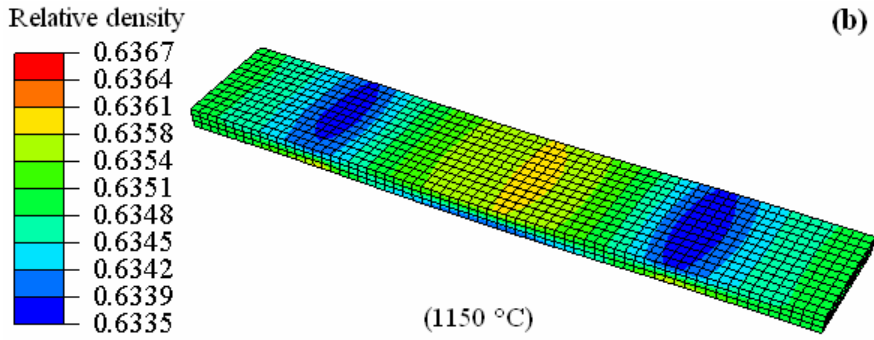
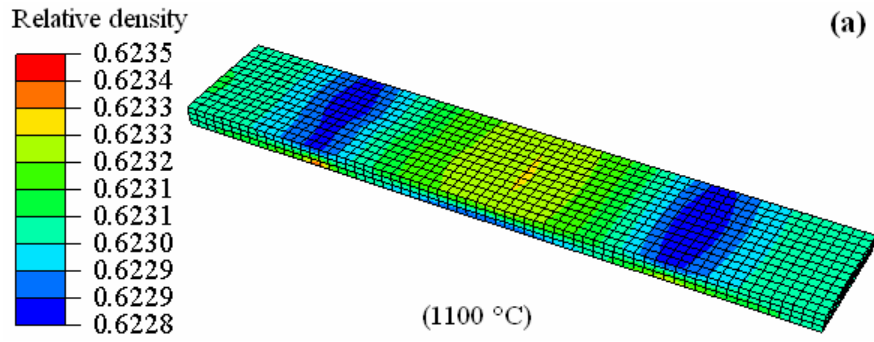


Figure 6.31: FE model for beam-bending tests under gravity in sintering furnace.

The thermal cycle used in simulation is heating to different temperatures at a rate equal 10 °C/min and then cooling to room temperature rapidly. The corresponding experiments are carried out with the same heating cycles. The simulation is made with a homogeneous green density equal 0.62, and the frictional coefficient is 0.5 for the support conditions. The density evolution and the distortion of the bending test specimens in the sintering are shown in Figure 6.31.



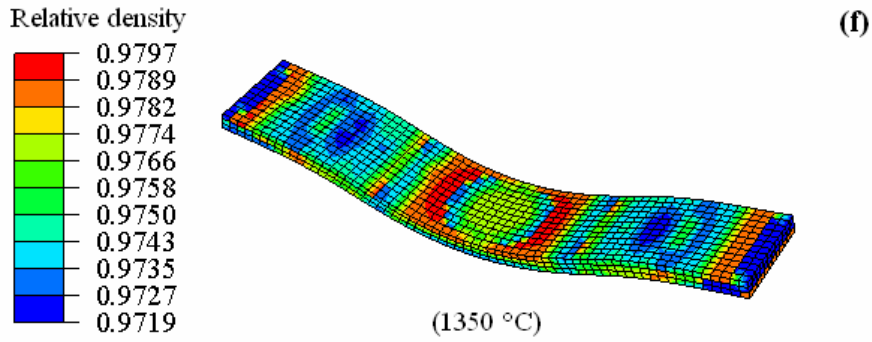
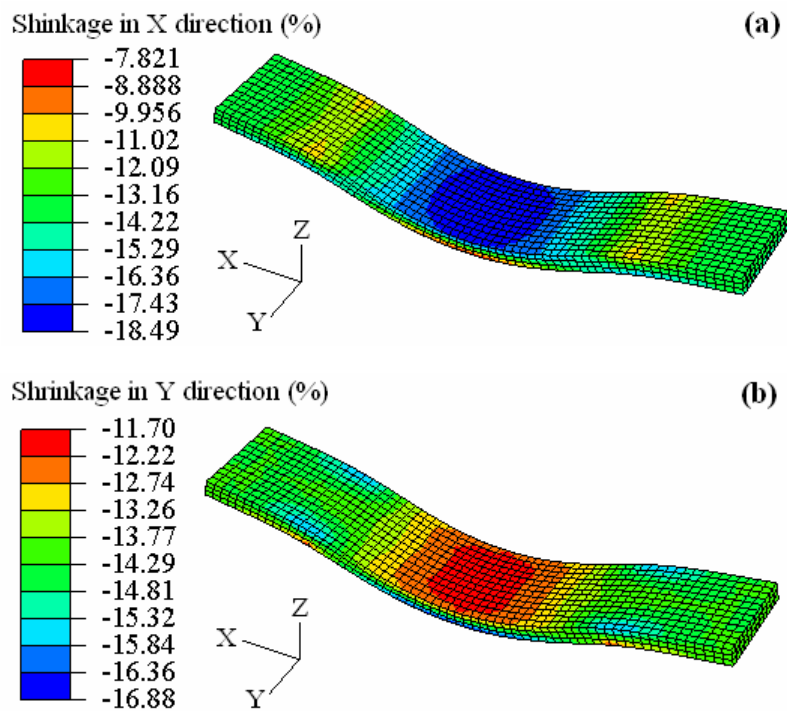


Figure 6.32: Density evolution and shape distortions of the bending test specimens in the sintering processes.

It can be observed that the tensile stress is unfavorable to densification, while the compression stress is represents the favorable effect. In the final state as show in Figure 6.32 (f), it is densified everywhere in the specimen to the relative density from 0.9719 to 0.9797, but important variation of the shrinkage from -7.82% to -18.49% is accompanied by the great distortions, as shown in Figure 6.33.



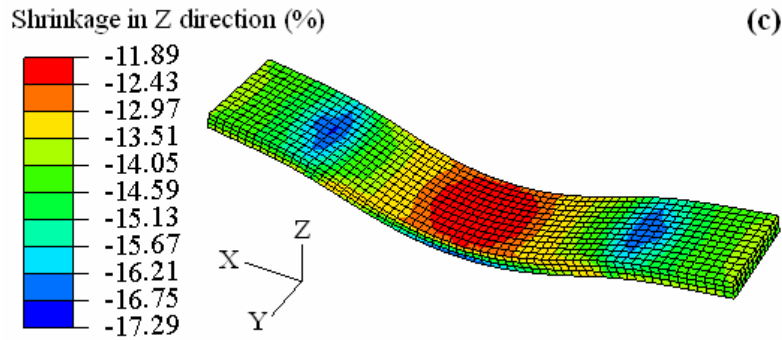


Figure 6.33: Variation of the final shrinkages in sintered bending test specimens.

The deflections at middle positions of the bending test specimens, obtained from the numerical simulations, are compared with the experimental ones, as shown in Figure 6.34.

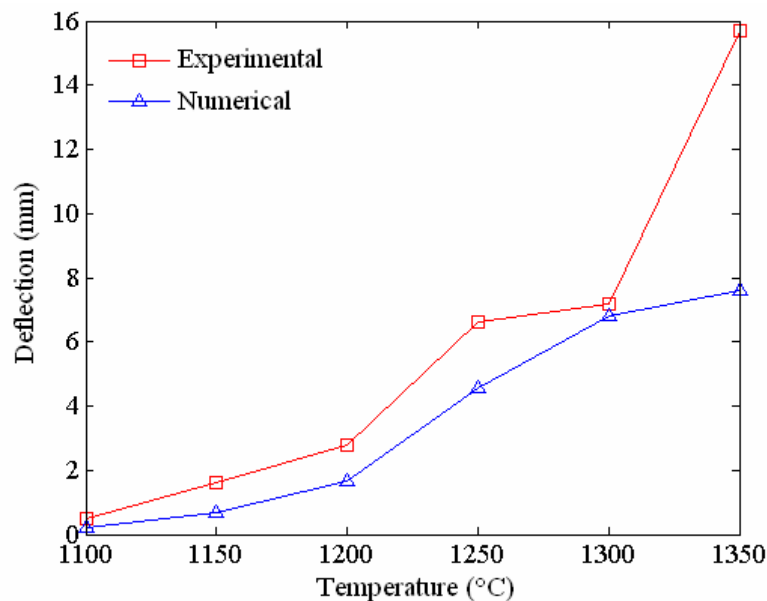


Figure 6.34: Comparison of the deflections in simulations and experiments at middle position of the bending test specimens when it is heated to different temperatures in sintering.

The deflections begin at temperatures about 1100 °C. The numerical simulations underestimate the distortions of the sintering bodies. It may be due to the fact that shear viscosity modulus is not accounted accurately. The identifications have not been made to determine this parameter. On the other hand, measurement of the deflections is not very accurate in the experiments. The deflections are measured by

vernier caliper after cooling to room temperatures. As shown in Figure 3.20, the material flow occurs when the sintering temperature is higher than 1300 °C. It is difficult to measure the deflection under this condition.

6.6 Evaluation of the Mechanical Strength

Based on the predicted density contours in the sintering bodies, the post- and *in-situ* sintering strength can be evaluated by employing the models presented in Chapter 4.

6.6.1 Evaluation of the Post-sintering Strength

For the PIM parts in 316L stainless steel, the apparent shrinkage occurs from a temperature equal 1080 °C, as shown in Figure 3.16. The empirical expression proposed by Skorohod presented in Table 4.1 is employed to evaluate the neck size ratio. The ultimate tensile strength and yield strength are calculated by the Equation (4.46) to Equation (4.48). The yield stress σ_y is chosen equal to 261 MPa and the ultimate tensile strength σ_{UTS} is chosen to be 580 MPa for the wrought materials corresponding to 316L stainless steel [OHA 04]. The constant α_s in Equation (4.48) is set to be 1.8. The predicted strength in the parts sintered to different temperatures are compared with the tensile tests results, as shown in Figure 6.35. The curves obtained by simulations have the same tendency as the experimental data, but it represents some deviations. This is due to the fact that the models for strength prediction are based on a series of the empirical equations. On the other hand, the tensile test experiments are only made with only one specimen for each peak sintering temperature. The measured strength in the sintered component can not be averaged by a group of the specimens. The measured values can be influenced by many random factors in the porosity, defects, and measurement techniques [SCH 97].

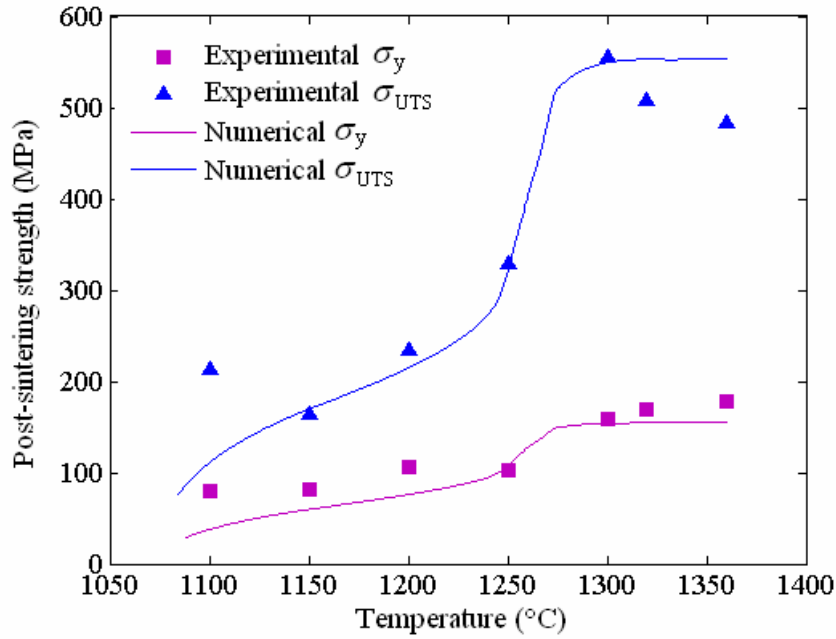


Figure 6.35: Numerical prediction for the yield strength and ultimate tensile strength of the sintered parts in 316L stainless steel and the experimental data for comparisons.

6.6.2 Evaluation of the *In-situ* Sintering Strength

Based on the data presented in Figure 6.35, the *in-situ* sintering strength is obtained by involving the thermal softening effects, as in the Equation (4.50) and (4.51). The transverse rupture strength σ_{TRS} issued of three point bending tests is often used for *in-situ* sintering strength. Generally it represents 1.6-2.1 times of the tensile strength [GER 03 b]. Here the mean value 1.85 is chosen. The calculated *in-situ* strength versus sintering temperature is shown in Figure 6.36.

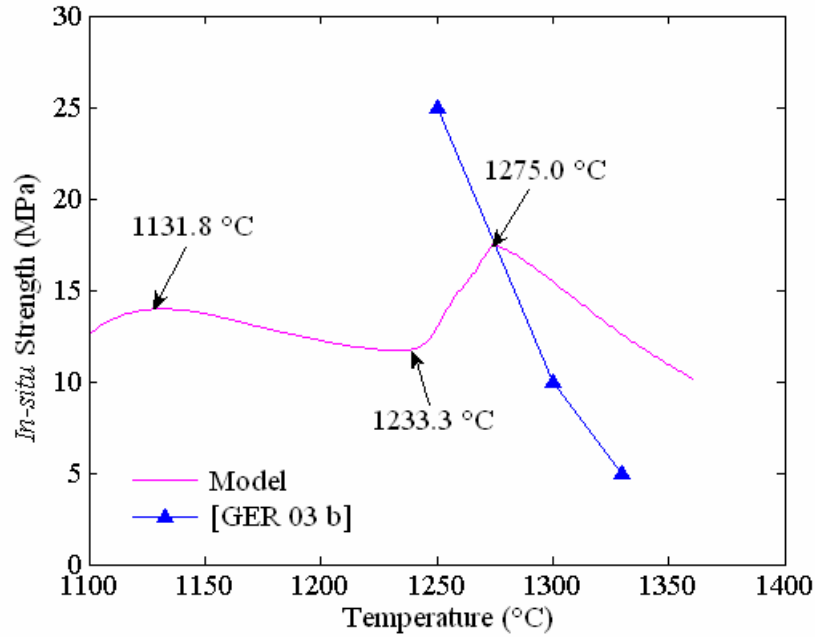


Figure 6.36: Numerical prediction for the *in-situ* sintering strength of 316L stainless steel parts.

The *in-situ* strength increases firstly until the temperature reaches 1131.8 °C. It is due to the initial neck growth that reduces greatly the strength concentration factor, as shown in Figure 4.7. After this stage, the thermal softening effect on the *in-situ* strength becomes more than the neck growth. The strength decreases rapidly until the temperature reaches to 1233.3 °C. The subsequent increase in strength is induced by the fast densification in the intermediate stage of sintering. In the later sintering stage with temperature higher than 1275°C, increase of the density becomes very slow. Continuous elevation of the temperature reduces significantly the strength by the thermal softening effect.

The estimated *in-situ* sintering strengths of PIM parts in 316L stainless steel powders with particle size of 10 μm are presented in [GER 03 b]. At 1250 °C, the strength is about 25 MPa after just 1% of the shrinkage. Above 1300 °C, the strength is below 10 MPa, allowing 2% of the shrinkage. At 1330 °C, the strength is down to 5 MPa. The predicted *in-situ* strength in Figure 6.36 is compared with the estimated values in [GER 03 b]. It varies in the small range of 5-25 MPa. The difference may be induced by the effect of different material characters, different chosen parameters in the strength prediction model, as well as the estimation method used in [GER 03

b]. The magnitude of the *in-situ* strength is in the same order of the sintering stress. So the sintering parts in 316L stainless steel powder are prone to distortion at the high temperature as observed in the experiments.

When the temperature is lower than 1050 °C in the sintering or pre-sintering of PIM parts in 316L stainless steel, there is no apparent shrinkage. The neck growth is governed by surface diffusion that can also improve the strength of the sintering parts. Equation (4.46) is proposed to describe this process. However, the parameters of surface diffusion in Equation (4.46) are not easy to be determined. On the other hand, it is very sensitive to the particle size. The calculated neck size and strength represent the large difference with our experimental data of flaming tensile tests. The more proper model should be developed to evaluate the neck size and strength controlled by surface diffusion.

6.7 Summary

With the sintering model and identified parameters presented in Chapters 4 and 5, the densification behaviors can be predicted well for the free sintering of 1D part in homogeneous green density. In fact, the densification behaviors of the PIM components are influenced by the factors such as gravity, inhomogeneous green density, friction between the parts and the supports, as well as the shape complexity that can induce the stress concentration. In Chapter 6, the numerical simulations for 3D parts with complex shapes are realized. Finite element analysis is proven powerful to handle the sintering problem with complex geometries and boundary conditions. The FE simulations are carried out using the in-house software and the commercial FEM software respectively.

The code built on Matlab[®] is used to implement the sintering model in FEM simulation. The governing equations are formulated in weak form by Galerkin method, with the implantation of viscoplastic constitutive model. The displacements and relative density are chosen as the nodal variables. The coupled equations of mass and momentum conservations are solved simultaneously. Being an in-house

software, it has the advantages to be modified easily. However, the FE equations are solved by the functions provided in Matlab[®]. The explicit Runge-Kutta method is employed. The computational efficiency should be improved, especially for the components in complex shapes. On the other hand, the friction effects should be realized in the programs. The numerical simulations are also realized by the commercial FE software Abaqus[®], a powerful tool for nonlinear FEM analysis. The involved works are concentrated on the implementation of the viscoplastic constitutive law in the user subroutines CREEP or UMAT. With this method, the simulations can deal with complex shapes, inhomogeneous green density, frictions, as well as large deformation problems such as in beam-bending tests.

The simulations for sintering process of the tensile test specimens, wheel shaped part and the hip implants indicate that the uneven shrinkages are due to various factors. The friction between the sintering parts and the supports is the most important factor that influences the shrinkage. The second one is the inhomogeneous distributions of green density due to segregations occurring in the injection process. The effect of gravity on shrinkage depends on the dimensions of the parts and the support conditions in sintering. The presented simulation example of beam bending test shows that distortion of the sintering bodies has the important influence on the densification. It can induce the values of uneven shrinkages in wide ranges. However, the predicted deflections of the beam bending tests are small than the experimental ones. It means that the proper model of shear viscosity modulus should be determined by the suitable way, and more accurate beam bending tests are expected to be conducted.

The predicted post-sintering strengths of the final parts, including the yield stress and tensile strength, represent the same tendency as the experimental ones. However, there exist still some deviations that may be induced by many factors in the numerical models and the experimental works. Prediction of the *in-situ* strength in the late sintering stage, based on the evolution of relative density, is presented and compared with the data incoming from various references. It proves that the sintering parts in 316L stainless steel is in the low strength state at high temperature

during the sintering. Its magnitude is in the same order of the sintering stress. So it is prone to distortions as observed in experiments. The evaluations of the strength in pre-sintering or the early sintering stage have not been realized with the reasonable results. More proper model should be developed for describing the strength increasing governed by surface diffusion.

Chapter 7 Conclusions and Perspectives

The present research has been realized as a part of the cooperative European COST 526 APOMAT F2 project on optimization of the mould design and process parameters for powder injection moulding [AYA 05], [GEL 05]. It focuses on the experimental investigations and numerical simulations of the sintering processes for metallic or ceramic powders. The most important developments and results, as well as the suggested future work are summarized below.

7.1 Conclusions

7.1.1 Improvements from Sintering Experiments

The experiments on the sintering processes of powder injection moulded components in 316L stainless steel or alumina powders are realized. The observed phenomena can be concluded as:

- The sintering parts in 316L stainless steel are prone to distortions at high temperatures above 1250 °C. The pre-sintering at 800 °C or 900 °C for 1h can improve the strength of the green parts. It is favorable to reduce the deformations in sintering. However, the specimens in alumina powder show the good ability to resist to distortion in sintering even though at the rapid heating rate 20 °C/min. It is not necessary to make the pre-sintering for alumina parts.
- There exist thresholds in temperature for different sintering parts at which the apparent densification begins. The sintering experiments in dilatometer show that the sintering parts in 316L stainless steel have the threshold temperatures in the range of 1050 °C-1080 °C. The threshold temperatures for alumina specimens locate in the range from 800 °C to 900 °C. The densification begins at the relatively low temperatures for alumina powders due to its smaller particle sizes. The fine powders are favorable to

densification.

- The densifications occur mainly in the heating period and are very sensitive to the heating rates. The rapid sintering is favorable to densification. The entire sintering process can be divided into three stages, the initial, intermediate and final one. The densification is accomplished mainly in the intermediate stage. Most of the densification for 316L stainless steel parts is realized very rapidly in the narrow temperature range of 1250 °C-1300 °C. The rapid densification of alumina is conducted in the wide temperature range from 1100 °C to 1600 °C. However, the densification rate for 316L stainless steel parts is higher than the one in alumina parts. At the heating rate 10 °C/min, the maximum shrinkage rate of 316L stainless steel powders is -3.3 %/min, while the one of alumina powder is -0.4 %/min.
- The tensile tests show that the strength and elongation of the sintered 316L stainless steel parts increase when the peak sintering temperature increases. The important increase of the tensile strength locates in the range of peak temperature between 1250 °C and 1300 °C, while the important increase of elongation occurs in the range of peak temperature between 1300°C and 1360 °C. The over sintering at the temperature higher than 1380 °C decreases the mechanical properties of the sintered parts.
- For 316L stainless steel, the rapid grain growth is observed in the final stage of sintering. When the sintering temperature is higher than 1300 °C, the grain size increases rapidly. The microstructural evolutions of alumina in sintering show that the process parameters such as temperature, heating rate and holding time have important effects on the final grain size.

7.1.2 Improvements from Modeling and Simulation for Sintering Process

Justified by the experimental investigations, the macroscopic models based on thermal elasto-viscoplastic constitutive law are used to predict the dimensional changes and density evolutions in sintering processes. The proper methods are developed for identification of the material parameters in the models under

prescribed processing conditions. The numerical simulations are realized by finite element method. The conclusions drawn from the numerical work can be summarized as following:

- The porous sintering parts can be regarded as the compressible continuum mediums. The macroscopic model for sintering based on continuum mechanics is proven effective to predict the shrinkages, distortions, as well as the density evolutions of the sintering parts. The most important aspects in application of the models are to determine the exact constitutive law. The thermal, elastic and viscoplastic strains are observed in the experiments for the sintering parts. For the pressureless sintering, the elastic strain is so small that it can be neglected. The thermal strains are dependent of the sintered materials. The thermal strain for 316L stainless steel in sintering is obvious, while the one for alumina is very small. The viscoplastic strain or creep strain includes shape deformation and volume change, which represents the distortion and shrinkage of the sintering parts. In order to obtain the accurate simulation results, the proper parameters in the viscoplastic constitutive law should be identified.
- The gravitational beam-bending tests are employed to determine the uniaxial viscosity of the sintering parts in 316L stainless steel. The identified parameters for viscosity modulus in the model are obtained by an optimization procedure. With the identified viscosity modulus, the *in-situ* shrinkage curves obtained by the sintering experiments in dilatometer are used to determine the sintering stress. Identifications of the parameters in the model are carried out for three stages respectively in the same sintering process, due to the unmixable behaviors for these three evidently distinguishable stages. The identifications are carried out for different thermal cycles.
- The beam-bending tests have not been implemented for the specimens in alumina. The curves of *in-situ* shrinkage and shrinkage rate are employed to identify the parameters in the sintering model for alumina. With the

identified parameters, the curves of shrinkage rate and shrinkage issued of numerical calculations match well the experimental ones. For the rate dependent constitutive law like the viscoplastic one, the sintering model with identified parameters can be used to predict accurately the stress and dimensional changes of the sintering parts. The initial values for different parameters in optimization are taken from the values in literature. The determined viscosity and sintering stress are in the reasonable orders, compared with the ones in literature. The identifications are conducted for the non-isothermal sintering at different heating rates from 2.5 °C/min to 20 °C/min, for the peak temperatures ranged from 1300 °C to 1600 °C. The calculated results show well that the shrinkages and shrinkage rates are dependent of the parameters in the models. Based on the identified parameters for the typical thermal cycles of non-isothermal sintering with different constant heating rates, the linear interpolations are employed to determine the parameters for the non-isothermal sintering cycle with intermediate values of constant heating rates. The results match well the experimental ones. For the isothermal sintering, the densification behaviors depends not only the holding temperatures, but also the earlier heating processes. In fact, the interpolation can not be used to determine the parameters for the isothermal sintering processes at different holding temperatures.

- The material parameters associated to the sintering models provided in various references can not be employed directly for simulations. The results issued of the simulations with the values incoming from various references represent a significant difference compared to the experimental ones. The presented identification methods based on the experiments can assure accuracy of the simulation results. Between the sintering experiments in loading dilatometer and sintering forging tests, the free sintering in dilatometer is easier to be conducted. It is appropriate for the pressureless sintering of PIM components.

- The numerical simulations for 3D PIM components have been conducted. The results show that the friction between the sintering parts and supports, the inhomogeneous green density distributions due to the segregation in injection moulding step, as well as the gravity have obvious effects on the final shrinkages. The FE simulations can be used to predict uneven shrinkages due to these factors. The results match well the experimental ones. The simulations for gravitational beam-bending tests indicate that the distortions of the sintering parts can induce important uneven shrinkages. The distortions must be controlled in sintering. The predicted deflections in bending tests are less than the measurements in experiments. It means that more accurate shear viscosity modulus should be determined.
- For pressureless sintering, the mechanical dissipation is very small. Then it can be neglected in the thermal-stress analysis to uncouple the analysis into two sequential and unilateral fractional steps. It improves greatly the computational efficiency. The simulation results match well the experimental ones, too.
- Predictions of the post-sintering and *in-situ* sintering strength have been carried out. The porosity, neck size, stress concentration factors, and thermal softening effects are taken into account. The predicted post-sintering strength of 316L stainless steel parts are compared with the results of tensile tests. The same general tendency in change of the strength is observed. However, the predicted strength is not very accurate as the prediction is based on a series of empirical expressions. Evaluation of the *in-situ* strength for the late stage in sintering is conducted. The results are close to the estimated ones in the literature. It shows that the *in-situ* sintering strength of the parts in 316L stainless steel at high temperature over 1300 °C is close to the sintering stress. It makes the sintering parts prone to distortion.

7.1.3 Complete PIM Process Modeling and Simulation

Injection moulding and sintering are the important steps of PIM process. In the

injection moulding step, the powders and binder may separate during the high speed filling process due to the different densities. In LMARC lab, the bi-phasic injection moulding software FEAPIM[®] has been developed to predict this segregation phenomena. In present study, the powder contours of the injection moulded part issued from bi-phasic injection simulation has been accounted in the following sintering simulation. The green inhomogeneity can induce the uneven shrinkage of the sintered parts. The combination of injection simulation and sintering one can make it possible to optimize the PIM process globally, including mould design, injection and sintering process parameters.

7.2 Future Work

The presented model, identification and simulation methods have proven their effectiveness in prediction of the final dimensions and mechanical properties of the sintered components. However, the relative works are far away to be finished. Some of the works in the near future can be suggested as below:

- The general method should be developed to identify the parameters in the sintering model for any thermal cycle. Afterwards, optimization for the process parameters in sintering can be conducted.
- The green density contours of PIM parts are obtained from the bi-phasic injection simulations. More accurate simulation results are desired to be achieved. Simultaneously, more precise experiments should be investigated to justify the computed segregation. Combination of the injection simulation and the sintering simulation is favorable for optimization of the entire PIM process. The sintering experiments in dilatometer for the feedstock with various powder loadings should be carried out in future.
- Because of the importance of an accurate determination of the viscosity modulus or viscous Poisson's ratio in the sintering models, the more accurate experiments of beam-bending tests or sintering in loading dilatometer should be realized.

- In order to perform simulation of the sintering process under real conditions, the parameters such as the friction coefficient, thermal conductivity and heat capacity of the porous materials should be determined.
- Production of the precise components is the main objective of PIM process. Accurate prediction of the shrinkages and distortions is very important for the design of injection moulds and process parameters. The equipments such as coordinate measuring machine should be employed to realize precise evaluation for shrinkages of the sintered parts. It is in fact a necessary way to justify the simulation results.
- The mechanical properties of the sintered parts are dependent of the microstructures. Besides the macroscopic models, the microscopic or mesoscopic models for sintering should also be developed. With the multi-scale modelling, the dimensional changes and the microstructural evolutions of the sintering parts can be predicted simultaneously.
- The more experiments should be conducted to measure the mechanical properties of the sintered components such as strength, elongation and hardness. The numerical models for predicting the mechanical properties can be developed from experimental investigations.

Appendix: Bi-phasic Injection Simulation for Predicting Segregation in PIM

For the prediction of the segregation effects between the powders and binders in the injection process of PIM, the mixture theory is adopted. The compositions of metallic or ceramic powders and binders in feedstock are described distinctly by two different fluid phases, named separately solid and fluid phase. The flows of each phase are represented by two distinct, but coupled stokes equations. Interaction between the flows of distinct phases is taken into account by a momentum exchange term. A brief introduction of the bi-phase model is summarized below.

A.1 Governing Equations Based on Mixture Theory

The volume fractions of each phase, which represent the distribution of their volume proportions at instant t , are assigned to be two field variables ϕ_s and ϕ_f . The mass conservation for each phase in mixture flow allows the detection of their density evolution. So the segregation effect can be determined. The flows of solid and fluid phases possess two co-existent velocity fields \mathbf{V}_s and \mathbf{V}_f . The effective velocity \mathbf{V}_{eff} for their combination, or so-called mixture's velocity, is defined as:

$$\mathbf{V}_{\text{eff}} = \phi_s \mathbf{V}_s + \phi_f \mathbf{V}_f \quad (\text{A.1})$$

A.1.1 Determination of Filling Flow Front

At each instant t in injection course, the domain filled by feedstock in the mould cavities should be known to apply the different flow behaviours. The filled domain is modelled by mixture theory, while a fictive flow model is used in the void portion for modelling the flow of air. The filling state variable F is used to represent the evolution of filled domain with value 1, and the void portion is assigned value 0. This filling state variable is governed by an advection equation:

$$\frac{\partial F}{\partial t} + \nabla \cdot (\mathbf{V}_{\text{eff}} F) = 0 \quad (\text{A.2})$$

A.1.2 Volume Saturation and Mass Conservation

In filled portion, the solid phase and fluid phase use two field variables (ϕ^s, ϕ^f) to represent their volume fraction in the mixture flow. Their values should certainly verify the so-called saturation conditions at each space position:

$$\phi_s + \phi_f = 1 \quad \text{and} \quad \frac{\partial \phi_s}{\partial t} + \frac{\partial \phi_f}{\partial t} = 0 \quad (\text{A.3})$$

The densities of each phase are considered to be intrinsically self incompressible. Their self-densities remain two constants ρ_{s0} and ρ_{f0} . The apparent density for each phase in the mixture is then related to its volume fraction, defined by the following relationship:

$$\rho_s = \phi_s \rho_{s0} \quad \text{and} \quad \rho_f = \phi_f \rho_{f0} \quad (\text{A.4})$$

where ρ_s and ρ_f are respectively the apparent density values in the mixture for solid and fluid phase. Naturally one should verify the mass conservation for the flows of each phase:

$$\frac{\partial \rho_s}{\partial t} + \nabla \cdot (\rho_s \mathbf{V}_s) = 0 \quad \text{and} \quad \frac{\partial \rho_f}{\partial t} + \nabla \cdot (\rho_f \mathbf{V}_f) = 0 \quad (\text{A.5})$$

With the intrinsic incompressibility of each phase, their mass conservation is written as:

$$\frac{\partial \phi_s}{\partial t} + \nabla \cdot (\phi_s \mathbf{V}_s) = 0 \quad \text{and} \quad \frac{\partial \phi_f}{\partial t} + \nabla \cdot (\phi_f \mathbf{V}_f) = 0 \quad (\text{A.6})$$

These two equations in (A.6) are coupled by saturation condition (A.3). They are very important especially in prediction of the segregation effects. The variation of two volume fractions represents directly the change of their proportions in mixture's flow.

The volume saturation and mass conservation for solid and fluid phase results in the incompressibility condition for mixture flow:

$$\nabla \cdot \mathbf{V}_{\text{eff}} = 0 \quad (\text{A.7})$$

A.1.3 Momentum Conservation and Exchange

In powder injection moulding, often the Reynolds number is considered enough small to neglect the advection term in material time derivative of the velocity field [LAN 06]. Then the mixture theory consists of two distinct Stokes equations coupled

by their momentum exchange term $\mathbf{m}_s = -\mathbf{m}_f$. These terms represent the interaction between the distinct flows of different phases. The two coupled Stokes equations are below:

$$\begin{aligned}\rho_s \frac{\partial \mathbf{V}_s}{\partial t} &= -\nabla(\phi_s \mathbf{P}) + \nabla \cdot \boldsymbol{\sigma}'_s + \rho_s \mathbf{g} + \mathbf{m}_s + \mathbf{F}_s^{\text{ext}} \\ \rho_f \frac{\partial \mathbf{V}_f}{\partial t} &= -\nabla(\phi_f \mathbf{P}) + \nabla \cdot \boldsymbol{\sigma}'_f + \rho_f \mathbf{g} + \mathbf{m}_f + \mathbf{F}_f^{\text{ext}}\end{aligned}\quad (\text{A.8})$$

where \mathbf{P} represents the pressure field in the mould. $\boldsymbol{\sigma}'_s$ and $\boldsymbol{\sigma}'_f$ are the deviators of Cauchy stresses which take into account only the effects in same phase. \mathbf{g} is the gravity acceleration. $\mathbf{F}_s^{\text{ext}}$ and $\mathbf{F}_f^{\text{ext}}$ are the external forces acting on the solid and liquid phase respectively.

The coupling terms for momentum exchange are proportional to the difference of velocity fields between solid and fluid phase:

$$\mathbf{m}_s = k(\mathbf{V}_f - \mathbf{V}_s) \quad \text{and} \quad \mathbf{m}_f = k(\mathbf{V}_s - \mathbf{V}_f) \quad (\text{A.9})$$

where k is a interaction coefficient. This coefficient may be identified by an inverse method referring to some experimental tests [RAC 99].

A.2 Viscous Behaviors for Bi-phasic Modelling

Taking into account nature of the mixture, the behaviours of both fluid and solid phase should be non-Newtonian ones. The deviators of stress tensors in fluid and solid phase take the following forms as the functions of temperature, volume fractions and the equivalent value for shear rate tensor:

$$\boldsymbol{\sigma}'_s = 2\mu_s(T, \phi_s, \bar{\dot{\boldsymbol{\epsilon}}}'_s) \dot{\boldsymbol{\epsilon}}'_s \quad \text{and} \quad \boldsymbol{\sigma}'_f = 2\mu_f(T, \phi_f, \bar{\dot{\boldsymbol{\epsilon}}}'_f) \dot{\boldsymbol{\epsilon}}'_f \quad (\text{A.10})$$

where μ_s and μ_f are the viscous behaviors for each phase. $\dot{\boldsymbol{\epsilon}}'_s$ and $\dot{\boldsymbol{\epsilon}}'_f$ are the deviators of their strain rates $\dot{\boldsymbol{\epsilon}}_s$ and $\dot{\boldsymbol{\epsilon}}_f$, named also shear rates. $\bar{\dot{\boldsymbol{\epsilon}}}'_s$ and $\bar{\dot{\boldsymbol{\epsilon}}}'_f$ represent the equivalent values of tensor $\dot{\boldsymbol{\epsilon}}'_s$ and $\dot{\boldsymbol{\epsilon}}'_f$. T indicates the temperature value. In the experimental tests, only behaviors of the mixture are the measurable quantities. The determination of flow behaviors for different phases has induced many significant works [LAN 96], [RAC 99], [LIU 05].

The governing equations are discretized by the finite element method under Eulerian description. The explicit procedures are developed to solve the coupled equations [BAR 01], [BAR 02], [CHE 04]. The numerical simulation software has been developed in LMARC.

Bibliography

- [ASH 90] **Ashby M.F.**, Background Reading HIP 6.0. University of Cambridge, UK, 1990.
- [AYA 05] **Ayad G., Barriere T., Gelin J.C., Song J., Liu B. and Renault D.**, Optimization of the PIM process: Segregation in injection and the parameters for sintering simulation. Proceedings of the First Invited COST 526 Conference on Automatic Process Optimization in Material Technology, Morschach, Switzerland, 30-31May 2005, Ed. by Buche D. and Hofmann N., 2005, pp. 164-173.
- [BAR 00] **Barriere T.**, Expérimentations, modélisation et simulation numérique du moulage par injection de poudre métalliques, Doctoral thesis, Université de Franche-Comté, 2000.
- [BAR 01] **BarriereT, Gelin J.C. and Liu B.**, Experimental and numerical analyses of powder segregations on the properties and quality of parts produced by MIM, Powder Metall., Vol. 44(3), 2001, pp. 228-234.
- [BAR 02] **Barriere T., Gelin J.C. and Liu B.**, Improving mould design and injection parameters in metal injection moulding by accurate 3D finite element simulation, J. Mater. Process. Technolo., Vol. 125-126, 2002, pp. 518-524.
- [BLA 02] **Blaine D. and German, R.**, Simulation of PIM Stainless Steel, Advances in Powder Metallurgy and Particulate Materials-2002, MPIF, Princeton, NJ., 2002, pp. 255-266.
- [BLA 05] **Blaine D.C., Bollina R., Park S.J. and German R.M.**, Critical use of video-imaging to rationalize computer sintering simulation, Compu. Ind., Vol. 56, 2005, 56(9), pp. 967-875.
- [BOR 88 a] **Bordia R.K and Scherer G.W.**, On constrained sintering-I Constitutive model for a sintering body, Acta Metall., Vol. 36(9), 1988, pp. 2393-2397.
- [BOR 88 b] **Bordia R.K. and Scherer G.W.**, On constrained sintering, II. Comparison of constitutive models, Acta Metall., Vol. 39(9), 1988, pp. 2399-2409.
- [BOU 99] **Bouvard D.**, Numerical simulation of sintering and dimensional change of complex parts, Sintering course notes, Ed. by EPMA, 1999, pp. 11-25.

- [BRA 98] **Brandt J. and Nilsson L.**, FE-simulation of compaction and solid-state sintering of cemented carbides, *Mech. Cohes-Frict. Mater.*, Vol. 3, 1998, pp. 181-205.
- [BRA 05] **Braginsky M., Tikare V. and Olevsky E.** Numerical simulation of solid state sintering, *Int. J. Solids Struct.*, Vol. 42, 2005, pp. 621-636.
- [BRO 82] **Brook R.J.**, Fabrication principles for the production of ceramics with superior mechanical properties, *Proc. Br. Ceram. Soc.*, Vol. 32, 1982, pp. 7-24.
- [CAI 97 a] **Cai P.Z., Messing G.L. and Green D.L.**, Determination of the mechanical response of sintering compacts by cyclic loading dilatometer, *J. Am. Ceram. Soc.*, Vol. 80(2), 1997, pp. 445-452.
- [CAI 97 b] **Cai P.Z., Green D.L. and Messing G.L.**, Constrained densification of alumina/zirconia hybrid laminates I: experimental observations of processing defects, *J. Am. Ceram. Soc.*, Vol. 80(8), 1997, pp. 1929-1939.
- [CAI 97 c] **Cai P.Z., Messing G.L. and Green D.L.**, Constrained densification of alumina/zirconia hybrid laminates II: viscoelastic stress computation, *J. Am. Ceram. Soc.*, Vol. 80(8), 1997, pp. 1940-1948.
- [CHE 04] **Cheng Z., Barriere T., Liu B. and Gelin J.C.**, An efficient vectorized approach for the simulation of metal injection molding, *J. Steel Grips.*, Vol.2, 2004, pp. 687-692.
- [CHI 92] **Chidiac S.E., Wilkinson D.S. and Mirza F.A.**, Finite-element modeling of transient heat-transfer and microstructural evolution in welds. II: Modeling of grain-growth in austenitic stainless-steels, *Metall. Trans., B, Process Metall.* Vol. 23(6), 1992, PP. 841-845.
- [COB 58] **Coble R.L.**, Initial sintering of alumina and hematite, *J. Am. Ceram. Soc.*, Vol. 32(5), 1958, pp. 55-62.
- [COB 61] **Coble R.L.**, Sintering crystalline solids. I. Intermediate and final state diffusion models, *J. Appl. Phys.*, Vol. 32(5), 1961, pp. 787-792.
- [COB 63] **Coble R.L.**, A model for boundary diffusion controlled creep in polycrystalline materials, *J. Appl. Phys.*, Vol. 34(6), 1963, pp. 1679-1682.
- [COB 70] **Coble R.L.**, Diffusion models for pressing with surface energy and

- pressure effects as driving force, *J. Appl. Phys.*, Vol. 41 (12), 1970, pp. 4798-4807.
- [COC 01] **Cocks A.C.F.**, Constitutive modeling of powder compaction and sintering, *Prog. Mater. Sci.*, Vol. 46, 2001, pp. 201-229.
- [COR 04] **Cornwall R.G., German R.M.**, Powder injection molding - world markets and technologies, Proceedings of PM2004 Powder Metallurgy World Congress, Vienna, Austria, October 17-21, Publ. EPMA, Shrewsbury, UK, 2004, Vol. 4, pp. 342-347.
- [DEO 84] **Dehoff R.T.**, A cell model for microstructural evolution during sintering, The Sixth International Conference on Sintering and Related Phenomena, 1984, University of Notre Dame, Plenum Press, New York.
- [DU 92] **Du Z. and Cocks A.C.F.**, Constitutive Models for the Sintering of Ceramic Components, *Acta Metall. Mater.*, Vol. 40, 1992, pp. 1969-1994.
- [FAN 03] **Fang T., Shiue J., Shiao F.**, On the evaluation of the activation energy of sintering. *Mater. Chem. Phys.*, Vol. 80, 2003, pp. 108-113.
- [FOL 60] **Folweiler R.C.**, Creep behavior of pore-free polycrystalline aluminum oxide, *J. Appl. Phys.*, Vol. 32 (5), 1961, pp. 773-778.
- [FRE 45] **Frenkel J.**, Viscous flow of crystalline bodies under the action of surface tension, *J. Phys.*, Vol. 9(5), 1945, pp. 385-393.
- [GAS 00] **Gasik M. and Zhang B.**, A constitutive model and FE simulation for the sintering process of powder compacts, *Compu. Mater. Sci.*, Vol. 18, 2000, pp. 93-101.
- [GEL 99] **Gelin J.C., Renualt D. and Barriere T.**, Experiments and computational modeling of sintering for metallic parts, International Conference Sintering 99, November 1-3, Pennsylvania State University, Ed. by German R.M., Penn. State Univ. Press, pp. 212-223.
- [GEL 00] **Gelin J.C. and Renualt D.**, Modelling and simulation of viscoplastic behaviors of metallic powders during solid state sintering, International Conference Metal Forming 2000, September 3-7, In Metal Forming 2000, Ed. by Pietrzyk and *et al.*, Balkema Publ., pp. 223-227.
- [GEL 02] **Gelin J.C., Barriere T. and Liu B.**, Mould design methods by

experiment and numerical simulation in metal injection molding, *J. Eng. Manuf.*, Part B, Vol.216(12), 2002, pp. 1533-1547.

[GEL 05] **Gelin J.C., Ayad G., Barriere T. and Renault D.**, Optimal design of material and process parameters in powder injection moulding, Proceedings of the 8th International Conference on Technology of Plasticity, ICTP 2005, October 9-13, 2005, Verona, Italy.

[GEL 06] **Gelin J.C., Barriere T., Song J. and Liu B.**, Experimental Investigations and Numerical Modelling of Sintering Process for 316L Stainless Steel MIM Components, International Conference on Powder Injection Molding of Metals, Ceramics and Carbides, 20-22 March 2006, Florida, USA.

[GER 96] **German R.M.**, Sintering theory and practice, John Wiley, New York, USA, 1996.

[GER 97] **German R.M. and Bose A.**, Injection moulding of metal and ceramics, MPIF, Princeton, New Jersey, USA, 1997.

[GER 00] **German R.M., Messing G.L. and Cornwall R. G.**, Sintering models move forward, *MPR*, Feb, 2000, pp. 10-13.

[GER 02] **German R.M.**, Computer modeling of sintering processes, *Int. J. Powder Metall.*, 38(2), 2002, pp. 48-66.

[GER 03 a] **German R.M.**, Powder injection molding - design and applications, IMS. Inc., Pennsylvania, USA, 2003.

[GER 03 b] **German R.M.**, Strength evolution in debinding and sintering, Proceedings of the 3rd International Conference on the Science, Technology & Applications of Sintering, September 15-17, 2003, State College, Pennsylvania, USA.

[GER 03 c] **German R.M. and Blaine D.**, New developments in continuum model in sintering, Proceedings of the 3rd International Conference on the Science, Technology & Applications of Sintering, September 15-17, 2003, State College, Pennsylvania., USA.

[GER 04] **German R.M.**, Green body homogeneity effects on sintered tolerances, *Powder Metal.*, Vol. 47, 2004, pp. 157-160.

- [GIL 01] **Gillia O., Gosserond C. and Bouvard D.**, Viscosity of WC-Co compacts during sintering, *Acta Mater.*, 2001, Vol. 49, pp. 1413-1420.
- [HAN 92] **Hansen J.D., Rusin R.P., Teng M.H. and Johnson D.L.**, Combined-stage sintering model, *J. Am. Ceram. Soc.*, Vol. 75(5), 1992, pp. 1129-1135.
- [HE 03] **He Z. and Ma J.**, Constitutive modeling of the densification and grain growth of fine-grained alumina ceramics, *Mat. Sci. Eng. A*, Vol. 361, 2003, pp. 130-135.
- [HE 05] **He Z. and Ma J.**, Constitutive modeling of alumina sintering: grain-size effect on dominant densification mechanism. *Compu. Mater. Sci.*, Vol. 32, 2005, pp. 196-202.
- [HEL 85] **Helle A.S, Easterling K.E and Ashby M.F.**, Hot-isostatic pressing diagrams: new developments, *Acta Metall.*, Vol. 33(12), 1985, pp. 2163-2174.
- [HER 50] **Herring C.**, Diffusional viscosity of a polycrystalline solid, *J. Appl. Phys.*, Vol. 21(5), 1950, pp. 437-445.
- [HER 51] **Herring C.**, Surface tension as a motivation for sintering, In: Kingston WE Ed., *The Physics of Powder Metallurgy*. New York: McGraw-Hill, 1951. pp. 143-179.
- [HOL 01] **Holm E.A. and Corbett C.B.**, The computer simulation of microstructural evolution, *JOM*, Vol. 53 (9), 2001, pp. 20-23.
- [HSU 86] **Hsueh C.H, Evans A.G, Cannon R.M and Brook R.J.**, Viscoelastic stresses and sintering damage in heterogeneous powder compacts. *Acta Metall.*, Vol. 34, 1986, pp. 927-936.
- [JOH 63] **Johnson D.L. and Cutler I.B.**, Diffusion sintering I. initial stage sintering models and their application to shrinkage of powder compacts, *J. Am. Ceram. Soc.*, Vol. 46(11), 1963, pp. 541-545.
- [JOH 03] **Johnson D.L.**, Finding and utilizing the master sintering curves sintering, *Proceedings of the 3rd International Conference on the Science, Technology & Applications of Sintering*, September 15-17, 2003, State College, Pennsylvania, USA.

- [KAN 04] **Kang S.-J.L. and Kang Y.I.**, Sintering kinetics at final stage sintering: model calculation and map construction. *Acta Mater.*, Vol. 52, 2004, pp. 4573-4578.
- [KAS 92] **Kashyap B.P.T.**, Grain growth behavior of type 316L stainless steel, *Mat. Sci. Eng. A: Structural Materials: Properties, Microstructure and Processing*, Vol. 149(2): 1992, pp. 13-16.
- [KIA 05] **Kiani S., Pan J. and Yeomans J.A.**, A practical constitutive laws for finite element analysis of sintering, *Proceedings of the 4th International Conference on the Science, Technology & Applications of Sintering*, August 29-September 1, 2005, Grenoble, France, pp. 224-227.
- [KIM 03] **Kim H., Gillia O. and Bouvard D.**, A phenomenological constitutive model for sintering of alumina powder, *J. Eur. Ceram. Soc.*, Vol. 23, 2003, 1675-1685.
- [KIN 55] **Kingery W.D. and Berg M.**, Study of the initial stages of sintering solids by viscous flow, evaporation-condensation, and self-diffusion, *J. Appl. Phys.*, Vol. 26, 1955, pp. 1205-1212.
- [KOR 05] **Korn K., Kraft T. and Riedel H.**, Modelling of anisotropic shrinkage during liquid phase sintering, *Proceedings of the 4th International Conference on the Science, Technology & Applications of Sintering*, August 29-September 1, 2005, Grenoble, France, pp. 260-263.
- [KOS 05] **Koseski R.P., Suri P., Earharat N.B., German R.M. and Kwon Y.S.**, Microstructural evolution of injection molded gas- and water-atomized 316L stainless steel powder during sintering, *Mat. Sci. Eng. A*, Vol. 390, 2005, pp. 171-177.
- [KRA 00] **Kraft T. and Riedel H.**, Computational optimization of parts produced from ceramic powders, In *Microstructure, mechanical properties and processes EUROMAT 1999*, Vol. 3, ed. Bréchet Y., Wiley-VCH, Weinheim, 2000, pp. 337-342.
- [KRA 02] **Kraft T. and Riedel H.**, Numerical simulation of die compaction and sintering, *Powder Metall.*, Vol. 45(3), 2002, pp. 227-231.
- [KRA 04] **Kraft T. and Riedel H.**, Numerical simulation of solid state sintering: model and application, *J. Eur. Ceram. Soc.*, 24, 2004, pp. 345-361.
- [KUC 49] **Kuczynski G.C.**, Self-diffusion in Sintering of Metallic Particles,

Transactions of the American Institute of Mining, Metallurgical and Petroleum Engineers, Vol. 185(2), 1949, pp. 169-178.

[KWO 03] **Kwon Y.S., Chu S.H., Ahn H.K., Chung S.T., Park S.J., Yoon D.T.S., Choi J.Y., Kim K.T., Park L.J. and Kim J.H.**, CAE analysis for sintering stage of powder injection molding, International Conference on Powder Metallurgy & Particulate Materials, May 13-17, 2001, New Orleans.

[LAM 02] **Lame O., Bouvard D. and Wiedemann H.**, Anisotropic shrinkage gravity induced creep during sintering of steel powder compacts, Powder Metall., Vol. 45(2), 2002, pp. 181-185.

[LAN 96] **Lanteri B., Burlet H., Poitou A. and Campion I.**, Powder injection molding, an original simulation of paste flow, Eur. J. Mech. A Solids, Vol.15(7), 1996, pp. 465-485.

[LEE 03 a] **Lee S.H., Messing G.L. and Green D.J.**, Bending creep test to measure the viscosity of porous materials during sintering, J. Am. Ceram. Soc., Vol. 86, 2003, pp. 877-882.

[LEE 03 b] **Lee S.H., Mohanram A., Messing G.L. and Green D.J.**, Measurement of Viscosity of Sintering Systems, Proceedings of the 3rd International Conference on the Science, Technology & Applications of Sintering, September 15-17, 2003, State College, Pennsylvania, USA.

[LIK 06] **Liksonov D.**, Experimental and numerical study of the manufacturing and behavior of the formal THR components produced by injection molding of fiber composite and by powder technologies, Doctoral thesis, Université de Franche-Comté, 2006.

[LIP 97] **Lippmann H. and Iankov R.**, Mathematical modeling of sintering during power forming processes, Int. J. Mech. Sci., Vol. 39(5), 1997, pp. 585-596.

[LIU 01] **Liu Z.Y., Loh N.H., Khor K.A. and Tor S.B.**, Sintering activation energy of powder injection molded 316L stainless steel, Scripta Mater., Vol.44(7), 2001, pp. 1131-1137.

[LIU 05] **Liu B., Barriere T., Cheng Z. and Gelin J.C.**, The bi-phase simulation of segregation in MIM and phase behaviors , Proceedings of the 8th International

Conference on Technology of Plasticity, ICTP 2005, October 9-13, 2005, Verona, Italy.

[LU 01] **Lu P., German R.M. and Xu X.**, Microstructural evolution and macroscopic behavior during solid state sintering, Powder Metall., Vol 44(4), 2001, pp. 363-368.

[MCM 92] **McMeeking R.M. and Kuhn L.T.**, A Diffusion creep law for powder compacts, Acta Metall., Vol. 40(5), 1992, pp. 961-969.

[MOO 89] **Moon J.R.**, Elastic moduli of powder metallurgy steel, Powder Metall., Vol. 32(2), 1989, pp. 132-139.

[MOR 04] **Mori K., Matsubara H. and Noguchi N.**, Micro-macro simulation of sintering process by coupling Monte Carlo and finite element methods. Int. J. Mech. Sci., Vol. 46, 2004, pp. 841-854.

[MPI 73] **Metal Powder Industries Federation**, MPIF Standard 41, Princeton, NJ 1973.

[NAB 48] **Nabarro F.R.N.**, Report of Bristol conference on the strength of solids. The physical Society, London, 1948.

[NAB 00] **Nabarro F.R.N.**, Grain size, stress and creep in polycrystalline solids, Physics of the Solid States, Vol. 42(8), 2000, pp. 1417-1419.

[NAB 02] **Nabarro F.R.N.**, Creep at very low rate, Metall. Mater. Trans. A, Vol. 33A, 2002, pp. 213-218.

[NET ETH] <http://www.e-thermal.com/dil402c.htm>, NETZSCH Instruments, Inc..

[NET TEC] <http://www.techceramics.com>, Mcdanel advanced ceramic technologies.

[OHA 04] **Ohani T., Ogi H. and Hirao M.**, Change of ultrasonic attenuation and microstructure evolution during creep of a stainless steel, Proceedings of the 16th World Conference on Non Destructive Testing, Montréal, Canada, August 30-September 3, 2004.

[OLE 98] **Olevsky E.A.**, Theory of sintering: from discrete to continuum, Mat. Sci. Eng. R, Vol. 23, 1998, pp. 41-100.

[OLE 00 a] **Olevsky E.A. and German R.M.**, Effect of gravity on dimensional change during sintering-I shrinkage anisotropy, Acta Mater., Vol. 48, 2000, pp. 1153-1166.

- [OLE 00 b] **Olevsky E.A., German R.M. and Upadhyaya A.**, Effect of gravity on dimensional change during sintering- II shape distortion, *Acta Mater.*, Vol. 48, 2000, 1167-1180.
- [OLE 00 c] **Olevsky E.A. and Molinari A.**, Instability of sintering of porous bodies, *Int. J. Plast.*, Vol.16, 2000, pp. 1-37.
- [OLE 01] **Olevsky E.A., Shoales G.A. and German R.M.**, Temperature effects on strength evolution under sintering, *Mater. Res. Bull.*, Vol. 36, 2001, pp. 449-459.
- [OLE 05] **Olevsky E.A., Maximenko A. and Tikare V.**, On multi-scale modeling of sintering, *Proceedings of the 4th International Conference on the Science, Technology & Applications of Sintering*, August 29-September 1, 2005, Grenoble, France, pp. 228-231.
- [OPF 98] **Opfermann J., Blumm J. and Emmerich W.D.**, Simulation of sintering behavior of a ceramic green body using advanced thermo-kinetic analysis, *Thermochim. Acta*, Vol. 318, 1998, pp. 213-220.
- [PAN 05] **Pan J. and Ch'ng H.**, Virtual power principle and sintering models at particle scale, *Proceedings of the 4th International Conference on the Science, Technology & Applications of Sintering*, August 29-September 1, 2005, Grenoble, France, pp. 244-247.
- [PER 04] **Peterson A. and Agren J.**, Constitutive behavior of WC-Co materials with different grain size sintered under load, *Acta Mater.*, 2004, Vol. 52, pp. 1847-1858.
- [RAC 99] **Racineux G.**, Rhéologie des pâtes minérales, cas du mélange TiO₂-HNO₃ destiné à l'extrusion de supports de catalyseurs, *Doctoral thesis*, École Normale Supérieure de Cachan, 1999.
- [RAH 03] **Rahaman M.N.**, *Ceramic Processing and Sintering*, 2nd ed., Marcel Dekker Inc., New York, USA, 2003.
- [REI 04] **Reiterer M., Kraft T., Janosovits U. and Riedel H.**, Finite element simulation of cold isostatic pressing and sintering of SiC components, *Ceram. Int.*, Vol. 30(2), 2004, pp. 177-183.

- [REN 01] **Renault D., Barriere T. and Gelin J.C.**, Numerical Simulations based on a micro-macro scale model for solid state sintering, 7th Int. Conf. in Numerical Methods in Forming Process, NUMIFORM 2001, Toyohashi, Japan, 18-20 June, In Simulation of Materials processing, Ed. By Mori K.I., Balkema Publ., pp. 227-232.
- [RIE 94] **Riedel H., Kozak V. and Svoboda J.**, Equilibrium pore surfaces, sintering stresses and constitutive equations for intermediate and late stages of sintering - Part II: Diffusional densification and creep, Acta Metall., Vol. 42, 1994, pp. 445-452.
- [SCH 97] **Schaff W. and Wieters K.P.**, Powder metallurgy: Processing and materials, EPMA, Shrewsbury, UK, 1997.
- [SHI 99] **Shinagawa K.**, Micromechanical modeling of viscous sintering and a constitutive equation with sintering stress, Compu. Mater. Sci., Vol.13, 1999, pp. 276-285.
- [SHO 99] **Shoales G.A. and German R.M.**, Combined effects of time and temperature and strength evolution using integral work-of-sintering concepts, Met. Mat. Trans. A, Vol. 30, 1999, pp. 465-470.
- [SKO 72] **Skorohod V.V.**, Rheological basis of theory of sintering, Naukova Dumka, Kiev, 1972.
- [SON 05] **Song J., Ayad G., Barriere T., Gelin J.C., Liu B. and Renault D.**, Modelling, simulation and identification of the solid state sintering after metal injection moulding, The 8th International Conference on Material Forming ESAFORM 2005, 27-28 April 2005, Cluj-Napoca, Romania, Proceedings of the 8th Esaform Conference on Material Forming, Ed. by Banabic D., Publ. by The Publishing House of The Romain Academy, Buchrest, Romania, 2005, Vol. 1, pp. 171-174.
- [SON 06 a] **Song J., Barriere T., Gelin J.C. and Liu B.**, Modelling and identification of physical and process parameters in solid state sintering of metallic powders after injection moulding , International Conference on Material Forming ESAFORM 2006, 26-28 April 2006, Glasgow, UK, Proceedings of the 9th Esaform Conference on Material Forming, Ed. by Juster N. and Rosochowski A., Publ. Publishing House Akapit, Krakow, Poland, 2006, Vol. 1, pp. 55-58.

[SON 06 b] **Song J., Gelin J.C., Barriere T. and Liu B.**, Experiments and numerical modelling of solid state sintering for 316L stainless steel components, *J. Mater. Process. Technol.*, Vol. 177, 2006, pp. 352-355.

[SON 06 c] **Song J., Barriere T., Liu B. and Gelin J.C.**, FE simulation on the uneven shrinkage and distortion of 316L stainless steel MIM components during sintering process, Euro PM2006 Congress & Exhibition, Ghent, Belgium, 23-25 October 2006, Proceedings of Euro PM 2006, Publ. by EPMA, Shrewsbury, UK, Vol. 2, pp. 11-16.

[SUR 03] **Suri P., Heaney D.F. and German R.M.**, Defect-free sintering of two material powder injection molded component Part II. Model, *J. Mater. Sci.*, Vol. 38, 2003, pp. 4875-4881.

[SVO 94] **Svoboda J., Riedel H. and Zipse H.**, Equilibrium pore surfaces, sintering stresses and constitutive equations for intermediate and late stages of sintering - Part I: Computation of equilibrium surfaces, *Acta Metall.*, Vol. 42, 1994, pp. 435-443.

[SVO 95] **Svoboda J. and Riedel H.**, New solutions describing the formation of interparticle necks in solid-state sintering, *Acta Metall. Mater.*, Vol. 43(1), 1994 pp. 1-10.

[TIK 03] **Tikare V., Braginsky M.V., Garino T. and Argüello J.G.**, Numerical simulation of sintering at multiple length scales, Proceedings of the 3rd International Conference on the Science, Technology & Applications of Sintering, September 15-17, 2003, State College, Pennsylvania, USA.

[VAG 05] **Vagnon A., Bouvard D. and Kapelski G.**, An anisotropic constitutive model for simulating the sintering of stainless steel powder compacts, Proceedings of the 4th International Conference on the Science, Technology & Applications of Sintering, August 29-September 1, 2005, Grenoble, France, pp. 232-235.

[XU 02 a] **Xu X., Yi W. and German G.M.**, Densification and strength evolution in solid-state sintering : Part I Experimental investigation , *J. Mater. Sci.*, Vol. 37, 2002, pp. 567-575.

[XU 02 b] **Xu X., Lu P. and German R.M.**, Densification and strength evolution in solid-state sintering: Part II Strength model, *J. Mater. Sci.*, Vol. 37, 2002, pp.

117-126.

[ZAV 00] **Zavaliange A. and Bouvard D.**, Numerical simulation of anisotropy in sintering due to prior compaction, *Powder Metal.*, Vol. 36(7), 2000, pp. 58-65.

[ZHA 02 a] **Zhang R., Engel R.S., Salamon N.J. and German R.M.**, Finite element analysis on the sintering of stainless steel 316L powder compacts, PM2TEC2002 World Congress on Powder Metallurgy & Particulate Materials, June 16-21, 2002, Orlando, FL.

[ZHA 02 b] **Zhang R., Engel R.S., Salamon N.J. and German R.M.**, Simulation of free sintering shrinkage and distortion behavior of stainless steel powder compacts, 2002 International Conference on Process Modeling in Powder Metallurgy & Particulate Materials, Oct. 28-29, 2002, Newport Beach, CA.

[ZHA 05] **Zhang R.**, Numerical simulation of solid-state sintering of metal powder compact dominated by grain boundary diffusion, Doctoral thesis, The Pennsylvania State University, 2005.

[ZUO 04] **Zuo R., Rodel J. and Easterling K.E.**, Temperature dependence of constitutive behavior for solid-state sintering of alumina, *Acta Mater.*, Vol. 52, 2004, pp. 3059-3067.

Vita

Jiupeng Song

Jiupeng Song was born in Rugao, China on September 29, 1978. He received his B.S. and M.S. in Automotive Engineering from Southwest Jiaotong University in Chengdu, China in 1999 and 2002 respectively. He had been employed as an engineer for stamping process in Sichuan Chengfei Integration Tech. Inc. in Chengdu from June 2002 to February 2004. In March 2004, he became a co-tutorial Ph.D. candidate between Southwest Jiaotong University and Franche-Comté University in Besançon, France. His research interests include powder injection moulding, sintering, stamping and finite element analysis.